Origin of the Galactic center non-thermal diffuse emission

Dilruwan Dehiwalage Don

THÈSE

Pour obtenir le grade de

DOCTEUR DE L'UNIVERSITÉ GRENOBLE ALPES

École doctorale : PHYS - Physique
Spécialité : Astrophysique et Milieux Dilués
Unité de recherche : Institut de Planetologie et d'Astrophysique de Grenoble

Origine de l'émission diffuse non-thermique détectée au centre Galactique

Origin of the Galactic center non-thermal diffuse emission

Présentée par :

Dilruwan DEHIWALAGE DON

Direction de thèse :

Gilles HENRI PROFESSEUR DES UNIVERSITES, UNIVERSITE GRENOBLE ALPES	Directeur de thèse
Maïca CLAVEL CHARGEE DE RECHERCHE, CNRS - Délégation Alpes	Co-encadrante de thèse

Rapporteurs :

REGIS TERRIER
DIRECTEUR DE RECHERCHE, CNRS ILE-DEFRANCE VILLEJUIF
DARYL HAGGARD
ASSOCIATE PROFESSOR, MCGILL UNIVERSITY

Thèse soutenue publiquement le **30 septembre 2024**, devant le jury composé de :

CECILIA CECCARELLI, ASTRONOME, UNIVERSITE GRENOBLE ALPES	Présidente
REGIS TERRIER, DIRECTEUR DE RECHERCHE, CNRS ILE-DEFRANCE VILLEJUIF	Rapporteur
DARYL HAGGARD, ASSOCIATE PROFESSOR, MCGILL UNIVERSITY	Rapporteure
ANNE DECOURCHELLE, DIRECTRICE DE RECHERCHE, CEA CENTRE DE PARIS-SACLAY	Examinatrice
PIERRE CRISTOFARI, ASTRONOME ADJOINT, OBSERVATOIRE DE PARIS	Examinateur

Contents

List of Figures

List of Tables

Chapter 1

Introduction

1.1 The Galactic Center Environment

The center of our Milky Way galaxy, hereafter referred to as the Galactic Center (GC), located $\sim 8\,\mathrm{kpc}$ from Earth, is one of the fascinating astronomical regions we can study. Central regions of galaxies are extremely dense in mass and energy. The enormous amount of matter in these regions initiates a wide range of physical processes, offering insights into high-energy astrophysics and the dynamics of galactic nuclei. The GC is by far the closest galactic nucleus to Earth, hosting an extremely large number of astronomical sources, including supernova remnants (SNRs), pulsar wind nebulae (PWNe), extensive molecular clouds (MCs), as well as vast star-forming regions. The densest region in the GC is called the Central Molecular Zone (CMZ). It is a thin layer of molecular material but makes up about 10% of the total neutral mass of the Galaxy (Morris & Serabyn 1996). Last but not least, the GC includes one of the most interesting sources, the nearest supermassive black hole (SMBH) to us, known as Sagittarius $A^\star$ (Sgr $A^\star$).

The GC cannot be viewed in visible light due to the massive interstellar dust along the line of sight. This dust scatters and absorbs light, obscuring our view like a fog obscures the view through a window. However, thanks to scientific advancements and new observational techniques and instruments, we can now penetrate this dust curtain using other electromagnetic (EM) wavelengths like radio, infrared, and X-rays. The GC is observable from Earth in radio frequencies due to continuum and molecular line emissions. In the far infrared, visibility decreases due to intense foreground emissions from dust. However, the GC becomes observable again in the near-infrared (NIR) range. NIR emissions are primarily from young, massive stars and older, cooler stars. The substantial dust present also effectively blocks observations in the ultraviolet (UV) bands since interstellar dust absorbs most strongly at UV wavelengths. The GC is observable again in the higher energies of X-rays and γ-rays, which can penetrate the dense interstellar medium along the Galactic Plane. This thesis will examine a specific type of X-ray emission prevalent in the GC region.

Contents

1.1.1 Multi-Wavelength View of the Galactic Center

1.1.1.1 Radio View of the Galactic Center

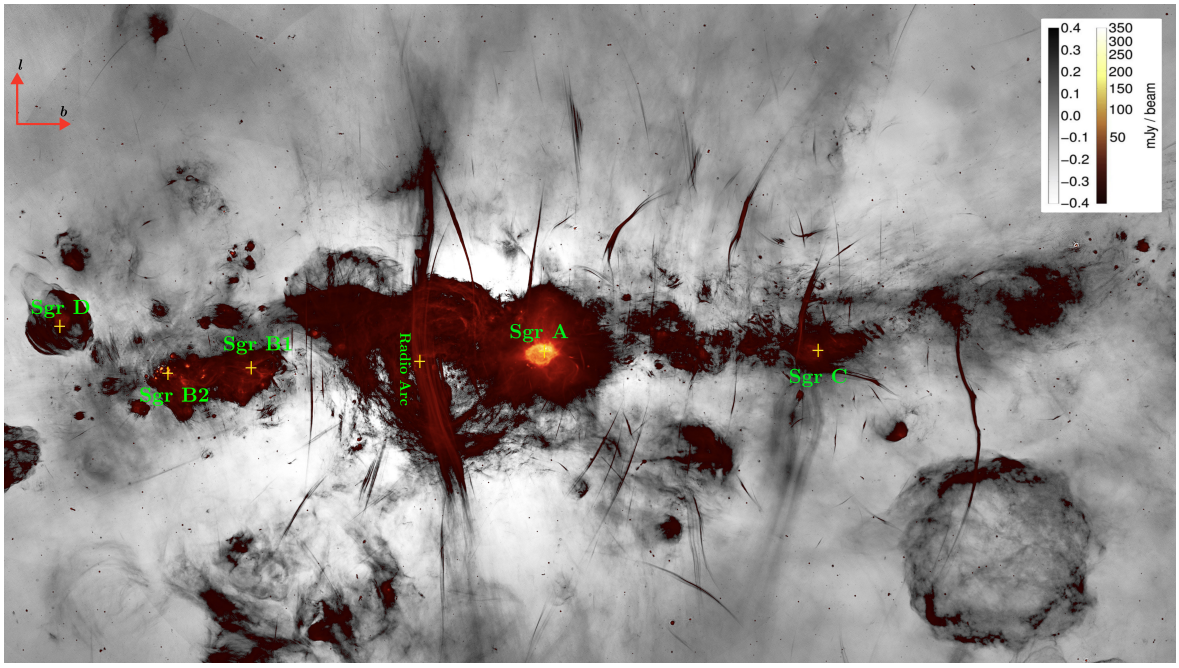

Figure 1.1: The full MeerKAT total intensity mosaic of the GC with the Galactic plane running horizontally across the image. This image covers 6.5 square degrees of the GC at an angular resolution of 4″. It features dual color schemes: a linear greyscale for the faint end and a heat map for the bright end. Several regional radio features are labeled, including major cloud complexes Sgr B1, B2, C, and D. *Figure from Heywood et al. (2022).*

Radio wavelengths occupy the longest wavelength regime of the EM spectrum, spanning from 1 mm to thousands of kilometers. These longer wavelengths are significantly larger than the dust particles and gas molecules in the interstellar medium (ISM). Consequently, the ISM exhibits a low absorption coefficient for radio waves. Earth's atmosphere is also transparent to radio waves within specific frequency bands, enabling detection by ground-based radio telescopes. In 1932, Karl Jansky observed radiation coming from the rough direction of the GC based on noise patterns in his instruments

(Jansky 1933). Since then, radio waves have become one of the most extensively studied bands in the electromagnetic spectrum.

A major milestone in GC radio astronomy was the detection of Sgr $A^\star$ (Balick & Brown 1974a). Radio observations have also mapped the magnetic field structures in the GC, filaments, and SNRs, primarily due to synchrotron radiation.[1] Moreover, radio waves detect emission lines from various molecules in the GC region. A common line used to trace gas in molecular clouds (MCs) is the CS (1-0) line. Furthermore, key instruments and missions, including the Very Large Array (VLA), the Atacama Large Millimeter/submillimeter Array (ALMA), and the Green Bank Telescope (GBT), have been pivotal in advancing our understanding of the radio universe. In 2022, a comprehensive survey using 1.28 GHz radio waves was conducted with the MeerKAT radio telescope (Heywood et al. 2022). This survey uncovered radio emissions from various phenomena in the GC with unprecedented clarity and detail (see Figure 1.1). The Radio Arc is visible in Figure 1.1 and comprises several filamentary structures. These structures, called non-thermal radio filaments (NRFs), are also found throughout the inner GC region in radio waves.

In this dissertation, I study molecular lines from the GC obtained from the MOPRA 3mm CMZ survey.

1.1.1.2 Submillimeter/Far-infrared View of the Galactic Center

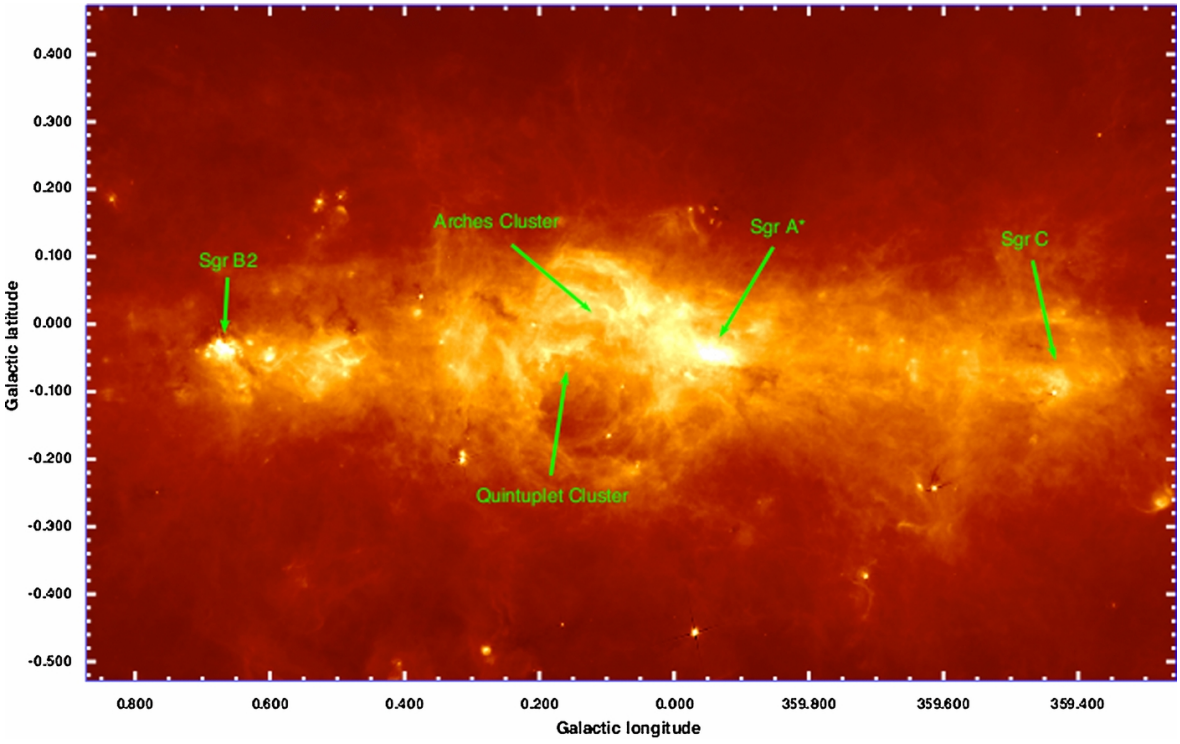

Figure 1.2: Herschel PACS 70 μm image of the GC region. *Figure from Molinari et al. (2011).*

Submillimeter/sub-mm (wavelengths from 0.3 mm to 1 mm) and far-infrared (FIR) (25 μm to 350 μm) astronomy, photons occupy the shorter wavelengths in the EM spectrum compared to radio waves. Infrared and sub-mm astronomy development began in the mid-20th century, opening another fascinating window into the GC. The ISM has a moderate absorption coefficient for these wavelengths,

[1] Synchrotron emission is the radiation produced when charged particles are accelerated in magnetic fields.

allowing them to pass through with relatively less attenuation than visible light. However, Earth's atmosphere poses a challenge for ground-based observations due to significant absorption by atmospheric water vapor.

Sub-mm and FIR wavelengths are excellent tracers of gas's physical conditions and chemistry in extreme star-forming environments (Santa-Maria et al. 2021). These wavelengths are crucial for studying cold dust, warm gas, and star-forming regions such as the CMZ in the GC. The CMZ was observed in the sub-mm band and observed similar structures to the radio band (Pierce-Price et al. 2000). Figure 1.2 shows a Herschel 70 μm image of the GC (Molinari et al. 2011). Sgr $A^{\star}$ surroundings and Sgr B2 are the brightest spots, filling the entire area with intense FIR emission. Moreover, a large bubble-like structure dominates at 70 μm from $0^{\circ} \leq l \leq +0^{\circ}.20$ (Molinari et al. 2011).

1.1.1.3 Near Infrared View of the Galactic Center

Near Infrared (NIR) astronomy spans wavelengths from 0.7 to 5 microns. For wavelengths under 1 micron, NIR observations are similar to those in visible light but require special infrared detectors at wavelengths beyond 1 micron. NIR observations have also led to significant discoveries, such as the detailed mapping of stellar distributions, including stars and star clusters like old, cool red giants, in the GC. One notable discovery is the NIR excess and recombination-line emitting source, the Dusty S-cluster Object called DSO/G2 in the GC (Gillessen et al. 2012). NIR light can distinguish cooler and older stars from hotter, younger stars more effectively than visible light. Instruments such as the Keck Observatory, the Very Large Telescope (VLT), and the Hubble Space Telescope's Near Infrared Camera and Multi-Object Spectrometer (NICMOS) have been used in NIR astronomy since the 1990s. Figure 1.3 shows the view of the GC obtained from the NICMOS instrument. NICMOS reveals a large number of massive stars distributed throughout the GC. These massive stars are mainly confined to one of the three known clusters of massive stars in the GC: the Central cluster, the Arches cluster, and the Quintuplet cluster. These three clusters are easily seen as tight concentrations of bright, massive stars. However, Figure 1.3 shows that these massive clusters are not the only places where massive stars are confined.

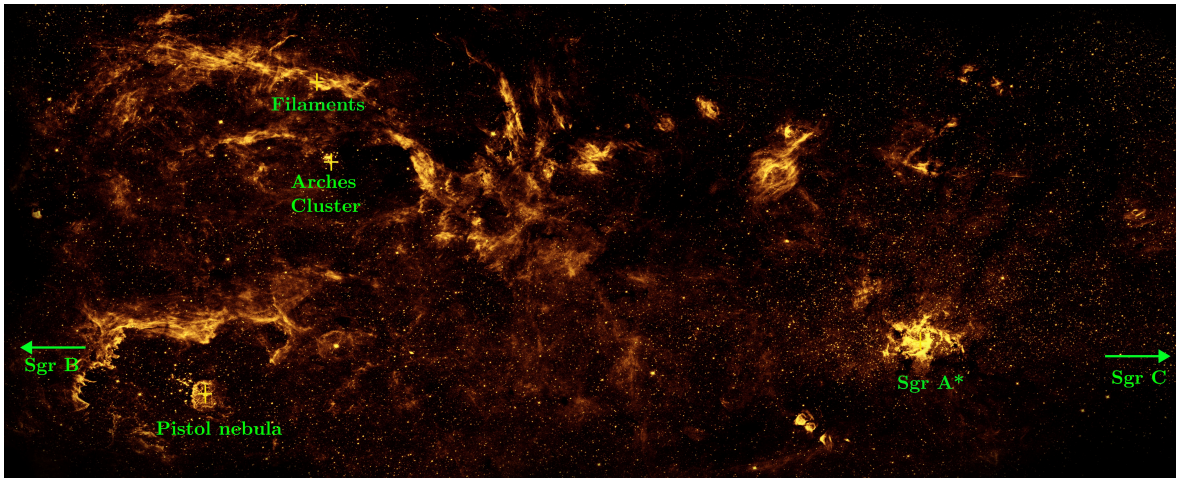

Figure 1.3: The near-infrared light captured by NASA's Hubble Space Telescope NICMOS instrument from GC in 2008. *Figure from NASA/ESA/STScI/D.Wang et al.*

NASA's James Webb Space Telescope (JWST) has recently revolutionized NIR astronomy with its advanced instrumentation, including the Near Infrared Camera (NIRCam) and Near Infrared Spectrograph (NIRSpec), offering the best sensitivity and resolution ever recorded for NIR instruments. Its large primary mirror and cool operating temperature allow hours of exposure to faint, distant objects

and the penetration of dust-obscured regions. Webb's first observation in the GC revealed $\sim$ 500,000 stars shining in the Sgr C region.

1.1.1.4 High Energy View of the Galactic Center

The GC reveals a new level of information when observed in the higher energy part of the electromagnetic spectrum. High-energy astrophysics focus on the X-ray and γ-ray regimes, which reveal unique features and processes that remain hidden at lower energies. This thesis primarily revolves around the X-ray perspective of the GC, which we will extensively discuss throughout this manuscript; we will limit our discussion to the global X-ray properties of the GC. Astronomers commonly use energy measurements instead of wavelengths to present their findings in this spectral regime.

X-rays

The X-ray waveband ranges from approximately 0.1 to 100 keV. The consensus of GC X-ray astronomy is that most of the X-ray emission from the GC comes from bright transient and persistent point sources (Muno et al. 2003, 2009). Thousands of persistent and transient point-like X-ray sources are embedded in the GC, including active stars, bright accreting binary systems, quiescent massive bodies, and cataclysmic variables. Figure 1.4 shows these sources in a composite image created from observations of the GC taken by the Chandra, HST, and Spitzer observatories (Wang & Stolovy 2009). It covers various wavelengths such as X-ray, IR, and NIR light, providing a multi-wavelength view of the GC ecosystem.

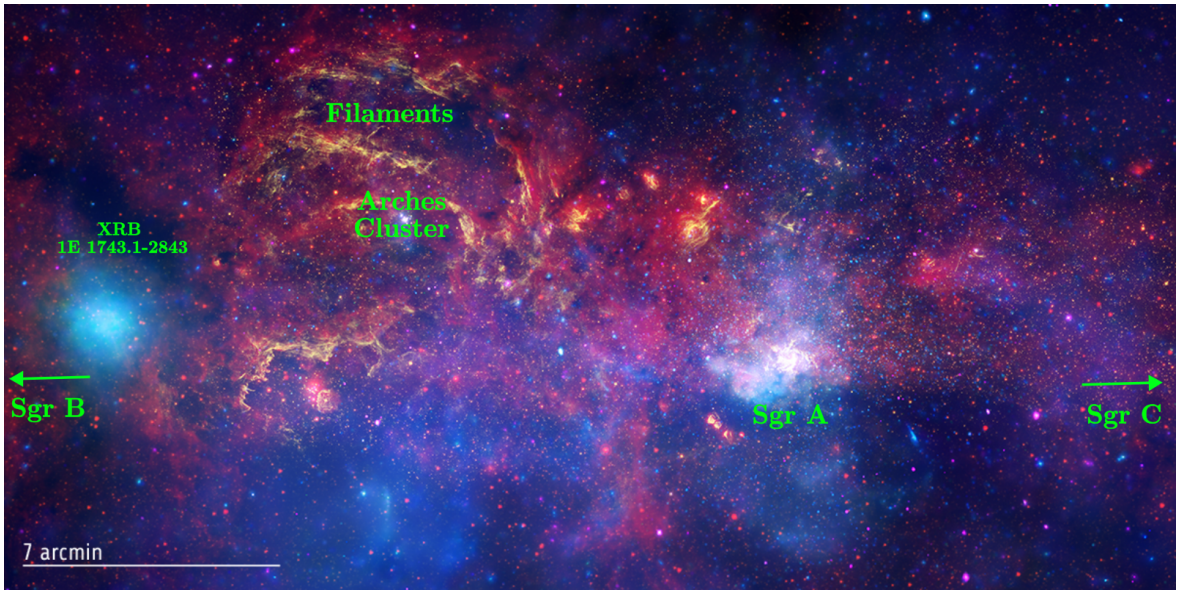

Figure 1.4: The global GC ecosystem. Yellow represents NIR observations from Hubble, red represents IR observations from Spitzer, and blue and violet represent X-ray observations from Chandra. *Figure from Wang & Stolovy (2009).*

Apart from the rich point source population, the GC also emits diffuse X-rays. This diffuse emission will be the topic of this thesis and will be discussed in the forthcoming chapters.

γ-rays

Gamma (γ)-rays are photons with energy greater than $\sim$ 100 keV. They can penetrate the ISM and provide valuable insights into the most energetic and violent processes occurring in the GC. Instruments such as the Fermi Gamma-ray Space Telescope (McEnery et al. 2012) and HESS (High Energy Stereoscopic System) have detected high-energy gamma-ray emissions from the GC (Goodenough & Hooper 2009; Aharonian et al. 2004). γ-ray observations reveal the presence of cosmic rays interacting with the interstellar material and the energetic processes associated with the supermassive black hole Sgr A*.

1.1.2 Key Objects in the Galactic Center Relevant to This Study

1.1.2.1 Sagittarius A*

The GC's supermassive black hole (SMBH) has been extensively studied for many years through theoretical research and observations across the electromagnetic spectrum. It is now clear that the GC contains an SMBH with an estimated mass of $4.3 \times 10^6\, M_\odot$ (Gillessen et al. 2017) at a distance of 8.2 kpc (GRAVITY Collaboration et al. 2019). The radio counterpart of this SMBH is named Sagittarius A* (Sgr A*) (Balick & Brown 1974b). The Eddington limit, which is the maximum luminosity at which the gravitational pressure of the SMBH balances the outward radiation pressure, is given by:

$$L_{\rm Edd} = 1.3 \times 10^{38} \left(\frac{M}{M_\odot} \right) \text{ erg/s} \tag{1.1}$$

$L_{\rm Edd}$ depends solely on the mass M of the body. For a mass of $4.3 \times 10^6\, M_\odot$, $L_{\rm Edd}$ can be calculated as 5.6×10^{44} erg/s. The first detection of an X-ray source coinciding with Sgr A* was made by Chandra in 2001 (Baganoff et al. 2001, 2003). Its position coincides within $0\farcs27 \pm 0\farcs18$ of Sgr A*. The calculated bolometric luminosity of $\sim 10^{33}$ erg/s is about ten orders of magnitude below the $L_{\rm Edd}$. However, Sgr A* undergoes short periods of regular flaring activity (a rate of about one event per day) lasting a few hours. During these flares, the X-ray luminosity can surpass its quiescent luminosity by up to two orders of magnitude (Neilsen et al. 2013). This behavior changes in the NIR wavelength range. NIR flares seem to recur more frequently (2–6 events per day), ranging from 1-2 hours (main flares) down to 7-10 minutes (sub-flares) as observed by the VLT (Genzel et al. 2003).

Over the past two decades, the scientific community has raised an intriguing question: Has Sgr A* always been so dim?, or Has it undergone periods of activity far higher than its current flaring suggests? Presently, it appears that the latter is correct. There is compelling evidence indicating that Sgr A* has experienced intense periods of past activity, such as the diffuse Fe Kα emission from the MCs in the GC area (Koyama et al. 1996). These emissions are now believed to result from the past activities of Sgr A*.

1.1.2.2 Cataclysmic Variables and Other X-ray Point Sources

Over the past two decades, a large number of X-ray sources with luminosities between 10^{31} and 10^{33} erg/s have been observed in the GC environment (Muno et al. 2009). For example, Muno et al. (2003) identified a large population of approximately 2000 faint, spectrally hard X-ray sources associated with the central 40 pc around Sgr A* using the Chandra X-ray Observatory. Based on the spectral hardness and the X-ray luminosity, these sources in the GC have been inferred to belong to a class of stars called cataclysmic variables (CVs) (Muno et al. 2003, 2004a; Zhu et al. 2018; Perez et al. 2019).

Cataclysmic Variables

Cataclysmic variables (CVs) are binary systems in close proximity, consisting of a white dwarf accretor and a low mass (spectral types K or M) donor star. The transfer of matter from the donor star to the white dwarf occurs through Roche lobe overflow[2]. CVs can be divided into two categories: magnetic and non-magnetic. In non-magnetic CVs, the transferred material forms an accretion disc before being deposited onto the surface of the white dwarf. CVs with white dwarfs possessing magnetic fields between 1 and 20 MG are known as intermediate polars (IPs). In these IP systems, the accretion disc is disrupted, and the material follows magnetic field lines to the magnetic poles of the white dwarf. When the magnetic field strength of the white dwarf exceeds 20 MG, the CV is termed a polar. In polars, the strong magnetic field prevents the formation of an accretion disc, causing the material to flow directly to the poles of the white dwarf. The majority of the CVs in the GC are magnetic systems (IPs), though non-magnetic CVs are also present in the dynamic GC environment (Mukai 2017; Xu et al. 2019). To identify CVs, spectral analysis shows a cumulative spectrum with strong iron emission lines at 6.4, 6.7, and 6.97 keV (Nobukawa et al. 2016).

Other Point Sources

In addition to CVs, there are many other astrophysical sources in the GC. An X-ray binary (XRB) is a binary system where the compact object is either a black hole or a neutron star. XRBs are further classified as either low- or high-mass X-ray binaries (LMXB/HMXB) depending on the spectral type of the companion star. LMXBs have companion stars of spectral type A or later, whereas HMXBs contain early-type OB supergiants and Be companions. Figure 1.4 shows an example of a prominent LMXB called 1E 1743.1-2843 (Watson et al. 1981) in the GC environment.

1.1.2.3 The Sgr B: A Starburst in the Galactic Center

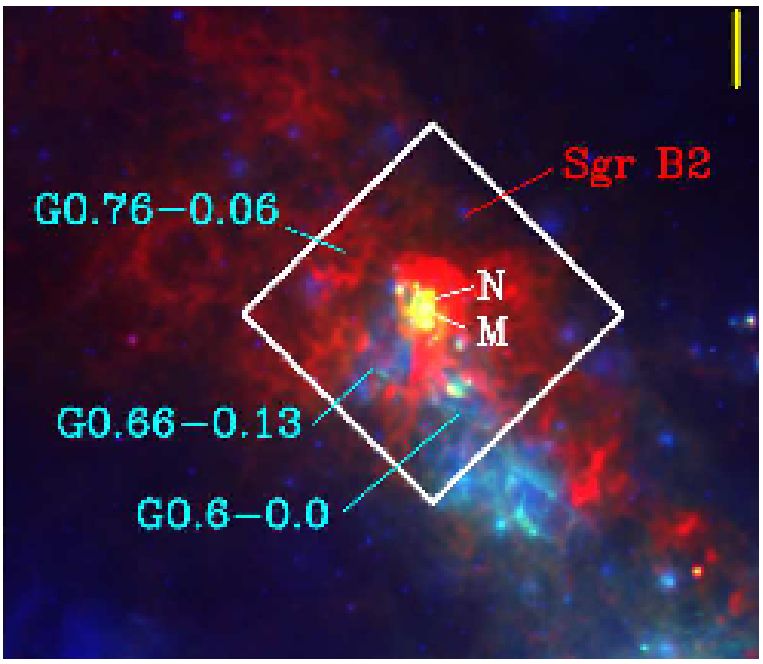

Figure 1.5: RGB view of the Sgr B/B2 region in the GC. Red: SPIRE 350µm tracing cold dust from the most prominent molecular clouds. Green: PACS 70µm tracing warm dust, mostly in extended PDR-like environments. Blue: MIPS 24µm tracing hot dust, mostly from ionized regions. The image is in the Equatorial Coordinate System. Figure from Santa-Maria et al. (2021).

[2]Roche lobe overflow refers to the process in binary star systems where the outer envelope of the donor star extends beyond its Roche lobe, causing the material to transfer to the accretor.

The central few hundred parsecs of the GC contain extremely massive MCs, including several of the most massive clouds in the Galaxy (Morris & Serabyn 1996). These are mostly contained in the CMZ; however, star formation is currently restricted to a few regions like Sgr B, which is known for its rich chemical diversity. The Sgr B molecular complex consists of several subregions, such as Sgr B1, Sgr B2, and G0.66-0.13, each contributing significantly to our understanding of the ISM and star formation processes.

Sgr B2 is the most massive molecular cloud in the entire Galaxy, with ongoing high mass star formation and lines of sight gas column densities above $N_{\rm H} \geq 10^{24}\,{\rm cm}^{-2}$. Sgr B2 is one of the most luminous star-forming regions in the galaxy ($\sim 10^7\,L_\odot$) (Goldsmith et al. 1992). Sgr B is located at a projected distance of $\sim$ 100 pc from the dynamical center of the GC. Figure 1.5 shows the multiwavelength view of Sgr B. Sgr B2 contains three main high-mass star-forming cores: Sgr B2(N), Sgr B2(M), and Sgr B2(S). Each of these cores is embedded in moderate density MCs with $n({\rm H}) \sim 10^5\,cm^{-3}$ and is collectively covered by a large envelope of approximately 40 pc (Santa-Maria et al. 2021). The heating mechanism of the molecular gas in Sgr B2's envelope remains an area of active research. In the X-ray regime, Sgr B2 is notable as the first molecular cloud from which a strong 6.4 keV Fe $K\alpha$ line was discovered (Koyama et al. 1996). The complete analysis of the X-ray observations of Sgr B2 (Sgr B) will be detailed throughout this dissertation.

G0.66–0.13 Further to the east in Figure 1.5, we find the G0.66–0.13 region. This MC was first reported in hard X-ray observations with NuSTAR (Zhang et al. 2015). Zhang et al. (2015) suggested G0.66–0.13 as a molecular clump and a local column density peak. In addition, this region, which appears to have a hollow hemispherical structure, is likely a site of ongoing cloud-cloud collision (Tsuboi et al. 2015). This MC plays an intriguing role in our study, and we will return to it in future discussions.

1.2 Diffuse X-ray Emission in the Galactic Center

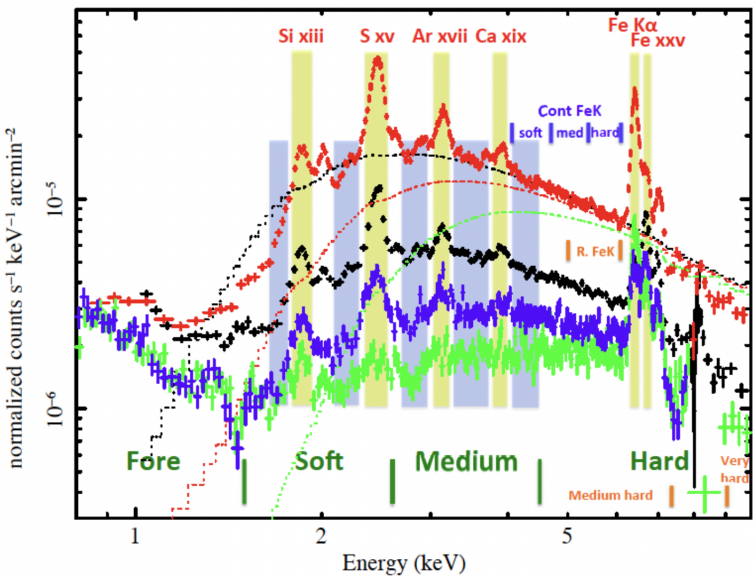

Figure 1.6: XMM-Newton EPIC-pn spectra from various regions within the GC. The central coordinates of each region are color coded as follows: red indicates $l = 0.11°, b = -0.11°$; black represents $l = 359.77°, b = -0.09°$; green denotes $l = 0.687°, b = -0.146°$; and blue corresponds to $l = 0.505°, b = -0.054°$. Specific energy bands are highlighted for analyzing neutral and ionized Fe lines. *Figure from Ponti et al. (2015).*

The diffuse X-ray emission observed in the GC originates from a diverse array of sources and mechanisms. This emission provides a unique window into the physical conditions and dynamics prevalent

in the GC. Despite extensive research, the exact origin and nature of this radiation remain subjects of ongoing investigation. In this review, I explore the three main spectral components of the diffuse X-ray landscape in the GC.

1. A warm plasma with a temperature of approximately 1 keV.
2. A hotter plasma with temperatures of 6 to 8 keV.
3. A non-thermal component modeled by a power-law continuum and an emission line from neutral iron at 6.4 keV.

Figure 1.6 illustrates these components with XMM spectra of the extended emission from several regions within the CMZ. Notably, photoelectric absorption plays a significant role in shaping the observed X-ray spectra. This effect profoundly impacts all X-ray emission components due to the dense ISM along the line of sight. X-ray photons from the GC are absorbed by the inner shell electrons of atoms within the ISM, effectively removing these photons from the flux reaching Earth. This not only diminishes the intensity of the X-ray signals but also modifies the spectral profile of the emissions. Photoelectric absorption is highly dependent on photon energy, with low-energy photons (below $E \leq 2$ keV) being more susceptible and fully absorbed (see Fig.1.6). Lower-energy X-rays are more readily absorbed by atoms in the medium, reducing their number relative to high-energy X-rays reaching X-ray detectors. Consequently, the observed X-ray spectrum tends to have a higher average energy than the original spectrum emitted by the source, making the spectrum appear harder. The absorption towards the GC is assumed to be uniform over the CMZ, with a value of $N_H = 6 \times 10^{22}$ cm^{-2} (Ryu et al. 2009).

1.2.1 Warm Plasma

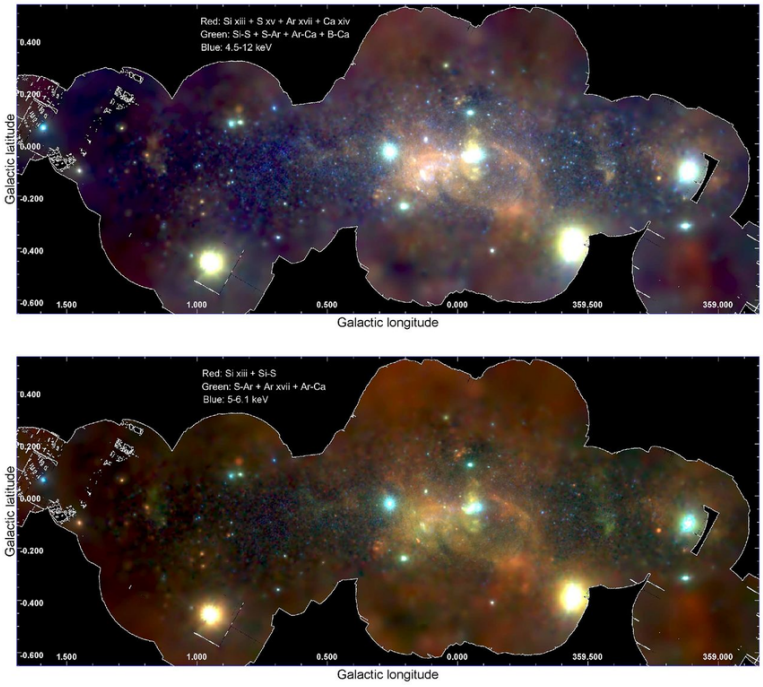

Figure 1.7: (Top panel) RGB image of the soft lines (continuum unsubtracted). The Si XIII (in red), S XV (in green), and a combination of Ar XVII and Ca XIX (in blue). (Bottom panel) RGB image representing the energy bands between soft emission lines. The Si-S band emission (in red), S-Ar (in green), and a combination of Ar-Ca and Ca (in blue). *Figure from Ponti et al. (2015).*

The warm plasma, or soft X-ray diffuse plasma, is a thermal component pervading the GC with a temperature of approximately $kT \sim 1$ keV. A comprehensive overview of this soft X-ray plasma has

been provided by Muno et al. (2004b) using the Chandra X-ray Observatory, Uchiyama et al. (2013) using Suzaku data, and Ponti et al. (2015) using the XMM-Newton Observatory. The spectral features of this plasma are primarily traced by the H-like and He-like lines of elements such as Si, S, Ar, and Ca. Figure 1.7 shows strong and narrow emission lines within the 1.5 to 5 keV bands, with the most intense being Si XIII, S XV, Ar XVII, and Ca XIX. This soft X-ray line image reveals strong color gradients towards several regions in the CMZ. The detailed study of these spectral lines helps derive the physical conditions and structure of the plasma. For instance, the intensity ratios of K-shell lines from He-like ions (Lyα/Kα) of sulfur indicate that the plasma in the GC maintains a temperature close to 1 keV (Uchiyama et al. 2013). The spectrum of this plasma component is typically fitted using the APEC model (Astrophysical Plasma Emission Code), which represents emission from a collisional ionized diffuse gas and is crucial for interpreting the observed X-ray spectra (Muno et al. 2004b).

The warm plasma in the GC exhibits a strongly non-uniform morphology characterized by patchy and clumpy structures, as illustrated in Figure 1.7. The patchy distribution of soft plasma shows higher concentrations (up to a factor of 10 variations within 50 pc) towards star forming regions[3] (Ponti et al. 2013). These higher-density regions are unlikely to remain intact over time due to the differential rotation of the galaxy, which tends to disrupt coherent structures within the plasma. Hence, the morphology of the soft plasma suggests that it is relatively young (Muno et al. 2004b). The prevalent theory for the origin of this young soft X-ray emission is the energy released in the ISM by supernova explosions and stellar winds. The radiative cooling of the soft diffuse plasma requires an energy input of approximately 3×10^{36} ergs/s. This scenario would be sustainable with a supernova rate of $10^{-5}\,\mathrm{year}^{-1}$ (Muno et al. 2004b). Given the total Galactic supernova rate of approximately one every 100 years, and considering the inner 20 pc of the Galaxy comprises about 0.1% of the Galactic mass, the expected supernova rate in this region is about $10^{-5}\,\mathrm{year}^{-1}$. Warm plasma in the GC may partially originate from the winds of massive Wolf-Rayet and O-type stars, which convert a fraction of their kinetic energy into X-rays when interacting with the ISM. This mechanism primarily affects regions near young star clusters and contributes, alongside supernovae, to the observed softer emissions. The morphology of the warm plasma further supports these hypotheses. Last, the warm plasma is stable over time due to the continuous energy input from supernovae and stellar winds.

In the context of our research, the warm plasma is an astrophysical background component.

1.2.2 Hot Plasma

The hot plasma, or hard X-ray diffuse plasma in the GC, is a thermal component with a temperature $kT \sim 6.5$ keV. Extensive research has been conducted on this diffuse thermal emission hard component. However, we limited our summary to studies conducted by Muno et al. (2004b); Koyama et al. (2007a); Revnivtsev et al. (2009); Anastasopoulou et al. (2023). The spectral feature of the hard component exhibits strong emission lines from Fe XXV and Fe XXVI at 6.7 and 6.97 keV and a hard X-ray continuum. The spectrum of hot plasma is typically fitted with the APEC model ($kT \sim 5 - 10$ keV) to represent optically thin plasma. The morphology of the hard component peaks towards the GC and more smoothly decreases outward through the Galactic plane. This component is more uniformly distributed than the soft emission component but is also stable over time. This relative homogeneity may result from the higher sound speed concerning the soft component, which would cause overdense regions in the hot plasma to expand and dissolve in a timescale of $\sim 10^4$ years (compared to $\sim 10^6$ years for the soft component) (Muno et al. 2004b). The energy required to sustain the expanding hard plasma is $\sim 10^{40}$ erg/s. This energy is four orders of magnitude larger than required to sustain the soft plasma, and the heating of this thermal component is unlikely to be provided by SNRs or W-R and early O stars as warm plasma.

[3] Although star formation is currently restricted to a few regions such as Sgr B2 (Hatchfield et al. 2020), warm plasma is not detectable around Sgr B2 (see Figure 1.7). This suggests that the star formation is likely identified by other factors, such as the presence of YSOs, gas, and other signs of stellar activity.

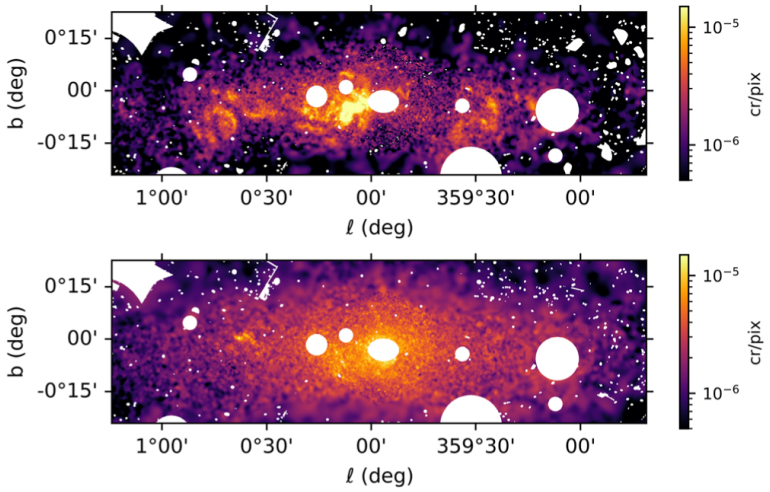

Figure 1.8: Reflection and thermal emission in the GC. Top: Non-thermal reflection emission (6.3-6.5 keV band) in the central degrees of the GC. Bottom: Fe XXV emission (6.62-6.8 keV band) after correction for contaminating non-thermal reflection emission. *Figure from Anastasopoulou et al. (2023).*

The origin of the hot component is the subject of ongoing research. At the CMZ scale, it has been proposed that the hard X-ray diffuse plasma may arise from the superposition of various contributions by unresolved weak point sources (Koyama et al. 1996). A very well-correlated hard X-ray emission and the Fe XXV 6.7 keV line emission were observed over the GC and Galactic plane (Revnivtsev et al. 2006) to support this hypothesis. Moreover, Revnivtsev et al. (2009) resolved more than 80% of the diffuse 6-8 keV emission into weak discrete sources such as accreting white dwarfs and coronally active stars. However, the scenario may vary in the GC. At the GC, only a maximum of 20% of the diffuse X-ray emission might be linked to these unresolved point sources, with the rest, about 80%, being truly diffuse (Muno et al. 2004b; Revnivtsev et al. 2007). Figure 1.8 illustrates the non-thermal reflection emission in the central degrees of the GC, with the bottom panel displaying the Fe XXV emission, corrected for the contaminating reflection emission (Anastasopoulou et al. 2023). The contribution from the Fe XXV line at 6.7 keV to the unresolved point sources was estimated, and as in all previous studies, they found an excess of hard X-ray emission remaining in the central degrees of the GC. This suggests that additional, unidentified factors or sources contribute to the X-ray emissions beyond those already accounted for. Anastasopoulou et al. (2023) measured the Fe XXV line emission using all available XMM-Newton observations of the GC and inner disk and claimed that the excess emission is pronounced in regions where known SNRs are located. It was suggested that a significant portion of this emission could be attributed to genuine diffuse, very hot plasma. However, they concluded that not all the excess can be ascribed to very hot plasma alone.

Through this work, the hot plasma will be considered an astrophysical background component.

1.3 Non-thermal Diffuse Emission

The final and most important diffuse emission component for this thesis is the non-thermal component of the X-ray spectrum from diffuse emissions in the GC. One of the main characteristics of the non-thermal emission is traced by the emission line from neutral Fe at 6.4 keV in the massive MCs in the GC region due to the Fe Kα fluorescence. This fluorescence line will be the subject of our study. Fe is the element with the highest (by a factor of ~ 5) abundance in the GC and the highest fluorescence yield (for the K-shell). Given the importance of this component to our study, the following subsections will present a succinct overview of the historical advancements in non-thermal emission research in the GC, the characteristics of the line (and other non-thermal features), and its morphology.

1.3.1 Historical Insights and Observation of the Fe Kα Emission Line

One of the earliest detections of non-thermal emissions from MCs was reported by Sunyaev et al. (1993), who observed a flux of X-rays from sources in the GC using the ART-P telescope on the GRANAT satellite in the 8.5-19 keV range. They predicted that the same process producing this signal could also efficiently produce the 6.4 keV line. Due to its limited spectral resolution, the ART-P telescope could not distinguish the fluorescence lines from Fe I (6.40 keV), Fe XXV (6.70 keV), and Fe XXVI (6.97 keV). It was suggested that the Fe Kα line emission could be effectively measured with better instrumentation. This foundational study provided the initial motivation to investigate the Fe Kα line emission in the vicinity of the most massive clouds. Moreover, Sunyaev et al. (1993) proposed that a large portion of the flux arises from reflection (Thomson scattering) by dense molecular clouds irradiated by a nearby X-ray source. However, no brighter source had been observed that produced at least 0.1% of the observed hard X-ray flux. The X-ray satellite ASCA was launched in late 1993. It was groundbreaking at the time, equipped with X-ray spectrometers capable of distinguishing the 6.4 keV and 6.7 keV emission lines from iron. This capability led to an important discovery in observing the Fe Kα line in the GC (Koyama et al. 1996). As predicted, the Fe Kα line was found to correspond with the densest molecular complexes in the CMZ, such as Sgr B and Sgr A. Further observations from ASCA of MCs revealed 6.4 keV line emission also from the Sgr C complex in 2000 (Murakami et al. 2001). Interestingly, an X-ray binary with a 2-10 keV luminosity of approximately 3×10^{36} erg s^{-1} was found 0.4° from the Sgr C cloud. This luminosity was insufficient to account for the observed 6.4 keV flux in Sgr C. If the reflection from a putative source is the reason, as suggested by Sunyaev et al. (1993), there should have been a much brighter source at that time, or one that was active a few hundred years ago.

1.3.2 Spectral Diagnostic of Non-thermal Emission

The spectral diagnostic for non-thermal emission is mainly driven by the emission lines from neutral and ionized Fe and a hard X-ray continuum characterized by a power law with a spectral index $\Gamma \approx 2$.

Emission lines from Fe: The most abundant Fe isotope is ^{56}Fe (26 protons and 30 neutrons). Whenever an inner shell electron vacancy occurs (see discussion of origin), the atom is excited and tends to return to a stable state by filling the vacancy with an outer shell electron. This transition leads to the emission of a photon. The quantum mechanical selection rules state that the only allowed transitions are those for which $\Delta l = \pm 1$ and $\Delta j = 0, \pm 1$ (Eisberg & Resnick 1985). Therefore, the Fe Kα line from neutral Fe can occur in two separate ways, defined as Kα_1 and Kα_2. The Kα_1 line occurs at 6.404 keV, and the Kα_2 line at 6.391 keV, with a branching ratio of 2:1. However, contemporary astronomical instruments cannot resolve these Fe doublets. The natural width of these lines is approximately 3.5 eV. Since the M-shells of neutral iron atoms are populated, there is also a fluorescent Fe Kβ line ($3p \rightarrow 1s$ transition) at 7.06 keV. The spectral ratio ($K\alpha/K\beta$) is approximately 0.12 (Murakami et al. 2001). The Equivalent Width (EW) of the Fe Kα line, which measures its strength relative to the continuum, is roughly proportional to the temperature and source luminosity. For solar abundances, the EW of Fe Kα is expected to be about 1 keV, with variations of around 30% (Ponti et al. 2013).

1.3.3 Morphology of the Fe Kα Emission Line

Which parts of the CMZ exhibit emission in the 6.4-keV line? Figure 1.9 illustrates the continuum-subtracted Fe Kα fluorescence emission at 6.4 keV within the inner CMZ, based on data obtained from two epochs across 10 years by the XMM-Newton X-ray observatory (Terrier et al. 2018). This emission is strongly associated with the locations of major molecular complexes within the CMZ, such as Sgr B, Sgr C, and Sgr A. The dotted box second from the left highlights the molecular complex

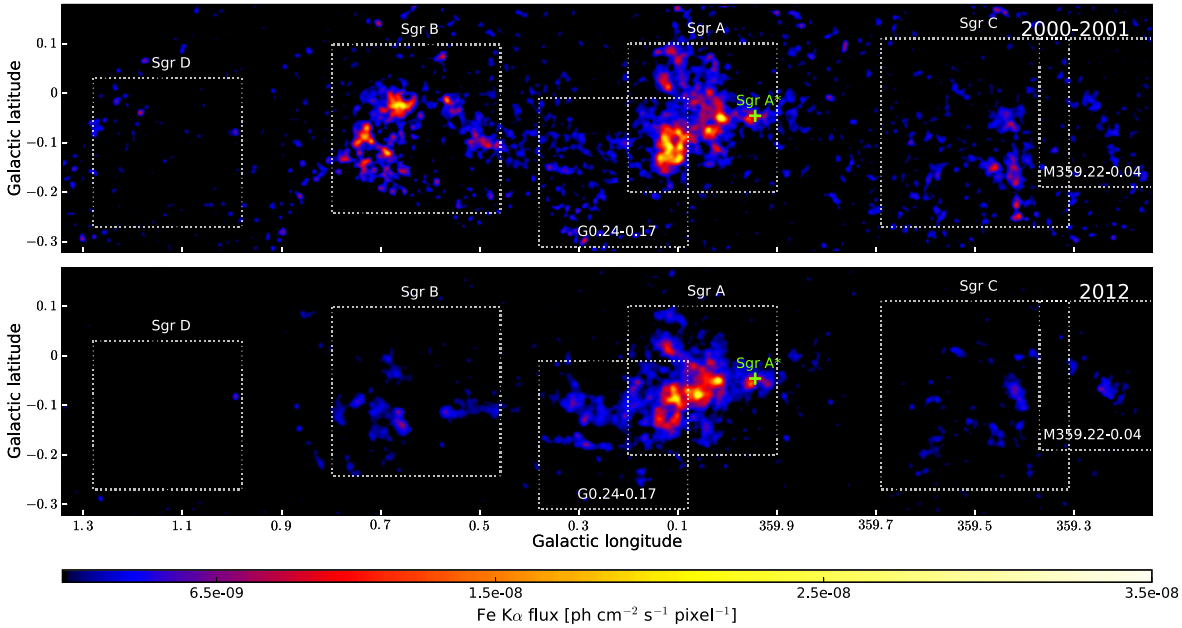

Figure 1.9: Background and continuum-subtracted Fe Kα intensity maps of the inner GC as captured by XMM-Newton at 6.4 keV. Epoch 2000-2001 (top) and 2012 (bottom). Measurements are shown in units of photons cm^{-2} s^{-1} pixel^{-1}, with a pixel size of 2.″5. The maps have been smoothed with a Gaussian kernel with a radius of 5 pixels. *Figure from Terrier et al. (2018).*

Sgr B (see Section 1.1.4 for more information). The 6.4 keV emission from Sgr B is widely discussed in the literature and will be our study's focus.

1.3.4 Variability of the Fe Kα Emission Line

X-ray observatories like XMM-Newton have been monitoring the Fe Kα line from the CMZ for the past two decades. Since its discovery, this line has been characterized by significant temporal variability. This variability has been investigated in several studies, including those by Inui et al. (2009); Terrier et al. (2010); Ponti et al. (2010); Clavel et al. (2013); Terrier et al. (2018). Inui et al. (2009) first quantified the Fe Kα variability in the Sgr B region using data from Suzaku, XMM-Newton, Chandra, and ASCA, spanning from 2000 to 2005. They observed a 60% decline in Fe Kα flux over 10 years from Sgr B. A year later, Terrier et al. (2010) observed consistent results in the 20-60 keV flux from the same molecular complex (see the discussion of variability in Sgr B). Nobukawa et al. (2011) observed a synchronized flux decrease in Fe Kα by a factor of 1.9-2.5 from both Sgr B2 and another cloud located in the GC. The matching variability between the molecular clouds suggested a common external source in action. In 2010, Ponti et al. (2010) observed the first superluminal echo[4] in the GC. This X-ray light front propagated with an apparent velocity of 3c in a molecular complex known as "the bridge." This apparent superluminal motion rules out an internal source for the observed emission, providing strong evidence of external irradiation, most likely from Sgr A* (Ponti et al. 2013). Although originally proposed by Ponti et al. (2010) to be a single irradiation event on a large scale, Clavel et al. (2013) found evidence from the Sgr A complex X-ray emission that there have been multiple bright flares in the recent past. On smaller scales, these appeared as fast variations (approximately 2 years compared to approximately 10 years). The most recent variability study by Terrier et al. (2018) observed rapid

[4] A superluminal echo is a phenomenon in which the X-ray light appears to travel faster than the speed of light due to the geometry of the reflecting surfaces or the motion of the source and observer. This effect gives the illusion of superluminal travel.

variations of the 6.4 keV bright emission throughout the CMZ and the absence of bright and stable Fe Kα emission.

1.3.4.1 Evolution of Fe Kα Variability in Sgr B

This dissertation extends the study of Fe Kα emission in Sgr B, building upon the foundation established by its variability. This section will discuss the evolution of the 6.4 keV variability within Sgr B.

From 2000 to 2009: The variability of the Sgr B (Sgr B2 and Sgr B1) molecular complex has been the subject of extensive studies from 2000 to the present. The first piece of evidence for this variability was provided by Inui et al. (2009). These authors produced the first light curve of the Fe Kα line flux. It showed the brightest behavior in 2000 and a linearly decreasing trend towards 2009 (see Fig. 1.10 in red). In 2010, Terrier et al. (2010) analyzed the Sgr B2 molecular cloud over a broad 2-100 keV energy range by integrating data from INTEGRAL and XMM-Newton. They reported a linear decay in the hard X-ray emission from Sgr B over an approximate timescale of ~ 8 years. This study was consistent with the findings of Inui et al. (2009) (see Fig. 1.10). The illuminating spectrum was found to be a hard continuum with a spectral index of $\Gamma \sim 2$.

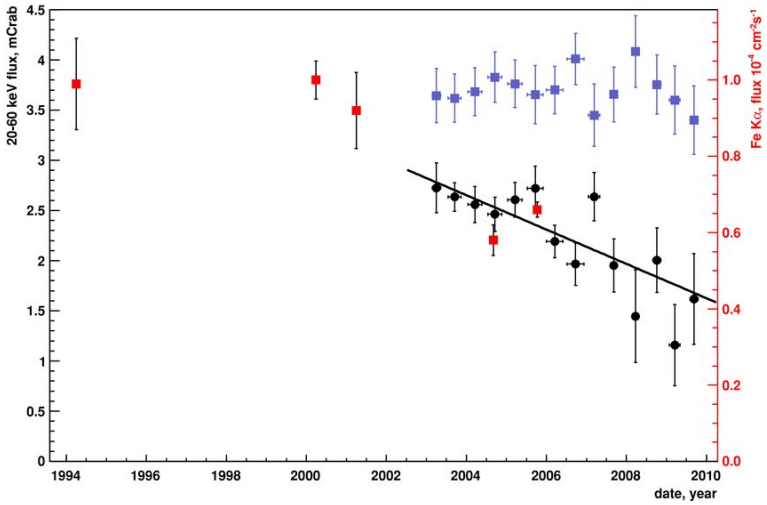

Figure 1.10: 20-60 keV Light curve of Sgr B2 as measured with IBIS/ISGRI from 2003 to 2009 (black circles). Red squares are the Fe Kα line fluxes obtained by Inui et al. (2009) using ASCA, Chandra, XMM-Newton, and Suzaku observations from 1994 to 2006. *Figure from Terrier et al. (2010).*

Expanding the View Up to 2018: A few years later, in 2012, Terrier et al. (2018) conducted a deep scan of the inner 300 pc of the CMZ in 6.4 keV Fe Kα using XMM-Newton. This scan used all the X-ray data from 2012, covering all molecular complexes, including Sgr B. The authors studied the decennial variability properties in these clouds. Figures 1.11 and 1.13 show the variability of the reflected Fe Kα emission in Sgr B, obtained from a region with a radius of $410''$ centered at $l = 0.643°$, $b = -0.078°$ (see Figure 1.11 for other regions). A study by Rogers et al. (2022), using the joint observations from XMM-Newton (0.1-15 keV range) and NuSTAR (3-79 keV range) at 6.4 keV Kα extends the temporal view of Sgr B2 even further. Figure 1.12 shows the Fe Kα line in a $24' \times 24'$ region surrounding Sgr B2 as observed by XMM-Newton in 2018. Although the region of interest and the continuum-subtraction technique differ from those used by Terrier et al. (2018), it provides an extended view of the morphological changes in the cloud.

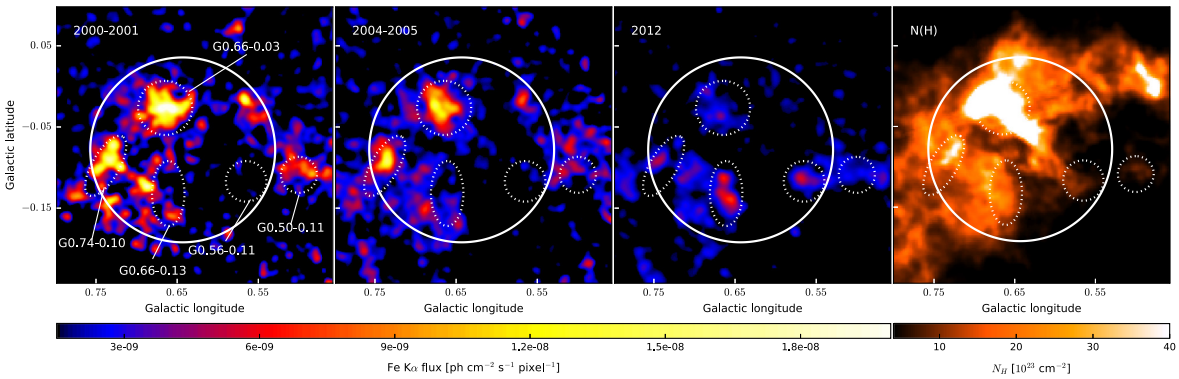

Figure 1.11: The 2000-2001 to 2012 continuum-subtracted Fe-Kα images of the Sgr B complex. The continuum subtraction was achieved by the method explained in Chapter 3. Key molecular clouds can be identified as Sgr B2 (G0.66-0.03) in $l = 0.665°$, $b = -0.027°$ radius $120''$, Sgr B1 (G0.50-0.11) in $l = 0.500°$, $b = -0.109°$ radius $80''$, G0.74–0.11 in $l = 0.738°$, $b = -0.098°$ radius ($60''$,$150''$), G0.66–0.13 in $l = 0.661°$, $b = -0.132°$ radius ($72''$,$144''$), and G0.56–0.11 in $l = 0.565°$, $b = -0.117°$ radius $90''$. The right panel shows the total gas column density for Sgr B. *Figure from Terrier et al. (2018).*

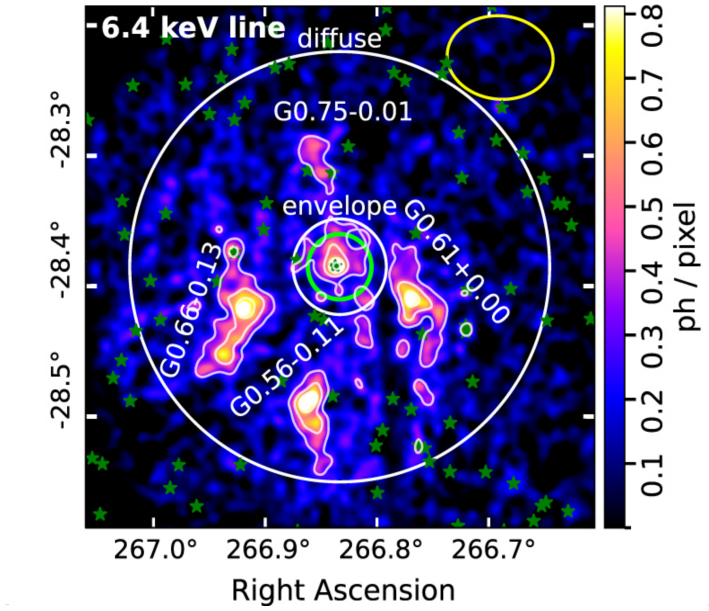

Figure 1.12: The 2018 continuum-subtracted Fe Kα image of the $24' \times 24'$ region surrounding Sgr B2 is shown as observed by XMM-Newton EPIC-pn in the 6.4 keV line. The continuum subtraction was achieved by removing the 5.8–6.2 keV continuum band image from the 6.2-6.6 keV signal band image. *Figure from Rogers et al. (2022).*

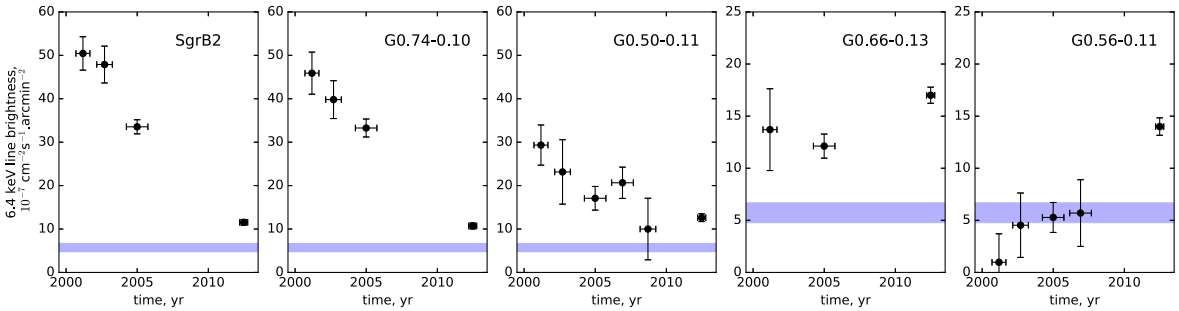

Figure 1.13: Fe Kα light curves of the Sgr B complex integrated over the regions indicated in Fig. 1.11. All errors shown on the light curves are 1 σ errors. The purple color band indicates the level of local background emission for each region with radius 280″ at $l = 0.490°$, $b = 0.008°$. *Figure from Terrier et al. (2018).*

The morphology maps and light curves in Figures 1.11, 1.12, and 1.13 suggest that on a large scale, the total flux luminosity peaked in 2000 and then experienced a rapid decrease of ∼50% over 10 years. Relative to the 2012 level, the 2018 emission represents a (29 ± 8)% decrease (Rogers et al. 2022). The light curves in Figure 1.13 show complex behaviors on small scales. In the early measurements, most of the flux is due to a few very bright regions. However, flux from localized regions decayed much more rapidly than the larger Sgr B complex. Without these dense, compact regions, the flux variation becomes less pronounced (Terrier et al. 2018).

Sgr B2: From Figure 1.13 (left), it is evident that the 2° area surrounding the core of the Sgr B2 molecular cloud was notably bright in 2000-2001. After a decade of decline, the Fe Kα emission in 2012 reached approximately 22.82% of its 2000–2001 levels. The Sgr B2 brightness in 2000–2001 was $(50.4 \pm 3.8) \times 10^{-7}$ ph cm^{-2}s^{-1}arcmin^{-2}, which declined by a factor of 4 to 5 to $(11.5 \pm 0.6) \times 10^{-7}$ ph cm^{-2}s^{-1}arcmin^{-2}. This Sgr B2 flux was closely aligned with the average brightness observed across the broader Sgr B region in 2012 (Terrier et al. 2018). In 2013, NuSTAR achieved sub-arcminute resolution in the 3-79 keV energy range for Sgr B2. Zhang et al. (2015) studied the hard X-ray continuum emission within the central 90″ of Sgr B2. The Fe Kα emission in 2012-2013 reached approximately 20% of its 2001 levels (Zhang et al. 2015). However, it remained at the same level during both 2012 and 2013. The data was not deep enough to determine whether the Fe Kα emission was still decreasing or had stabilized at constant background levels.

G0.66-0.13: Figure 1.13 (4th from left) reveals a slowly increasing trend in the Fe Kα X-ray flux for G0.66-0.13 prior to 2012, reaching a peak in 2012. The peak Fe Kα emission from G0.66-0.13 was brighter than that of the Sgr B2 core, Sgr B2(M) (Zhang et al. 2015). After 2012, the Fe Kα emission from this cloud region decreased linearly until 2018 (Zhang et al. 2015).

1.3.5 Origin of the Fe Kα Emission Line

When the Fe Kα line was first detected from the MCs in the GC, there was no known source within the GC with such high X-ray luminosity. This led Koyama et al. (1996) to propose that the ionizing source of the Fe fluorescence was likely a period of high activity from Sgr A* in the past. Currently, Sgr A* is in a quiescent state, with an X-ray luminosity of around $\sim 10^{33}$ erg/s. However, more recent studies using nearby clouds, such as Sgr B2, indicate that Sgr A* was much brighter a few hundred years ago, with at least two significant outbursts (Clavel et al. 2013; Chuard et al. 2018). Considering the measured 6.4 keV line flux and the cloud's proximity to the GC, it was suggested that these past flaring activities of Sgr A* were the likely cause of the Fe fluorescence observed in the MCs in the CMZ. This hypothesis has been tested and is now the favored interpretation. The intense X-rays

produced by the flaring activities of Sgr A* propagate through the inner CMZ, ionizing iron atoms in the surrounding MCs. This process leads to the pronounced Fe Kα fluorescence line at 6.4 keV and a hard X-ray continuum. Such interactions are classified as an X-ray Reflection Nebula (XRN).

Theory of XRN

Here, we take the example of a spherical molecular cloud irradiated by an external source, as illustrated in Figure 1.14. The distance from the cloud to the observer is D, and the line of sight position is given by θ. The solid angle ω represents the surface of the cloud that is illuminated by the source. The likelihood of photoionization leading to fluorescence is determined by two main factors: the probability of X-rays being absorbed by the iron atoms (called the photoionization cross-section) and the number of iron atoms present in the cloud. The photoionization cross-section depends on the energy of the incoming X-ray photons, typically decreasing as the energy of the photons increases.

To calculate the rate at which 6.4 keV photons are emitted, we consider both the number of iron atoms and the rate at which these iron atoms absorb X-rays from the source. The emission rate also depends on the spectrum of the source, especially the flux of X-rays in the 7-9 keV range, where photoionization is most effective (Sunyaev & Churazov 1998). The observable flux of these 6.4 keV photons from the molecular cloud, as seen by an observer on Earth, depends on several factors: the geometry of the cloud, D, the inverse square law, abundance of iron relative to hydrogen in the cloud and the optical thickness of the cloud for Thomson scattering.

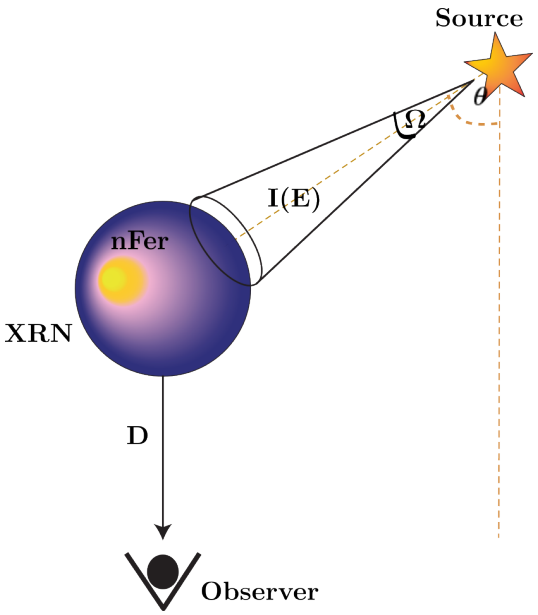

Figure 1.14: Schematic of XRN geometry of a MC and illuminating external source.

$$F_{6.4} = \phi \frac{\Omega}{4\pi D^2} \frac{\delta_{Fe}}{3.3 \times 10^{-5}} \tau_T I(8\text{keV}) \tag{1.2}$$

Equation 1.2 describes the flux of 6.4 keV photons ($F_{6.4}$) as a function of the flux from the source at approximately 8 keV (within the 7-9 keV range). Here, Ω represents the solid angle subtended by the cloud as seen from the primary source, D is the distance to the observer, ϕ is a factor of order unity that weakly depends on the shape of the source spectrum, and δ_{Fe} denotes the iron abundance (Sunyaev & Churazov 1998). This equation helps estimate the luminosity required from the hypothetical X-ray source to produce the observed flux.

$$L_8 = 6 \times 10^{38} \left(\frac{F_{6.4}}{10^{-4}}\right) \left(\frac{0.1}{\tau_T}\right) \left(\frac{\delta_{Fe}}{3.3 \times 10^{-5}}\right)^{-1} \left(\frac{d}{100\,\text{pc}}\right)^2 \tag{1.3}$$

Where d represents the distance between the source and the cloud. When a cloud is illuminated by an external source, the geometry of the X-ray illumination is illustrated in Figure 1.14. An observer positioned far from both the source and the cloud will observe fluorescence emission (along with the associated reflected continuum) from the areas of the cloud that are presently exposed to the X-ray photons. See detailed explanation in (Sunyaev & Churazov 1998).

Line of sight position: The geometry of the reflection has a major influence on the flux and spectral shape of the cloud emission (see Figure 1.14). The geometry is parametrized by the angle between the cloud, the illuminating source, and the observer, referred to as the line-of-sight angle (θ_{XRN}). The total continuum flux at low energies notably increases with this angle because photons only superficially penetrate the cloud before being scattered toward the observer. Figure 1.15 shows reflected spectra from the MC in Fig.1.14 for the incident spectrum with $\Gamma = 2$ from the source, obtained by Monte Carlo simulations (Walls et al. 2016).

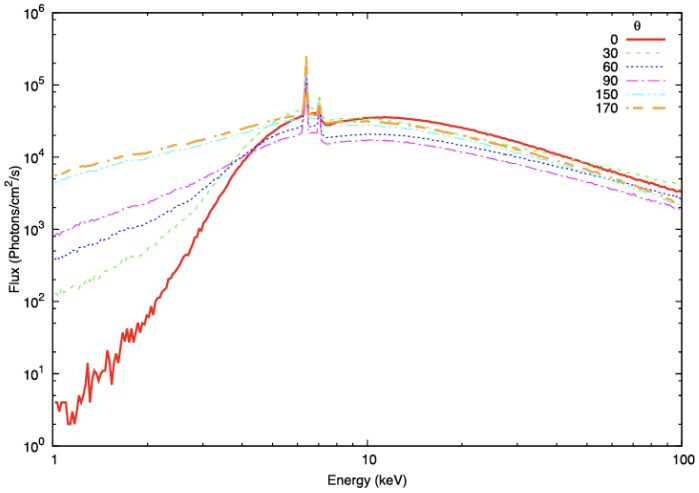

Figure 1.15: Reflected spectra produced by the MC code for a 2 pc diameter, uniform density sphere with an N_H of $6 \times 10^{23}\,\mathrm{cm}^{-2}$, and a photon index of 2.0. Showing the changes in flux and continuum shape resulting from a changing line of sight angle. *Figure from Walls et al. (2016).*

The 0° case has significantly increased low energy absorption because observed photons must travel through the entire cloud before escaping. The depth of the Fe edge decreases with increasing angle because absorption is less likely at higher angles. We discuss these effects further in Chapters 5 and 6.

Polarization of Fe Kα Emission Line Thomson scattering on electrons causes the reflected emission to become linearly polarized. The predicted polarization degree is defined by $P = \frac{1-\cos^2\theta}{1+\cos^2\theta}$, with θ representing the scattering angle (Basko et al. 1974). Observing polarized light from the MCs in the GC will provide definitive evidence for the X-ray external illumination scenario. Additionally, the scattering angle inferred from the polarization can eventually help determine the MC's distance along the line of sight. This distance is a crucial parameter for reconstructing the three-dimensional gas distribution in the CMZ and understanding the recent history of X-ray emissions from the GC. The polarization properties of the GC were predicted by Churazov et al. (2002). Recently, Marin et al. (2023) reported observations of polarized X-ray emission in the direction of the GC molecular clouds using the Imaging X-ray Polarimetry Explorer (IXPE).

1.4 Towards a Steady Non-thermal Emission in the CMZ

Since the discovery of the Fe-Kα line, multiple studies have consistently reported a decline in X-ray emission from Sgr B, attributed to the reflection of X-ray flares from Sgr A*. Despite this observed trend, it remains an open question how long the decrease in Sgr B's emission will continue and which mechanisms will predominate once the X-ray light front from Sgr A* no longer influences the cloud. Recent findings since 2012 suggest a stabilization of the X-ray emission in Sgr B, indicating a trend toward steadiness. The latest investigations conducted by Kuznetsova et al. (2022); Rogers et al. (2022) have further supported this observation of potential steadiness over $\sim$ six years since 2011. In

this section, we discuss the constraints on the existence of a steady level, the current constraints we have on it, and the hypotheses about its origin as observed by INTEGRAL (Kuznetsova et al. 2022), and the 6.4 keV Fe-Kα line, as observed by XMM-Newton and NuSTAR (Rogers et al. 2022) in the Sgr B region.

1.4.1 Constraints on Sgr B2 Reaching a Steady Level

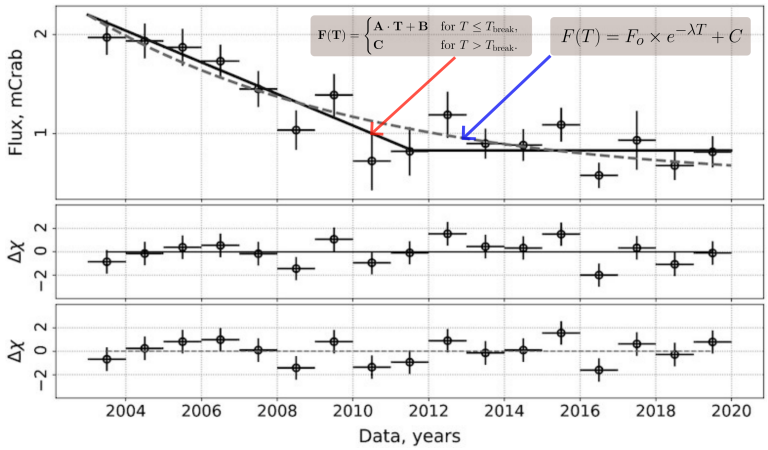

Figure 1.16: The 30–80 keV INTEGRAL/ IBIS light curve of Sgr B2 approximated with the linear piecewise and exponential functions, as shown in the upper plot with solid and dashed lines, respectively. The corresponding residuals are shown in the middle and bottom panels. *Figure from Kuznetsova et al. (2022).*

The long-term X-ray emission from the GC observed by INTEGRAL/ IBIS in the 30–80 keV range is illustrated in Figure 1.16 (Kuznetsova et al. 2022). This light curve aggregates all available data from 2003 to 2020 and highlights significant features of the emission from Sgr B2 (INTEGRAL source IGR1747). Up to 2009, there was a pronounced decline in intensity, which then transitioned into relatively stable emission. The observed stabilization pattern in the Sgr B2 region is discussed using a simple piecewise linear model and/or exponential decay with a constant. The piecewise linear model fitted the data with $\chi^2/\mathrm{dof} = 1.09/14$, and it was superior to those obtained from simple linear decay models, suggesting that the emission is more likely to stabilize at steady levels. The time at which the INTEGRAL flux decreases to half of its initial value (6 ± 2 years) aligns well with the estimations made by Terrier et al. (2010) within the given uncertainties. After the breaking point at approximately 2011, a constant flux level is obtained from the fit as $C = 0.8 \pm 0.1$ mCrab. This level is significantly different from a zero flux background, providing an initial indication that the background flux may be reaching steady values. The exponential decay with a constant model provided fit statistics of $\chi^2/\mathrm{dof} = 1.04/14$. The lifetime was estimated as $\tau = 7.5^{-3.4}_{+7.1}$ years, which was in agreement with the $\tau \sim 11$ years provided by Zhang et al. (2015) for the central 90″ of Sgr B2. The constant flux level was obtained from the fit as $C = 0.5^{-0.6}_{+0.3}$ mCrab, maintaining consistency with the constant value in the piecewise linear model.

Sgr B was jointly observed in 2018 by XMM-Newton (0.1-15 keV range) and NuSTAR (3-79 keV range) in the 6.4 keV Kα line (Rogers et al. 2022). A 2018 observation confirms previous findings of significant hard band X-ray emission from the INTEGRAL observations, suggesting the existence of non-zero, non-faded residual X-ray emission within the cloud. The 6.4 keV Kα light curve in Fig. 1.17 covers most of the diffuse emission (around 6′ in cyan) and is compatible with the INTEGRAL light curve in Fig. 1.16. The total decrease in the Fe Kα emission from this region from 2004 to 2018 is consistent with the total decrease in the 30–80 keV continuum observed by INTEGRAL over the same sky region (Rogers et al. 2022). The light curve for the central 90″ region showed consistency with Zhang et al. (2015) 's work. The constant level in the Sgr B2 Kα line emission was assessed using an exponential decay model similar to Kuznetsova et al. (2022). The best fit constant flux was obtained as $C = (0.5 \pm 0.2) \times 10^{-5}$ ph cm^{-2} s^{-1} at the 1σ confidence level. The constant flux C, being

significantly different from zero, implies the presence of a Fe Kα emission component that remains stationary over the considered timescale.

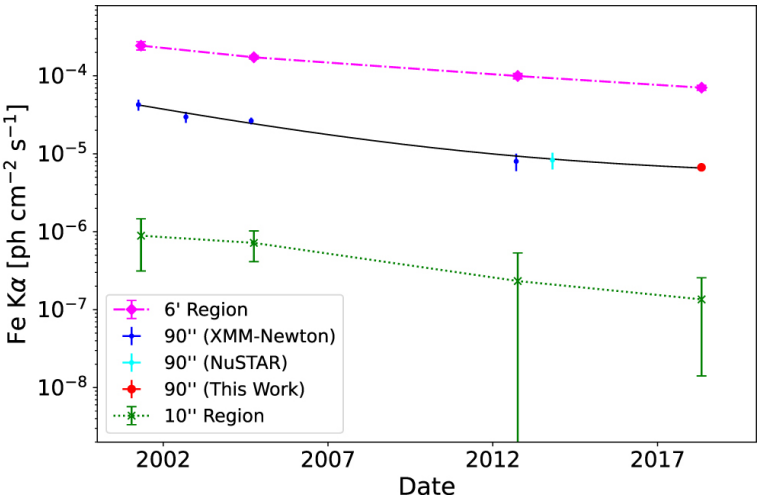

Figure 1.17: Fe Kα light curve for 6′ radius region representing the Sgr B2 overall (magenta), the central 90″ (red, blue, and cyan) and the core(red). *Figure from Rogers et al. (2022).*

Both studies by Kuznetsova et al. (2022); Rogers et al. (2022) have suggested that the 6.4 keV Fe Kα emission (and hard X-ray continuum) is approaching baseline levels ($C = 0.5^{-0.6}_{+0.3}$ mCrab and $C = 0.5^{-0.2}_{+0.2} \times 10^{-5}$ ph cm^{-2} s^{-1}, respectively). The Fe Kα line now shows strong hints of approaching steady levels after approximately two decades of variability. However, we cannot definitively argue whether the flux has reached constant levels or whether it will reach zero background levels in the future based solely on these trends. Despite these observations, it remains uncertain whether the flux will ultimately stabilize at these values or diminish to background levels. Nonetheless, recent observations compellingly support the presence of a non-zero baseline emission in the GC. For clarity, this constant level of emission will be referred to as diffuse X-ray steady emission or steady emission throughout the remainder of this dissertation. This concept will form the core of our ongoing study and will be extensively discussed in this thesis.

1.4.2 The Origin of the Diffuse Steady Emission

The true nature and origin of the suggested steady emission component at 6.4 keV Fe Kα remain open and intriguing questions. This steady emission might result from a mechanism different from the widely accepted theory involving past X-ray flares. Could the steady emission level observed in MCs be attributed to an alternative origin? Understanding the true nature of this component is crucial, as it would provide a more comprehensive understanding of the underlying mechanisms shaping the X-ray landscape of the GC. When considering the faint, steady emission in an MC, three mainstream hypotheses are possible regarding its origin:

1. Reflection scenario
2. Unresolved point-source scenario
3. Cosmic ray scenario

In the following section, I will discuss the most recent investigations and conclusions concerning each hypothesis. After establishing the statistical upper limits for the steady emission, I will thoroughly explore each of these scenarios in Chapter 5 and 6.

1.4.3 Reflection Scenario

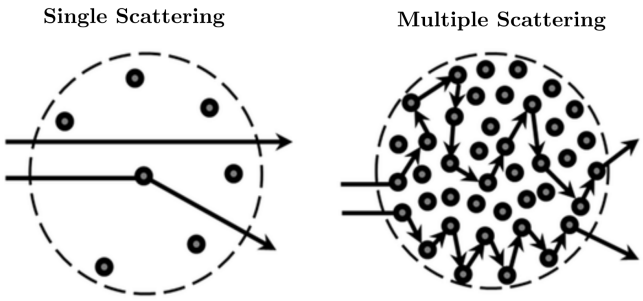

Figure 1.18: Illustration of single and multiple scattering regimes in spherical clouds.

The widely accepted theory of reflection of past X-ray flares remains a possible origin of the diffuse steady emission. The fainter steady signal could be due to a fainter and longer event from Sgr A*, or it could be a reflection from nearby fainter sources. However, in denser regions like Sgr B2, multiple scattering could also offer an origin for faint Fe Kα emission. When an incoming photon enters a cloud, it undergoes scattering and loses energy proportional to the incident photon energy and the scattering angle. In regions with higher densities, the photon can undergo multiple scatterings. In this scenario, X-ray photons emitted from an external flare are postulated to undergo a series of scattering events within the dense molecular clouds of regions like Sgr B2 (see Fig. 1.18). This repeated scattering results in prolonged emissions that persist even after the primary flare has diminished. Kuznetsova et al. (2022) suggested that this multiple scattering of X-rays from the primary external flare likely accounts for the steady $30 - 80$ keV hard X-ray emission observed post-2011. The effect is more noticeable in the hard X-ray continuum rather than in the Fe Kα line. Observational evidence supporting this scenario includes the detection by NuSTAR of multiple cores within Sgr B2 that emit above 10 keV (Zhang et al. 2015). The multiple scattering scenarios will be explored in greater depth in Chapter 6.

1.4.4 Unresolved Point-Source Scenario

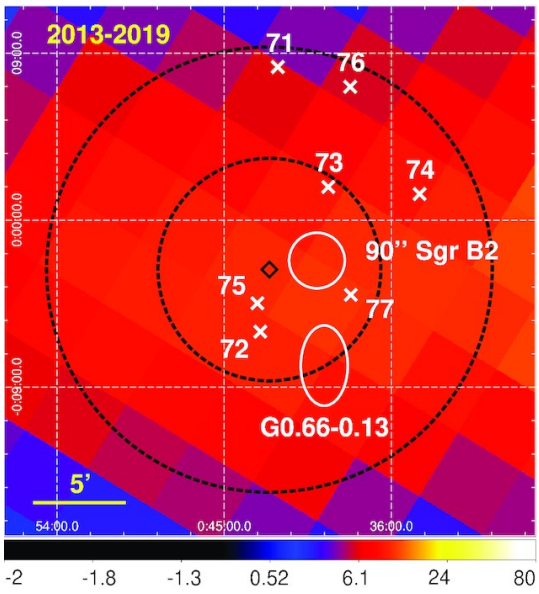

Figure 1.19: The 30–80 keV INTEGRAL/ IBIS steady level Sgr B2 image. The black dashed circles with radii $R =$ 6–12 arcmin centered on the INTEGRAL Sgr B2 position (diamond symbol). The region of Sgr B2 is further highlighted by a solid circle with a radius of $R = 90$ arcsec. The G0.66 is shown as an ellipse. *Figure from Kuznetsova et al. (2022).*

The steady X-ray emission (in hard continuum) observed after 2011 could be explained by an integrated flux from unresolved X-ray sources in the region. The most straightforward hypothesis is that the cumulative flux from unresolved sources could account for this emission. Kuznetsova et al. (2022) added up the known X-ray source fluxes in Sgr B2 as shown in Fig. 1.19. Kuznetsova et al. (2022) calculated cumulative hard source fluxes from NuSTAR observations in the 25–50 keV energy band and obtained a flux of $\sim 3.4 \times 10^{-12}\,\mathrm{erg\,cm^{-2}\,s^{-1}}$. This flux is approximately two times lower than the flux measured by INTEGRAL. The integrated flux from known X-ray sources did not account for more than half of the observed Sgr B2 emission in the hard energy band after 2011.

1.4.5 Cosmic Ray Scenario

Could the observed steady Fe Kα levels be a result of cosmic ray (CR) particle bombardment on MCs? When low-energy cosmic ray particles encounter neutral or mildly ionized iron atoms in the ISM, they have the potential to transfer sufficient energy to eject an inner-shell electron from iron atoms, which can lead to the production of a nonthermal Fe Kα line in the GC. Several studies support the idea that such constant Fe Kα emissions might result from low-energy cosmic ray particles (Valinia et al. 2000; Predehl et al. 2003; Dogiel et al. 2011; Tatischeff et al. 2012). Tatischeff et al. (2012) investigated the production of nonthermal X-rays in the Arches cluster[5] by interactions between low-energy cosmic ray (LECR) electrons and ions with a neutral ambient medium using a steady state slab model. The schematic of this model and the resulting spectra are illustrated in Fig. 1.20. Accelerated particles penetrate at a constant rate inside a cloud of neutral gas. The nonthermal X-rays are produced by atomic collisions until they either stop or escape from the cloud. The model depends on five parameters: the power-law slope of the accelerated CR spectrum (s), which describes the energy distribution of cosmic rays, where higher energy cosmic rays are less frequent; the minimum energy of the cosmic rays (E_{min}), which sets the baseline energy for cosmic rays to effectively penetrate the cloud or produce X-rays; the metallicity of the ambient medium ($Z/Z_{\odot}$), which is the ratio of the metallicity of the medium to that of the Sun, affecting the interaction rate and the types of X-rays produced; the path length of cosmic rays in the region (Λ), which is the average distance cosmic rays travel within the cloud before stopping or escaping, determining the likelihood of significant interaction; and the normalization factor ($N_{\mathrm{LECR}p}$), which adjusts the overall intensity of cosmic ray input into the model, scaling the number of cosmic rays considered.

Tatischeff et al. (2012) claimed that the 6.4 keV Fe Kα line around the Arches cluster likely stems from interactions of LECR ions with the ambient medium but not from electrons. However, after Clavel et al. (2014) detected variability in the Arches cluster, the LECR ion model was excluded. If the non-thermal emission has reached baseline levels, the applicability of the LECR ion model will become relevant once again. The 6.4 keV Fe Kα emission in Sgr B has been examined using the slab model in several studies (Zhang et al. 2015; Kuznetsova et al. 2022; Rogers et al. 2022). For instance, in 2013, Zhang et al. (2015) analyzed the X-ray emission from the central 90″ of Sgr B2 using NuSTAR data and obtained good fit statistics with a self-consistent LECR proton (LECRp) model. If the Fe Kα emission reached steady levels by 2013, then the reflected X-rays might have completely faded, marking the LECRp process as a major contributor. The LECR electron (LECRe) contribution to the Fe Kα emission was excluded due to unphysical fit parameters.

[5] Arches cluster is a massive star cluster located approximately 11 arcminutes northeast of Sgr A*.

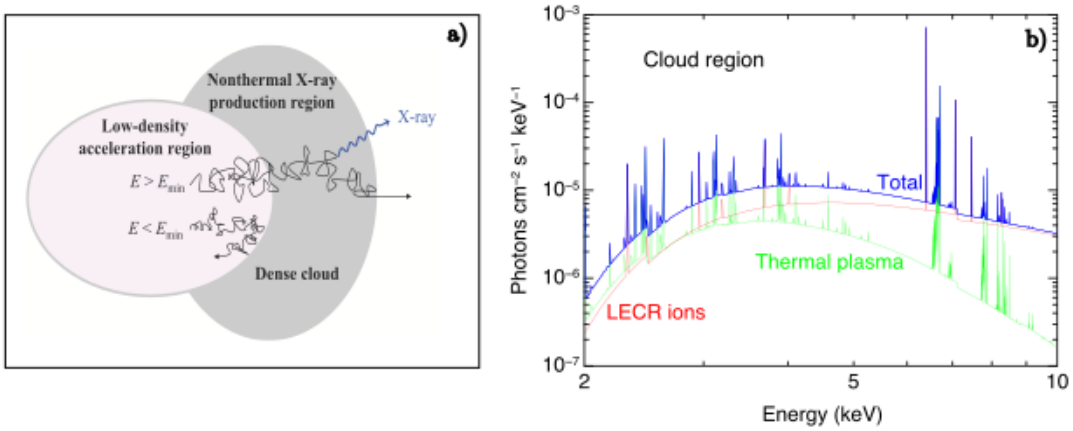

Figure 1.20: a) Schematic illustration of the cosmic-ray interaction model. Fast particles produced in a low-density acceleration region can diffusively penetrate a denser cloud and then produce nonthermal X-rays by atomic collision. b) Model components assuming that the emission comes from a combination of a collisionally ionization equilibrium plasma (APEC model) and a nonthermal component produced by interactions of LECR ions with the cloud constituents. *Figure from Tatischeff et al. (2012).*

1.5 Thesis organization and content

The GC is home to a diverse array of astronomical phenomena, ranging from supermassive black holes to dense MCs. Observations across multiple wavelengths, including radio, infrared, X-rays, and gamma-rays, have revealed unique details about the GC's structure and activity. Objects like Sgr $A^\star$ and the Sgr B molecular complex provide valuable insights into star formation activities and high-energy X-ray phenomena such as diffuse X-ray emission. The soft 1 keV plasma is primarily associated with SNRs and massive stars, while the harder 6.5 keV plasma has been the subject of ongoing research, often attributed to unresolved point sources, primarily compact objects. The nonthermal emission traced by the 6.4 keV line from Fe fluorescence, the subject of my research, was first observed two decades ago. This line emission is predominantly associated with massive molecular clouds in the CMZ. The most widely accepted theory for the origin of this emission is the reflection from molecular clouds due to the recent past activities of Sagittarius $A^\star$, explained by X-ray reflection nebula/XRN models. This theory is strongly supported by extensive studies conducted on clouds like Sgr B, based on observed variability features of the Fe Kα line. An intriguing question is whether the Fe Kα line will eventually decrease and stabilize at a steady baseline level. Particle bombardment models/LECR could explain this steady level of the observed 6.4 keV emission, which was previously attributed to XRN.

Two recent studies (Kuznetsova et al. 2022; Rogers et al. 2022) have suggested that the 6.4 keV Fe Kα emission is approaching steady levels after approximately 20 years of variability. However, these studies were based on single observations with limited statistical significance. This thesis answers the question of the most probable value for this steady component of the Fe Kα emission in Sgr B MC? using two decades of XMM-Newton observations, including newly acquired data in 2020. A novel spectral technique was also developed to extract deep spectra of this faint emission and investigated various origin mechanisms. To advance our understanding, I tested both past accretion models and particle bombardment models, which are crucial for understanding the physics of this faint, steady emission, as they could shed light on the global X-ray landscape of the GC. In the remainder of this thesis, I will explain the roadmap for this extraction, analyze the steady emission from the Sgr B region, interpret the results, and provide future perspectives for studying steady Fe Kα emission.

The layout of this thesis is as follows:

Chapter 2 **X-ray observation and Data reduction** presents an overview of X-ray astronomy and its technology, along with the dataset used in this thesis. It also outlines the main data reduction pipeline based on the XMM-Newton observations.

Chapter 3 **Extraction of 6.4 keV flux maps** details the technique for extracting the non-thermal Fe Kα line from the X-ray observations. The technique is based on Terrier et al. (2018), and this chapter explains possible challenges that may occur in faint-level analysis, especially focusing on small spatial scales. The Poisson method, based on discrete photon statistics, will be introduced here as a modified approach to evaluate the Fe Kα line.

Chapter 4 **Constraining the steady 6.4 keV emission** presents the foundational concepts for estimating the upper limits of the steady 6.4 keV emission. The steady emission has been defined over 20 years, and the morphological maps for the Sgr B region have been presented for the first time.

Chapter 5 **A Study of Steady Diffuse Emission in Sagittarius B** presents the analysis of the steady emission in the Sgr B region. The origin hypotheses for the steady emission are tested using point sources, XRN models, and LECRp models.

Chapter 6 **Discussion and Future Prospects** concludes our study with an interpretation of the diffuse steady emission and a look at future work.

Chapter 2

X-ray Observation and Data Reduction

Observing is just the beginning. The raw data collected by XMM-Newton is a mixture of spectral and temporal signals, referred to as events. To interpret this data, we use XMM-Newton's core pipeline and a series of algorithms to filter, analyze, and refine the raw data to transform it into scientifically significant information: the Fe Kα emission.

Contents

2.1 X-ray Astronomy and the XMM-Newton Observatory

2.1.1 A Brief History of X-ray Astronomy

X-ray astronomy is a branch of astronomy concerned with detecting and measuring high-energy electromagnetic radiation ranging from 0.1 keV to 100 keV. X-ray astronomical detectors are specialized instruments designed to detect and analyze X-rays from celestial sources, such as black holes, neutron stars, and molecular clouds in galaxies. Unlike visible or radio light, cosmic X-rays are completely absorbed by Earth's atmosphere and cannot be observed directly from the ground. Therefore, X-ray detectors are often placed on satellites and launched into space. X-ray astronomy has a rich history that dates back to the mid-20th century when the first X-ray detectors were flown on rockets, which led to the discovery of X-ray emissions from the solar corona. The launch of the Uhuru satellite in 1970 marked the beginning of X-ray astronomy as a dedicated field and the development of increasingly sophisticated X-ray telescopes, such as the Einstein Observatory in the late 1970s and the ROSAT satellite in the 1990s. These early successes laid the foundational pillars for the ongoing evolution of X-ray astronomy. Over the past 50 years, X-ray astronomy has continued to evolve with cutting-edge X-ray observatories. The XMM-Newton of the European Space Agency remains a cornerstone among its contemporary peers, offering insights into the unknown universe for more than two decades. While other significant observatories, such as NASA's Chandra (1999) and JAXA's Suzaku (2005), have contributed greatly, the depth and range of discoveries from XMM-Newton are particularly noteworthy. Recent advancements include the eROSITA of 2019 and NASA's NuSTAR from 2012.

A unique feature of X-ray detectors is their ability to measure individual photons. This contrasts many instruments for longer wavelengths, which measure integrated flux. This distinction is because X-ray photons have relatively high energies, enabling their individual detection. However, they also have relatively low fluxes, making them easier to count. Often, these detectors use materials like silicon, which produce an electric charge when an X-ray photon interacts with them. This charge is then measured and translated into information about the energy and direction of the incoming X-ray. Astronomers can construct images and spectra of X-ray-emitting astronomical objects by gathering data from numerous X-ray photons. In X-ray astronomy, focusing X-ray telescopes[1] inevitably confront a set of distinct challenges, such as the reflection of X-rays and the formation of an image. Once these challenges are overcome, a sensitive detector is essential to register the X-rays and convert them into data that can be stored for later analysis. We will delve deeper into each of these aspects using the XMM-Newton observatory, the primary data source for this thesis.

2.1.2 XMM-Newton Observatory

The XMM-Newton (X-ray Multi-Mirror) observatory, named in honor of Sir Isaac Newton, was launched on December 10, 1999, marking the first commercial launch of an Ariane-5 rocket (Jansen et al. 2001). XMM-Newton has made groundbreaking discoveries over its operational span. Among its key recent findings are the ability to determine the mass and spin of black holes (Pasham et al. 2019), observations of mysterious flashes from a black hole in the galaxy GSN 069 (Miniutti et al. 2019), and visuals of the dust rings from gamma-ray burst 221009A, the brightest gamma-ray burst ever observed (Tiengo et al. 2023). The list of discoveries continues to grow; XMM-Newton identified the universe's youngest pulsar (Esposito et al. 2020) and unveiled the first-ever observation of hot gas moving turbulently within a galaxy cluster (Sanders et al. 2020). On a larger scale, XMM-Newton illuminated the presence of diffuse hot gas across the intergalactic medium (IGM), addressing previously unresolved mysteries concerning the universe's 'normal' matter composition (Nicastro et al. 2018).

[1] Focusing mirrors are just one of the many design elements used in X-ray telescope construction. For example, the Rossi X-ray Timing Explorer (RXTE) lacks focusing X-ray mirrors but possesses the ability to study rapid time variability in the emission of cosmic X-ray sources across a broad spectrum of X-ray energies.

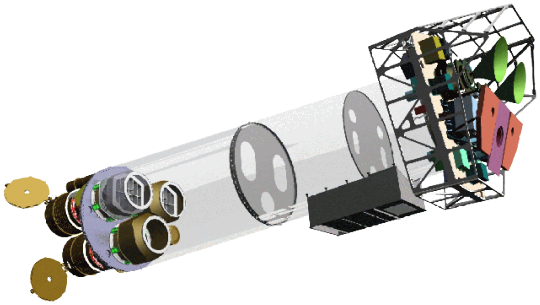

Figure 2.1: The XMM-Newton payload. The green cones at the right-hand side are the radiators for the EPIC-MOS cameras, while the pn and RGS radiators are shown in violet and light blue, respectively. The Optical/U.V. Monitor Telescope (XMM-OM) is almost obscured from view but can be seen as a dark cylinder towards the left of the image. *Figure from Jansen et al. (2001).*

Although initially projected for a ten-year service life, as of 2024, the XMM-Newton continues its mission. Its 48-hour orbit, ranging from a 7000 km perigee to a 114,000 km southern apogee and inclined at 40° to the equator, is optimized for data collection. This positioning minimizes disturbances from the Van Allen radiation belts and Earth's shadow (Page 2003).

2.1.3 X-ray Focusing Mirrors

Detecting X-rays from space is a particularly complex challenge. Unlike visible light, X-rays incident on a material generally penetrate and, if the material is thick enough, are absorbed. This is why X-rays are used in medical imaging; they pass through the body and can be detected on the other side. Traditional optical telescopes use mirrors to gather and focus visible light, but X-ray telescopes require a different approach to reflection. This characteristic significantly complicates the design and construction of telescopes for observing X-rays. X-rays must strike the material at a very shallow angle, almost parallel to the surface. This technique is known as grazing incidence. At these shallow angles, X-rays can skip off the surface, similar to a stone skipping across water. Attaining sharp focus and maximizing the collecting area for X-rays pose notable challenges for X-ray telescopes, given their shallow reflection angle. The common solution is the nested configuration of the mirrors. This arrangement allows X-rays to undergo multiple reflections before converging on the detector, leading to X-ray observatories often having extended focal lengths. A prime example of this design principle is the Wolter telescope design (Wolter 1952). Specifically, the Wolter Type I configuration (see Figure 2.2) combines parabolic primary mirrors with hyperbolic secondary mirrors. This design is especially advantageous in X-ray astronomy imaging due to its optimal aperture-to-focal length ratio. By nesting multiple mirror shells in the Wolter Type I design, a considerable collecting area is achieved without resorting to bulky, heavy mirrors, effectively reducing spherical aberration.

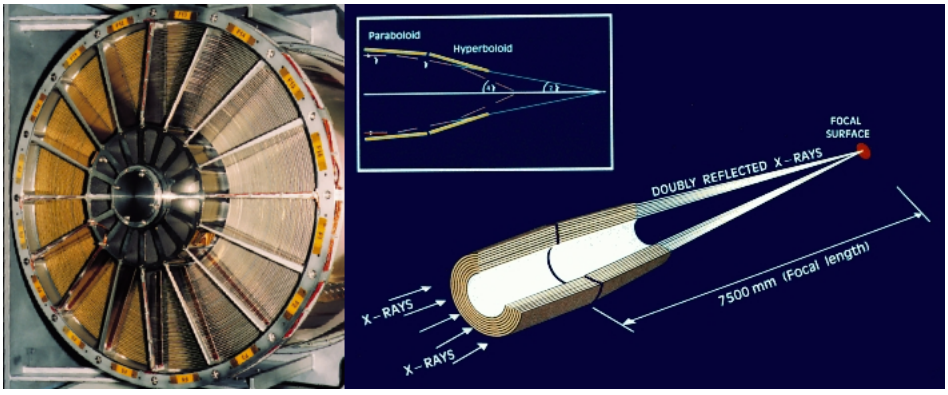

Figure 2.2: The mirror module of XMM-Newton with 58 nested mirrors *(left)*. Light path in the XMM-Newton telescope showing only one EPIC camera in its primary focus *(right)*. Schematic view of a Wolter Type-I telescope illustrating the use of a hyperbolic and parabolic mirror combination to decrease the focal length *(right-top)*. *Figures from XMM-Newton-SOC (2023).*

The XMM-Newton observatory is equipped with three Wolter Type I telescopes. To optimize reflectivity, the nickel mirrors are coated with gold. The XMM-Newton telescope nests 58 mirrors, as shown in Figure 2.2. These mirrors are typically arranged in a conical shape, with each subsequent mirror capturing X-rays from a wider field of view ($\sim 30°$). Accordingly, the size of the mirrors varies with diameters ranging between 306 mm and 700 mm. Altogether, they provide a collecting area of 1500 cm^2 at 2 keV and 900 cm^2 at 7 keV, offering a significant photon collecting area across a wide energy range. The XMM-Newton optics module has a focal length of 7.5 meters.

2.1.4 Detection of X-rays

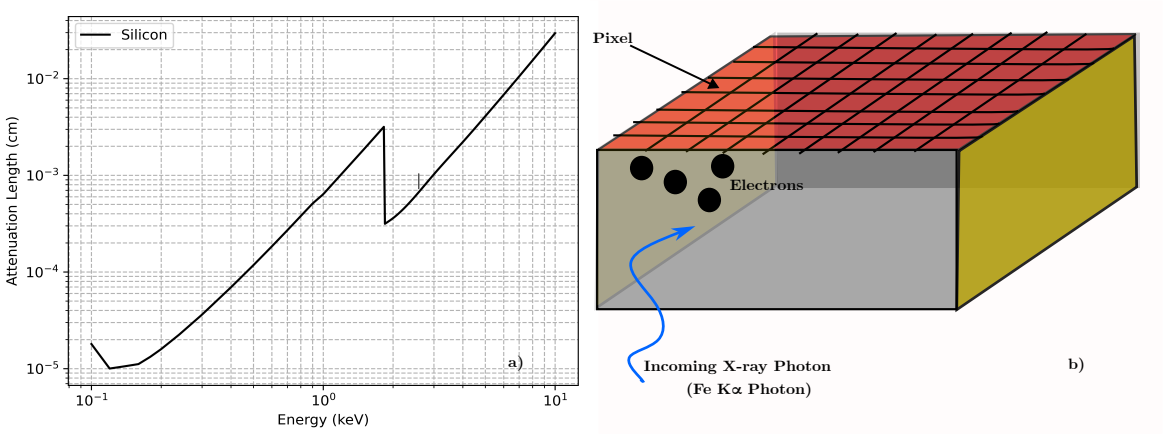

Figure 2.3: The linear attenuation length or mean absorption depth of an X-ray photon in silicon as a function of photon energy. Figure obtained using the `xraylib` package in Python (*left*). Basic principle of a CCD. When a photon enters from below, it generates a certain number of free electrons depending on its energy. These electrons are then gathered and held in a specific location within each pixel because of the applied voltages. Later, controlled pulses are used to move the accumulated charge to the edge of the CCD, where the readout electronics are situated (*right*).

Once X-rays are focused by optimizing the collecting areas, the detectors placed at the focal plane must exhibit exceptional sensitivity to capture and transform the X-ray photons into electrical signals effectively. Invented at Bell Laboratories in 1969, Charge-Coupled Device (CCD) detectors have emerged as particularly effective tools in this context. Combined with precision designs like the Wolter Type I optics, CCDs have pushed the boundaries of what we can observe and understand in X-ray astronomy. A CCD is an array of linked capacitors made from semiconductor materials (see Figure 2.3, right panel). X-ray photons interact in a semiconductor substrate and are converted into electron-hole pairs. This phenomenon is known as photoelectric absorption. An applied electric field is then used to collect the charge carriers (usually electrons) and store them in pixels. Each pixel can pass its signal to its neighbor, moving it across the grid. At the end of this chain, there is a readout amplifier, which converts the signal into a digital form we can use.

The sensitivity of these detectors is significantly influenced by the photoelectric absorption of X-rays within the silicon material. The attenuation length (i.e., the inverse of absorption probability[2]) defines the energy range for optimal X-ray sensitivity, from roughly a few hundred eV to 10 keV. Photons with energies below a few hundred eV will interact close to the surface and may be incompletely detected or absorbed in the surface and not detected at all. Photons with higher energies will likely pass through the active region without interacting (see left panel in Figure 2.3).

[2]The attenuation length is the average distance a photon of a particular energy will penetrate before interacting.

2.1.5 European Photon Imaging Camera (EPIC)

Once an X-ray photon has created a charge cloud, it must be collected and stored using either a metal-oxide-semiconductor (MOS) structure CCD or a p-n junction. The XMM-newton X-ray observatory uses both types of detectors. All together, it is called the European Photon Imaging Camera (EPIC). Both the EPIC-MOS (Turner et al. 2001) and EPIC-pn (Strüder et al. 2001) cameras are placed in the focal plane of two telescopes. In general, the charge collection and storage of the two technologies are similar, but the physical structures are quite different. The EPIC CCDs are sensitive not only to X-ray photons but also to I.R., visible, and U.V. light. Therefore, if an astronomical target has a high I.R., U.V., or optical flux, there is a possibility that the X-ray signal becomes contaminated by those photons. To address this challenge, each EPIC camera is equipped with three separate filters: thick, medium, and thin.

2.1.5.1 EPIC-MOS

Each MOS camera consists of seven front-illuminated CCDs, and the imaging area is covered by 600×600px for each CCD. The individual pixel size stands at $40\mu m$, which corresponds to $1\farcs1$. These pixels collectively span an area measuring 2.5cm. To cover the whole focal plane with a diameter of $6.2cm$ (which corresponds to $28\farcm4$), the seven CCDs are arranged into a mosaic pattern[3], whereas the focal point lies in the middle of the central CCD (XMM-Newton-SOC 1998).

2.1.5.2 EPIC-pn

The EPIC-pn camera uses p-n CCDs, which enables it to capture both low and high-energy X-rays. Its back-illuminated design ensures excellent sensitivity to low-energy emissions, while the thicker active regions allow for the accumulation of high-energy events. The entire EPIC-pn wafer encompasses twelve distinct CCDs, each possessing 200×64 pixels. Every pixel measures $150 \times 150\,\mu$m, equating to $4\farcs1$. For imaging, a 6×6 cm area is used, represented by a 400×384 pixel matrix. This comprehensive coverage is achieved by overlaying the twelve CCDs. The EPIC-pn camera, much like its EPIC-MOS counterpart, is primarily operated in the 0.2-10.0 keV energy range. However, the EPIC-pn is also sensitive above 10 keV, which allows us to obtain detections up to 15 keV (XMM-Newton-SOC 1998). The observational capabilities of this setup are impressive. It boasts a spectral resolution represented by $E/\delta E$, which varies between 20 and 50. The camera offers specialized readout modes for its CCDs to deal with different sources. The MOS modes are similar to those of the EPIC-pn camera. One special readout mode is notable in the context of faint extended X-ray emission and will be described in the following section.

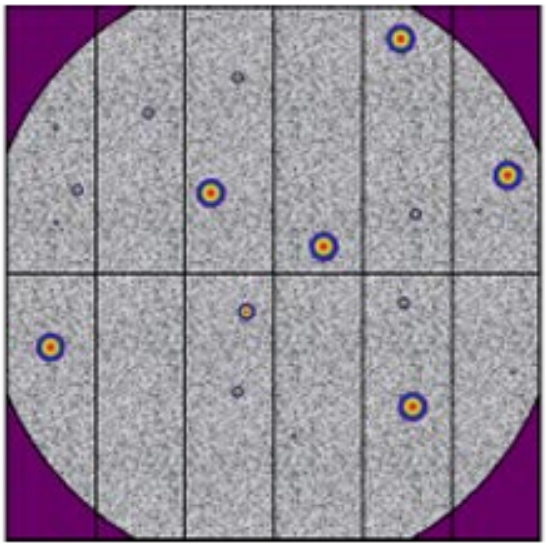

Figure 2.4: Full frame and extended full frame operating mode of the pn-CCD camera. *Figure from Strüder et al. (2001).*

[3] multiple CCDs or images are pieced together to form a single, larger CCD or image

2.1.5.3 Operating Mode - Full Frame (Extended)

As mentioned above, the EPIC cameras provide different readout modes for various count rates. The extended full frame mode is the most important mode in detecting faint extended X-ray emission. When studying diffuse X-ray emission, gathering as many photons as possible is crucial. Because of the nature of such diffuse emissions, they tend to be faint, and obtaining a high signal-to-noise ratio can be challenging. The extended full-frame readout mode of XMM-Newton has an X-ray integration time of 199.2 ms with 4.6 ms readout, leading to 2.3% OOT events (Strüder et al. 2001) (see Figure 2.4). This mode covers the entire detector field of view (with 398 × 394 pixel format; 27.°2 × 26.°2), which is beneficial for studying extended diffuse structures.

2.1.6 Comparison of X-ray Observatories for Diffuse Emission Detection

Precision optics (Wolter type I optics), coupled with unparalleled detector sensitivity (EPIC-MOS, EPIC-pn) and a large field of view (Extended FF-30°), make the XMM-Newton X-ray observatory an exemplary choice for observing diffuse emission structures in the G.C. Nonetheless, it is important to highlight the advantages of the XMM-Newton observatory over its contemporary peers. These specifications are listed in Table 2.1.

Table 2.1: A basic comparison of XMM-Newton's properties with those of Chandra, ROSAT, ASCA, RXTE, Swift, Suzaku, and NuSTAR in the context of observing faint diffuse emission.

X-ray Observatory	Launch Year	Optics (coating)	E range (keV)	A_e at 1 keV (cm^2)[a]	FOV[b]
XMM-Newton	1999	Wolter-I(Ni)	0.5-12	4650	30′ diameter (EPIC-pn)
Chandra	1999	Wolter-I(Ir)	0.1-10	555 (ACIS)	16′ on a side (ACIS-I)
NuSTAR	2012	Wolter-I(W/Si)	3-79	∼ 100	13′ on a side
Suzaku	2005	Wolter-I(Au)	0.2-600	1760 (XIS)	19′ on a side

[a] Mirror effective area.
[b] Field of view.

XMM-Newton advances in detecting diffuse X-ray emission with its wide energy range (0.2-12 keV), substantial collecting area (4650 cm^2 at 1 keV), and larger field of view (30°). Chandra specializes in high-resolution imaging and is superior for faint point source detections. Two primary factors make Chandra exceptionally suitable for observing faint point sources in the G.C. Firstly, Chandra's Point Spread Function (PSF) has a resolution of 0.°5[4] FWHM (as opposed to the FWHM of 6° observed with XMM-Newton), enabling the precise differentiation and analysis of individual point sources against the backdrop of diffuse emission. Second, Chandra's design and orbit substantially minimize background noise, which can otherwise obscure faint signals. Its detectors focus on X-ray emissions and filter out noise signals. This capability to maintain a low background noise level is important for detecting faint point sources.

NuSTAR specializes in high-energy X-rays (3-79 keV) and is not ideal for softer X-ray emissions. It is important to note that NuSTAR also faces significant background issues, including strong stray light and ghost rays that hinder observations of certain portions of the G.C. region. Suzaku is significant for

[4]The Chandra High-Resolution Camera (HRC) spatial response closely matches the mirror resolution, with the intrinsic on-axis PSF of the HRC being accurately modeled by a Gaussian with a Full Width at Half Maximum (FWHM) of 0.4 arcseconds. The spatial resolution for on-axis imaging with the Advanced CCD Imaging Spectrometer (ACIS) instrument is limited by the physical size of the CCD pixels, which is 0.492 arcseconds, rather than by the mirrors.

observing the G.C. emissions and holds historical importance. However, compared to XMM-Newton, Suzaku has a smaller effective area at all energies and a narrower field of view (FOV). Given these factors, XMM-Newton is the preferred choice for observing the faint signatures of steady diffuse X-ray emission.

2.1.7 XMM-Newton (EPIC) X-ray Background

All X-ray detectors, including EPIC detectors on the XMM-Newton observatory, inevitably confront X-ray backgrounds. These backgrounds are a mixture of noise within the desired cosmic X-ray photons. The origin of these backgrounds can be diverse. The X-ray background is classified into two major components: they might come from charged particles interacting with the detector material (often called Non X-ray Background) or intrinsic X-rays emitted from distant and diffuse celestial sources (called Cosmic X-ray Background (CXB)). Additionally, fluorescence from materials within the telescope itself may contribute. Understanding, characterizing, and subtracting these background components is crucial to ensure the accuracy of scientific analyses.

2.1.7.1 The Cosmic X-Ray Background (CXB)

The cosmic X-ray background (CXB) is a diffuse background radiation observed in the X-ray spectrum. It is similar to the cosmic microwave background (CMB) radiation, which is observed in the microwave portion of the electromagnetic spectrum, though they have different origins. The first evidence for the CXB was obtained by (Giacconi et al. 1962) during the same rocket experiment, which led to the discovery of Sco X-1. The CXB is dominated by three main components: the Galactic local foreground, solar wind charge exchange emission, and unresolved X-ray emission by distant celestial sources. The CXB is usually defined as the integrated emission of all the extragalactic sources in the X-ray energy band $\approx 2 - 100keV$ (Bulbul et al. 2020).

2.1.7.2 The Quiescent Particle Background (QPB)

The QPB is mainly caused by high-energy particles, predominantly protons, interacting with the detectors. Hence, it is Non X-ray background. These particles are not associated with any astronomical source and produce a continuous background level in the data. This "particle-induced background" has multiple components, and each component is temporally variable, although on different scales. For many observations, especially those targeting faint diffuse emission, the QPB can be comparable to, or even dominate, the actual astrophysical signal. Thus, properly modeling and subtracting this background is crucial for accurate analysis.

2.1.7.3 The Solar Activity

XMM-Newton observatory might undergo episodes during which the X-ray detectors are bombarded by low-energy ($\approx 100keV$) proton from the solar wind. We called this contamination soft protons flares (SPF). These soft protons can bounce off the telescope's mirrors and interact with the detectors. These unpredictable episodes cause an up to 100 times (or even more) increase in the quiescent background rate. Data collected during these intervals are unusable.

2.1.8 XMM-Newton Science Analysis System (SAS)

The complexity of XMM-Newton's instrumentation, with its multiple detectors and technologies, demands a specialized approach to processing data, handling backgrounds, etc. The XMM-Newton Science Analysis System and Extended Source Analysis Software (XMM-SAS and XMM-ESAS, or SAS and ESAS, with ESAS being a subpackage of SAS) (version 19.0 (ESA 2023)) play a central role in decoding the raw data captured by the observatory and converting them into so-called "clean reprojected events." One of the core functionalities of ESAS is its ability to model and subtract

background signals effectively. ESAS creates both quiescent particle background spectra for spectral fitting and exposure-corrected, background-subtracted (particle, soft proton, and solar wind charge exchange) images. The spectra and images are produced for user-defined regions within an observation field of view. The output files are in standard FITS[5] format.

To fully decode and understand the events regarding energy and spatial distribution, ESAS requires the use of response files: the Auxiliary Response File (ARF) and the Redistribution Matrix File (RMF). Observers need to understand the structure of the X-ray data (i.e., events) and the response files to interpret X-ray phenomena.

Event file

X-ray (or γ-ray) astronomy, which observes radiation at energies greater than 50 eV, the primary data set is an "events list." This list is essentially a table detailing individual photons (i.e., counts), recording 4 attributes like their spatial position on the detector, time of arrival, and photon energy. From this event list, several common data products can be derived, each with its specific emphasis: images involve spatial binning at the expense of energy and time information, spectra entail binning along the spectral axis while sacrificing spatial and temporal details, and light curves are generated through binning along the time axis, with the cost of spatial and energy particulars.

Response files

The Auxiliary Response File (ARF) contains information about the effective area of the telescope as a function of energy, encoding energy-dependent variations due to the telescope's optics, detector characteristics, and filters. Filters play a crucial role in this context. Figure 2.5 presents the effective area of the EPIC cameras considering these filters. Essentially, it describes the efficiency with which the instrument detects incoming photons of a given energy. Measured in units of cm^2, the ARF provides a way of translating a flux, in units of photons $cm^{-2}s^{-1}$, into count. Conversely, the dimensionless Redistribution Matrix File (RMF) provides insights into how a monochromatic photon incident on the detector is spread out in the detected energy spectrum, largely because of the intrinsic energy resolution of the detector. The RMF gives the probability that a photon of a given energy is registered in a given channel. The ARF and RMF are fundamental in converting the raw event data into a physical spectrum. By applying these response files to background-subtracted data, observers can model and interpret the observed X-ray spectra in terms of astrophysical phenomena. In addition, the response files of the XMM-Newton can be employed to convert photon counts into photon fluxes directly without the need for spectral modeling. This allows for a direct comparison with the flux obtained through spectral analysis (this approach is described in Chapter 3).

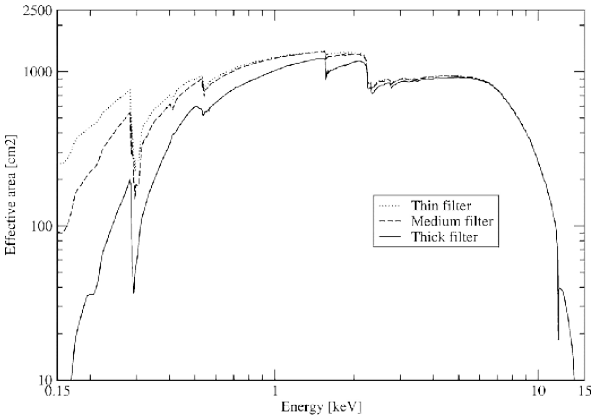

Figure 2.5: Combined effective area of all telescopes assuming that the EPIC cameras operate with the same thin, medium, or thick filters. *Figure from (ESA 2023).*

[5]Flexible Image Transport System (FITS) is an open standard defining a digital file format useful for storage, transmission, and processing of data formatted as multi-dimensional arrays (for example, a 2D image), or tables. FITS is the most commonly used digital file format in astronomy.

2.2 Observation Selection and Standard Reduction

2.2.1 Observation Selection

Within the CMZ, the Sgr B molecular complex is a compelling region for studying steady diffuse X-ray emission (Chapter 1). The work in this thesis is based on the deep XMM-Newton scan of the CMZ conducted in 2020 (480 ks, P.I.: M. Clavel), supplemented by all archival data covering our region of interest in the CMZ throughout the mission's duration. A notable possibility with such an extended data set is its capacity to evaluate the time variability of the diffuse X-ray emission (refer to Chapter 1 for variability discussion). The main rationale for relying on this region is its established history of extensive research concerning non-thermal diffuse emission (Inui et al. 2009; Terrier et al. 2010; Nobukawa et al. 2011; Zhang et al. 2015; Terrier et al. 2018; Rogers et al. 2022; Kuznetsova et al. 2022). Sgr B contains a significant fraction of the Milky Way's dense molecular gas (Schmiedeke et al. 2016). Compared to other parts of the Galaxy, giant molecular clouds like Sgr B in the G.C. are 10 to 100 times denser and more turbulent (Morris & Serabyn 1996). However, star formation is currently limited to a few regions, such as Sgr B2 (Hatchfield et al. 2020), making Sgr B an even more intriguing area to study.

2.2.1.1 Region Size and Data Selection

For this study, a region size of $900'' \times 900''$ centred on the $RA = 266.86°$, $Dec = -28.427°$ in Galactic coordinates was chosen. This site includes the region description of the Terrier et al. (2018) for the Sgr B molecular complex, which includes multiple sub-regions such as Sgr B2, G0.74–0.11, G0.66–0.13, and others. We filtered all the XMM-Newton observations within this specified box region from the XMM-Newton Science archive, gathered over 20 years from 2000 to 2020.

Within this 20-year time frame, we have identified 5 main epochs: 2000-2001, 2004, 2012, 2018, and 2020 as temporal snapshots of our study. Each observation was grouped based on its observation date into the appropriate epoch. This comprehensive dataset enabled us to reach the steady diffuse emission below the variable emission on (20 yr) time scale. All the XMM-Newton data used in this work is detailed in Table 2.2 and the time exposure maps for the 5 epochs in which the XMM-Newton data have been grouped (in units of seconds, with 2.500 pixel size, and in Galactic coordinates) can be found in Figure 2.6.

Table 2.2: XMM-Newton observations covering at least part of Sgr B.

Observation ID	Epoch (yr)	Start Time (UTC)	Exposure (s)	Pointing RA (hh:mm:s)	Pointing Dec (dd:mm:s)
0112970301	2000	2000-09-15 17:54:05.000	20788	17:47:09.99	-28:28:03.0
0112971501	2001	2001-04-01 00:25:11.000	25332	17:47:09.99	-28:28:03.0
0203930101	2004	2004-09-04 02:52:56.000	50918	17:47:40.02	-28:24:44.0
0694640601	2012	2012-09-06 10:33:15.000	41921	17:47:47.57	-28:26:30.2
0694641301	2012	2012-09-26 18:11:18.000	56713	17:47:12.76	-28:30:59.5
0802410101	2018	2018-04-02 00:59:38.000	103000	17:47:20.40	-28:23:07.0
0862471001	2020	2020-09-27 13:23:33.000	44000	17:47:20.40	-28:30:59.5
0862471101	2020	2020-09-28 01:56:53.000	44000	17:47:47.58	-28:26:30.2

2.2.2 Standard Data Reduction

First, the calibrated event files from the XMM-Newton observations were generated by ESAS using `emchain` for MOS and `epchain` for pn. Then ESAS tasks `mos-filter` and `pn-filter` were used to exclude the SPF emission. After these filtering and correction steps, spectra and images from the

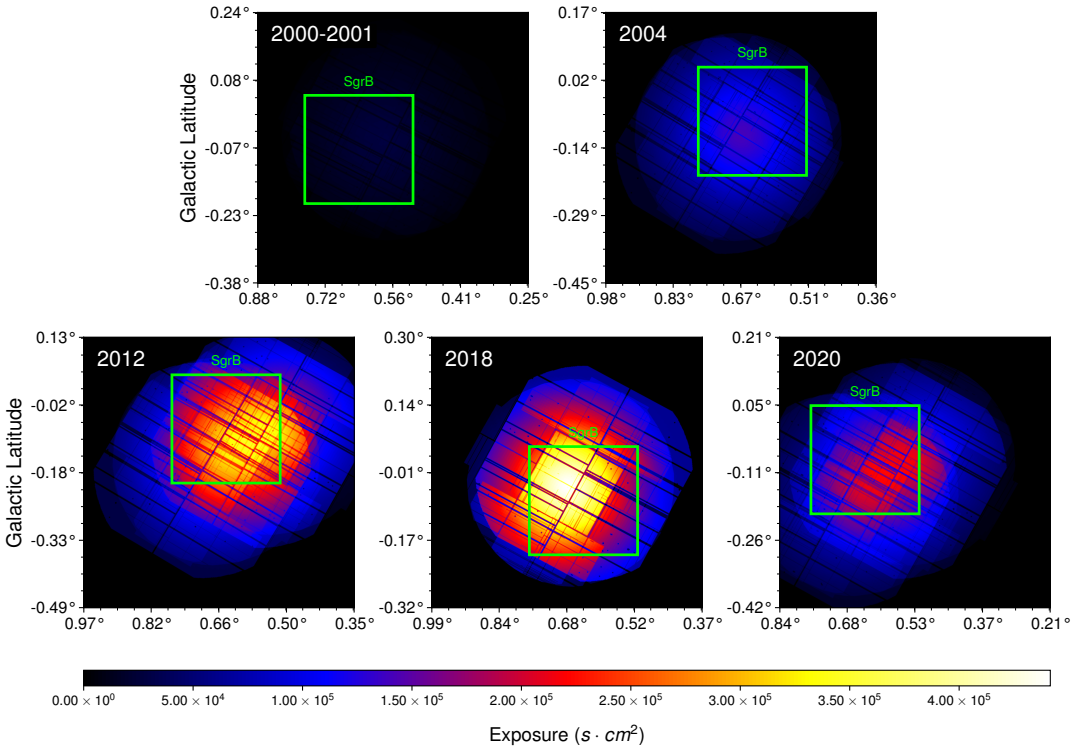

Figure 2.6: Time exposure maps for the 5 epochs in which the XMM-Newton data have been grouped (in units of seconds, with 2.500-pixel size, and in Galactic coordinates). The Sgr B region is marked in a green box. The top row shows the shallow XMM-Newton observations (in epochs 2000-2001 and 2004), while the bottom row features deep scans for the epochs 2012, 2018, and 2020. The color scale spans from 0 to $4 \times 10^8 s\, cm^2$.

full XMM field of view of $30^{'}$ were extracted using `pn-spectra` for EPIC-pn and `mos-spectra` for EPIC-MOS. After extracting the spectra and images, we focused on the background handling. Dealing with backgrounds in X-ray astronomy presents several challenges, especially when the morphology of the signal of interest is unknown. In such scenarios, local background methods may not be optimal. There are two non-local methods available for addressing this challenge.

Blank Sky Observations Firstly, there are blank sky observations pointed at sky regions with zero or very low X-ray emission from celestial sources. They do not entirely lack signals but are chosen because they are quieter than other parts of the sky in X-ray activity. However, the CXB exhibits significant variations across the sky. A good background in one region might be unsuitable for another. Moreover, blank-sky data can contain uncertain residual Solar Proton and Solar Wind Charge Exchange (SWCX) contaminations. Most importantly to our research, which focuses on the study of the diffuse X-ray background, relying on blank-sky data could over-subtract our desired signal during background corrections (S. L. Snowden 2019).

Filter Wheel Closed Observations: On the other hand, we have the Filter Wheel Closed (FWC) observations taken with the XMM-Newton filter wheel in a closed position, meaning the detectors are not exposed to X-ray photons from celestial sources. Therefore, what is measured primarily represents the particle-induced background of the instrument under the same conditions as the observing

conditions. The unexposed corners of the XMM-Newton EPIC-MOS detector[6] that are masked off. The MOS data obtained with the FWC data serve as estimators of the particle background for each observation used in the X-ray analysis of faint extended sources (Bulbul et al. 2020). Given our objectives, the FWC data correctly modeled the non-X-ray background in the given context and was accepted as the most appropriate approach for our background analyses.

The QPB background spectra and images were generated with the `pn-back` and `mos-back` commands. At the end of the standard reduction pipeline, for each observation, cleaned X-ray photon count maps, QPB background maps, and exposure maps were created for a given energy band (See the Figure 2.7 for Photon, background and exposure map for an observation from 2018 epoch (OBSID:0802410101))

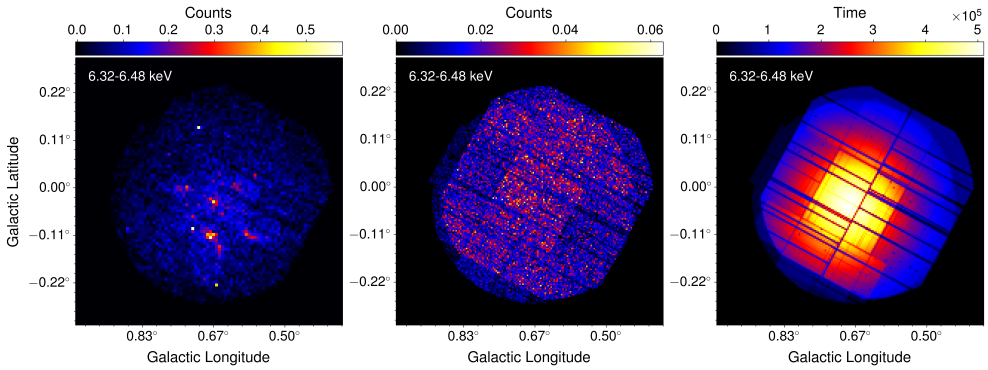

Figure 2.7: Combined Images for the three EPIC (MOS1, MOS2 & pn) instruments from the observation ID (0802410101) for the 6.32-6.48 keV energy band. Individual EPIC exposures were combined using the ESAS `comb` task. The count image (Left) was smoothed to 10×10 blocks by taking the mean of the blocks as a downsampling function. The FWC image (middle) was smoothed to 5×5 blocks by taking the mean of the blocks as a downsampling function. The exposure image (right) and the color scale are presented in seconds.

[6]The particle background of XMM-Newton EPIC-MOS are difficult to predict and eliminate because the unexposed region on the detector is small, i.e., statistics on the background level is limited (Bulbul et al. 2020).

Chapter 3

Extraction of 6.4 keV flux maps

We separate the observed diffuse Fe $K\alpha$ emission into two distinct components: a steady and variable parts. Our primary focus is on the steady emission beneath the more dynamic variable component. Due to the complexities of extracting the steady emission, I have developed specialized statistical tools designed to isolate it confidently.

Contents

The primary goal of this thesis was to analyze the non-thermal steady diffuse emission from Sgr B, which is traced by the 6.4 keV Fe $K\alpha$ line. To achieve this, I first extracted the 6.4 keV maps based on the methodology explained in Terrier et al. (2018). This chapter aims to provide a detailed examination of the extraction process of the diffuse Fe $K\alpha$ emission at 6.4 keV. A notable challenge encountered in the methodology of Terrier et al. (2018) is the occurrence of "negative flux anomalies" in regions exhibiting low 6.4 keV flux values. Considering my focus on the steady emission, which is a characteristic of these low flux areas, it is imperative to accurately identify and examine these faint fluxes. I have analyzed this specific issue and developed a statistical method to address it. The subtleties of this approach will also be discussed in this chapter, which is structured into two main parts. Section 3.1 focuses on the methodology outlined by Terrier et al. (2018). Following this, Section 3.2 identifies and examines the occurrence of negative flux anomalies. To address these challenges, Sections 3.3 and 3.4 discuss the state-of-the-art approaches developed.

All the investigations presented in this thesis are based on a fundamental concept called pixel analysis paired with photon counting statistics. In this context, 'pixel' refers to a designated unit of analysis in our data set, equivalent to $30'' \times 30''$, distinct from the native XMM-Newton pixels of $2''.5 \times 2''.5$. Each pixel ($Pixel_{i,j}$) in all the maps presented in this chapter is treated as a discrete entity, and various calculations are performed on a pixel-by-pixel basis to extract information or make decisions.

3.1 Estimation of the Continuum and Diffuse 6.4 keV Line

3.1.1 Introduction

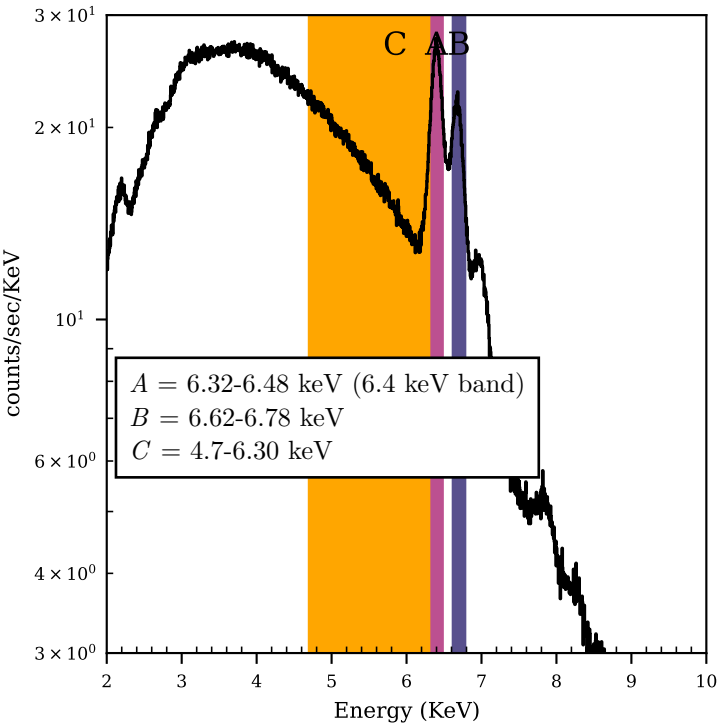

Figure 3.1: Simulated X-ray spectrum of the Galactic Center generated using a `Python sherpa.astro.ui` module for an observational exposure time of 40,000 seconds. The defined source model incorporates a combination of thermal and non-thermal components (`tbabs*(apec+po+ga+ga)`) as detailed in the text. Energy band 6.32-6.48 keV, band 4.7-6.30 keV and band 6.62-6.78 keV are shaded in respective text colors.

The overall emission characteristics of the GC are essential to understand the nature of the 6.4 keV emission (see Chapter 1) and its extraction. Figure 3.1 shows the simulated X-ray spectrum of the GC,

including essential diffuse emission components. I use Figure 3.1 to illustrate the extraction process throughout this section. The technique for extracting the 6.4 keV line from the GC begins with the identification of a narrow band that contains the 6.4 keV line (Band A covering the energy range from 6.32 to 6.78 keV), followed by the removal of the underlying continuum emission to effectively isolate the 6.4 keV line. This approach is known as continuum subtraction. Accurate estimation of the continuum is crucial before the 6.4 keV emission can be extracted. The model flux from adjacent energy bands estimates the continuum level for Band A. To accomplish this, two contiguous energy bands were identified, as shown in Figure 3.1. The first, Band C, covers a continuum energy range from 4.7 to 6.3 keV, while the second, Band B, is a narrow band including continuum and the 6.7 keV line. Band B covering energy ranges from 6.62 to 6.78 keV.

3.1.2 Leakage Correction Applied to XMM-Newton Maps

The methodologies of Terrier et al. (2018) were developed for the extraction of the 6.4 keV Fe $K\alpha$ flux from XMM-Newton images, enabling the Fe $K\alpha$ morphology to be analyzed consistently across different epochs. The aim was to ensure that the flux extracted from XMM-Newton imagery would be comparable to that obtained through standard spectral analysis. The flux from X-ray sources is typically acquired through spectral analysis. This process involves collecting X-ray data from the target, processing to remove background, and then using theoretical models to fit the spectrum using software such as `Sherpa`. The X-ray flux can be precisely determined by fitting these models to the observed data. The need for such precision is important because X-ray detectors face challenges with energy dispersion, meaning they record photons across a range of energies rather than at one specific energy level. This dispersion can lead to "leakage" with X-ray events expected to fall within a specific range detected at slightly higher or lower energies. The RMF matrix quantifies this dispersion (see Chapter 2). In a perfect world, the RMF would present a direct one-to-one relationship between the energy of the incoming X-ray and the channel in which it is detected, appearing as a diagonal matrix.

Nonetheless, imperfections in real-world detectors lead to the registration of photons of a given energy in adjacent channels.Terrier et al. (2018) used pre-calculated response matrices (canned RMF files) for XMM-Newton's EPIC-pn and MOS cameras to address this challenge. These matrices include predetermined correction factors that account for the position-dependent characteristics of the detectors. These correction factors were applied as leakage corrections to the XMM-Newton maps.

The first leakage correction was applied to the fraction of flux expected to be contained in the 6.7 keV line following the model and parameters considered in section 3.1.4. Figure 3.1 illustrates that Band B includes both a continuum and the 6.7 keV line. This correction enables precise measurements of X-ray photon counts for the 6.7 keV line in Band B, thereby enhancing the accuracy of continuum flux calculations for this band. After isolating the 6.4 keV emission (refer to section 3.1.4), another round of leakage correction was implemented. This provided an accurate estimation of X-ray photon counts within the diffuse 6.4 keV Fe line, subsequently improving the precision of flux calculations.

3.1.3 Creation of Flux Maps

The conversion of the photon count (corrected for energy dispersion) into photon flux is achieved using the exposure map and the ARF. Flux for each energy band (6.32-6.48 keV (A), 6.62-6.78 keV (B), and 4.7-6.30 keV (C)) is obtained using the average spectral response of the telescope within the given energy range.

$$F_i = \frac{IMA_i - BKG_i}{EXP_i \times ARF_i} \tag{3.1}$$

where i is A, B, or C. Here, BKG_i refers to the instrumental background, and IMA_i refers to the photon counts for each band.

3.1.4 Continuum Estimation and Subtraction

Continuum Estimation

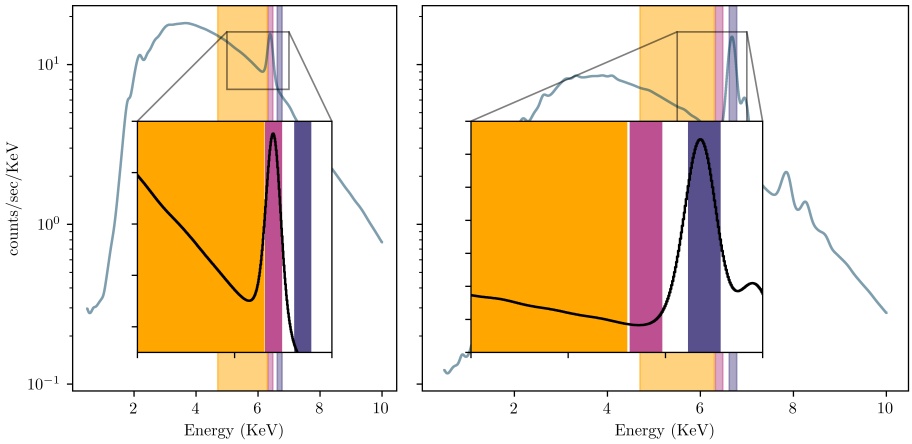

Figure 3.2: Simulated X-ray spectra without background, producing a dataset with 40,000 counts and a background rate of 1 count/s (with standard instrument response). All the model parameters are given in the text. Left: `Xspec` model `wabs*(po+ga)`; Right: `Xspec` model `wabs*apec`. `wabs` component is used to model absorption in Xspec, while the `po` is used to model the power-law continuum, and the `ga` is used to emission line using the Gaussian profile. `apec` is used to model thermal plasma emission. Energy bands 6.32-6.48 keV, 4.7-6.30 keV, and 6.62-6.78 keV are shaded in respective text colors. The 6.4keV and 6.7keV lines are zoomed in the figure.

Estimating the continuum in Band A relies on the flux measurements from Bands B and C. These fluxes are derived using a basic GC X-ray spectrum, which is modeled to account for various astrophysical components (see Chapter 1). The model includes absorption by interstellar material, represented by the hydrogen column density (N_H), a power law component to describe the continuum emission, and thermal emission from hot, diffuse gas. The flux for the continuum-dominated Band C was determined using a simple absorbed power law model (`wabs*po` in `Xspec`) with a power law index of $\Gamma = 2$ (see Figure 3.2 left). For Band B, the flux was obtained with an absorbed plasma model (`wabs*apec` in `Xspec`). The plasma component, with a temperature $kT = 6.5\,\mathrm{keV}$ and solar abundances, was used (see Figure 3.2, right). Both components are subjected to absorption by a foreground column density of $N_H = 7 \times 10^{22}\,\mathrm{cm}^{-2}$ (Terrier et al. 2018).

The contributions from the plasma component (hot_i) and the power law component (po_i) to the continuum of each energy band were obtained as model photon fluxes, where i can be B, or C (`flux 4.7 6.3` and `flux 6.62 6.78` in `Xspec`). These model fluxes from Band B and C were then used to interpolate the continuum level in the 6.4 keV band. This interpolation process ensures that the continuum emission in Band A is estimated with the highest possible accuracy to enable a more precise subtraction. The contributions from the plasma (n_{pl}) and the power law (n_{po}) components from the continuum-dominated bands to the continuum underlying the 6.4 keV line were determined as follows.

$$n_{pl} = \frac{\mathrm{po_B} \times \mathrm{F_C} - \mathrm{po_C} \times \mathrm{F_B}}{\mathrm{hot_C} \times \mathrm{po_B} - \mathrm{hot_B} \times \mathrm{po_C}} \tag{3.2}$$

$$n_{po} = \frac{\mathrm{hot_B} \times \mathrm{F_C} - \mathrm{hot_C} \times \mathrm{F_B}}{\mathrm{hot_C} \times \mathrm{po_B} - \mathrm{hot_B} \times \mathrm{po_C}} \tag{3.3}$$

where $F_{\mathrm{B/C}}$ represents the flux of the continuum bands. The photon counts for the continuum of Band A, ($\mathrm{Cont_A}$) can be interpolated using the coefficients n_{pl} and n_{po} from equations 3.2 and 3.3 as follows:

$$\mathrm{Cont_A} = (n_{pl} \times \mathrm{hot_A} + n_{po} \times \mathrm{po_A}) \times \mathrm{EXP_A} \times \mathrm{ARF_A} \tag{3.4}$$

Where, $\mathrm{EXP_A}$ and $\mathrm{ARF_A}$ denote the exposure and the average spectral response for Band A, respectively.

Continuum and Background Subtraction

As the name suggests, the photon count for the 6.4 keV line ($N_{6.4\ \mathrm{keV}}$) can be obtained by simply subtracting the associated instrument background ($\mathrm{BKG_A}$) and the continuum from the total counts ($\mathrm{IMA_A}$) in Band A.

$$N_{6.4\ \mathrm{keV}} = \mathrm{IMA_A} - \mathrm{BKG_A} - \mathrm{Cont_A} \tag{3.5}$$

The total background component ($N_{\mathrm{BKG},A}$) in Band A is defined as,

$$N_{\mathrm{BKG},A} = \mathrm{BKG_A} + \mathrm{Cont_A} \tag{3.6}$$

The total net counts included in the 6.4 keV line within Band A ($6.32 - 6.48$ keV) are obtained after applying the efficiency correction (see Section 3.1.2). Finally, the net flux included in the 6.4 keV line is given by:

$$F_{6.4\ \mathrm{keV}} = \frac{N_{6.4\ \mathrm{keV}}}{\mathrm{EXP_A} \cdot \mathrm{ARF_A}} \tag{3.7}$$

3.1.5 Reprojection

After the photon count maps were obtained, they were aligned onto a single, coherent World Coordinate System (WCS)[1] reference frame. The process is done using the tool `reproject_image_grid`, which is provided by the Chandra Interactive Analysis of Observations (CIAO[2]) program (Fruscione et al. 2006). This tool is used to project one image from its original tangent point to another in order to effectively align images from different observations with a common coordinate frame. The continuum-subtracted 6.4 keV photon count maps (originally in the Equatorial coordinate system with native XMM-Newton resolution of $2.5'' \times 2.5''$) were reprojected onto a 30×30 pixel grid in the Galactic coordinate system, with each pixel covering an area of $30'' \times 30''$. The center of the reference output was set to the center of Sgr B at RA = 266.862° and Dec = −28.427°. The applied transformation matrix involves rotation (to the GC orientation angle of 58.72°), scale, and translation from the source to the target coordinate system.

All photon count maps, such as $\mathrm{N_{6.4\ keV}}$ and $\mathrm{N_{BKG},A}$, were reprojected in such a manner that the integral over an aperture on the input and output images would yield the same value. This means that a single pixel in the output grid includes the sum of the photon counts of the $30'' \times 30''$ area in the input image. Exposure maps (EXP_i) were reprojected so that the output pixel value represents an average of the input values corresponding to a $30'' \times 30''$ area, ensuring the reprojection accurately reflects the desired normalization method for counts and the exposure. Figure 3.3 displays the 6.4 keV

[1] World Coordinate Systems (WCSs) describe the spatial transformations between one set of coordinates and another.

[2] CIAO is the software package developed by the Chandra X-Ray Center for analyzing data from the Chandra X-ray Telescope. It is also compatible with data from other astronomical observatories, such as XMM-Newton.

photon count map $N_{6.4\ \mathrm{keV}}$ for OBSID:0802410101 (EPIC-pn) within the Galactic coordinate system before reprojection (at the original XMM-Newton resolution of $2.5'' \times 2.5''$), and post-reprojection on a 30×30 pixel grid, with each pixel measuring $30'' \times 30''$.

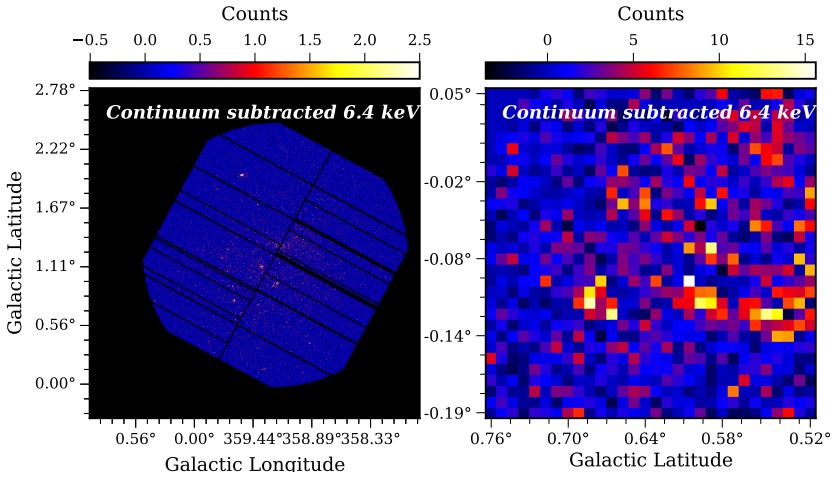

Figure 3.3: 6.4 keV Fe $K\alpha$ photon count map for the XMM-Newton EPIC-pn observation for the 2018 epoch (OBSID:0802410101) before reprojection (*left*). The color scale is normalized to the log scale. Resolution is $2\farcs5$. Reprojected 6.4 keV Fe $K\alpha$ photon count map into the WCS grid (centered at RA = 266.862° and Dec = −28.427°) with Sgr B cut (*right*). The output image dimensions are designated as 30×30 pixels. Resolution is $30''$.

3.1.6 Creation of Flux Mosaics

Composite images, often referred to as mosaics, were constructed using multiple exposures obtained from three EPIC cameras: MOS1, MOS2, and pn. This process was extended to include multiple observations across various epochs, specifically during the years 2000-2001, 2012, and 2020. For each epoch e, the summed count maps and the summed exposure time maps were created. The 6.4 keV X-ray flux per epoch, per pixel i, j is given by:

$$F_{6.4\ \mathrm{keV}}(i,j,e) = \frac{\Sigma N_{6.4\ \mathrm{keV}}(i,j,e)}{\Sigma \mathrm{EXP}_A(i,j,e) \cdot \mathrm{ARF}_A(i,j,e)} \tag{3.8}$$

Where $F_{6.4\ \mathrm{keV}}(i,j,e)$ represents the flux at a specific pixel (i,j) for a given epoch e, $\Sigma N_{6.4\ \mathrm{keV}}(i,j,e)$ denotes the sum of 6.4 keV net counts for that pixel, and $\Sigma \mathrm{EXP}_A(i,j,e) \cdot \mathrm{ARF}_A(i,j,e)$ is the sum of response times exposure from all relevant observations affecting that pixel in question. The associated uncertainties with these flux measurements were obtained using the formula by Gehrels (1986), used for pixels with relatively low photon counts.

$$\sigma(i,j,e) = 1 + \sqrt{\Sigma N_{6.4\ \mathrm{keV}}(i,j,e) + 0.75} \tag{3.9}$$

Here, $\sigma(i,j,e)$ represents the uncertainty for a specific pixel (i,j) and epoch e. Two exclusion criteria were applied to ensure the accuracy of the analysis and minimize the potential impact of less exposed regions, such as the image borders. The first criterion involved the removal of pixels with exposure times accounting for less than 10% of the maximum exposure time within each specific observation. The second criterion focused on mosaics, where pixels with exposure times representing less than 20% of the median exposure time within that specific mosaic were excluded (Terrier et al. 2018). Figure 3.4, the continuum-subtracted 6.4 keV flux mosaics ($F_{6.4\ \mathrm{keV},e}(i,j)$) are presented. The epoch e can be 2000-2001, 2004, 2012, 2018, or 2020. The indices i, j can vary from 0 to 30.

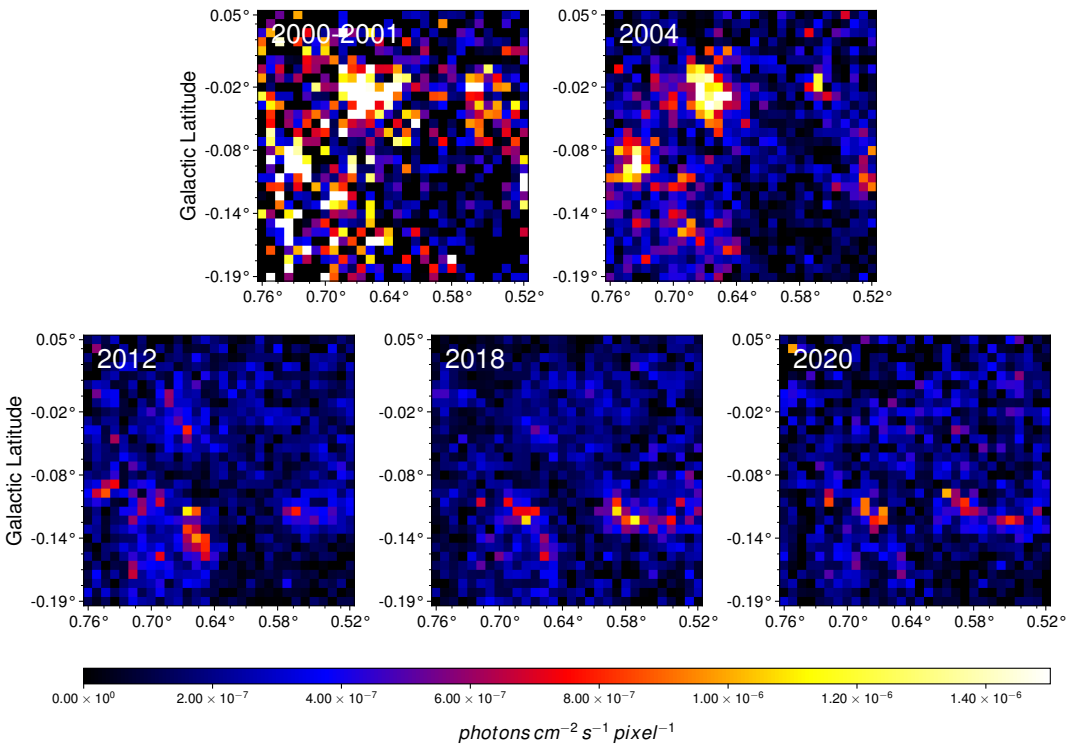

Figure 3.4: Continuum-subtracted 6.4 keV mosaics for various epochs (2000-2001, 2004, 2012, 2018, 2020). The coordinate axes are given in Galactic coordinates in degrees. The 6.4 keV X-ray flux intensities are measured in photons $\mathrm{cm}^{-2}\mathrm{s}^{-1}\mathrm{pixel}^{-1}$ units. Each pixel corresponds to a size of $30'' \times 30''$.

3.1.6.1 Exposure mosaics

The mosaic exposure per pixel i, j in band A is represented as $\delta t_{i,j,e}$.

$$\delta t_{i,j} = \sum_{\mathrm{instr},e} \mathrm{EXP}_A(i,j,e) \cdot \mathrm{ARF}_A(i,j,e) \tag{3.10}$$

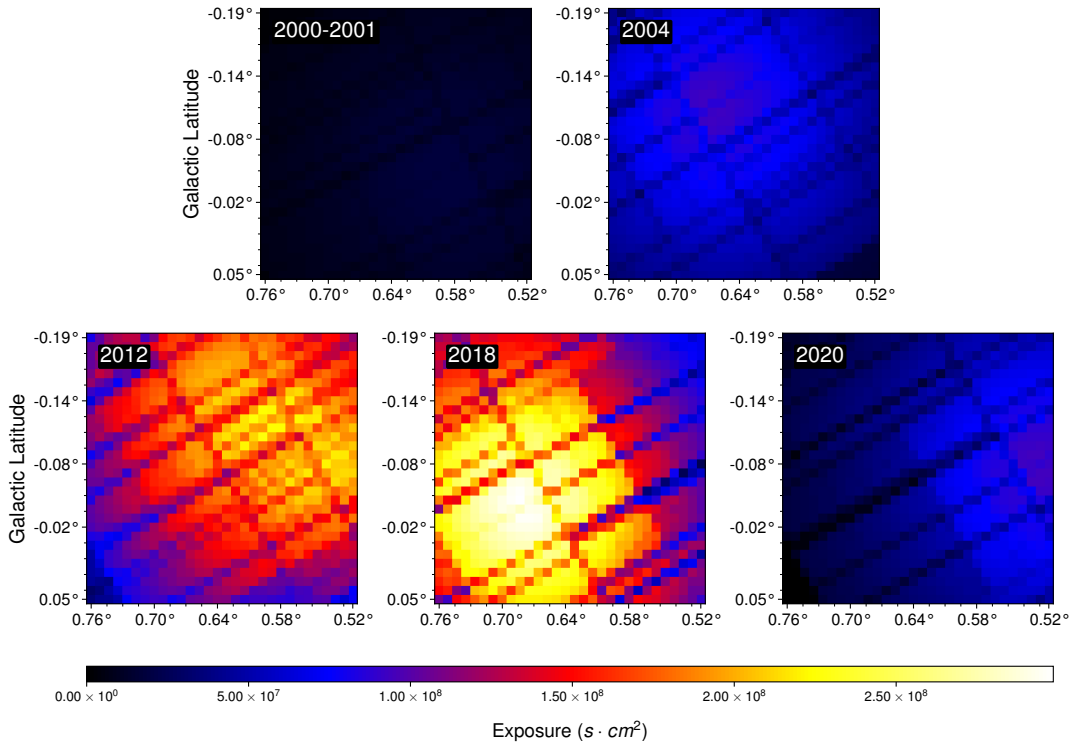

Figure 3.5: Exposure mosaics for the epochs 2000-2001, 2004, 2012, 2018, and 2020, displayed in Galactic coordinates. The exposures are measured in $s\,cm^2$, providing insights into the telescope's collecting area and observation duration. This measurement plays a crucial role in determining the total number of photons that the XMM-Newton telescope can gather. Each pixel represents a $30'' \times 30''$ area.

3.1.6.2 Continuum mosaics

The photon count from the continuum estimation for the pixel i, j is mathematically represented as $N_{cont}^{i,j}$

$$N_{\text{cont}}^{i,j} = \sum_{\text{instr},e} \text{Cont}_A(i,j,e) \tag{3.11}$$

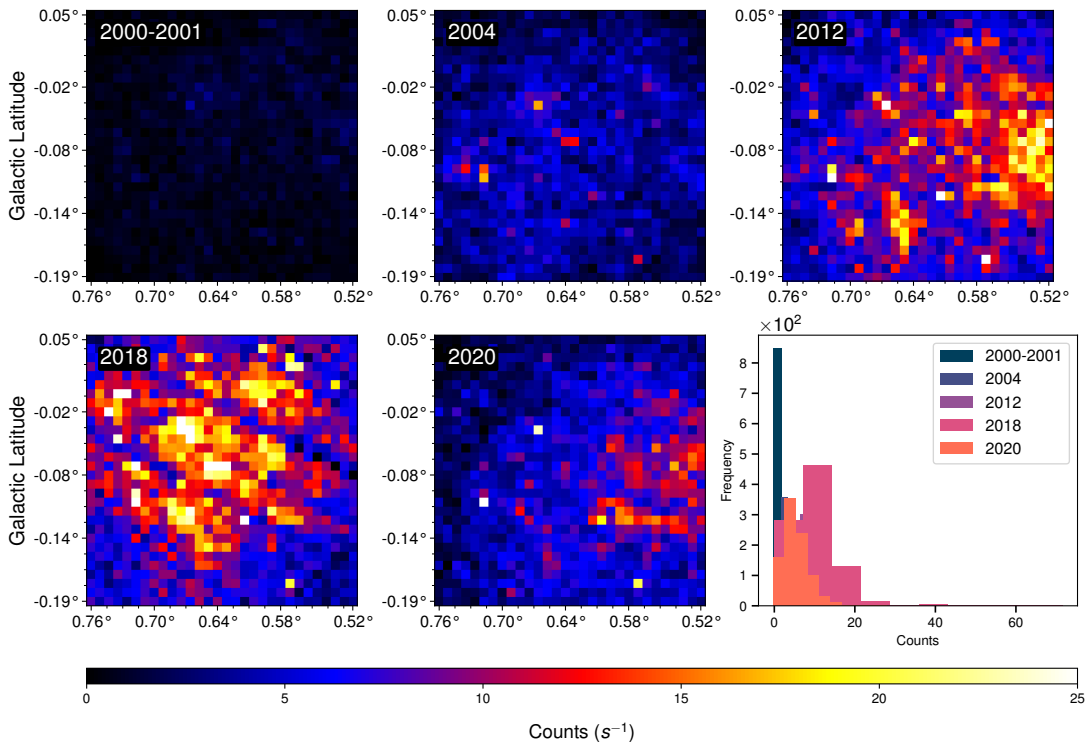

Figure 3.6: Continuum mosaics for various epochs (2000-2001, 2004, 2012, 2018, 2020). The coordinate axes are given in Galactic coordinates in degrees. The continuum intensities are presented in photon count units. Each pixel corresponds to a size of $30'' \times 30''$, and counts in $pixel_{i,j}$ represent as $N_{cont}^{i,j}$. In the bottom right, a histogram shows the distribution of photon counts throughout the observed epochs.

3.1.6.3 The net 6.4 keV mosaics

The continuum subtracted net count from the pixel i, j in band A is mathematically represented as $N_{net}^{i,j}$

$$N_{\rm net}^{i,j} = \sum_{\rm instr,e} N_{\rm 6.4\ keV}(i,j,e) \tag{3.12}$$

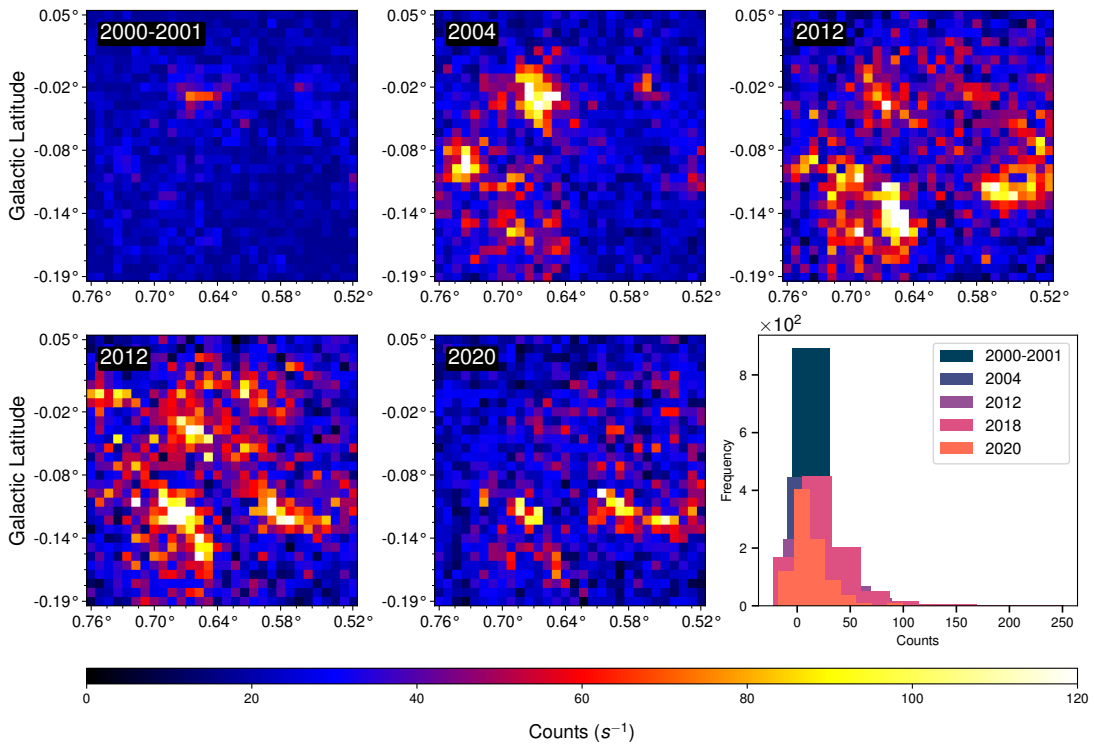

Figure 3.7: Continuum-subtracted net 6.4 keV photon count mosaics for the epochs 2000-2001, 2004, 2012, 2018, and 2020 are presented. The coordinate axes are given in Galactic coordinates and are measured in degrees. The continuum-subtracted net intensities are represented in photon count units. Each pixel corresponds to a size of $30'' \times 30''$. The counts in $pixel_{i,j}$ are represented as $N_{\rm line}^{i,j}$. In the bottom right, a histogram shows the distribution of photon counts throughout the observed epochs.

3.1.6.4 Total background mosaics

The total background photon counts are obtained as the photon count from the local background in pixel i, j and the photon count from the continuum estimation.

$$N_{\rm bkg}^{i,j} = \sum_{\rm instr,e} N_{{\rm BKG},A}(i,j,e) = \sum_{\rm instr,e} \left({\rm BKG}_A + {\rm Cont}_A\right)(i,j,e) \tag{3.13}$$

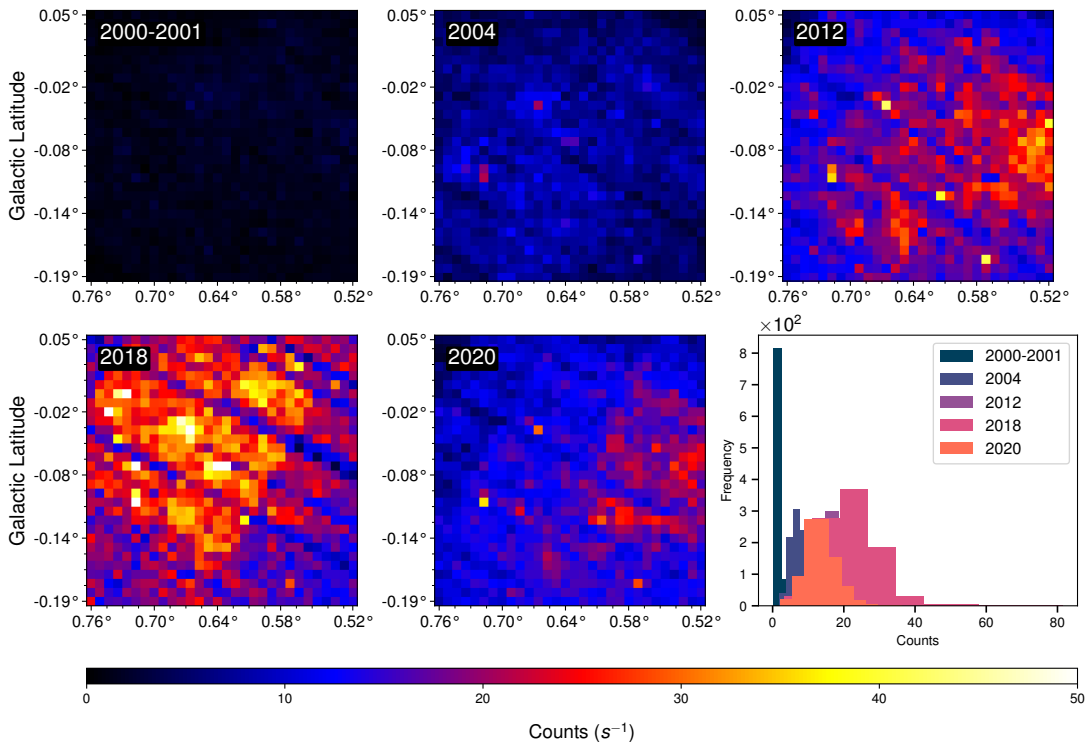

Figure 3.8: Background mosaics for various epochs (2000-2001, 2004, 2012, 2018, 2020). The coordinate axes are given in Galactic coordinates in degrees. The background intensities are presented in photon count units. Each pixel corresponds to a size of $30'' \times 30''$, and counts in $pixel_{i,j}$ represent as $N_{bkg}^{i,j}$. In the bottom right, a histogram shows the distribution of photon counts throughout the observed epochs.

3.1.6.5 Total Photon counts mosaics

The total photon count in each $pixel_{i,j}$ in band A, is denoted as $N_{tot}^{i,j}$, can be written as

$$N_{\rm tot}^{i,j} = \sum_{\rm instr,e} \left(N_{\rm 6.4\ keV} + N_{BKG,A}\right)(i,j,e) \tag{3.14}$$

or

$$N_{\rm tot}^{i,j} = \sum_{\rm instr,e} \left({\rm IMA}_A\right)(i,j,e) \tag{3.15}$$

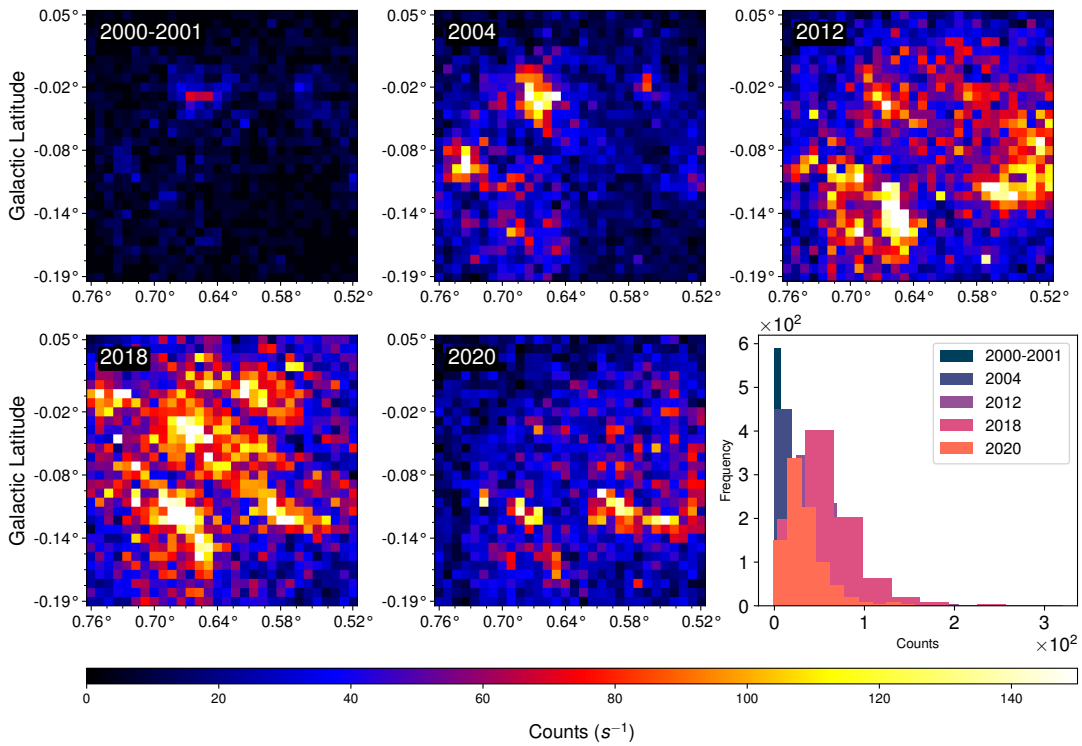

Figure 3.9: Total photon (N_{tot}) mosaics for epochs 2000-2001, 2004, 2012, 2018, and 2020. The coordinate axes are given in Galactic coordinates in degrees. The photon count intensities are presented in photon count units. Each pixel corresponds to a size of $30'' \times 30''$. In the bottom right, a histogram shows the distribution of total photon counts throughout the observed epochs.

The notations introduced in this section will be used throughout the following sections to provide a better understanding of the topics discussed.

3.2 Limitations of the Continuum Subtraction Method

This section focuses on the challenges encountered in the analysis of 6.4 keV mosaics, revealing two primary issues: the emergence of negative estimation for the continuum and the occurrence of negative fluxes in certain pixels post-continuum subtraction. Initially, we will examine the essence of these challenges and their broader consequences. Although the presence of negative continuum levels might be mitigated through straightforward filtering techniques, the issue of negative 6.4 keV flux complicates the precise handling of faint signals. This section will thoroughly investigate an approach called 'Poisson Method' that was developed to tackle this challenge.

3.2.1 The Phenomenon of Negative Flux

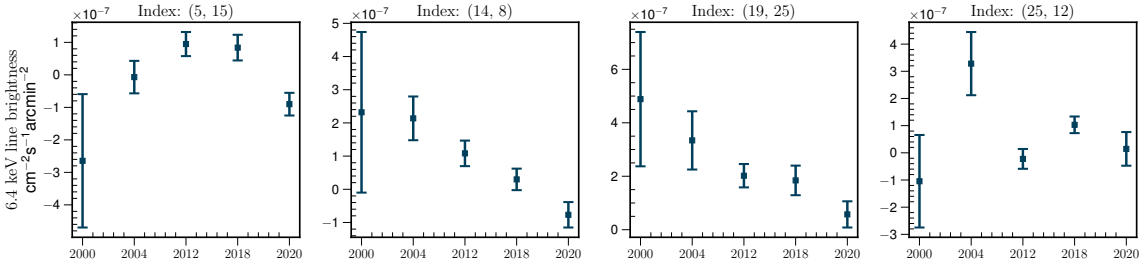

Figure 3.10: Variations in the 6.4 keV surface brightness over the five epochs within an area corresponding to a single pixel ($30'' \times 30''$). These variations are presented for the arbitrary pixel coordinates (5, 15), (14, 8), (19,25) and (25, 12).

Figure 3.10 illustrates the variations in brightness of the continum subtracted Fe $K\alpha$ emission line at 6.4 keV over a $30'' \times 30''$ region of the sky (single pixel in the 6.4 keV map in Figure 3.4). The flux intensity variation was observed across five epochs for a selection of arbitrary pixels ((5, 15), (14, 8), (19,25), and (25, 12) in pixel coordinates). Each panel in the figure represents the light curve for a unique pixel, where the y-axis shows the brightness in units of 10^{-7} photons cm^{-2} s^{-1} arcsec^{-2} and the x-axis represents time in years (epoch). Certain epochs of these pixel-level light curves exhibit negative flux values, particularly in pixels representing faint fluxes (see epoch 2000 at index (5,15) and epoch 2020 at index (25,12)). This occurs when there is an overestimation of the continuum; subtracting this overestimated continuum from the total observed flux can result in negative values. While these negative values are typically overlooked in variability analyses focusing on high flux values (in larger regions like Sgr B or smaller regions like Sgr B2), they pose significant challenges in faint pixel-level evaluations. The occurrence of negative pixels is an inevitable consequence of statistical fluctuations, fundamental to observational data when assuming Gaussian statistics with low photons or limited observation time (i.e., low statistics). This constraint demands a more sophisticated method to accurately isolate the 6.4 keV line where precision at low fluxes is critical. Addressing this challenge leads us to implement a new method called Poisson methodology, a statistical technique used to manage data characterized by low flux values (either due to low photon count or low exposure).

Additionally, negative continuum estimations may lead to incorrect 6.4 keV levels post-subtraction. Negative continuum estimations arise because of the interpolation errors. Data with high background noise or a low signal-to-noise ratio (SNR) could lead to such errors. During the analysis, pixels with these inaccurately interpolated continuum values are ignored from the calculations.

3.3 The Poisson Statistics

In this section, we address the issue of negative flux during post-continuum subtraction for pixels characterized by low flux values. By applying Poisson statistics and using probability density estimations, we've developed a technique to estimate the upper limits[3] of faint flux values. This approach not only addresses the negative flux problem but also significantly enhances the reliability and precision of data interpretation. However, an understanding of certain statistical principles is vital for grasping our method, which we will present in the following subsections prior to discussing the methodology.

3.3.1 Random variables and distribution functions

In statistics, a random or stochastic variable is a variable whose possible values are numerical outcomes of a quantity that is subject to random variations. The "distribution function" is a function that describes the probability distribution of such a random variable.

The univariate distribution function describes the likelihood of different outcomes for a single random variable. The Uniform Distribution stands as the simplest univariate distribution. It is applicable when each outcome within a specific range is equally likely, offering a constant probability. This distribution was explored in our discussion of the perfect toy model case, illustrating its foundational role in modeling evenly distributed outcomes. Among the common univariate distribution functions, the Normal (or Gaussian) and the Poisson distribution are the most used in astrophysics. The Gaussian distribution is central due to its prevalence in describing statistical noise and background fluctuations in observational data. Similarly, the Poisson distribution is crucial for its ability to model discrete events, such as photon counts, which are fundamental in any X-ray astronomical observations. In the following sections, we will thoroughly examine the Poisson distribution, exploring its mathematical formulation, properties, and the contexts in which it becomes applicable in our work.

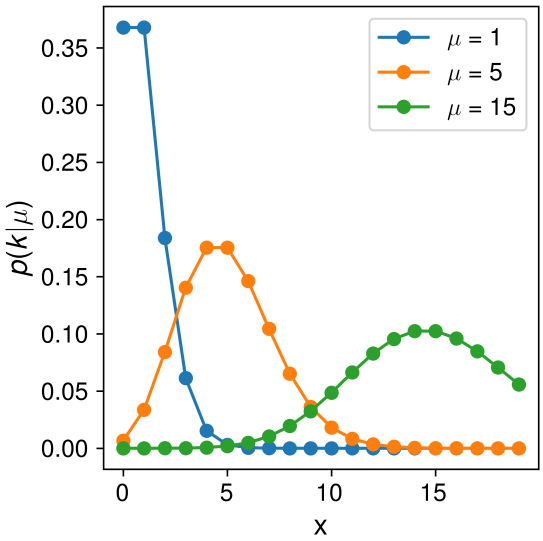

Figure 3.11: Example of a Poisson distribution for the Equation 3.16 for varying μ.

3.3.2 The Univariate Poisson Distribution

The Poisson distribution is used to model the probability of a specific number of events occurring within a fixed interval, whether in time or space. Let X be the discrete random variable that represents the number of events observed over a given time period. Let μ be the expected value (average) of X. If X follows a Poisson distribution, then the probability of observing k events over the time period is,

$$p(X = k|\mu) = \frac{\mu^k e^{-\mu}}{k!} \tag{3.16}$$

where e is Euler number. The Figure 3.11 presents the Poisson distribution for several mean (μ) values. The μ fully describes a Poisson distribution: The mode (most probable value) is $\mu - 1$, the

[3]Here, "upper limit" refers to the maximum plausible value of the flux in a given pixel, especially when direct measurement is challenging due to low signal strength.

standard deviation (σ)[4] is $\sqrt{\mu}$[5], the skewness [6] is $\frac{1}{\sqrt{\mu}}$, and the kurtosis [7] is $\frac{1}{\mu}$. As μ increases, both the skewness and the kurtosis decrease, and thus, the Poisson distribution becomes more and more similar to a Gaussian distribution. This is the fundamental reason to claim that for high X-ray flux (i.e., photon counts), Gaussianity is valid. This convergence towards Gaussianity underpins the assertion that Gaussian assumptions become valid for high photon counts. However, it is crucial to acknowledge that the Poisson approximation remains applicable across the spectrum of photon counts, not limited to low values alone. Interestingly, although the Poisson distribution morphs into a Gaussian distribution for large μ, the expectation value of the difference between the mean and the median does not become 0, but rather $\frac{1}{6}$. Because of this transition to a Gaussian for large μ, the Poisson distribution is sometimes called the "law of small numbers". It is also referred to as the "law of rare events", but we emphasize that μ need not be a small number. Even when it is replaced in practice by a Gaussian distribution for large μ, its Poissonian origin can always be recognized from the relationship $\sigma^2 = \mu$ (Pagano 2018).

3.3.3 Bivariate Poisson Distribution

The Bivariate Poisson distribution is an extension of the Univariate Poisson distribution that describes the probability of two related random events occurring. This distribution is particularly useful in scenarios where two events are interdependent. The probability mass function (PMF) of the Bivariate Poisson distribution in this context, with X and Y representing the counts from two interdependent events. These are random variables that denote the counts of events in the two Poisson processes

$$p(X = x, Y = y|\mu_1, \mu_2, \mu_{12}) = e^{-(\mu_1+\mu_2+\mu_{12})} \times \frac{\mu_1^x}{x!} \times \frac{\mu_2^y}{y!} \times \sum_{k=0}^{\min(x,y)} \binom{x}{k}\binom{y}{k} k! \left(\frac{\mu_{12}}{\mu_1\mu_2}\right)^k \quad (3.17)$$

where x and y are specific observed values or realizations of the random variables in X and Y, respectively. Here, μ_1 and μ_2 represent the mean counts expected in each Poisson process, while μ_{12} is the mean rate of shared events between the two Poisson processes. The sum over k accounts for the correlation between X and Y, and the binomial coefficients and factorial account for the combinations of counts that can contribute to the correlation.

[4] The standard deviation of a distribution is a measure of the amount of variation or dispersion in a set of values. It quantifies how much the values in the distribution deviate, on average, from the mean (average) of the distribution.

[5] This unique relationship where both the mean and variance are equal to μ is a characteristic property of the Poisson distribution. It implies that as the mean number of events increases, the dispersion (or spread) of the distribution also increases

[6] Skewness is a measure of the asymmetry of a distribution

[7] Kurtosis is a measure of the tailedness of a distribution

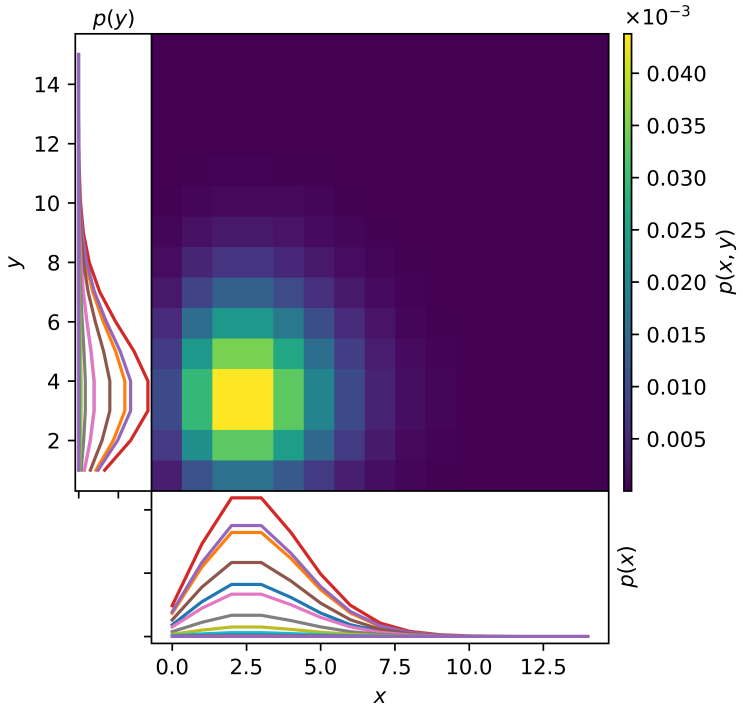

Figure 3.12: Example of an independent bivariate Poisson distribution in Equation 3.18. for parameters $\mu_x = 3$ and $\mu_y = 4$. The heatmap displays the bivariate Poisson distribution values over a (15,15) grid, specifically focusing on combinations where $X + Y = 15$. The marginal probability distributions for all possible pairs of x and y satisfying $X + Y = 15$ are illustrated in the subplots to the left and bottom.

3.3.4 Independent Bivariate Poisson Distributions

When there is no correlation between the two events X and Y, the Bivariate Poisson distribution simplifies significantly. In the absence of correlation, $\mu_{12} = 0$, and the two events are independent. Under this condition, the probability mass function of the Bivariate Poisson distribution can be factorized into the product of two independent Poisson distributions:

$$p(X = x, Y = y|\mu_1, \mu_2) = \frac{e^{-\mu_1}\mu_1^x}{x!} \times \frac{e^{-\mu_2}\mu_2^y}{y!} \tag{3.18}$$

This can be expressed as the product of two separate Poisson PMFs:

$$p(X = x, Y = y|\mu_1, \mu_2) = p(X = x|\mu_1) \cdot p(Y = y|\mu_2) \tag{3.19}$$

In this scenario, the joint probability $p(X, Y|\mu_1, \mu_2)$ is simply the product of the marginal probabilities $p(X|\mu_1)$ and $p(Y|\mu_2)$. The events X and Y do not influence each other, and their occurrences are solely determined by their respective average rates μ_1 and μ_2.

3.4 The Poisson Methodology: Application

Using the theoretical framework outlined in Section 3.3, we have developed a method to estimate the upper limits of 6.4 keV emission for both negative and faint fluxes in continuum-subtracted 6.4 keV Fe flux maps. Section 3.4.1 will explore the assumptions used in this formalism, and Section 3.4.3 will describe the statistical technique that is used to reconstruct the line emission using the Poisson method.

3.4.1 Data Representation

Throughout this analysis, I will consistently use the notations introduced in Section 3.1.6. The total observed photon count in each $pixel_{i,j}$ of continuum-subtracted 6.4 keV Fe flux maps, defined as $N_{tot}^{i,j}$:

$$N_{\text{tot}}^{i,j} = \sum_{\text{instr},e} \left(N_{\text{net}}^{i,j} + N_{\text{bkg}}^{i,j}\right)(i,j,e) \quad = \sum_{\text{instr},e} \left(N_{6.4\text{ keV}} + BKG_A + Cont_A\right)(i,j,e) \tag{3.20}$$

where $N_{net}^{i,j,e}$ is the continuum-subtracted 6.4 keV counts in $pixel_{i,j}$ in epoch e, and $N_{bkg}^{i,j,e}$ is the total background counts in $pixel_{i,j}$. The total background consists of the summation of the instrumental background and the model continuum. From now on, the continuum, including the XMM-Newton instrumental background ($N_{i,j,e}^{bkg}$) will be referred to as continuum-background. For the purpose of simplification and further analysis, indices are omitted. A random variable associated with the total count of the 6.4 keV spectral line is denoted as N_{line}, whereas the continuum background is represented by N_{cont}. The random variable N_{tot} is introduced as the sum of N_{line} and N_{cont}. Consequently, N_{tot} represents the total number of photons within the spectral band that includes the 6.4 keV line.

3.4.2 Poisson Process Assumptions

Our study operates under the specific assumption that the photon counts from the continuum background and the emission line are independent Poisson processes. Consequently, these counts are modeled as independent bivariate Poisson processes. Under this assumption, we can model this scenario using separate Poisson distributions without accounting for their correlation. The independent Poisson processes for the counts in two different parts of band A can be modeled as follows:

$$N_{\text{line}} \sim \text{Poisson}(\mu_{\text{line}}) \tag{3.22}$$

$$N_{\text{cont}} \sim \text{Poisson}(\mu_{\text{cont}}) \tag{3.23}$$

where N_{line} and N_{cont} are the photon counts observed in the 6.4 keV line and the continuum-background, respectively, and μ_{line} and μ_{cont} are the expected counts (mean rates) for these components. The key property here is that the events in the 6.4 keV line do not affect the events in the continuum-background, and vice versa, making $\mu_{\text{line, cont}} = 0$ (indicating no correlation). In our analysis, we used the parameter μ_{cont} of the Poisson distribution as the continuum-background level provided by Terrier et al. (2018).

3.4.3 Most Probable Photon Count for the 6.4 keV Line

PMFs for independent Poisson distributions are:

$$P(N_{\text{line}} = n_{\text{line}}) = \frac{e^{-\mu_{\text{line}}}\mu_{\text{line}}^{n_{\text{line}}}}{n_{\text{line}}!} \tag{3.24}$$

$$P(N_{\text{cont}} = n_{\text{cont}}) = \frac{e^{-\mu_{\text{cont}}}\mu_{\text{cont}}^{n_{\text{cont}}}}{n_{\text{cont}}!} \tag{3.25}$$

Since N_{line} and N_{cont} are independent, the joint probability of observing n_{line} events in 6.4 keV line and n_{cont} events from continuum-background is simply the product of their individual probabilities:

$$P(N_{\text{line}} = n_{\text{line}}, N_{\text{cont}} = n_{\text{cont}} | \mu_{\text{line}}, \mu_{\text{cont}}) = \left(\frac{e^{-\mu_{\text{line}}} \mu_{\text{line}}^{n_{\text{line}}}}{n_{\text{line}}!} \right) \times \left(\frac{e^{-\mu_{\text{cont}}} \mu_{\text{cont}}^{n_{\text{cont}}}}{n_{\text{cont}}!} \right) \tag{3.26}$$

The PMF in equation 3.26 shows the joint probability distribution of two independent Poisson processes of a random variable N_{line} and N_{cont}. This model provides the behavior of line emission and continuum-background processes under given mean rates, μ_{line} and μ_{cont}. However, in our case, we are interested in the inverse problem: given the observed data, how can we infer the underlying parameters of the process? We have at our disposal the total number of photons within spectral band A, represented as N_{tot}, and the mean continuum-background rate, as obtained from the Terrier et al. (2018) estimations. This scenario invites the general problem of Bayesian inference of the parameters (μ) in the Poisson distribution based on the observed data N. Applying Bayes' theorem (Bayes & Price 1763), the posterior distribution is equal to the product of the $L(\mu) = f(N|\mu)$ and the prior distribution $f(\mu)$, normalized by the data's probability $f(N)$.

$$f(\mu|N) = \frac{f(\mu) \cdot f(N|\mu)}{\int_0^\infty f(\mu) \cdot f(N|\mu)\, d\mu} \tag{3.27}$$

Since we are interested in the 6.4 keV line, we can apply Equation 3.27 to obtain the posterior distribution of the mean rate of the 6.4 keV line (μ_{line}).

$$\frac{dP_{\mu_{\text{line}}}(\mu_{\text{line}} \mid N_{\text{tot}}, \mu_{\text{cont}})}{d\mu_{\text{line}}} = \frac{P(N_{\text{tot}} \mid \mu_{\text{line}}, \mu_{\text{cont}}) \times P(\mu_{\text{line}})}{\int P(N_{\text{tot}} \mid \mu_{\text{line}}, \mu_{\text{cont}})\, d\mu_{\text{line}}} \tag{3.28}$$

Here, $dP_{\mu_{\text{line}}}(\mu_{\text{line}} \mid N_{\text{tot}}, \mu_{\text{cont}})/d\mu_{\text{line}}$ represents the posterior probability density, indicating the Bayesian inversion of the parameter μ_{line} given the prior information and belief about N_{tot} and μ_{cont}. The likelihood $P(N_{\text{tot}} \mid \mu_{\text{line}}, \mu_{\text{cont}})$ is the probability of observing the total count N_{tot} given the means μ_{line} and μ_{cont}, as given by Equation 3.26. The prior distribution $P(\mu_{\text{line}})$ reflects our initial beliefs about the distribution of μ_{line}. When there is no prior knowledge about a parameter, non-informative priors, including the uniform prior[8] and Jeffreys' prior[9], are particularly useful. These priors are designed to minimize the influence of the prior on the posterior distribution, thereby allowing the data to play the primary role in informing about the parameter's likely values. In these cases, the prior does not influence the shape of the posterior distribution, and thus, the posterior distribution's form is determined solely by the likelihood function. Thus, we can simply assume that the posterior is proportional to the likelihood.

$$\frac{dP_{\mu_{\text{line}}}(\mu_{\text{line}}|N_{\text{tot}}, \mu_{\text{cont}})}{d\mu_{\text{line}}} \propto P(N_{\text{tot}}|\mu_{\text{line}}, \mu_{\text{cont}}) \tag{3.29}$$

$$\frac{dP_{\mu_{\text{line}}}(\mu_{\text{line}}|N_{\text{tot}}, \mu_{\text{cont}})}{d\mu_{\text{line}}} \propto \left(\sum_{N_{\text{cont}}+N_{\text{line}}=N_{\text{total}}} \frac{e^{-\mu_{\text{cont}}} \mu_{\text{cont}}^{N_{\text{cont}}}}{N_{\text{cont}}!} \times \frac{e^{-\mu_{\text{line}}} \mu_{\text{line}}^{N_{\text{line}}}}{N_{\text{line}}!} \right) \tag{3.30}$$

Equation 3.30 represents a Bayesian inversion used to estimate the probability density[10] of μ_{line}, given a total observed count N_{tot} and a known mean μ_{cont}. This transition from a discrete probability model

[8] The uniform prior (or flat prior) assigns equal probability to all possible values of the parameter within a specified range

[9] It is defined as proportional to the square root of the determinant of the Fisher information matrix

[10] The distribution is discrete in terms of photon counts, so it can be represented as a PMF, but it is continuous in terms of average rates, so we use the term "density".

to a continuous model represented by "density" allows us to infer the unknown parameter μ_{line} from a continuous sample space. When obtaining $P(N_{\text{tot}} \mid \mu_{\text{line}}, \mu_{\text{cont}})$, we consider the cumulative likelihood of observing a specific total number of events N_{tot}, considering all possible distributions of these events between continuum and line emission. Each term in the summation calculates the likelihood for one specific way the total count could have arisen from the two processes. This approach ensures that our inference on μ_{line} leverages the full range of possible outcomes that could have led to the observed data.

$$\frac{dP}{d\mu_{\text{line}}} = C \sum_{N_{\text{cont}}+N_{\text{line}}=N_{\text{total}}} \frac{e^{-\mu_{\text{cont}}}\mu_{\text{cont}}^{N_{\text{cont}}}}{N_{\text{cont}}!} \times \frac{e^{-\mu_{\text{line}}}\mu_{\text{line}}^{N_{\text{line}}}}{N_{\text{line}}!} \tag{3.31}$$

where C is the normalization parameter. To find C, one can use the fact that the total integral of the density is 1,

$$\int_0^\infty \frac{dP}{d\mu_{\text{line}}}\, d\mu_{\text{line}} = 1 \tag{3.32}$$

$$\int_0^\infty C \left(\sum_{N_{\text{cont}}+N_{\text{line}}=N_{\text{total}}} \frac{e^{-\mu_{\text{cont}}}\mu_{\text{cont}}^{N_{\text{cont}}}}{N_{\text{cont}}!} \times \frac{e^{-\mu_{\text{line}}}\mu_{\text{line}}^{N_{\text{line}}}}{N_{\text{line}}!} \right) d\mu_{\text{line}} = 1 \tag{3.33}$$

$$C = \frac{1}{\int_0^\infty \left(\sum_{N_{\text{cont}}+N_{\text{line}}=N_{\text{total}}} \frac{e^{-\mu_{\text{cont}}}\mu_{\text{cont}}^{N_{\text{cont}}}}{N_{\text{cont}}!} \times \frac{e^{-\mu_{\text{line}}}\mu_{\text{line}}^{N_{\text{line}}}}{N_{\text{line}}!} \right) d\mu_{\text{line}}} \tag{3.34}$$

Normalized "density probability" for the line is given by,

$$\frac{dP}{d\mu_{\text{line}}} = \frac{\sum_{N_{\text{cont}}+N_{\text{line}}=N_{\text{total}}} \frac{e^{-\mu_{\text{cont}}}\mu_{\text{cont}}^{N_{\text{cont}}}}{N_{\text{cont}}!} \times \frac{e^{-\mu_{\text{line}}}\mu_{\text{line}}^{N_{\text{line}}}}{N_{\text{line}}!}}{\int_0^\infty \left(\sum_{N_{\text{cont}}+N_{\text{line}}=N_{\text{total}}} \frac{e^{-\mu_{\text{cont}}}\mu_{\text{cont}}^{N_{\text{cont}}}}{N_{\text{cont}}!} \times \frac{e^{-\mu_{\text{line}}}\mu_{\text{line}}^{N_{\text{line}}}}{N_{\text{line}}!} \right) d\mu_{\text{line}}} \tag{3.35}$$

Generally, two important metrics can be derived from the distribution: the most probable value and the credible interval, each essential for interpreting the outcome of μ_{line}.

3.4.4 The Most Probable Line Estimation

The most probable value, often referred to as the mode, is defined as the value of the variable for which the posterior probability density[11] has its maximum value. In more formal terms, the most probable value $\mu_{\text{line, mode}}$ is determined by:

$$\mu_{\text{line, mode}} = \arg\max_{\mu_{\text{line}}} \left(\frac{dp}{d\mu_{\text{line}}} \right) \tag{3.36}$$

Here, $\mu_{\text{line, mode}}$ denotes the peak of the density distribution where $dP/d\mu_{line}$ is highest. In mathematical terms, this translates to finding the value of μ_{line} where the first derivative of $dP/d\mu_{line}$ with

[11] Here the term "posterior density" is used because it reflects our updated beliefs about the possible values of μ_{line} after observing the data, incorporating both the likelihood of the data given different values of μ_{line} and μ_{cont}. The distribution provides a full picture of the uncertainty and variability of μ_{line}, beyond just identifying the most probable value.

respect to μ_{line} is zero and its second derivative is negative (indicating a maximum point). Furthermore, if the exposure time of a simulated pixel is represented by t, the flux upper limit of the line at 6.4 keV (F_P) can be determined using the formula:

$$F_P = \frac{\mu_{\text{line, mode}}}{t} \tag{3.37}$$

The selection of the mode as the estimator for μ_{line} is informed by the distribution's asymmetry. In instances where the distribution of $\frac{dP}{d\mu_{\text{line}}}$ manifests Gaussian characteristics, particularly during epochs of high flux, the mode, mean, and median of the distribution converge at a singular point. Conversely, in scenarios characterized by low flux leading to a skewed distribution, the mode directly represents the value with the highest density, regardless of the symmetry of the distribution.

3.4.5 Credible Interval for Line Emission

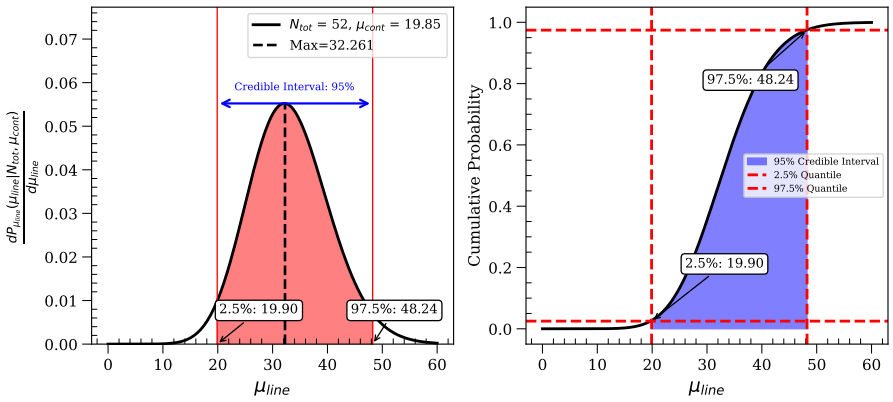

Figure 3.13: Probability density of the line emission as a function of μ_{line} for $\mu_{\text{cont}} = 4$ and $N_{total} = 10$ for a simulated pixel.

In the Bayesian framework, it is often useful to express the uncertainty of the parameter μ_{line} in terms of a credible interval. Unlike frequentist confidence intervals, which are based on long-run frequencies of observations, a credible interval provides a range within which the parameter is likely to fall with a certain posterior probability, given the observed data and prior information. For a symmetrical posterior distribution, the 95% credible interval is typically defined as:

$$CI = [\mu_{\text{line, 2.5\%}}, \mu_{\text{line, 97.5\%}}] \tag{3.38}$$

where $\mu_{\text{line, 2.5\%}}$ and $\mu_{\text{line, 97.5\%}}$ are the 2.5th and 97.5th percentiles of the posterior distribution, respectively. The credible interval can be calculated by integrating the posterior distribution to find the smallest interval that contains 95% of the probability density.

$$\int_{\mu_{\text{line, 2.5\%}}}^{\mu_{\text{line, 97.5\%}}} dP/d\mu_{line}, d\mu_{\text{line}} = 0.95 \tag{3.39}$$

In practice, this interval is computed from the cumulative distribution function (CDF) of the posterior density. Figure 3.13 illustrates the probability density function for a 6.4 keV emission line derived

from a fake pixel. The total photon count is set to $N_{\rm tot} = 10$, and the continuum background averages at $\mu_{\rm cont} = 4$. The distribution's maximum occurs at a density of 0.12, corresponding to $\mu_{\rm line} = 6.030$. This maximum probability represents the most probable line emission given the other parameters. The credible interval is obtained as (1.61, 14.27).

3.4.6 Gamma Approximation

The total number of observed photons, $N_{\rm total}$, is not a direct measurement of incoming photons from the Galactic center but rather the outcome of convolving these photon counts with the detector's response. This convolution alters the original photon counts and results in measured values of $N_{\rm total}$ with fractional numbers. Despite this, the total count in a pixel is always the sum of its two components:

$$N_{\rm total} = N_{\rm cont} + N_{\rm line} \tag{3.40}$$

The convolution process by the X-ray observatory significantly affects the parameter space by introducing new dynamics while maintaining the overall Poissonian distribution of photon counts. These changes are evident in the appearance of fractional values in $N_{\rm total}$, a shift in the parameter space. This shift reflects the transformed characteristics of photon counts post-convolution and can be inferred through the Gamma distribution approximation. The parameters of this distribution, particularly the shape parameter r, play a critical role in defining its characteristics. r is defined over the continuous interval $[0, \infty)$, representing any real number greater than or equal to 0. This characteristic highlights the Gamma distribution's ability to adapt to changes in the parameter space of the Poisson distribution caused by the convolution (Withers 2011).

$$k \mapsto \frac{\mu^k e^{-\mu}}{k!} \tag{3.41}$$

becomes,

$$r \mapsto \frac{\mu^r e^{-\mu}}{\Gamma(r+1)}\, d\mu \tag{3.42}$$

$\Gamma(x)$ is often taken to be the definition of the Gamma function in the form in which it is most often stated,

$$\Gamma(s) = \int_0^\infty \mu^{s-1} e^{-\mu}\, d\mu \tag{3.43}$$

The equation 3.30 becomes,

$$\frac{dP_{\mu_{\rm line}}(\mu_{\rm line}|N_{\rm tot}, \mu_{\rm cont})}{d\mu_{\rm line}} \propto \sum_{N_{cont}+N_{line}=N_{total}} \frac{e^{-\mu_{cont}} \mu_{cont}^{N_{cont}}}{\Gamma(N_{cont}+1)!} \times \frac{e^{-\mu_{line}} \mu_{line}^{N_{line}}}{\Gamma(N_{line}+1)!} \tag{3.44}$$

The following sections will discuss the concept of Poisson methodology (modified using the Gamma approximation) and its applications. Initially, the method will be applied in the Gaussian regime. The standard PMF can be employed without the Gamma approximation for cases with higher photon counts in the Gaussian regime (Equation 3.30). Later, an example will demonstrate the use of Poisson methodology in the regime where statistics are low (Equation 3.44), either due to a low photon count or short observing time.

3.4.7 Example I: Poisson analysis for the Gaussian regime

In this section, we use the Poisson method to analyze the light curves shown in Figure 3.10 (pixel coordinates (15,18)). Pixels with relatively high fluxes are indicative of the Gaussian regime. Although initially developed for pixels with negative and faint fluxes, this Poisson approach is adaptable to scenarios with higher fluxes as well.

Figure 3.14 presents the light curve for the pixel coordinate (15,18). We apply the Poisson method to estimate the flux in the Poisson context for the epoch 2012. The Gaussian flux for this epoch is $1.60 \times 10^{-7}\,\mathrm{cm^{-2}s^{-1}arcmin^{-2}}$ with an uncertainty of $3.78 \times 10^{-8}\,\mathrm{cm^{-2}s^{-1}arcmin^{-2}}$. The μ_{cont} from Terrier et al. (2018) is 19.85, and the modified N_{total} is calculated to be 51.7. Finally, the exposure value for this pixel is recorded as $2.01 \times 10^{8}\,\mathrm{s \cdot cm^{2}}$.

Figure 3.15 illustrates the probability density of line emission as a function of the average line emission rate, μ_{line}. The density curve reaches its most probable value at a μ_{line} of 32.26. This curve exhibits a near-symmetrical distribution, gradually resembling a normal distribution, in line with the expected Gaussian behavior at higher photon counts. For the CI estimation of line emission, μ_{line} is determined to be within $19.90 \leq \mu_{\mathrm{line}} \leq 48.24$. Using the exposure data for epoch 2012, the most probable flux is calculated to be $1.59^{+2.39}_{-0.99} \times 10^{-7}\,\mathrm{cm^{-2}s^{-1}arcmin^{-2}}$ These updated flux values are highlighted in red in Figure 3.14.

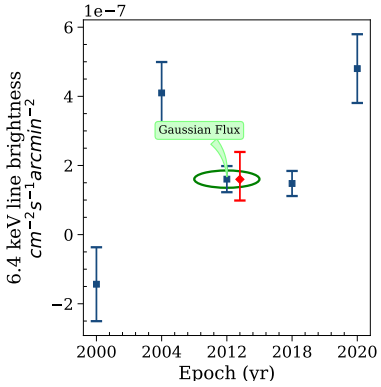

Figure 3.14: Variations in the 6.4 keV surface brightness over the five epochs within an area corresponding to a single pixel ($30'' \times 30''$) in pixel coordinates (15,18). Poisson estimations for the pixel corresponding to epoch 2012 are present in red.

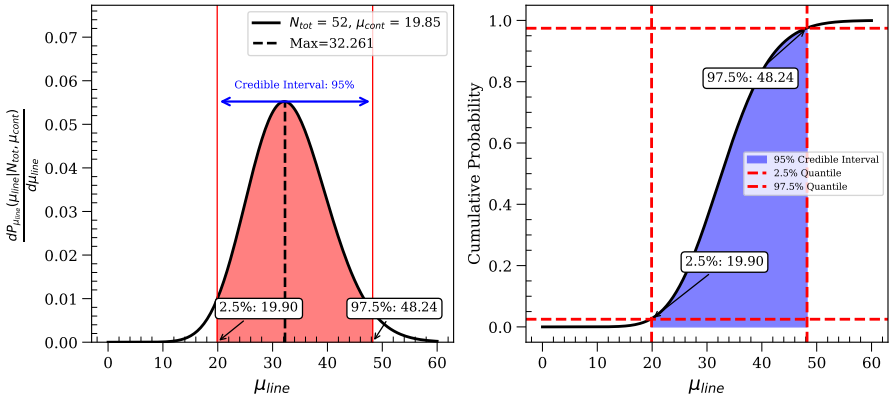

Figure 3.15: Probability density of the line emission as a function of μ_{line} for $\mu_{\mathrm{cont}} = 19.85$ and $N_{total} = 52$ for a pixel in epoch 2012 (*left*). 95% credible intervals are shown in dashed red area (*right*).

3.4.8 Example II: Poisson Analysis for the "negative" regime

Negative pixels, arising from inherent statistical fluctuations due to low photon counts (or even higher photon counts with low exposure), result in an overestimation of the continuum level. However, the Poisson probabilistic approach can be effectively useful for modeling such situations and providing reasonable upper limit estimations. When there is a negative pixel (i.e., overestimated continuum), the straightforward correction one can think of for the upper limit of the line is that it could be 0.

Given that negative pixels result from very low photon counts close to zero, for simplicity, let's assume the flux to be 0 ($N_{\rm tot} \approx 0$). (Note that it is practically impossible to have no photons for a pixel.) In Equation 3.31, setting $N_{\rm tot} = 0$ reduces all continuum and line contributions to zero. We observe that any value of $\mu_{\rm line}$ and $\mu_{\rm cont}$ raised to the power of 0 becomes 1, and the factorial of 0 (0!) is also 1. It is crucial to recognize that the respective average rates $\mu_{\rm line}$ and $\mu_{\rm cont}$ cannot be zero.[12] Consequently, the density equation simplifies to:

$$\frac{dP_{\mu_{\rm line}}(\mu_{\rm line}|N_{\rm tot},\mu_{\rm cont})}{d\mu_{\rm line}} = C \cdot e^{-\mu_{\rm line}} \cdot e^{-\mu_{\rm cont}} \quad (3.45)$$

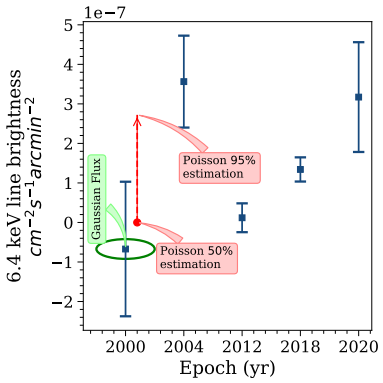

Figure 3.16: Variations in the 6.4 keV surface brightness over the five epochs within an area corresponding to a single pixel ($30'' \times 30''$) in pixel coordinates (25,12). Poisson estimations for the pixel corresponding to epoch 2012 are present in red.

Here, C represents the normalization constant (refer to Equation 3.31). Thus, the density exhibits exponential behavior. When $N_{\rm tot} > 0$, it still appears close to an exponential curve but transitions towards a more Gaussian shape.

Let's consider the pixel corresponding to epoch 2000 in Figure 3.16, which is characterized by the Gaussian flux (invalid) of $-1.3929 \times 10^{-7}\,{\rm cm}^{-2}{\rm s}^{-1}{\rm arcmin}^{-2}$. The value of $\mu_{\rm cont}$ is observed as $\mu_{\rm cont} = 2.383$, and $N_{\rm total}$ equals 2. Finally, the exposure value for this pixel is recorded as $1.7456 \times 10^7\,{\rm s\,cm}^2$.

Figure 3.17 shows the density curve for the line emission in this scenario. In this Poisson-dominated regime, the characteristic density curve deviates from the typical bell shape seen in Gaussian cases, instead resembling an exponential-shaped curve[13]. The most probable estimation or the upper limit of the line emission in this scenario is $\mu_{\rm line} = 0$[14]. For the 95% estimation, the value is $\mu_{\rm line} = 5.08$. The typical CI estimation is not applicable here due to the deviation from the symmetric bell-shaped curve (see section 3.4.5). Consequently, we rely only on the 95% upper limit level by leaving 5% on the right tail of the density curve. Using the exposure for epoch 2000, the central flux estimation can be converted into flux as 0, and the 95% upper flux limit value is $< 2.533 \times 10^{-7}\,{\rm cm}^{-2}{\rm s}^{-1}{\rm arcmin}^{-2}$. These new fluxes are shown in red color in Figure 3.16.

[12] The average rate (or mean, μ) of a Poisson distribution cannot be zero, as this contradicts the inherent characteristics of the distribution. A zero μ implies no expected events, which is mathematically and practically nonsensical for a model intended to describe the occurrence of events.

[13] For the purely hypothetical situation where $N_{\rm tot} = 0$, the result is a purely exponential curve. In this hypothetical scenario, both $N_{\rm line}$ and $N_{\rm cont}$ are zero (resulting in $N_{\rm tot} = 0$), although it is unlikely to detect no photons from a $30^\circ \times 30^\circ$ sky area, including the background.

[14] Without an explicit second derivative of $\mu_{\rm line}$, and given that the density function's maximization is tied to $\mu_{\rm line}$, influence on the Poisson probability, we are limited to numerical methods for a precise solution.

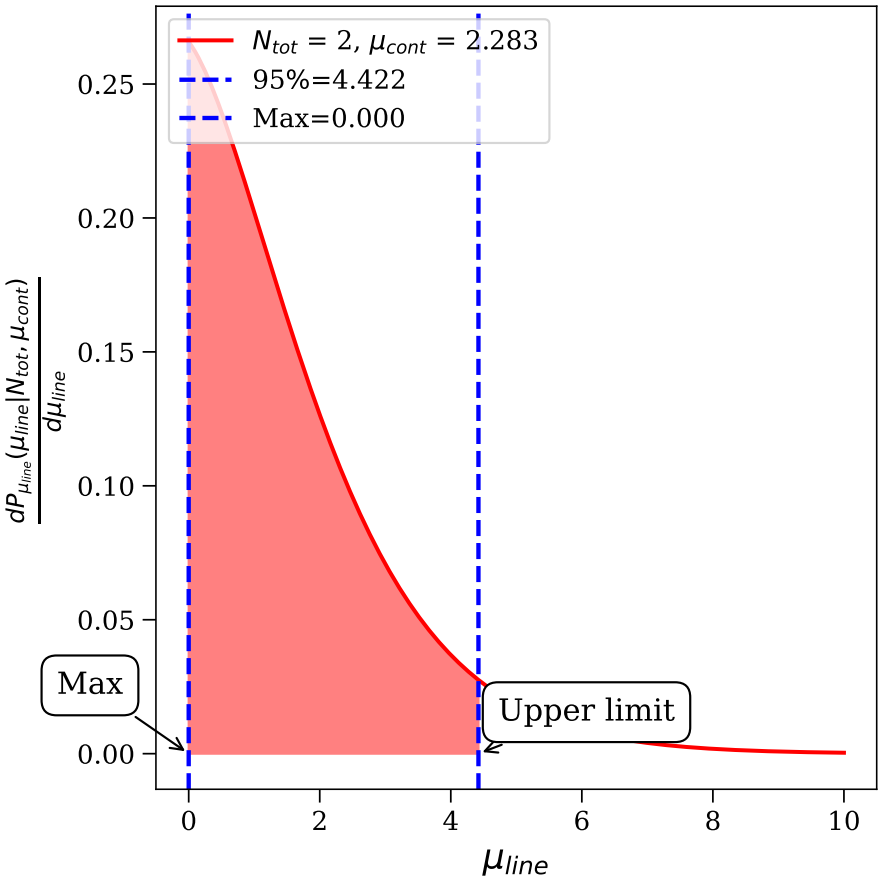

Figure 3.17: Probability density of the line emission as a function of $\mu_{\rm line}$ for $\mu_{\rm cont} = 2.383$ and the modified $N_{total} \sim 2$ for a pixel in epoch 2000 (*left*). 95% credible intervals are shown in dashed red area (*right*)

3.5 Construction of 2D Poisson Maps

Section 3.2.1 discusses how some pixels in our study showed negative values for the 6.4 keV flux. These pixels are important because they have faint photon flux and they play a key role in stabilizing the minimum flux levels and, hence, the steady emission[15]. We used the Poisson method to set the most probable values for low or negative flux pixels (either due to low photon count or exposure time). Conversely, for pixels with high photon counts, we employed the Gaussian approach proposed by Terrier et al. (2018). Together, these two approaches provide robust flux estimations for all pixels.

To accurately determine the most probable values of the minimum flux values and to address the issue of negative flux values, we have reconstructed the 6.4 keV in Section 3.1.6. This reconstruction incorporates a hybrid of both the Poisson method and the Terrier et al. (2018) method. We have established a threshold to determine the applicable method for each set of pixel values: the Poisson method is utilized for values below the threshold. The optimal threshold is derived based on the equation $F_{i,j} \times t_{i,j} = 10\, pixel^{-1}$, where $F_{i,j}$ represents the flux for the specific pixel and $t_{i,j}$ is the

[15] also, it is important to note that pixels with higher photon counts have a minimal impact on the steady emission observed in any given pixel.

corresponding expousure value. Additionally, it is noteworthy that the Poisson methodology, while comprehensive, necessitates a significant amount of computational time. Thus, the implementation of this threshold also aims to enhance the computational efficiency of our calculations, striking a balanced approach between accurately constraining faint flux values and managing computational time.

The reconstructed 50 % 6.4 keV flux ($F^{50\%}_{i,j,e}$) from the hybrid Poisson-Gaussian method is given by:

$$F^{\,50\ \%}_{i,j,e} = \begin{cases} F^{k=0.5}_{P,i,j,e} \text{ if } F_{C,i,j,e} \times t_{i,j,e} \leq 10 & \text{(Poisson regime)} \\ F_{C,i,j,e} \text{ if } F_{C,i,j,e} \times t_{i,j,e} > 10 & \text{(Gaussian regime)} \end{cases} \tag{3.46}$$

Where: e is the epoch, $F^{k=0.5}_{P,i,j,e}$ is the Poisson 50% estimation flux value for Poisson regime pixels, $F_{C,i,j,e}$ is the continuum-subtracted 6.4 keV flux in $pixel_{i,j}$ (see Figure 3.4) for Gaussian dominated pixels.

Similarly, reconstructed 6.4 keV upper limit flux ($F^{95\%}_{i,j,e}$) or 95% from the hybrid Poisson-Gaussian method is given by:

$$F'^{\,95\ \%}_{i,j,e} = \begin{cases} F^{k=0.05}_{P,i,j,e} \text{ if } F_{C,i,j,e} \times t_{i,j,e} \leq 10 & \text{(Poisson regime)} \\ 2 \cdot \sigma_{C,i,j,e} \text{ if } F_{C,i,j,e} \times t_{i,j,e} > 10 & \text{(Gaussian regime)} \end{cases} \tag{3.47}$$

$F^{k=0.05}_{P,i,j,e}$ represents the Poisson upper limit estimation of the flux value for pixels in the Poisson regime. Additionally, $\sigma_{C,i,j,e}$ denotes the uncertainty in the continuum-subtracted 6.4 keV flux for $pixel_{i,j}$ (as shown in Figure 3.4) in cases where Gaussian characteristics dominate. To align the Gaussian upper limit with Poissonian upper limits, we accounted for 2σ Gaussian uncertainty.

Figures 3.18, 3.19, 3.20, 3.21, and 3.22 showcase the 6.4 keV mosaics in Figure 3.4 and reconstructed mosaics using the Poisson method, adhering to the threshold $F_{i,j} \times t_{i,j} = 10\,cm^2\,pixel^{-1}$. The right pannel of each figure also provide a comparision between Terrier et al. (2018) flux estimations and this hybrid method. According to these graph, the 50% map from the Poisson method yelled 0 as the most probable value for all the negative estimations from the Terrier et al. (2018) method.

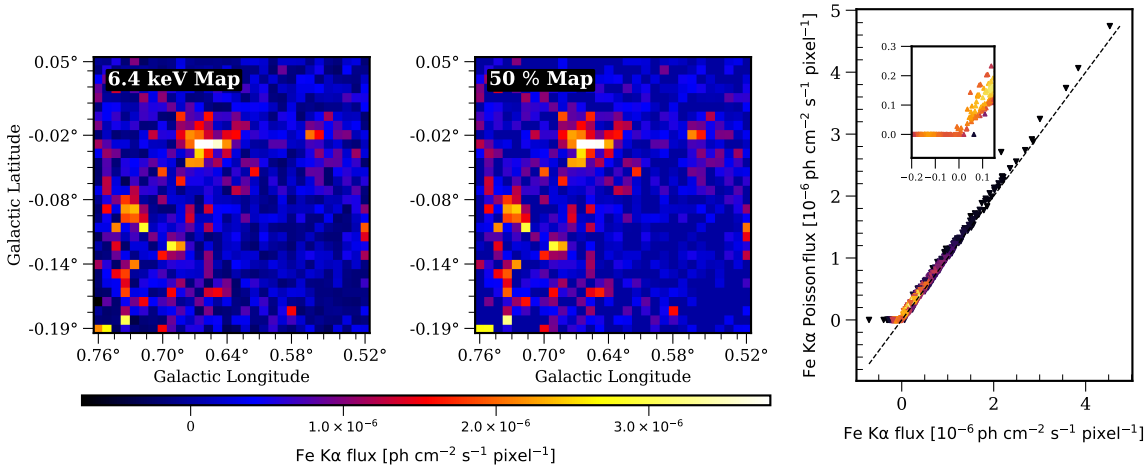

Figure 3.18: 6.4 keV mosaics map for epoch 2000. Terrier et al. (2018) map (left), hybrid Terrier et al. (2018) and Poisson map (middle), X-ray flux scatter plot between Terrier et al. (2018) and hybrid Terrier et al. (2018) and poisson with the threshold (right).

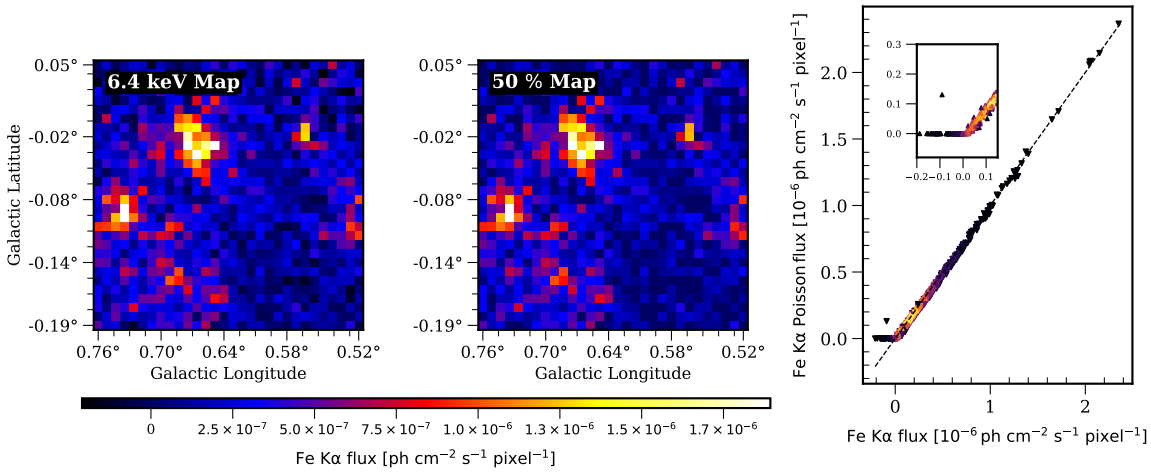

Figure 3.19: 6.4 keV mosaics map for epoch 2004. Terrier et al. (2018) map (left), hybrid Terrier et al. (2018) and Poisson map (middle), X-ray flux scatter plot between Terrier et al. (2018) and hybrid Terrier et al. (2018) and poisson with the threshold (right).

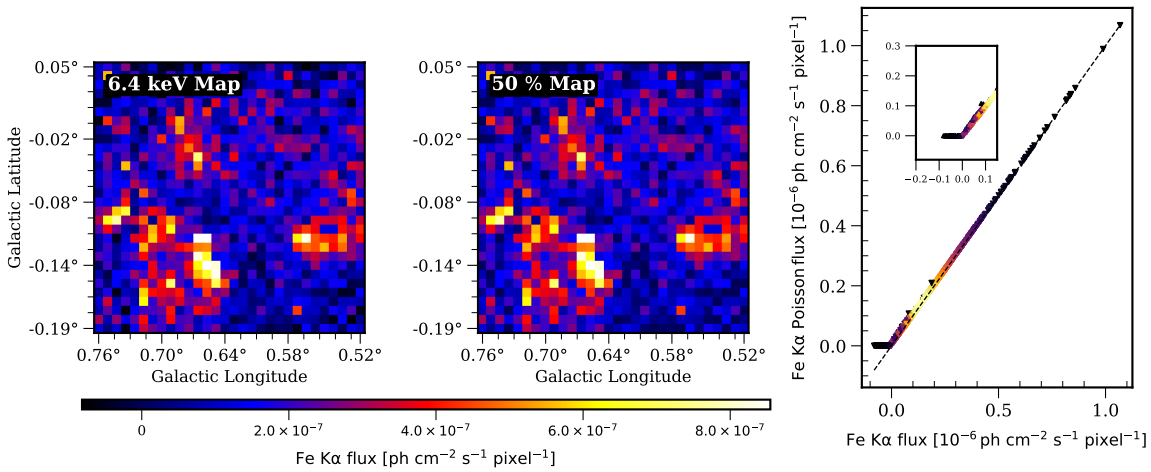

Figure 3.20: 6.4 keV mosaics map for epoch 2012. Terrier et al. (2018) map (left), hybrid Terrier et al. (2018) and Poisson map (middle), X-ray flux scatter plot between Terrier et al. (2018) and hybrid Terrier et al. (2018) and poisson with the threshold (right).

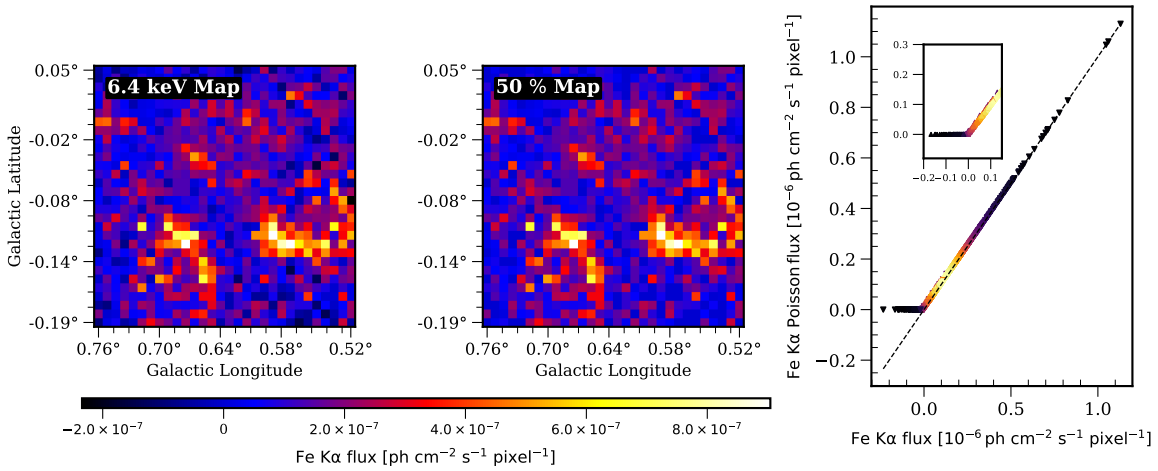

Figure 3.21: 6.4 keV mosaics map for epoch 2018. Terrier et al. (2018) map (left), hybrid Terrier et al. (2018) and Poisson map (middle), X-ray flux scatter plot between Terrier et al. (2018) and hybrid Terrier et al. (2018) and poisson with the threshold (right).

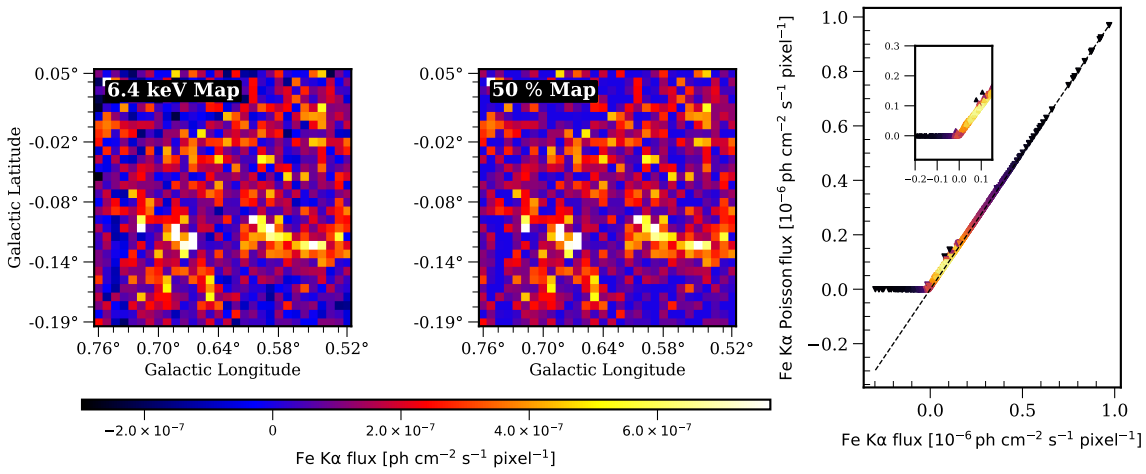

Figure 3.22: 6.4 keV mosaics map for epoch 2020. Terrier et al. (2018) map (left), hybrid Terrier et al. (2018) and Poisson map (middle), X-ray flux scatter plot between Terrier et al. (2018) and hybrid Terrier et al. (2018) and poisson with the threshold (right).

3.5.1 Conclusion

The Poisson Method has shed light on faint X-ray emissions in the GC. Developed in theory and applied in practice, this state-of-the-art method has effectively quantified and interpreted faint X-ray emission from low photon/low statistics regimes. This method also holds for higher statistics/photon count regimes such as Sgr A*, though with increased computational time. Our approach has enabled confident estimation of photon counts and the establishment of upper limits. The methodologies and findings presented in this chapter will form a solid foundation for future discussions, focusing on quantifying steady emission.

Chapter 4

Constraining the Steady 6.4 keV Emission

This chapter focuses on the core of our research: identifying and analyzing the non-thermal steady diffuse emission in the GC's Sgr B molecular complex. Building upon the pixel-level analysis and the Poisson methodology introduced in the previous chapter, our objective is to establish a baseline for steady emission in Sgr B. Initially, we tackle the simpler case of determining steady emission from a single epoch in a pixel. Subsequently, we expand our methodology to handle scenarios involving multiple epochs (from 2000 to 2020). This approach allows us to define the X-ray morphology of steady emission for the first time in this region with the highest spatial resolution ever measured. Moreover, we have developed an extensive methodology to extract the deep XMM-Newton spectroscopy for this steady emission.

Contents

4.1 Steady emission for a single epoch

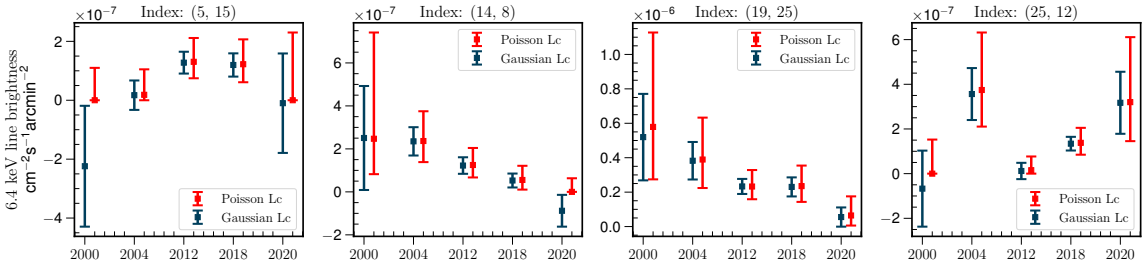

Figure 4.1: Variations in the 6.4 keV surface brightness, measured across five distinct epochs within a single pixel region of $30'' \times 30''$, are presented. These measurements, derived through the Poisson method, are illustrated in red. The corresponding dark blue light curve is based on the values provided by Terrier et al. (2018). The variations are shown for selected pixel coordinates: (5,15), (14,8), (19,25), and (25,12).

Figure 4.1 illustrates the variations in the brightness of the $Fe\ K\alpha$ emission line at 6.4 keV, as derived using both the Poisson method (shown in red) and the continuum-subtracted method (shown in dark blue), according to Terrier et al. (2018). The light curves generated by the Poisson method are reliable at both very faint and high flux levels. However, it is important to note that the Poisson method can only provide upper limits for the negative values encountered. Over two decades, significant flux variations in the 6.4, keV line within the entire Sgr B region have been observed. The objective is to assess the uniform baseline diffuse X-ray emission beneath the observed variability. The analysis of these baseline faint flux levels, hereafter referred to as "steady emission" and their interpretations, will be extensively discussed throughout this chapter and the rest of the thesis.

Initially, the steady emission within a single epoch will be discussed, while the following section will use a bottom-up approach to evolve into more complex situations across multiple epochs. The definition (4.1.1) and the initial methods employed to estimate the steady emission in a single epoch will be discussed in sections 4.1.2.1 and 4.1.2.2. Finally, a comprehensive discussion on the successful approach to estimating steady emission using the Poisson Methodology will be presented in section 4.2.

4.1.1 The steady emission

The uniform baseline emission, or steady emission, below the observed variability is defined as a "consistent and stable faint diffuse X-ray emission component". This component does not show significant variations within the uncertainties over the 20-year timescale considered. For each pixel, the steady emission is thus recognized as a uniform quantity. In this study, we employed synthesizing observations from individual epochs into a comprehensive understanding of a complex system evolving over 20 years. Initially, we define the steady emission for each epoch in mathematical terms.

For a single epoch (e), if the reconstructed 6.4 keV flux for a pixel is $F^{50\%}_{i,j,e}$, then the steady emission's value could range anywhere from zero to $F^{50\%}_{i,j,e}$, and the $F^{50\%}_{i,j,e}$ could be a combination of the faint steady value and another value that represents the variable emission (however, for a single epoch,

it's just a snapshot of a larger temporal variation). Building upon this foundation, the observed flux within each pixel is said to consist of two components: the time-independent "steady flux" (since it is constant) and the time-dependent "variable flux". These components are mathematically represented as:

$$\textbf{Observed Flux (t)} = \textbf{Steady flux} + \textbf{Variable flux (t)}. \tag{4.1}$$

Estimating the steady flux requires a probabilistic approach. Steady emission is inherently uncertain, much like attempting to hear a constant, faint humming sound in a noisy environment. We lack prior information about both the precise behavior of steady emission and variable flux. Our objective is to define a limit of steady emission using the observed flux while working with fundamental yet promising assumptions.

4.1.2 Evolution of Methods

This section reflects on the evolution of the main strategies employed in this study to estimate steady emission.

4.1.2.1 The Toy Model

To facilitate a clearer understanding of the concepts of steady emission in a single epoch, we begin by examining an idealized scenario, which we refer to as the "toy model". In this simplified setting, we imagine having just a single perfect observation characterized by a single flux value, denoted as F_o, and without any associated error bars or uncertainties. When faced with the task of estimating the "steady flux" in such a scenario, where we possess no prior knowledge of variability, our conclusion would be that the steady flux could potentially be any value between 0 and F_o. This leads to the conceptualization of a "flat" distribution spanning the range from 0 to F_o, as any value within this interval could be considered a reasonable estimate of the steady flux (see Figure 4.2).

In the nonideal case of the toy model for steady emission, the scenario incorporates inherent observational uncertainty. Here, the observed flux value (F_o) is represented by a Gaussian-like curve (see black curves in Figure 4.2), acknowledging the spread of possible values due to the uncertainty associated with the F_o. This results in a probability distribution for observing a particular flux value that is spread across a range rather than being concentrated at a single point. Consequently, the estimation of the steady flux value diverges from the ideal model's flat, uniform distribution to a "sigmoid-shaped"[1] distribution.

4.1.2.2 Complementary Error Function Method

To extend our analysis beyond the idealized case discussed in the toy model, we employ the Gaussian error function, also known as the complementary error function[2]. Instead of assuming that the steady flux can take on any value between 0 and F_o, we choose the steady flux within a range of N discrete samples[3] denoted as F_t, ranging from a minimum of 0 to the maximum observed flux F_o. We then examine the observed flux value F_o in relation to these sample values F_t, searching for the most likely F_t value.

The determination of the optimal F_t is achieved through the application of a specialized weight function that incorporates the complementary error function. This weight function diminishes as

[1] A sigmoid function is any mathematical function whose graph has a characteristic S-shaped curve or sigmoid curve.

[2] The complementary error function, often denoted as erfc(x), does not have a sigmoid shape in the same way that the standard sigmoid function $\sigma(x) = \frac{1}{1+e^{-x}}$ does.

[3] The steady flux has no reason to be discrete, it's only for practical computation and plotting that we choose discrete values

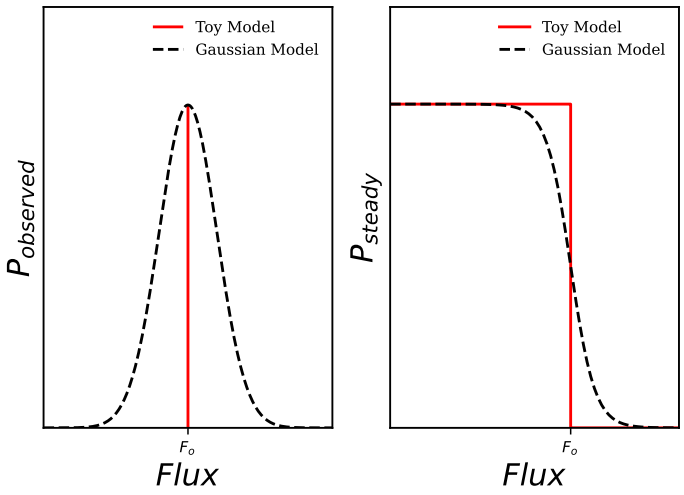

Figure 4.2: Toy Model Illustration: Ideal Case (Red) vs Nonideal Case (Black). In the ideal scenario, the observed flux value is represented by a δ function, where the probability mass is entirely concentrated at a single point. This implies a 100% probability of an event occurring precisely at F_0 and 0% probability elsewhere. The corresponding steady flux value distribution is presented as a flat uniform distribution from 0 to F_0 in a stepwise function (on the right). Below F_0, the probability of finding the steady value is 1, and it is 0 elsewhere. In the nonideal case, observed probability mass is affected by inherent uncertainties. Hence, the δ function is better represented by a Gaussian curve with finite width (left). The probability of observing the steady value, on the other hand, obtained by a step function in the ideal case, converges to a Sigmoid shape in the Gaussian assumption (right).

the observation moves significantly above F_t (effectively excluding F_t) and converges to 1 when the observation is substantially below F_t.

$$P_k(\mathrm{e}) = \frac{1}{2}\mathrm{erfc}\left(\frac{F_t - F_k}{\sqrt{2}\sigma_k}\right) \tag{4.2}$$

The complementary error function method is relevant for estimating steady flux based on the fact that it replicates the nonideal situation illustrated in Figure 4.2 (black) and reproduces the sigmoid curve for the steady flux probability representation. To assess the steady value, we can consider F_t values that correspond to a global likelihood with a $P_k = 0.5$ significance level, representing a 50% estimate, and $P_k = 0.05$, representing the 95% upper limit estimation.

Figure 4.3 provides a practical example of the complementary error function's application in estimating the steady-state value. The analysis utilizes the light curve data from $Pixel_{i=15,j=8}$ as shown in Figure 4.1 for the year 2012. The Poisson estimate for this epoch is $1.208 \times 10^{-7}\,\mathrm{cm}^{-2}\,\mathrm{s}^{-1}\,\mathrm{pixel}^{-1}$ with an uncertainty of $6.645 \times 10^{-8}\,\mathrm{cm}^{-2}\,\mathrm{s}^{-1}\,\mathrm{pixel}^{-1}$. The right panel of Figure 4.3 illustrates the complementary error function (or Gaussian erfc) curve for the 2012 epoch. The F_t value corresponding to $P_k = 0.5$ is determined to be $1.208 \times 10^{-7}\,\mathrm{cm}^{-2}\,\mathrm{s}^{-1}\,\mathrm{pixel}^{-1}$, with its 95% limit value at $2.649 \times 10^{-7}\,\mathrm{cm}^{-2}\,\mathrm{s}^{-1}\,\mathrm{pixel}^{-1}$.

This approach provides a statistically weighted methodology for determining F_t as the steady flux. However, it's important to note that the use of the complementary error function (erfc) is based on the assumption that the probability distribution of the real flux follows a Gaussian distribution around the observed value. This assumption may not hold in cases involving low photon counts or when the underlying distribution significantly deviates from a Gaussian distribution. In such situations, the

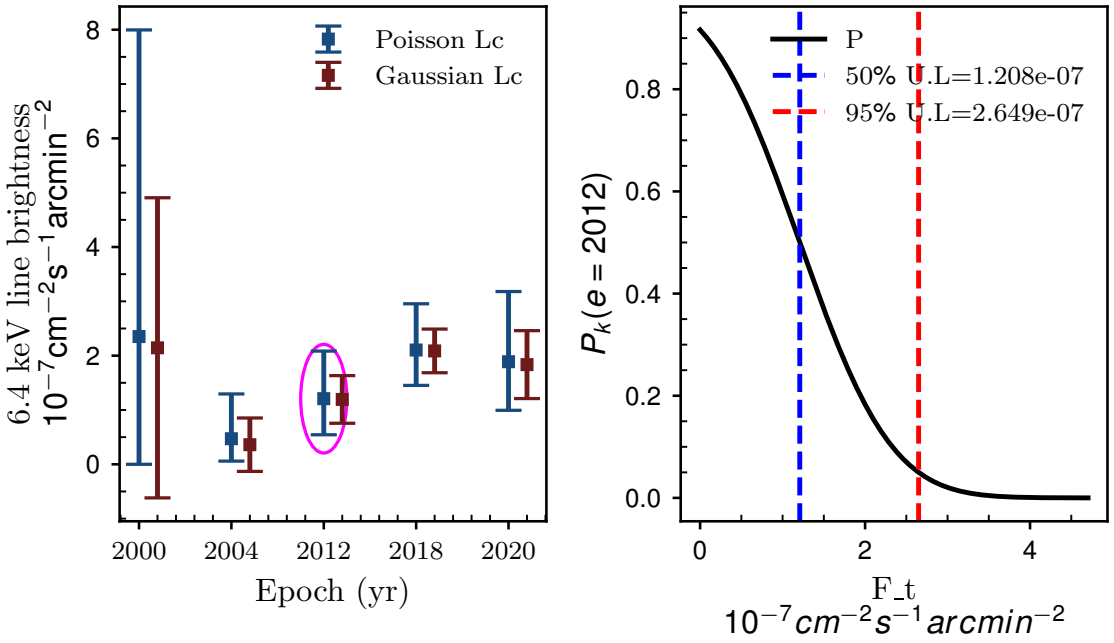

Figure 4.3: Light curve (left) and the Gaussian error function curve (right) for $Pixel_{i=15,j=8}$ in Epoch 2012. The left panel shows the y-axis representing flux units and the x-axis indicating the epoch. On the right, the graph of the global likelihood $P_k(e = 2012)$ versus the test flux values F_t is presented. The values of F_t corresponding to $P = 0.5$ (50% estimation) and $P = 0.05$ (95% estimation) are highlighted in blue and red, respectively.

use of the erfc method may not yield accurate results. In subsequent sections, we will discuss the treatment for cases involving low photon counts.

4.2 Poisson Method for Steady Emission Estimation

In the previous section, the nonideal toy model characterized by a sigmoid shape revealed the probability density of steady emission. The Gaussian complementary error function (erfc) was used to model this density for pixels with high statistics (Gaussian regime). The focus of our study now shifts toward accurately characterizing steady emission behaviors in scenarios characterized by low statistics. The Complementary Cumulative Distribution Function (CCDF) of the Poisson posterior distribution of the 6.4 keV diffuse $K\alpha$ line will be used to address this challenge. The CCDF is suitable for analysis in environments with low photon counts and within the Gaussian regimes.

4.2.1 Complementary Cumulative Distribution Function

In probability theory, the Cumulative Distribution Function (CDF) is a fundamental concept that provides comprehensive insights into the probability structure of a random variable X. While the CDF offers the probability that a variable will take a value less than or equal to a particular threshold evaluated at x, its counterpart, the Complementary Cumulative Distribution Function (CCDF), presents the probability of the variable X exceeding a specified value x. Concepts of CDF and CCDF can be used to describe the probability of a discrete, continuous, or mixed variable.

For any random variables, the CDF is a step function that sums up the probabilities of all possible outcomes less than or equal to x.

$$F_X(x) = P(X \leq x) \tag{4.3}$$

In contrast, for continuous random variables, the CDF is a continuous function obtained by integrating the probability density function (PDF) from negative infinity to x.

$$F_X(x) = \int_{-\infty}^{x} f_X(t)\, dt \tag{4.4}$$

The CCDF is simply $1 - F_X(x)$ and represents the probability that X is greater than x. The Poisson distribution discussed in an earlier section is discrete when modeling the number of events within a fixed interval. However, in a Bayesian inversion approach, it is adapted for continuous contexts when modeling mean rates. The CCDF of X in equation 4.4 can be updated to $X = \mu$ and expressed as the integral of its probability density function f_μ as follows:

$$F_\mu(x) = 1 - \int_{-\infty}^{x} f_\mu(t)\, dt = \int_{x}^{\infty} f_\mu(t)\, dt \tag{4.5}$$

Figure 4.4 (on the left) shows the probability distribution discussed in equation 3.13 and its CDF curve (F_X). To smooth the empirical CDF, which is inherently a step function for a discrete distribution, an interpolation method is used. It exhibits the behavior of a probability distribution that is not strictly Gaussian but bears Gaussian symmetry and tail behavior.

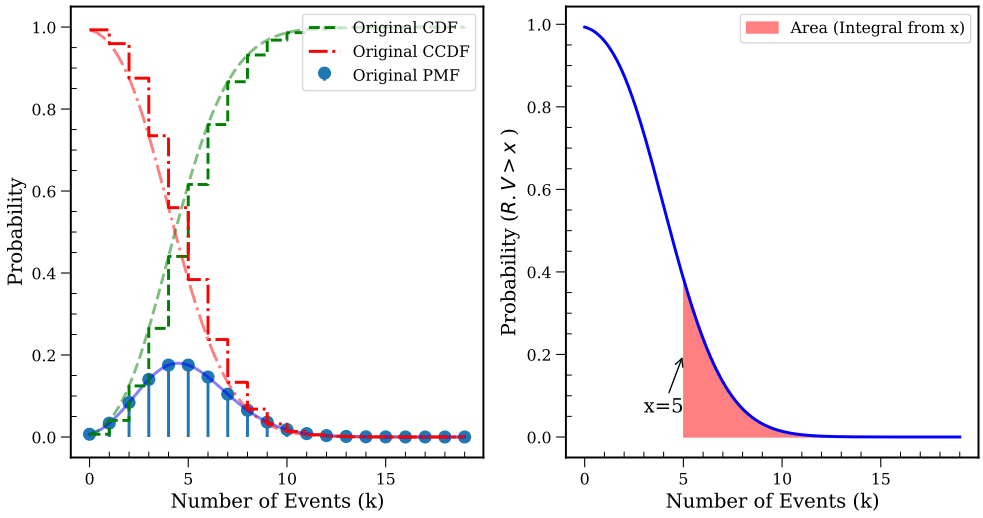

Figure 4.4: PMF, CDF, and the CCDF for a Poisson distribution with $\mu = 5$ (*left*). The shaded area to the right of the blue line at $x = 5$ represents the integral of the CCDF from x onwards, corresponding to the probability of the number of events being greater than 5 (*right*).

The integral of the right panel (shaded area in red) of Figure 4.4 quantifies the cumulative probability density within the tail of the distribution, starting from x. This area corresponds to the likelihood

of observing values greater than x and is a measure in assessing the extremeness of events. On the other hand, this also implies that if x denotes the upper boundary for a specific random variable of interest, the unshaded region of Figure 4.4 (right) represents the "probability mass or density in terms of μ" associated with the random variable remaining below x. Therefore, computing the integral of the shaded area represents x as the upper limit of a particular random variable.

4.2.2 Probability Density Function

In probability theory, a probability density function (PDF), or "density function", or "density" of a continuous random variable is denoted as $f_x(\mu)$. It is a function whose value at any given sample (or point) in the sample space (the set of possible values taken by the random variable) can be interpreted as providing a relative likelihood that the value of the random variable would be equal to that sample.

$$f_x(\mu) = \frac{dF'_x}{d\mu} \tag{4.6}$$

Here, F'_x is the CCDF. One can use the empirical CCDF curve as a non-parametric way to estimate the density of a continuous random variable of interest and estimate the density associated with the continuous random variable. The integral quantifies the cumulative probability density within the tail of the distribution.

4.2.3 Estimating the Steady Flux from 6.4 keV Line

We extend our discussion from Section 3.3 to apply the Poisson method for estimating the probabilistic upper limit of the "steady emission". In the previous chapter, we derived the probability density of the 6.4 keV line using a Bayesian inversion approach. The density of the line can then be defined using the equation 4.13.

The observed 6.4 keV line is a combination of two components, a steady component and a time variable component (see equation 4.1), which can further decompose into two Poisson processes based on the same analogy explained in Section 3.3.4. Hence, $\mu_{\rm line}$ can be written as the arrival rates of the steady and variable components.

$$\mu_{\rm line} = \mu_{\rm steady} + \mu_{\rm var} \tag{4.7}$$

Following our prescription, the probability density for the steady emission can be taken as proportional to the tail distribution within the line,

$$\frac{dP_{\mu_{\rm steady}}}{d\mu_{steady}}(\mu_{steady}|N_{\rm tot}, \mu_{\rm cont}) \propto \int_{\mu_{steady}}^{\infty} \frac{dP_{\mu_{\rm line}}}{d\mu_{\rm line}} d\mu_{\rm line} \tag{4.8}$$

$$\frac{dP_{\mu_{\rm steady}}}{d\mu_{steady}}(\mu_{steady}|N_{\rm tot}, \mu_{\rm cont}) = K \int_{\mu_{steady}}^{\infty} \frac{dP_{\mu_{\rm line}}}{d\mu_{\rm line}} d\mu_{\rm line} \tag{4.9}$$

The normalization condition requires that:

$$\int_0^{\infty} \frac{dP_{\mu_{\rm steady}}}{d\mu_{steady}} d\mu_{steady} = 1 \tag{4.10}$$

$$\int_0^{\infty} K \left(\int_{\mu_{\rm steady}}^{\infty} \frac{dP_{\mu_{\rm line}}}{d\mu_{\rm line}} d\mu_{\rm line} \right) d\mu_{\rm steady} = 1. \tag{4.11}$$

$$K = \frac{1}{\int_0^\infty d\mu_{\text{steady}}[\int_{\mu_{\text{steady}}}^\infty \frac{dP_{\mu_{\text{line}}}}{d\mu_{\text{line}}} d\mu_{\text{line}}]} \tag{4.12}$$

$$\frac{dP}{d\mu_{steady}}(\mu_{steady}|N_{tot},\mu_{cont}) = \frac{\int_{\mu_{steady}}^\infty \frac{dp_{\mu_{line}}}{d\mu_{line}}(\mu_{line}|N_{tot},\mu_{cont})d\mu_{line}}{\int_0^\infty d\mu_{steady}\left[\int_{\mu_{steady}}^\infty \frac{dp_{\mu_{line}}}{d\mu_{line}}(\mu_{line}|N_{tot},\mu_{cont})d\mu_{line}\right]} \tag{4.13}$$

The equation 4.13 gives an estimation for the posterior probability density of the mean rate of steady emission μ_{steady}. This density demonstrates how slight changes in μ_{steady} affect the likelihood of recording N_{tot} events and the Bayesian viewpoint, and vice versa. The numerator integral of this derivative can be represented as the CCDF of the posterior of the 6.4 keV line. It calculates the cumulative probability of a mean rate exceeding μ_{steady} photons per unit time, given the observed total number of events N_{total} and μ_{cont}. The denominator integral acts as a normalization element, ensuring that the cumulative probabilities are scaled appropriately across all possible photon counts of μ_{line}; hence, the integral is normalized to 1.
To determine the instance of the mean rate for steady emission (μ_{steady}), we find the value $\mu_{\text{steady}} = \mu_k$ for a given value of $k \in [0, 1]$, at which the posterior probability density of steady emission reaches a specified probability level k. At this point, the posterior density of the steady emission becomes k times its maximum value. This relationship can be expressed as:

$$\frac{dP}{d\mu_{steady}}(\mu_{steady} \mid N_{tot},\mu_{cont})_{[\mu_{steady}=\mu_k]} = k \times \frac{dP}{d\mu_{steady}}(0 \mid N_{tot},\mu_{cont}) \tag{4.14}$$

The equation 4.14 is useful to understand the instance of the probability of obtaining the steady emission s.t $k = 0.5$ representing the 50% & 95% limits, respectively. We use the normalized CCDF curve of the line for the numerical calculations of the posterior of steady emission.

4.2.4 Estimating the steady emission via empirical CCDF

Determining the posterior probability density function for the steady emission ($\frac{dP}{d\mu_{steady}}$) presents several challenges. Firstly, there is an absence of prior knowledge regarding the behavior of steady emission (μ_{steady}). Similarly, there is a lack of information about the variability (μ_{var}). Consequently, deterministic approaches are not viable, necessitating reliance on alternative methods to estimate the density function of steady emission.

In our case, we estimated this posterior probability density from an empirical CCDF curve of the 6.4 keV line. While this approach may lack a robust mathematical foundation, it serves as a pragmatic method that can be justified based on the empirical data's CCDF characteristics. The CCDF typically diminishes significantly above the observed flux and remains relatively constant below the observed flux. This pattern also aligns with the uniform prior assumption we built into our toy model scenario. Hence, the CCDF can be used to constrain the upper limits for the mean rate of steady emission within the posterior of the line[4]

The average rate of steady emission is inferred using the equation 4.14 and the CCDF. Two important posterior probability levels, known as the "50% upper limit estimation" and the "95% upper limit estimation", are determined based on the value of k.

[4]The precision of this method improves with more measurements (increased number of epochs).

4.2.5 50 % Upper limit Estimation

For $k = 0.5$, this value represents the point at which the posterior probability density of steady emission reaches 50% of its maximum value. It represents a μ_k value in which the posterior curve is reduced to half of its peak value. Here, the "maximum value" denotes the highest point on the density curve, signifying the most likely value or mode $\mu_{\rm steady}$.

$$\frac{dP}{d\mu_{steady}}(\mu_{steady}|N_{tot},\mu_{cont})_{[\mu_{steady}=\mu_k]} = 0.5 \times \frac{dP}{d\mu_{steady}}(\mu_{steady}|N_{tot},\mu_{cont})_{[\mu_{line}=0]} \tag{4.15}$$

Practically, $\mu_{k=0.5}$ is obtained by considering the value of $\mu_{\rm steady}$ at which the maximum of CCDF decreases by a factor of 2. Furthermore, if the exposure time of the pixel is represented by t, the 50% flux upper limit of the steady emission can be determined as follows

$$F^S_{50\%} = \frac{\mu_{\rm k=0.5,\ 50\ \%}}{t} \tag{4.16}$$

4.2.6 95 % Upper limit Estimation

The posterior distribution of the steady emission exhibits a sigmoid shape, skewed towards the left, with the majority of its density concentrated near zero and a long tail extending towards the right. Therefore, defining a credible interval is not feasible. This suggests that the focus is on constraining the upper bounds of the parameter rather than pinpointing a specific interval.

$k = 0.05$ represents the point where the posterior steady emission becomes only 5% of its maximum value. By using the density at $\mu_{k=0.05}$, we are 95% confident that the true value of steady emission is below $\mu_{k=0.05}$.

$$\frac{dP}{d\mu_{steady}}(\mu_{steady}|N_{tot},\mu_{cont})_{[\mu_{steady}=\mu_k]} = 0.05 \times \frac{dP}{d\mu_{steady}}(\mu_{steady}|N_{tot},\mu_{cont})_{[\mu_{line}=0]} \tag{4.17}$$

Practically, μ_k is obtained by considering the value of $\mu_{\rm steady}$ at which the CCDF decreases by a factor of 20. If the exposure time of the pixel is represented by t, the 95 % flux upper limit of the steady emission can be determined using

$$F^S_{95\%} = \frac{\mu_{\rm k=0.05,\ 95\ \%}}{t} \tag{4.18}$$

The following sections will examine the concept of steady emission through examples and simulations. Initially, the steady emission of a pixel will be estimated in a single epoch using a single CCDF (Example I). Later, a more complex scenario will be discussed, involving the estimation of steady emission for a pixel over 20 years. This example will also address the challenges associated with this estimation (Example II). Finally, the steady emission will be estimated for multiple pixels (covering all pixels in Sgr B) using the novel methodology (Example III), and the first-ever steady emission maps in Sgr B will be presented.

4.2.7 Example 1: Steady emission for a single epoch

Figure 4.5 presents a real-world application discussed in Section 4.1.2.2 within the context of Poisson statistics and CCDF functions. The figure is composed of two panels: the left panel depicts the density curve for the epoch 2012 6.4 keV line corresponding to Pixel$_{i=15,j=8}$, while the right panel displays the CCDF for the same epoch. The steady emission exhibits a uniform prior density below the observed value of $1.208 \times 10^{-7}\,{\rm cm^{-2}s^{-1}arcmin^{-2}}$ and vanishes above this value. The 50% upper limit, where the probability density of steady emission reaches half of its maximum value, is $1.30 \times 10^{-7}\,{\rm cm^{-2}s^{-1}arcmin^{-2}}$. Moreover, the 95% upper limit is at $1.90 \times 10^{-7}\,{\rm cm^{-2}s^{-1}arcmin^{-2}}$, offering a decent estimation for the upper limit of steady emissions for a single epoch.

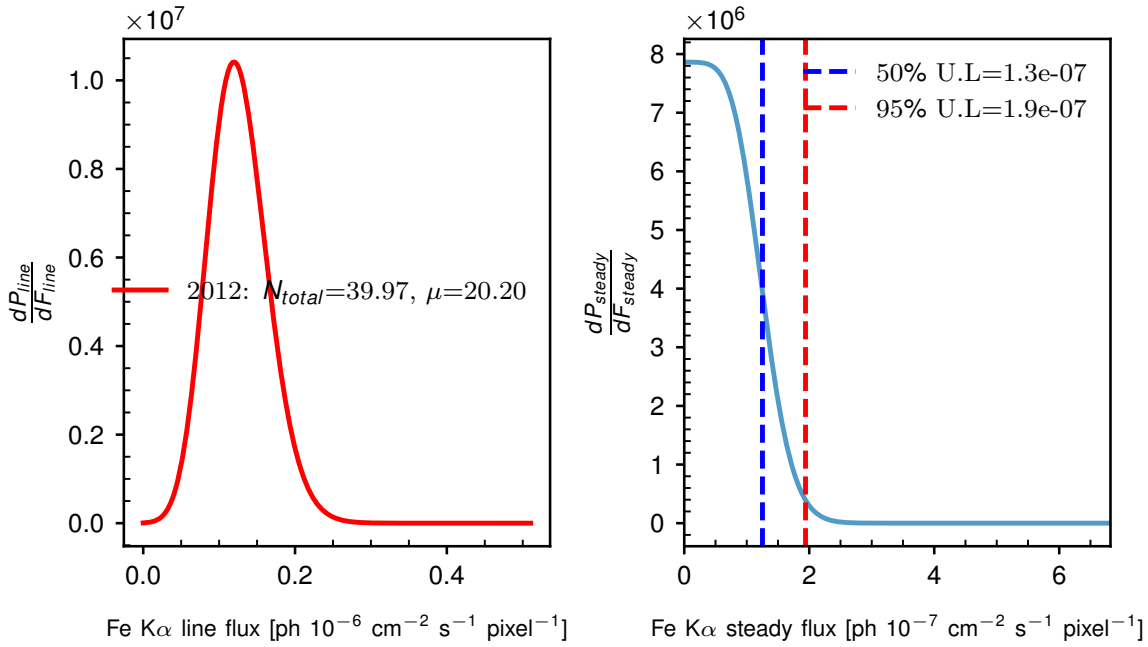

Figure 4.5: Probability density curves for line emission, represented by $\frac{dP_{\text{line}}}{d\mu_{\text{line}}}$ as a function of μ_{line}, for Pixel$_{i=15,j=8}$ for epoch 2012 (*left*). Probability density curves for the steady emission, or $\frac{dP_{\text{steady}}}{d\mu_{\text{steady}}}$ as a function of μ_{steady}, are represented as the tail distributions (CCDF) of the line (*right*).

4.3 Steady Emission for Multiple Epochs (Two Decades)

In this section, we use the Poisson method along with probability density curves to determine the steady emission levels in a scenario where observations of a single pixel span multiple epochs over 20 years. A bottom-up approach is proposed[5] to evaluate the steady emission across two decades. It is crucial to recognize that the level of steady emission identified over this period is derived from a cumulative result of the contributions from individual epochs.

When addressing the analysis across multiple epochs, it is essential to apply the criteria for distinguishing between the Gaussian and Poisson statistical regimes. For epochs characterized by low flux, thereby falling into the Poisson regime, we employ the CCDF curve to estimate steady values. Conversely, for pixels exhibiting high fluxes, classified within the Gaussian regime, the Gaussian error function can be used to assess steady values.

4.3.1 Estimating the steady flux across 20 years

Our original dataset was a three-dimensional $30 \times 30 \times 5$ array. It consisted of five 6.4 keV maps, where each Pixel$_{i,j}$ represented the 6.4 keV Fe $K\alpha$ flux values obtained over five different epochs (see Figure 4.6). First, we assumed that each flux was a combination of a uniform steady component and a time-variable component, and our initial goal was to estimate this steady emission in a single epoch. We successfully obtained a 50% estimation for the upper limit of steady values for a single epoch using the Poisson method. With these developments, we were prepared to apply this technique to all the observed 6.4 keV epochs and find the steady emission value per pixel across 20 years.

[5] A bottom-up approach entails piecing together systems to give rise to more complex systems, thereby making the original system's subsystems of the emergent system.

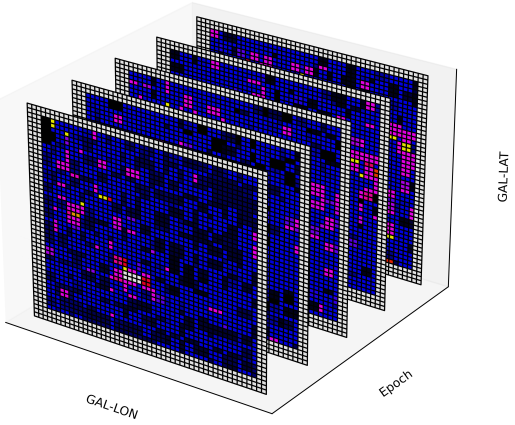

Figure 4.6: The dataset used in this work, a 3 3-dimensional ($30 \times 30 \times 5$) array represents the stacked 6.4 keV maps from 5 epochs.

4.3.2 Estimating the steady flux from multiple epochs

Handling steady emission data over a span of 20 years necessitates the manipulation of multiple CCDF curves. Therefore, it is critical to normalize these density curves by their exposure values. The exposure-normalized version of Equation 4.13 (initially, all the density curves were represented as a function of rates rather than flux) can be derived using the chain rule:

$$\frac{dP}{dF_{\text{steady}}}(F_{\text{steady}}|N_{\text{tot}},\mu_{\text{cont}}) = \frac{dP}{d\mu_{\text{steady}}}(\mu_{\text{steady}}|N_{\text{tot}},\mu_{\text{cont}}) \times \frac{d\mu_{\text{steady}}}{dF_{steady}} \tag{4.19}$$

The term $\frac{dP}{dF_{\text{steady}}}(F_{\text{steady}}|N_{\text{tot}},\mu_{\text{cont}})$ is characterized by the exposure-normalized empirical CCDF curve, obtained by dividing the CCDF curve by the exposure value for the pixel (t). For multiple epochs $e = 2000, 2004, \ldots, 2020$, we can derive multiple curves. The combined CCDF, representing the steady emission, is determined as the "minimum" CCDF at each steady flux sample space :

$$\frac{dP}{dF^{S}_{\text{steady}}}(F_{\text{steady}}|N_{\text{tot}},\mu_{\text{cont}}) = \min\left\{\frac{dP}{dF^{e}_{\text{steady}}}(F_{\text{steady}}|N_{\text{tot}},\mu_{\text{cont}})\right\} \tag{4.20}$$

where $\frac{dP}{dF^{e}_{\text{steady}}}(F_{\text{steady}}|N_{\text{tot}},\mu_{\text{cont}})$ represents the exposure-normalized CCDF for each epoch e, and $\frac{dP}{dF^{S}_{steady}}$ denotes the combined exposure-normalized CCDF characteristic curve for steady emission over multiple epochs. The choice of the minimum is fundamental, as it offers the simplest method to limit the faint, steady emission.

Figure 4.7 demonstrates the application of the method to $\text{Pixel}_{i=15,j=8}$ within the data cube shown in Figure 4.6. In this figure, the left panel displays the individual density curves of 6.4 keV line emission as a function of line flux F_{line} in $\text{cm}^{-2}\text{s}^{-1}\text{arcmin}^{-2}$ units across 20 years (under the gamma approximation). Conversely, the right panel illustrates the "probability density of steady emission" as interpreted using the empirical CCDF curves corresponding to each epoch as a function of steady flux F_{steady} in $\text{cm}^{-2}\text{s}^{-1}\text{arcmin}^{-2}$ units (in black). The density curve of steady emission in Figure 4.7 is not normalized[6]. However, the choice of 50% and 95% is not affected by the rescaling of the y-axis.

[6]The density curve must be normalized so that its total area equals 1 to be considered a proper density curve.

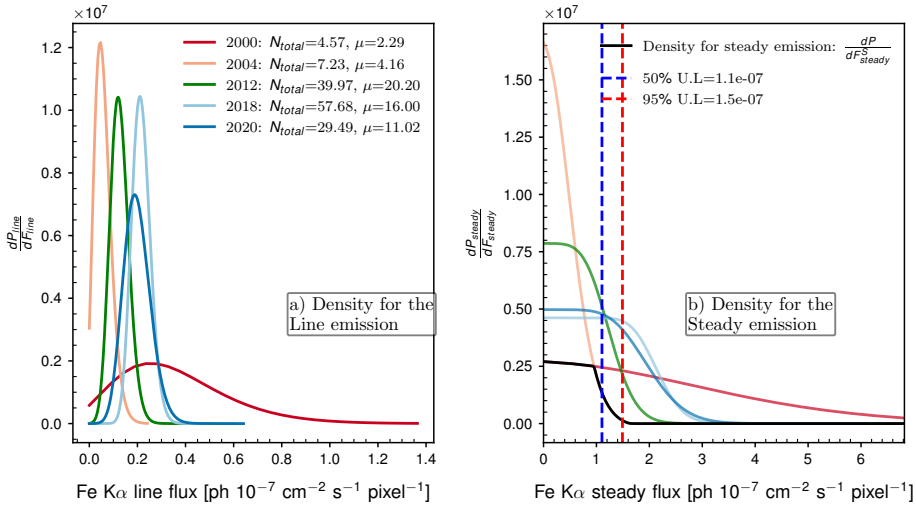

Figure 4.7: Probability density curves for line emission, represented by $\frac{dP_{\text{total}}}{d\mu_{\text{line}}}$ as a function of μ_{line}, for Pixel$_{i=15,j=8}$ in the data cube 4.6 (*left*). Probability density curves for the steady emission, or $\frac{dP_{\text{steady}}}{d\mu_{\text{steady}}}$ as a function of μ_{steady}, are represented as the CCDF of the line (*right*). The combined density of the steady emission is plotted in black, representing the minimum of each density curve. The density curve for the steady emission is not normalized (although the proper density curve should be normalized), as it rescales the y-axis only but does not affect the flux values of the x-axis. The 50% estimation and the 95% estimation for the steady emission values are indicated by vertical dashed red lines.

$F_{\text{steady}} = F_k$ is identified as the flux at which the posterior probability density of steady emission reaches a specified probability level denoted as F_k^{steady}:

$$\left.\frac{dP}{dF^S_{\text{steady}}}\right|_{F_{\text{steady}}=F_k^{steady}} = 0.5 \times \left.\frac{dP}{dF^S_{\text{steady}}}\right|_{F_{\text{steady}}=0} \tag{4.21}$$

where $k = 0.5$ and $k = 0.05$. $F^{\text{steady}}_{k=0.5}$ can be interpreted as the 50% upper limit estimation and $F^{\text{steady}}_{k=0.05}$ for the steady emission across 20 years.

4.3.3 Does the 50% Upper Limit Truly Constrain the Steady Emission?

The right panel of Figure 4.7 also demonstrates the combined density function of the steady emission, derived from the "minimum" densities of each epoch, illustrated by the black curve in the plot. This function's 50% estimate is measured as $1.1 \times 10^{-7}\,\text{cm}^{-2}\text{s}^{-1}\text{arcmin}^{-2}$. Similarly, the 95% upper limit estimation yields a value of $1.5 \times 10^{-7}\,\text{cm}^{-2}\text{s}^{-1}\text{arcmin}^{-2}$.

However, this analysis also reveals that incorporating CCDF curves corresponding to the high flux values across the sample space can inevitably add constraints to the overall steady emission estimations. While using the minimum value across these distributions is typically a reliable method for constraining faint, steady emissions, this approach can sometimes lead to overestimations due to the variability of the curves (in this instance, from epoch 2000). To mitigate the potential bias introduced by variability and high flux values in certain epochs, we propose the implementation of new criteria for rejecting outliers.

4.3.4 Rejection-Estimation Criteria

Upon determining the $F^{steady}_{k=0.5}$ and $F^{steady}_{k=0.95}$ values, which represent the 50% and 95% upper limits for steady emission, a subsequent step involves a critical comparison of all individual flux measurements for the pixel ($F^{50\%}_{i,j,e}$) against the $F^{steady}_{k=0.95}$ threshold. This process involves removing all flux measurements that exceed the 95% threshold. Following the exclusion of these outliers, we then proceed to recompute both the 50% and 95% upper limits.

This approach ensures that the estimation of steady emission is not influenced by high flux values, thereby providing a more accurate representation of the steady emission. Mathematical representation of the rejection-estimated density and estimators are expressed as follows:

$$\frac{dP}{dF^{S'}_{\text{steady}}}(F_{\text{steady}}|N_{\text{tot}},\mu_{\text{cont}}) = \min\left\{\frac{dP}{dF^{e<F^{steady}_{k=0.95}}_{\text{steady}}}(F_{\text{steady}}|N_{\text{tot}},\mu_{\text{cont}})\right\} \tag{4.22}$$

Rejection-estimated upper limits :

$$\left.\frac{dP}{dF^{S'}_{\text{steady}}}\right|_{F_{\text{steady}}=F^{steady}_{k}} = k \times \frac{dP}{dF^{S'}_{\text{steady}}}_{F_{\text{steady}}=0} \tag{4.23}$$

where $k = 0.5$ and $k = 0.05$ correspond to the 50% and 95% upper limits, respectively.

4.3.5 Example II: Steady Emission Analysis Over 20 Years (A Single Pixel Investigation)

Building upon the previously established example and introducing new criteria for rejection estimates, panel (c) of Figure 4.8 illustrates the density curve for continuous emission after applying a rejection threshold of $\geq$ 95% ($\frac{dP}{dF^{S'}_{\text{steady}}}$). The initial 95% upper limit estimate, set at $1.491 \times 10^{-7}\,\text{cm}^{-2}\text{s}^{-1}\text{arcmin}^{-2}$, acts as a reference point for evaluating flux measurements displayed in Figure 4.9. With the enforcement of the rejection criteria, flux values surpassing this 95% threshold, recorded during the years 2000, 2018, and 2020, were excluded. The process then updates the 50% and the 95% upper limits, incorporating only fluxes compatible at the 95% level, specifically from the years 2004 and 2012. Consequently, the updated upper limit estimates from the rejection method are yielded to be $8.260 \times 10^{-8}\,\text{cm}^{-2}\text{s}^{-1}\text{arcmin}^{-2}$ and $1.347 \times 10^{-7}\,\text{cm}^{-2}\text{s}^{-1}\text{arcmin}^{-2}$ for the 50% and 95% upper limits, respectively.

Figure 4.9 presents the light curve for $\text{Pixel}_{i=15,j=8}$ with updated steady emission estimates under both criteria. The estimation for the 50% threshold has decreased by 25.18% for this pixel. This reduction is attributed to the exclusion of potential variability effects from high flux measurements when transitioning from $\frac{dP}{dF^{S}_{\text{steady}}}$ to $\frac{dP}{dF^{S'}_{\text{steady}}}$.

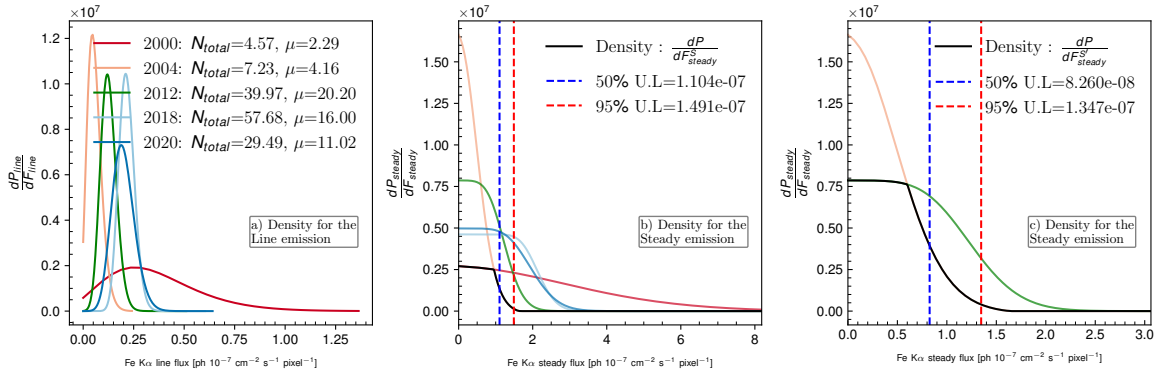

Figure 4.8: Probability density curves for line emission, represented by $\frac{dP_{\text{total}}}{d\mu_{\text{line}}}$ as a function of μ_{line}, for Pixel$_{i=15,j=8}$ (a). Probability density curves for the steady emission, or $\frac{dP_{\text{steady}}}{d\mu_{\text{steady}}}$ as a function of μ_{steady} (b). The combined density of the steady emission ($\frac{dP}{dF^{S}_{\text{steady}}}$) is plotted in black (b). Probability density curves for steady emission with 95% compatible pixels and the aggregate density of the recomputed steady emission density ($\frac{dP}{dF^{S'}_{\text{steady}}}$) (c). Both density curves in (b) and (c) for the steady emission are not normalized (although the proper density curve should be normalized), as it rescales the y-axis only but does not affect the upper limit flux values of the x-axis.

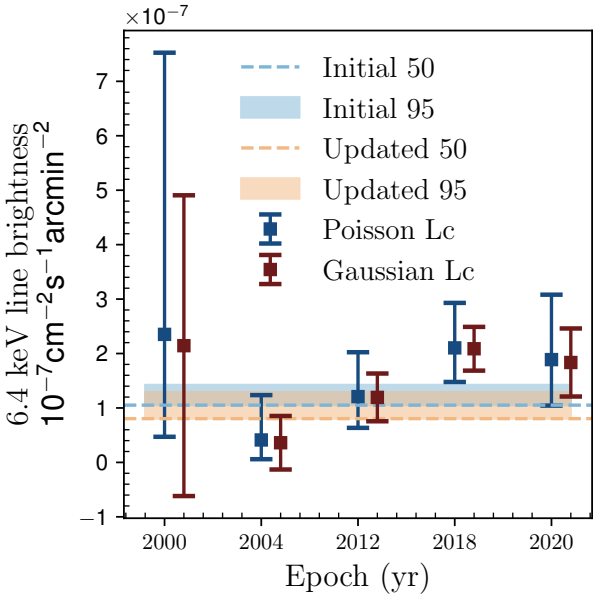

Figure 4.9: Variations in the 6.4 keV surface brightness over the five epochs within an area corresponding to a single pixel ($30'' \times 30''$) at pixel coordinates (15,8) (Gaussian and Poisson light curves). Both the 50% and 95% steady emission estimates before and after the application of rejection criteria ($F^{steady}_{k=0.5}$ and $F^{steady}_{k=0.05}$ respectively) are shown.

4.3.6 Example III: Steady Emission Analysis Over 20 Years (Complete Pixel Coverage of Sgr B)

Prior to analyzing the steady emission across the entire Sgr B region, we employed the methodology on the light curves presented in Figure 4.1, which initiated our discussion on steady emission. Figure 4.10 illustrates the light curves alongside their estimated steady emissions (50% and 95%) using the density curve $\frac{dP}{dF^{S'}_{\text{steady}}}$.

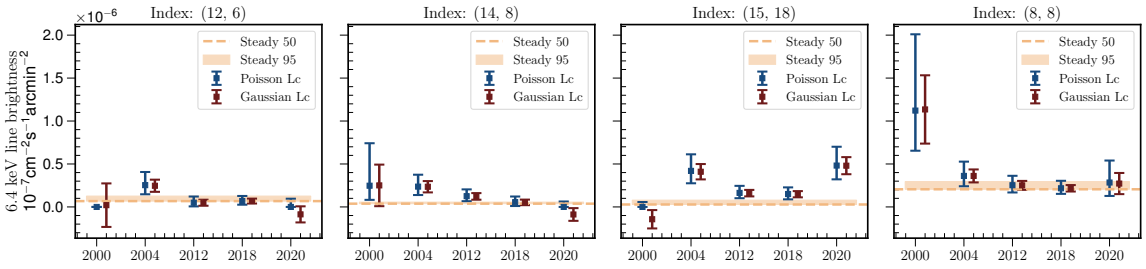

Figure 4.10: Variations in the 6.4 keV surface brightness across five epochs for a single pixel area of $30'' \times 30''$, as estimated using the Poisson method (blue). The variations are shown for pixel coordinates: (12,6), (14,8), (15,18), and (8,8). 50% steady flux level and 95% steady flux limit are also presented.

Figure 4.10 reveals that the steady emission for pixels $(12, 6)$, $(14, 8)$, $(15, 18)$, and $(8, 8)$ displays a significant variation in the 50% estimation values, highlighting a substantial disparity in the steady emission levels across these pixels. During the application of rejection criteria, we systematically excluded potential contributions from higher flux values to mitigate their impact on our analysis. Despite these measures, the observed inhomogeneity in emission could arise from a variety of underlying causes, which will be thoroughly examined in Chapter 5 as we delve into potential interpretations for the steady emission.

The analysis was then extended to encompass all pixels within the "Sgr B" region by creating a global morphology map that shows the upper limit of the steady emission. Figure 4.11 shows two critical estimations for the steady X-ray flux originating from the Sgr B molecular cloud. Specifically, the top left panel of Figure 4.11 showcases the 50% estimation ($F^{steady}_{k=0.5}$), whereas the top right panel provides a heatmap indicating the number of epochs compatible with the 50% level. Conversely, the bottom left panel illustrates the 95% upper limit estimation ($F^{p'=0.95}_{s_{i,j}}$), and the bottom right panel displays the number of epochs compatible with the 95% limits. These comprehensive maps will serve as foundational references for spectral extraction, as detailed in Section 4.4.

Figure 4.11 presents the first X-ray flux map to showcase baseline steady X-ray intensity within one of the main molecular complexes in the CMZ. Our methodology employed a probabilistic approach grounded in rigorous statistical interpretations. Despite the inherent complexities of such an analysis, our assumptions and statistical methods have been carefully validated, ensuring that our findings represent the most accurate description of the upper limits of baseline X-ray emission within this region. As shown in Figure 4.11, three key sub-regions demonstrating prominent steady emission can be identified. Among these, the "Sgr B2" region is notable for its significant steady emission levels. Equally remarkable is the area south of Sgr B2 known as "G0.66", which also displays a high level of brightness, matching that of Sgr B2. We revisit these sub-regions in our discussion of the origin of the steady emission in Chapter 5.

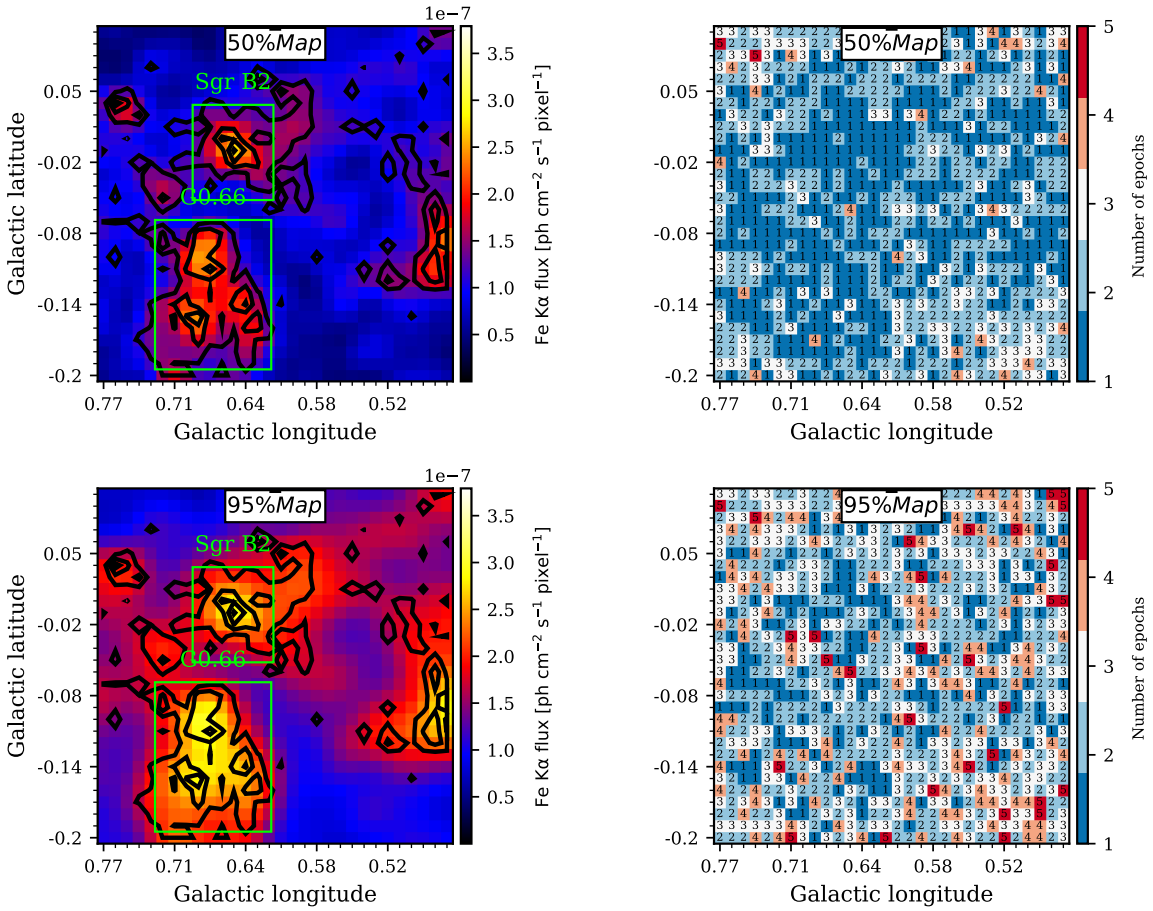

Figure 4.11: Upper Limit for Steady X-ray Emission from the Sgr B: The figure illustrates the 50% estimation of steady X-ray intensities (top-left) alongside the epochs compatible with this estimation (top-right). The 95% upper limit estimation (bottom-left) and the epochs are compatible with this 95% limit (bottom-right). Contours overlaying these maps indicate the intensity levels of X-rays in Galactic coordinates, with flux measured in units of $Ph\ cm^{-2}\ s^{-1}\ pixel^{-1}$.

4.4 Extraction of Steady Spectra

In this section, the method for obtaining a deep XMM-Newton steady X-ray spectrum is presented. The process begins with the identification of pixels compatible with steady emission across five epochs, ensuring that spectral information is exclusively extracted from these regions. An overview of this procedure is detailed in Section 4.4.1. The extraction process, further detailed in Section 4.4.2, is complicated due to pixel-level extraction complexities, but a customized script has been developed to achieve the task effectively. Section 4.4.4 explains how the merging process involves combining data from multiple epochs to create a deep, unified spectrum representing the steady X-ray emission.

4.4.1 Binary Mask

For each $Pixel_{i,j}$ in every epoch of the 6.4 keV Poisson map, a comparison is made with the steady maps, defined by the 50% and 95% upper limits. The purpose of this comparison is to identify and preserve pixels in each X-ray map that are compatible with the steady emission estimations while

masking out pixels exhibiting fluxes that do not align with the steady emission criteria. The flux value of $Pixel_{i,j}$ in each 6.4 keV X-ray maps is denoted by $F^{50\%}_{i,j,e}$, and the 50% and 95% steady emission estimations are denoted by $F^{steady}_{k=0.50}$ and $F^{steady}_{k=0.95}$ respectively. The binary mask for each pixel, based on the 95% upper limit, is defined as follows:

$$Mask_{95} = \begin{cases} 0 & \text{if } F^{50\%}_{i,j,e} \leq F^{steady}_{k=0.95}, \\ 1 & \text{if } F^{50\%}_{i,j,e} \geq F^{steady}_{k=0.95}, \end{cases}$$

Figure 4.12 displays the 95% upper limit compatible $Mask_{95}$ for observed epochs, where black pixels are masked out, and white areas are retained for spectral extraction.

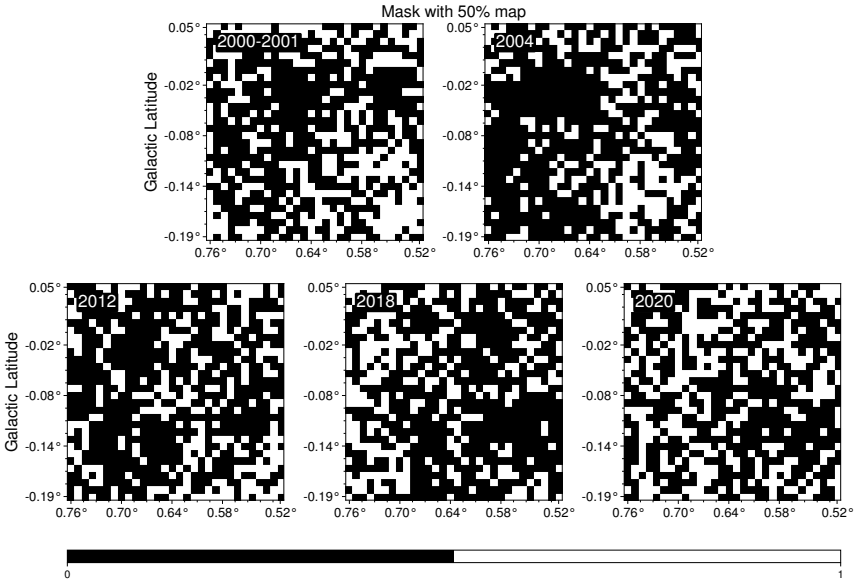

Figure 4.12: Binary masks ($Mask_{95}$) for the epochs 2000, 2004, 2012, 2018, and 2020. The masked regions are indicated in black.

Similarly, the binary mask based on the 50% upper limit is defined as:

$$Mask_{50} = \begin{cases} 0 & \text{if } F^{50\%}_{i,j,e} \leq F^{steady}_{k=0.50}, \\ 1 & \text{if } F^{50\%}_{i,j,e} \geq F^{steady}_{k=0.50}, \end{cases}$$

In Figure 4.13, the 50% upper limit compatible $Mask_{50}$ for the 6.4 keV maps is presented, with black areas representing pixels that are incompatible with the 50% steady emission estimation. Comparison with 50% upper limits results in fewer white areas being available for spectral extraction, highlighting the stricter selection criteria applied by $Mask_{50}$.

A comparison between Figure 4.13 and Figure 4.12 demonstrates that $Mask_{50}$ enforces more strict constraints on compatibility selection than $Mask_{95}$, consequently exposing less region for analysis. The more strict selection is set to enhance the precision of spectral estimations of steady emission.

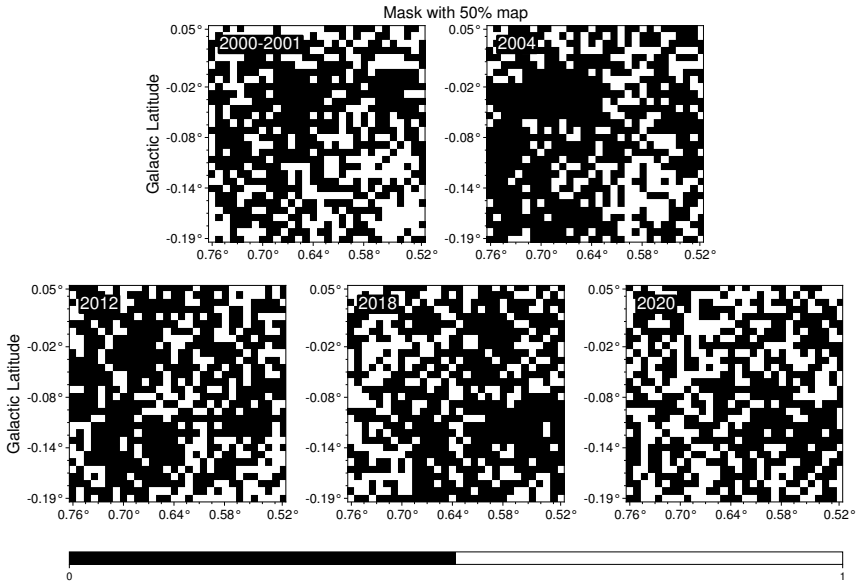

Figure 4.13: Binary masks ($Mask_{50}$) for the epochs 2000, 2004, 2012, 2018, and 2020. The masked regions are indicated in black.

4.4.2 Spectral extraction

Spectral extraction begins with the conversion of binary masks into DS9[7] region files in XMM-Newton detector coordinates. These region files are then used to filter individual observations relevant to each epoch, producing steady spectra for each observation. The details of this procedure are explained in the following sections.

Preparation of region files

For each pixel where $F^{50\%}_{i,j,e} \geq F^{steady}_{k=0.95,k=0.50}$ in the masks described in Section 4.4.1 are first converted into simple region files in image coordinates. This conversion results in a complex region definition with multiple box-shaped region components. These regions are then organized into equatorial coordinates in degrees, using the WCS coordinate system stored in their header files. Conversion of these sky coordinates into the XMM-Newton detector coordinate system in detector units (DETX, DETY) is subsequently conducted using the SAS routine `ecoordconv`[8] for all three XMM-Newton instruments (pn, MOS1, MOS2). The size of each box (width and height) in detector coordinates is determined based on the resolution of the XMM-Newton detector and the physical size of each box.

Upon converting the pixel coordinates from each mask into XMM-Newton detector coordinates, these are stored in a FITS table as a source list, including a table extension named SRCLIST. This format follows the ASC region specification(McDowell & Rots 1998). For better understanding, a few details of the source list for one observation (Observation ID: 0802410101) are provided in Table 4.1.

[7] SAOImage DS9 is an astronomical imaging and data visualization application

[8] `ecoordconv` is used to transform celestial sky positions (RA, DEC) into XMM-Detector coordinates (DETX, DETY). The center coordinates of each box-shaped region in equatorial coordinates are converted into XMM-Newton detector coordinates.

Table 4.1: List of Sources from a Single Observation (Observation ID: 0802410101). The FITS files holding this source list have been stored in designated extensions. For the EPIC-pn instrument, the file is named *pnS003-bkg_region-det.fits*, for EPIC-MOS1, it's *MOS1S001-bkg_region-det.fits*, and for EPIC-MOS2, the file is *MOS2S002-bkg_region-det.fits*. Each FITS file includes 211 region components.

Instrument	SHAPE	DETX	DETY	R	ROTANG	COMPONENT
Pn	!ROTBOX	13288.883	223.6773	610.0, 615.0	58.72	1
	!ROTBOX	12717.383	-831.493	610.0, 615.0	58.72	1
	...	...	...	..., ...	...	...
MOS1	!ROTBOX	-101.767	12974.423	610.0, 615.0	148.72	1
	!ROTBOX	951.247	12398.956	610.0, 615.0	148.72	1
	...	...	...	..., ...	...	...
MOS2	!ROTBOX	-13145.149	-251.796	610.0, 615.0	58.72	1
	!ROTBOX	951.247	12398.956	610.0, 615.0	58.72	1
	...	...	...	..., ...	...	...

4.4.3 Spectral extraction

Full spectral data from all three XMM-Newton instruments (EPIC-pn, EPIC-MOS1, EPIC-MOS2), corresponding to the six observations as defined in Table 2.2, were processed using a specially developed script. The standard data reduction procedures, described in Section 2.2.2, involved generating calibrated event files using ESAS with `emchain` for the MOS instruments and `epchain` for the EPIC-pn. Subsequently, the ESAS tasks `mos-filter` and `pn-filter` were employed for further filtering. The filtered event files were then processed with an extraction region of 30° and the source list defined in Section 4.4.2, employing both single and double X-ray events for pn (`PATTERN < 4`) and all events for MOS (`PATTERN < 12`), using the `evselect` routine. The required RMF and ARF files were produced by the `arfgen` and `rmfgen` tasks. Local background was extracted from each quadrant of the XMM-Newton detector. Finally, the `pn-back` and `mos-back` routines were used to merge all the quadrant background files, creating a global background file for both pn and MOS background spectra. Figure 4.14 from $Mask_{95}$ and Figure 4.14 from $Mask_{50}$ represent the individual XMM-Newton spectra for the observations in Table 2.2. The Y-axis of each panel represents the photon counts in units (*counts* $\sec^{-1}$ keV^{-1}), while the X-axis denotes photon energy in keV. I extracted XMM-Newton spectra in the 0.5-10 keV range (but the Figure presents spectra in the 2-10 keV range). The spectral data were grouped such that each bin has a signal-to-noise ratio of at least 10 (the background is not included in this calculation).

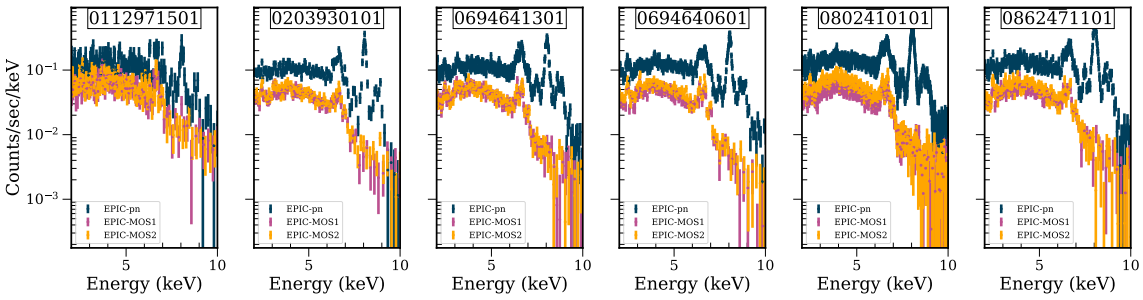

Figure 4.14: 2-10 keV XMM-Newton spectra (EPIC-pn, EPIC-MOS1 and EPIC-MOS2) were generated using the $Mask_{95}$.

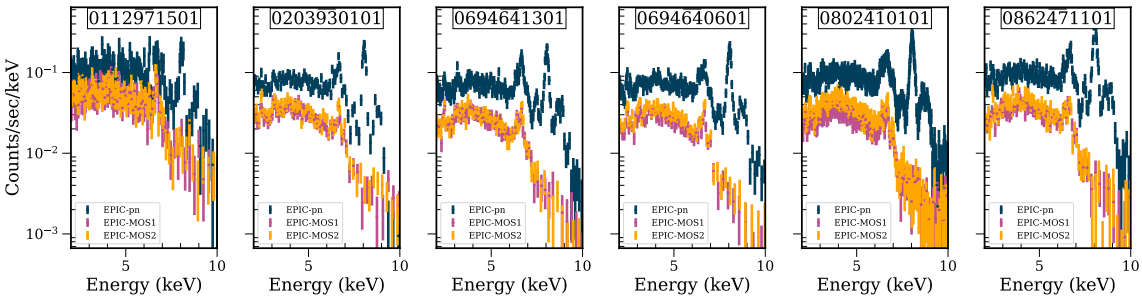

Figure 4.15: 2-10 keV XMM-Newton spectra (EPIC-pn, EPIC-MOS1 and EPIC-MOS2) were generated using the $Mask_{50}$.

4.4.4 Deep XMM-Newton spectrum for steady emission

All steady spectra from the observations were merged into one deep XMM-Newton spectrum using the following criteria. The input spectra were combined so that the output spectrum contains merged source spectra, which is the sum of the counts in all input source spectra. This process is represented by the equation:

$$S = \Sigma_e S_e \tag{4.24}$$

where e denotes the epochs. The merged exposure is the mean of the sum of the exposure for each instrument, averaged over the epochs, given by:

$$Exposure = \frac{\Sigma_e exp_e}{\text{number of epochs}} \tag{4.25}$$

The response matrix is the sum of the exposure-weighted average of the individual spectra, expressed as:

$$Resp = \text{number of epochs} \times \frac{\sum_e R_e \times \exp_e}{\sum_e \exp_e} \tag{4.26}$$

For the background spectrum, the counts are the sum of the counts in all input background spectra:

$$B = \Sigma_e B_e \tag{4.27}$$

and the statistical errors are calculated as the Root Mean Square Error (RMSE) of the statistical errors in all input background spectra, formulated as:

$$B_{\text{RMSE}} = \sqrt{\frac{\sum_{e=1}^{\text{number of epochs}} (B_e)^2}{\text{number of epochs}}} \tag{4.28}$$

Figure 4.16 presents the deep XMM-Newton spectra for the steady emission in the Sgr B region following the merging process. The spectrum from $Mask_{95}$ is shown on the left, and the spectrum from $Mask_{50}$ is on the right. These spectra, covering the 2-10 keV energy range, have been grouped such that each spectral bin achieves a minimum signal-to-noise ratio of 20. The 20 SNR grouping enhances the statistical significance of the photon count features relative to the background.

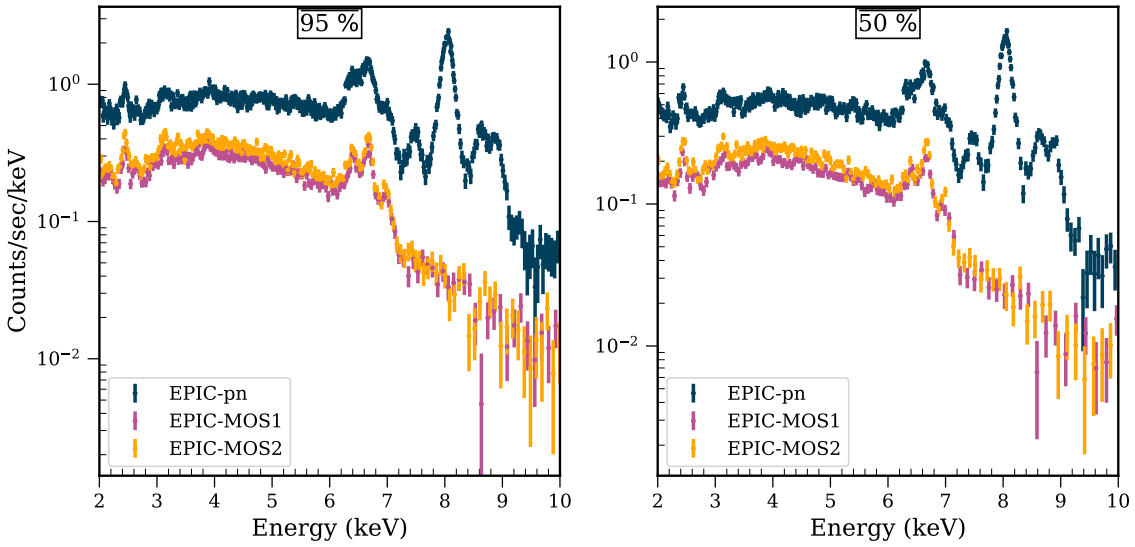

Figure 4.16: Deep XMM-Newton spectra of the steady emission in the Sgr B region, post-merging process. The left panel shows the spectrum from $Mask_{95}$, and the right panel from $Mask_{50}$, both adjusted for a minimum SNR of 20 per bin.

Figure 4.16 provides the first in-depth X-ray spectral analysis of the baseline steady emission. This spectrum is used to understand the possible origin hypotheses in Chapter 5.

4.5 Conclusion

This chapter begins with an exploration of the Poisson methodology, a tool developed to rectify the issue of negative fluxes inherent in the existing methodology. A Poisson statistical framework has been further discussed for its applicability in estimating the baseline X-ray emission within the GC. Adopting a bottom-up approach, we initially define the steady emission for a single epoch, introduce a non-parametric method, and obtain the upper limits of steady emission via the CDF curves. This methodology has been founded on a set of reasonable assumptions, making it possible to extrapolate the information obtained from the single epoch analysis to estimate the baseline steady emission over a period of two decades. We presented the first in-depth analysis of the X-ray morphology and spectroscopy related to the steady emission within the Sgr B region. In the next chapters, a detailed astrophysical discourse will be conducted, expanding our knowledge of this region with new insights.

Chapter 5

A Study of Steady Diffuse Emission in Sagittarius B

The nature of the steady non-thermal diffuse emission within the Sgr B region opens a new window into the high-energy processes of the GC. The complexity of this steady emission is related to various astrophysical processes and the intricate interstellar environment of the GC. As introduced in Chapter 1, this emission could potentially be created by several key factors, including the presence of faint point sources, interactions between molecular clouds and cosmic rays, and the reflection of X-rays from dense gas clouds. This discussion will methodically address these factors, contrasting our findings with those of previous research. Through this comparative analysis, we aim to understand the underlying mechanisms driving the observed steady emission, thereby enhancing our understanding of the broader astrophysical processes in the GC in X-rays.

Contents

5.1 Point Source Contributions

One hypothesis regarding the origin of the steady non-thermal diffuse emission is that it might be the result of the collective X-ray emission from the faint, persistent point sources prevalent in the GC. Many sources do not exhibit significant long-term variability in XMM observations, and they were not subtracted from our analysis. Hence, their influence needs to be quantified. To understand how these point sources within the GC contribute to the observed steady diffuse X-ray emission, I utilized the capabilities of cutting-edge X-ray observatories, including Chandra and XMM-Newton, to systematically identify, catalog, and analyze point sources compatible with steady emission within the GC's Sgr B region. In this section, I quantify the contributions of those identified point sources to the steady emission and shed light on the astrophysical processes that contribute to the GC's diffuse steady emission environment.

5.1.1 Chandra Point Sources

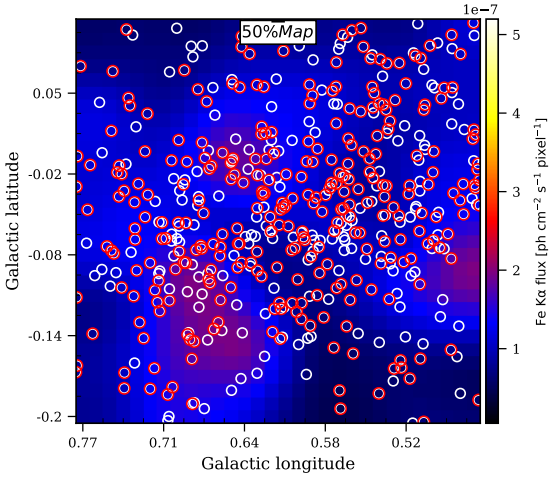

Figure 5.1: Chandra point sources within the Sgr B steady map (50% limit). This figure covers a 900″ square arcsecond area centered at $RA = 266.86°$, $Dec = -28.427°$. A total of 483 candidate sources were identified (marked in white), among which 296 were confirmed as true detections (highlighted in red).

The Chandra X-ray Observatory facilitates the precise analysis of individual point sources amidst the diffuse emission prevalent in the GC. This capability is primarily due to two reasons: its PSF (of 0.5″ compared to 6″ in XMM-Newton) and its ability to maintain a low level of background noise (see Chapter 2). The Chandra Source Catalog 2.1 (CSC 2.1) was released on April 2, 2024, (Evans et al. 2010), and it represents a comprehensive list of X-ray sources detected by the Chandra X-ray Observatory. Version 2.1 includes measured properties for 407,806 unique, compact, and extended X-ray sources across the sky. The catalog details extracted properties from 928,280 individual observation detections, identified across 10,382 Chandra ACIS and HRC-I imaging observations.

I extracted the faint point sources from the CSC 2.1, targeting those within the Sgr B region. For the purposes of this study, a square region with a size of 900″, centered on equatorial coordinates $RA = 266.86°$ and $Dec = -28.427°$, was selected. All the distinct X-ray sources within this defined region were initially filtered to isolate potential contributors to the faint, steady emission. These distinct sources were obtained from the master sources table in CSC, where each entry represents a distinct source characterized by the observation block with the largest total exposure in cases where multiple observations exist. This process yielded a total of 483 candidate sources (see Figure 5.1, white circles). At first glance, there appears to be no clear correlation between these point sources and the steady emission. However, a thorough spatial correlation analysis between the point sources and the steady emission map is necessary to draw robust conclusions about their correlation. It is also important to note that not all identified point sources can be directly attributed to the steady emission. The most suitable candidates for this emission will be further determined based on their detection likelihood and source variability metrics.

5.1.1.1 Detection Likelihood

The reliability of source detection is a critical metric in astronomical catalogs, with the likelihood of detection serving as a primary determinant in classifying a source's presence as either a true astrophysical phenomenon or a mere fluctuation of the background or an artifact. Within the context of the CSC 2.1, various likelihood scores serve as indicators of a source's existence. A source attribute called `likelihood_class` is used to categorize detections as either "TRUE" or "MARGINAL". A "TRUE" `likelihood_class` denotes a high likelihood value, signifying a strong probability that the observed source is an astrophysical object rather than a background noise fluctuation. It suggests that the change in the fit statistic due to the inclusion of a source model is significantly better than what a background-only model would predict. On the other hand, a "MARGINAL" classification is attributed to sources whose likelihood values exceed background noise levels yet fall short of the "TRUE" classification threshold. These are cases where there is some evidence for the presence of a source, but the evidence is not strong enough to conclusively rule out fluctuations in the background as the cause. As our study focuses on establishing upper limits for faint point sources to compare with the upper limits of steady emission, I considered sources classified with both "TRUE" and "MARGINAL" likelihood classes. Out of 483 candidates, we filtered 296 true detections and 187 marginal detections (see Figure 5.1).

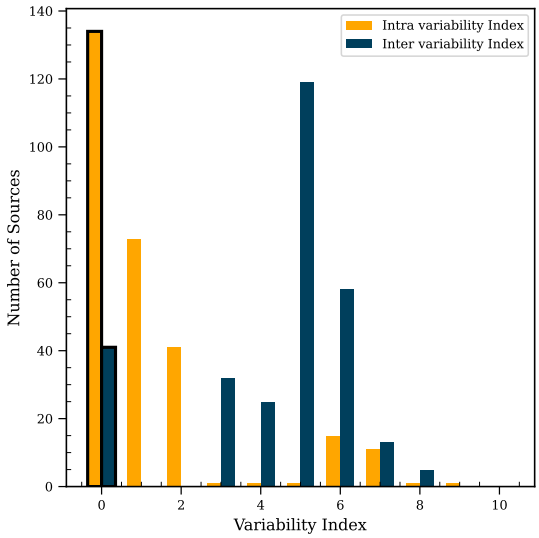

Figure 5.2: Histogram showcasing both intra- and inter-observational variability indices of confirmed detections within the Sgr B region.

5.1.1.2 Variability Probability

Detected sources within the observational data may exhibit a range of behaviors, from quiescent to transient, over the observation period. The presence of significant flux variability in a source is inversely correlated with the characteristics of steady emission. Consequently, distinguishing between steady and variable sources is essential, as this differentiation plays a critical role in accurately assessing the contribution of each source to the overall steady emission. The CSC 2.1 provides several ways to evaluate source variability, including the Gregory-Loredo Probability, the Kolmogorov-Smirnov (K-S) Test Probability, and Kuiper's Test Probability. These metrics are calculated based on the counts observed in the source region. Two important variability flags associated with CSC 2.1 need to be considered:

- **Intra-observation Source Variability**: This refers to the variability of a source observed within a single observation period, assessing changes in the source's emission (photon flux) throughout that specific observation.
- **Inter-observation Source Variability**: This refers to the variability observed between different, separate observations of the same source, allowing for the comparison of the source's behavior or characteristics across multiple sessions that could be spaced out over time.

The inter-observation variability index (`var_inter_index`) is an integer value in the range $[0, 8]$, and the intra-observation variability index (`var_intra_index`) is in the range $[0, 10]$, used to gauge variability. An index of 0 indicates a definitively non-variable source, 1 denotes marginally constant sources, and higher indices suggest increasing variability. Figure 5.2 displays a histogram of the variability index of Chandra detections within Sgr B. Since my approach aims to isolate steady sources, I selected sources with no inter-observation variability (`var_inter_index` = 0) to focus on the assumption of steadiness. In total, 41 sources were identified with a `var_inter_index` of 0, indicating steady behavior across observations. Figure 5.3 highlights the distribution of these steady faint point sources within the Sgr B region (in red crosses). This distribution highlights the absence of correlation between steady emission and point source detections, which will be further explored through spectral analysis in Section 5.1.2.

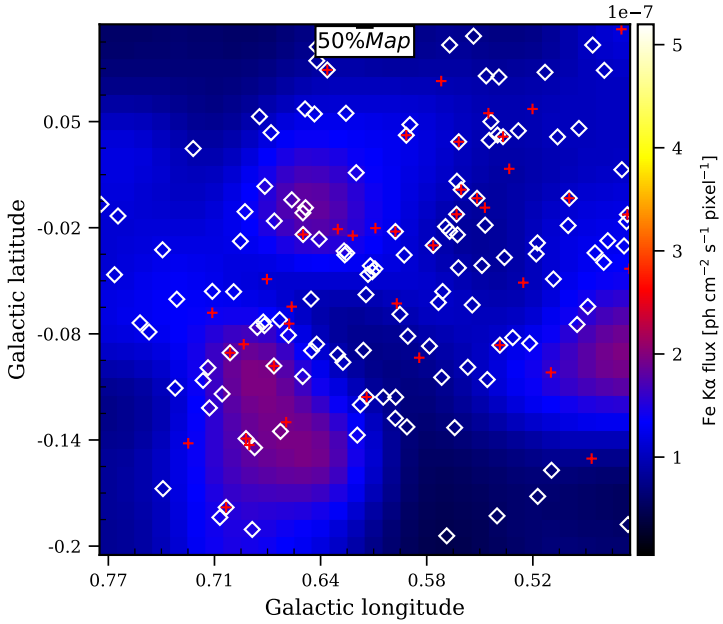

Figure 5.3: Distribution of TRUE/MARGINAL point sources with no inter-observation variability within the Sgr B region. White diamond markers represent steady sources within a single observation (`var_intra_index`=0), while red crosses indicate 41 steady sources across multiple observations (`var_inter_index`=0).

5.1.2 Chandra Point Source Spectrum

The apparent mismatch between the faint point sources and the steady emission is further analyzed through spectral comparison. For the spectral analysis of the faint steady point source contribution, I used CSC 2.1 to download all the source and background spectra for the selected 483 candidates. The per-observation detection files, namely ARF (`arf3.fits`), PHA (`pha3.fits`), and RMF (`rmf3.fits`), specifically tailored for each source region in each observation, were also downloaded from the Chandra Source Archive. The CIAO `combine_spectra` script was employed to merge PHA files along with their corresponding response files. The merging process was conducted in two steps: first, combining all true point sources[1], followed by the 41 steady detections. The merged point source spectra were then fitted with a `tbabs*(pow + gauss + gauss + gauss)` model in `Sherpa`. The model comprises a power-law continuum (`pow`) and the neutral Fe Kα (6.40 keV), Fe XXV (6.70 keV), and Fe XXVI (6.97 keV) lines (`gauss`), modeled with an intrinsic absorption column density. All model components

[1]Only true sources were used in order to minimize the impact of fake detections on the spectral analysis

are subject to foreground absorption (`tbabs`). The energies of the lines are set to 6.40 keV, 6.70 keV, and 6.97 keV, while the line widths are maintained at 10 eV. The spectral index for the `pow` component and all the normalization values and the absorption were fitted. The best-fit parameters were obtained and are presented in Table 5.1, and the spectra and residuals are shown in Figure 5.4.

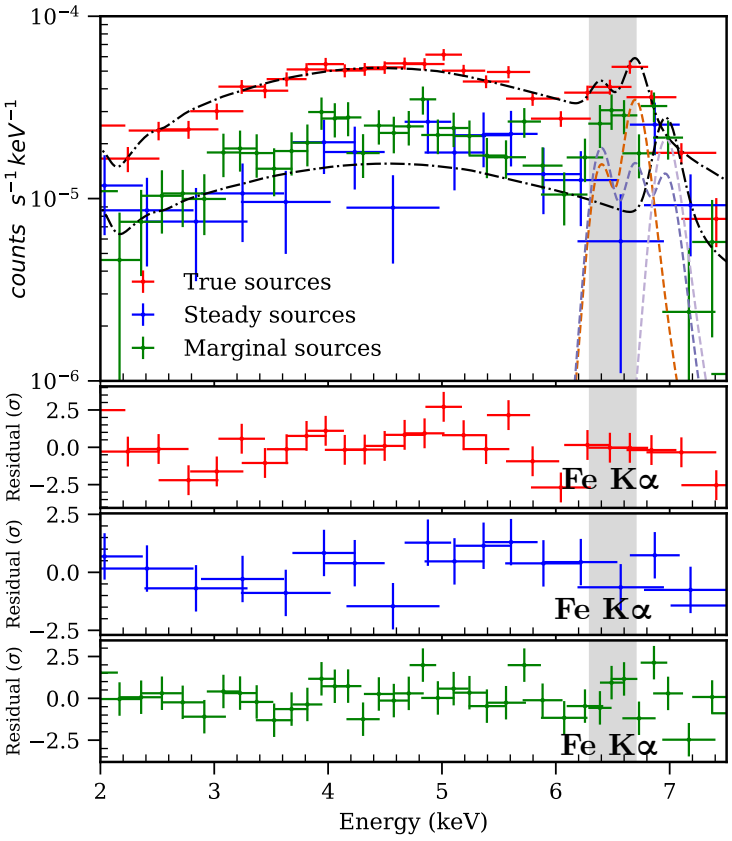

Figure 5.4: Spectral fit and residuals for the Chandra merged point source spectra in Sgr B. Top panel: spectrum and model component for true detections (red), marginal detections (green), and steady detections (blue). Second panel: Residual for true sources. Third panel: Residual for marginal sources. Bottom panel: Residual for steady sources. The spectra were fitted using the `tbabs*(pow + gauss + gauss + gauss)` model in `Sherpa`.

Table 5.1: Spectral parameters of the combined point source spectra for 1) true detections within the Sgr B, 2) marginal sources, and 3) steady sources. The spectra were fitted using the `tbabs*(pow + gauss + gauss + gauss)` model in `Sherpa`.

Parameter	Unit	True Detections	Marginal Detections	Steady Detections
$N_H(f)$	10^{22} cm^{-2}	$2.00^{+0.75}_{-0.57}$	$4.81^{+3.02}_{-2.30}$	< 2.90
Γ	–	$-0.30^{+0.19}_{-0.14}$	$0.29^{+0.61}_{-0.51}$	$-0.66^{+0.63}_{-0.41}$
$F_{2-7.5keV}$	10^{-7} ph cm^{-2} s^{-1}	$1.03^{+0.41}_{-0.22}$	$1.32^{+2.65}_{-0.79}$	$1.66^{+0.33}_{-0.78}$
$F_{FeK\alpha,6.4keV}$	10^{-8} ph cm^{-2} s^{-1}	$2.29^{+0.88}_{-0.73}$	$0.30^{+0.10}_{-0.01}$	$< 8.42 \times 10^{-5}$
$F_{FeXXV,6.7keV}$	10^{-8} ph cm^{-2} s^{-1}	$6.64^{+0.85}_{-1.10}$	0.29 ± 0.11	$< 1.78 \times 10^{-4}$
$F_{FeXXVI,6.97keV}$	10^{-8} ph cm^{-2} s^{-1}	< 0.85	0.32 ± 0.13	5.54 ± 2.77
χ^2 (d.o.f)	...	2.19 (21)	1.12 (32)	1.13 (12)

In the Sgr B region, the 6.4 keV flux fitted across all true detections was determined to be $2.29^{+0.88}_{-0.73} \times 10^{-8}$ ph cm^{-2} s^{-1}, whereas the upper limit flux for steady sources was measured at $< 8.42 \times 10^{-12}$ ph cm^{-2} s^{-1}. These findings were compared with the total steady X-ray intensity

derived from the steady emission map, which stands at 9.81×10^{-5} ph cm^{-2} s^{-1}. The spectral analysis of the steady point sources in the Sgr B region suggests that they constitute only a minor fraction of the baseline steady emission of Sgr B. The 6.4 keV flux from marginal detections, which is $0.30^{+0.10}_{-0.01} \times 10^{-8}$ ph cm^{-2} s^{-1}, has no significant impact on the outcome. This, in addition to the absence of correlation, excludes the possibility that faint point sources significantly contribute to the observed steady emission.

5.1.3 XMM-Newton Point Sources

Since we rely on XMM-Newton data to study steady emission, ensuring consistency in our Chandra point source analyses with XMM-Newton is important. Despite XMM-Newton's lower spatial resolution compared to Chandra, its larger effective area allows XMM-Newton to collect more photons in a given time, enhancing its sensitivity to bright sources and allowing it to detect point source contributions that might not be listed in the Chandra catalog. This section evaluates the contribution of such point sources detected within the Sgr B region with XMM-Newton. Section 5.1.3.1 describes the catalog of steady point sources detected by XMM-Newton in the area. Section 5.1.3.2 addresses the analysis of point sources detected in the XMM-Newton broadband (0.5 - 10 keV) steady mosaic map.

5.1.3.1 4XMM-DR13 Catalog data

The XMM-Newton source catalog (4XMM-DR13) (Webb et al. 2020) includes source detections from 13,243 public XMM-Newton EPIC observations. These observations span an energy interval from 0.2 keV to 12 keV, and the latest update for data release 13 contains 656,997 unique "clean" source detections across 1328 deg^2 of the sky, of which 20,971 detections have spectra. The median flux in the total photon energy band (0.2 keV-12 keV) of the catalog detections is approximately 2.2×10^{-14} erg cm^{-2} s^{-1}. About 23% of the sources have total fluxes below 1×10^{-14} erg cm^{-2} s^{-1}. For this study, all the sources within a $900'' \times 900''$ region centered on ($RA = 266.86°, Dec = -28.427°$) were selected. A total of 244 unique "clean" sources were filtered in this area. To select non-variable point sources from these filtered sources, an estimation based on the variable flag (`VAR_FLAG`) in the catalog was used. This flag is set to `True` if the source was detected as a variable (based on the χ^2 hypothesis testing) in at least one exposure, and `False` if the source failed in the null hypothesis (not qualifying as a variable). 75 sources were identified as non-variable sources (`VAR_FLAG = False`) for further study

Given XMM-Newton's larger collecting area, which enhances its sensitivity to faint sources and its capacity to gather more photons from extended sources, extended source contributions were excluded from these 75 sources. This was achieved by setting the source extent parameter to zero (`sc_extent = 0`), filtering sources compatible with the native XMM-Newton PSF (i.e., $6''$), resulting in 44 point sources meeting this criterion. Figure 5.5 displays these sources overlaid on the steady X-ray emission map, with all 244 point sources marked by red circles, non-variable sources highlighted in white, and the final selection of point sources indicated by black crosses.

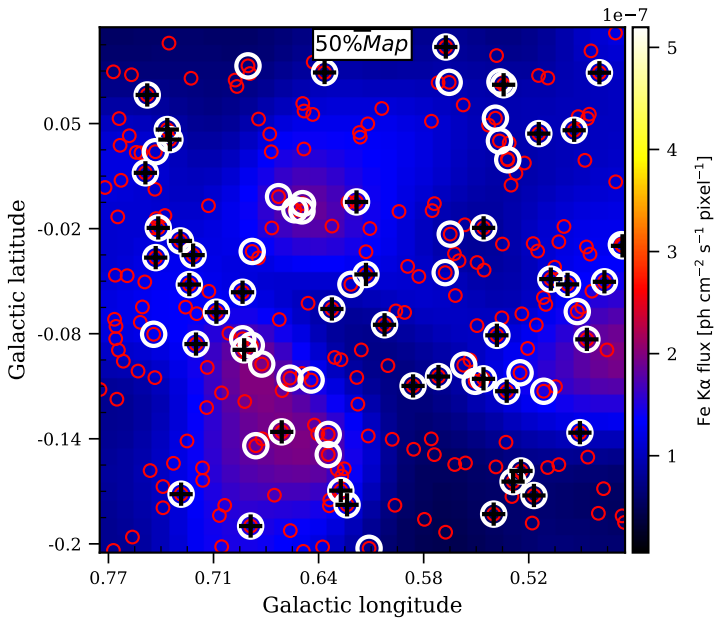

Figure 5.5: Point sources from the 4XMM-DR13 Catalog within the Sgr B region. The figure marks all point sources with red circles, non-variable sources (`VAR_FLAG = False`) with white circles, and point sources (non-extent sources) with black crosses.

5.1.3.2 XMM-Newton Detection Pipeline

This analysis focuses on identifying point sources within regions compatible with steady emission. The process begins with the generation of a steady broadband mosaic compiled from all the XMM-Newton observations across all epochs. Subsequently, the source detection pipeline is used to identify point sources within the merged mosaic. The aim is to assess the influence of these detected point sources (bright) on the field's overall steady emission profile.

5.1.3.3 0.5-10.0 keV Broadband Mosaics

For the construction of 0.5-10.0 keV merged mosaics, a structured methodology was implemented. First, the `SAS` task `evselect` was used to filter the cleaned event files within an energy range of 0.5-10.0 keV. Subsequent to the initial filtering, a 95% binary mask was applied to select the steady emission-compatible pixels. These procedures were executed across all the observations in all epochs for XMM-Newton EPIC-pn, MOS1, and MOS2 instruments. The count, exposure, and background maps were created using these cleaned and filtered steady event files. To merge these maps, the `SAS` task `merge_comp_xmm` was used. The merged mosaics were projected onto a field with a central longitude of $RA = 266.86°$ and a latitude of $Dec = -28.427°$, with a chosen pixel size of 0.0416°. Figure 5.6 illustrates the mosaic flux map and the exposure map.

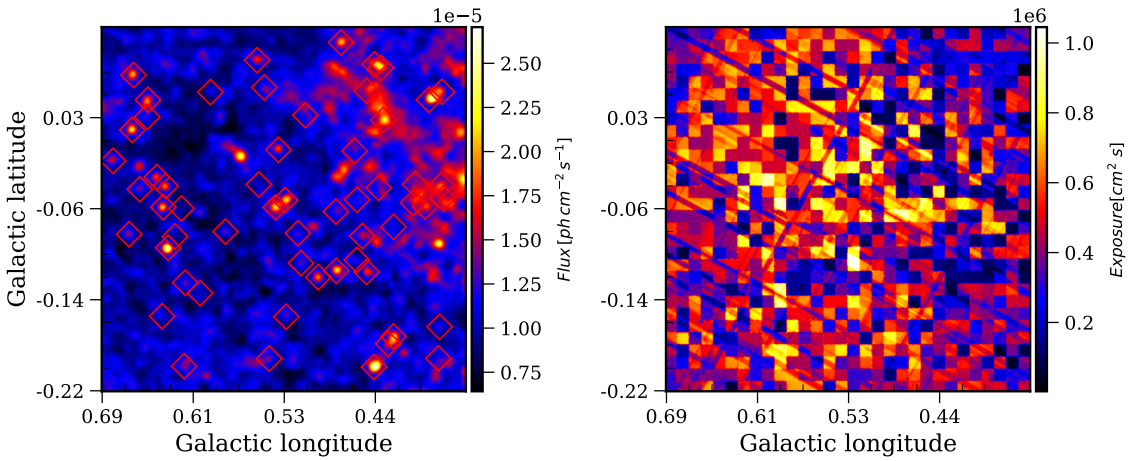

Figure 5.6: Broadband XMM-Newton flux mosaics (0.5-10.0 keV) covering the Sgr B field from epoch 2000 to 2020. These mosaics align with the steady emission map (defined by the 95% confidence interval). The flux map (*left*) was smoothed with a Gaussian kernel of $\sigma = 3$, and the exposure map is shown on the *right*.

Figure 5.6 shows the equivalent steady map (but not limited to 6.4 keV emission) in a broad energy band and with higher angular resolution to spot point sources. Pixels compatible with steady emission (as identified by the binary mask) are visible in the exposure map presented in Figure 5.6 (right). This modification in the exposure map poses challenges during the detection of sources, as it can anomalously detect false sources near the pixel edges.

5.1.3.4 Source Detection

The `SAS` task `ewavelet` was used to detect sources in the mosaic shown in Figure 5.6 (left), using the Mexican Hat wavelet algorithm. This algorithm is capable of detecting both point sources and extended sources. A detection threshold, σ was set to 7, and the edge threshold parameter was set to **10**. This parameter controls the suppression of spurious detections near sharp edges in the exposure mask. A total of 226 sources were detected in the Sgr B field. To obtain the point sources and exclude the extended sources, the `WSCALE` parameter of the output source list was adjusted. This parameter indicates the wavelet scale at which the source was detected, providing a measure of the source's extent (in Gaussian σ). The σ values of the XMM-Newton PSF function 2.355 were used to filter the point sources by excluding the extended sources. In total, 57 point sources were detected in the steady broadband mosaic. Figure 5.7 (left) shows the XMM-Newton broadband mosaic (steady 95% compatible map). The white diamonds represent the detected point sources, and the green circles represent the XMM catalog sources. Note that a few sources are incompatible with the XMM catalog. All of these sources are detection anomalies, which couldn't be resolved with the highest edge threshold parameter.

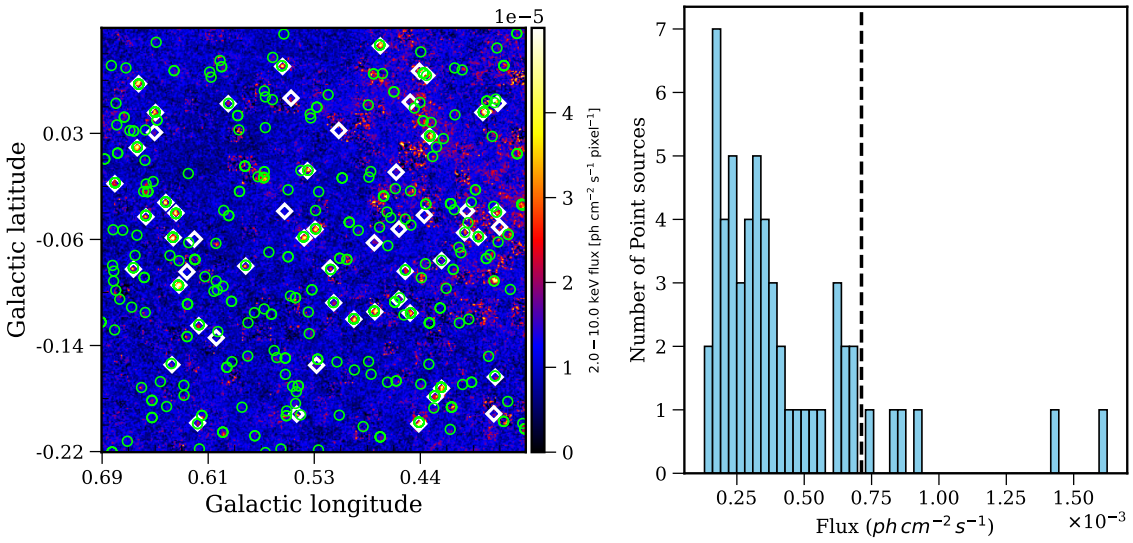

Figure 5.7: Detected point sources (with the `ewavelet` task) overlaid on the XMM-Newton broadband mosaic (2-10 keV) (*left*). Flux histogram of the detected 57 sources (*right*). The 90th percentile flux value is shown with a vertical dashed line.

Figure 5.7 (right) presents the flux histogram for the 57 detected sources. The flux distribution's 90th percentile value (7.125×10^{-4} ph cm^{-2}) was obtained as a threshold to identify brighter detections in the XMM-Newton broadband mosaic. Six bright sources were identified above this 90th percentile threshold and are listed in Table 5.2. The flux column was obtained by dividing the source counts (in cts) by the exposure (PSF-weighted mean around the source, in seconds, vignetting corrected). Identified bright detections were cross-matched with VizieR and the 4XMM-DR13 databases. The Name column gives the 4XMM-DR13 resolved name. However, they do not overlap with the bright regions identified in the broadband steady mosaic.

Table 5.2: Bright point sources detected in the Sgr B region. The table lists the name, coordinates (RA, DEC), and flux of each source.

Name	Coordinates (RA, DEC)	$F_{0.5-7.5keV}$ (ph/cm^2)
4XMM J174741.3-283214	$(266.923, -28.538)$	1.62×10^{-3}
4XMM J174723.2-282534	$(266.848, -28.426)$	0.75×10^{-3}
4XMM J174742.4-282227	$(266.927, -28.375)$	1.42×10^{-3}
4XMM J174736.3-282124	$(266.901, -28.357)$	0.82×10^{-3}
4XMM J174726.8-281841	$(266.863, -28.312)$	0.92×10^{-3}
4XMM J174718.1-281734	$(266.825, -28.293)$	0.87×10^{-3}

5.1.4 Conclusion

The contributions of point sources to the steady emission profile in the Sgr B region have been assessed using both the Chandra and XMM-Newton X-ray observatories. Systematic identification, cataloging, and analysis of point sources have revealed negligible contributions from point sources to the GC steady emission. Spectral analysis further indicated a very weak correlation between the 6.4 keV flux from the distribution of point sources and the 6.4 keV Fe Kα steady emission. This suggests

the presence of other significant contributors or mechanisms responsible for the observed baseline steady emission.

5.2 Correlation with Molecular Clouds

Another potential explanation for the observed steady emission could be its association with molecular clouds. To investigate the potential correlation between molecular materials and the observed steady emission, I analyzed data from the Mopra Central Molecular Zone Molecular Line Mapping Survey (Jones et al. 2012). This survey recorded 20 spectral lines in the CMZ around the GC, with frequencies ranging from 85.3 to 93.3 GHz. This survey achieved approximately 2 km s^{-1} spectral resolution and 40° spatial resolution using the 22-m Mopra radio telescope. The lines were measured from molecules including c-C_3H_2 [2], CH_3CCH, $HOCO^+$, SO, $H^{13}CN$, $H^{13}CO^+$, $H^{13}NC$, C_2H, HNCO, HCN, HCO^+, HNC, HC_3N, ^{13}CS, and N_2H^+. The surveyed area spans Galactic longitudes from $-0.7°$ to $1.8°$ and latitudes from $-0.3°$ to $0.2°$ covering prominent dust cores around Sgr A, Sgr B2, Sgr C, and G1.6-0.025 (Jones et al. 2012).

5.2.1 Molecular Matter Distribution over Sgr B

To investigate the molecular matter distribution within the Sgr B region, I used the CMZ data cube from the Mopra 3mm Survey (Jones et al. 2012). The data cube for each molecule consists of two spatial coordinates and velocity in the third dimension. Each slice of the data cube along the velocity axis represents the distribution of emission (or absorption) at a different LSR velocity[3] (velocity range $-200 \rightarrow +200$ km/s). The value of each voxel[4] is represented by the antenna temperature (T_A^* in Kelvin), which denotes the antenna temperature of the telescope's detector corrected for atmospheric absorption. The intensity of a spectral line is proportional to the power received by the antenna and thus to the antenna temperature.

Some of the molecular tracers exhibited structural similarities with Sgr B2 and G0.66 steady emission at certain LSR velocity ranges, discernible to the naked eye. To quantify these similarities, I used an iterative procedure to determine the optimal LSR velocity range that closely matches the steady emission. For each molecule, I extracted a part of the spectral cube that corresponds to the Sgr B2 and G0.66 regions. I then divided the cube's entire velocity range into steps of 10 km/s. I created intensity maps (or moment 0 maps) by summing (integrating) the intensity values along the velocity axis. These intensity maps represent the total emission at each spatial position. This integration collapses the 3D data cube into a 2D map resulting in the total integrated intensity of the spectral line across the 10 km/s range. These maps also help in identifying areas with significant spectral line emission within the selected velocity range. The `moment(order=0)` method in the `spectral_cube` package in the `astropy` library was used to obtain the intensity maps.

To quantify the structural similarities, I normalized all the FITS data files (steady emission maps and intensity maps for each velocity range) to the range [0,1] and then reprocessed them into 8-bit images. All images were resized to 256×256 pixels[5] for analysis. I used a metric called the Structural Similarity Index (SSIM) to measure similarities with good agreement with human perception (Wang et al. 2004). The SSIM measures image luminance, contrast, and structure and takes a decimal value between -1 and 1, where 1 indicates perfect similarity, 0 indicates no similarity, and -1 indicates perfect anti-correlation. The SSIM was obtained for all velocity steps for each molecule. The highest SSIM values (SSIM ≥ 0.5) and their corresponding velocity ranges for each molecule are presented in Figures

[2] cyclic (c) hydrocarbon represents a molecule where the carbon atoms are arranged in a ring structure.
[3] LSR velocity refers to the velocity of an object relative to the Local Standard of Rest within the galaxy
[4] 3D equivalent of a pixel in 2D images
[5] The choice of 256×256 pixels for rescaling is a standard practice in modern image processing algorithms. While it is possible to use the native resolution of the steady X-ray maps, lower resolutions can negatively impact structure matching outcomes. Therefore, this resolution provides an effective compromise for our analysis while maintaining sufficient detail.

5.8 and 5.9. The analysis of the molecular lines revealed that most of the molecules showed spatial similarities for Sgr B2 steady emission and weak similarities for G0.66 steady emission. Moreover, most of the spatially compatible structures have positive LSR velocity ranges between approximately 0 and 100 km/s.

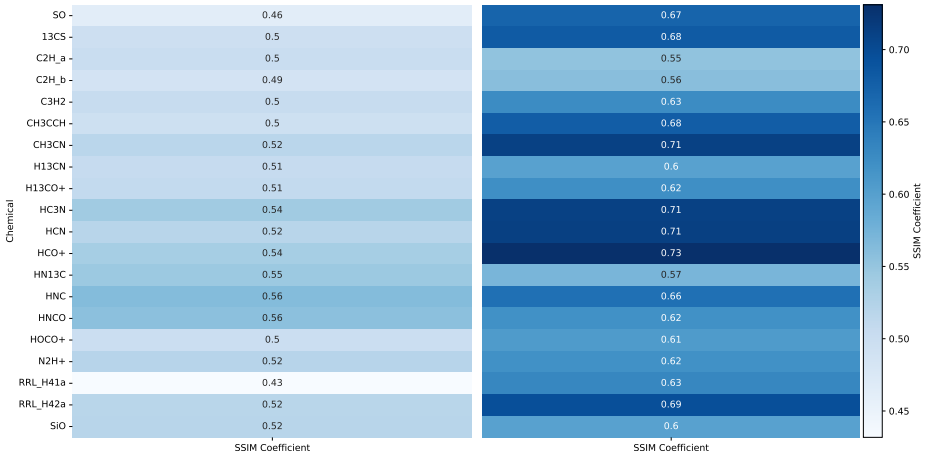

Figure 5.8: The optimal Structural Similarity Index (SSIM) coefficients between the steady emission maps for G0.66 (*left*), Sgr B2 (*right*), and the MOPRA CMZ 3mm Band survey (18 molecular lines and 2 atomic lines). The optimal SSIM values were identified as the highest values within LSR velocity ranges, divided into 10 km/s steps. The SSIM coefficients were calculated using the `structural_similarity` method from the `skimage` library in `Python`.

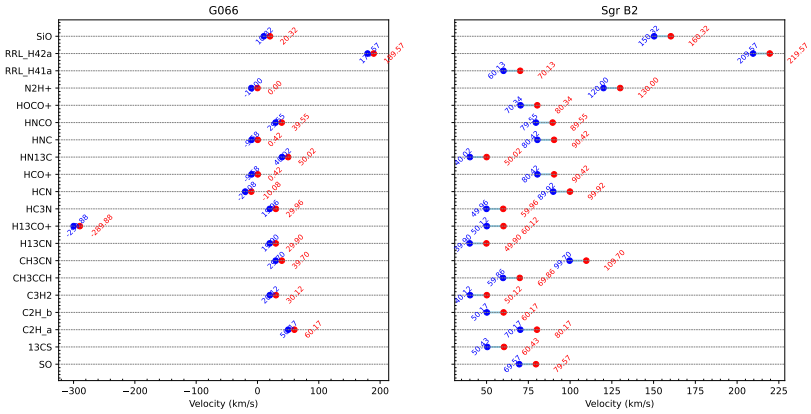

Figure 5.9: The LSR velocity range (in km/s) for the best SSIM coefficient maps in Figure 5.8 (G0.66 (*left*), Sgr B2 (*right*)). The blue represents the lower LSR velocity, while the red shows the higher LSR velocity.

Figures 5.10 and 5.11 show snapshots of 8-bit images of the intensity maps for each molecule at the best velocity range (or highest SSIM value). Figure 5.10 displays the structures of G0.66, while Figure 5.11 shows the structures of Sgr B2.

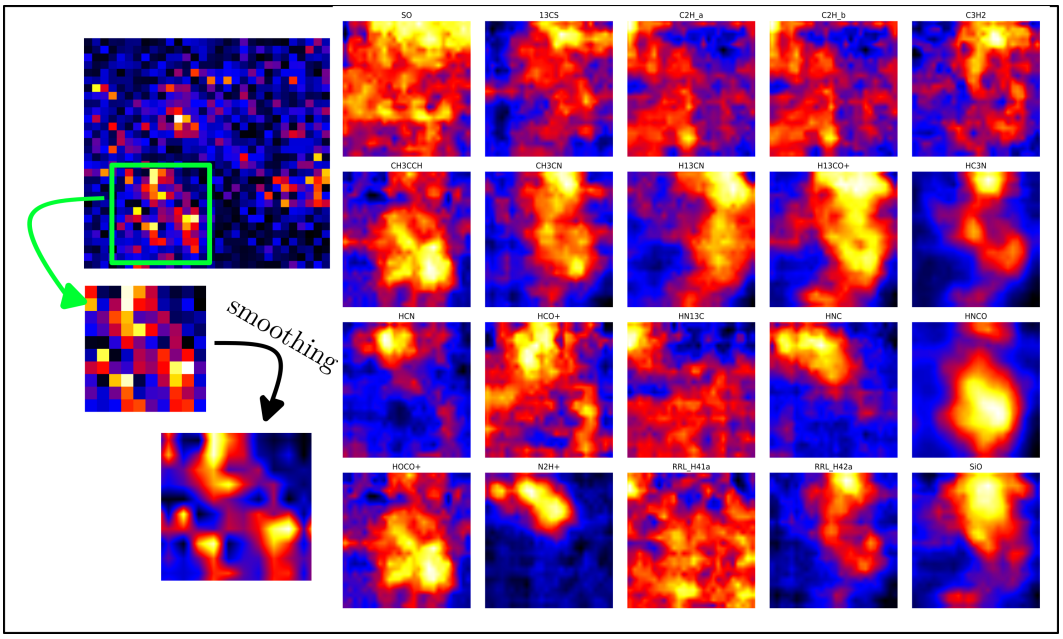

Figure 5.10: Snapshots of 8-bit images (256 × 256 pixels) of steady emission G0.66 (*left*). The unsmoothed images are also presented. The best-matched snapshots of MOPRA CMZ 3mm Band survey products (*right*) include 18 molecular lines and 2 atomic lines.

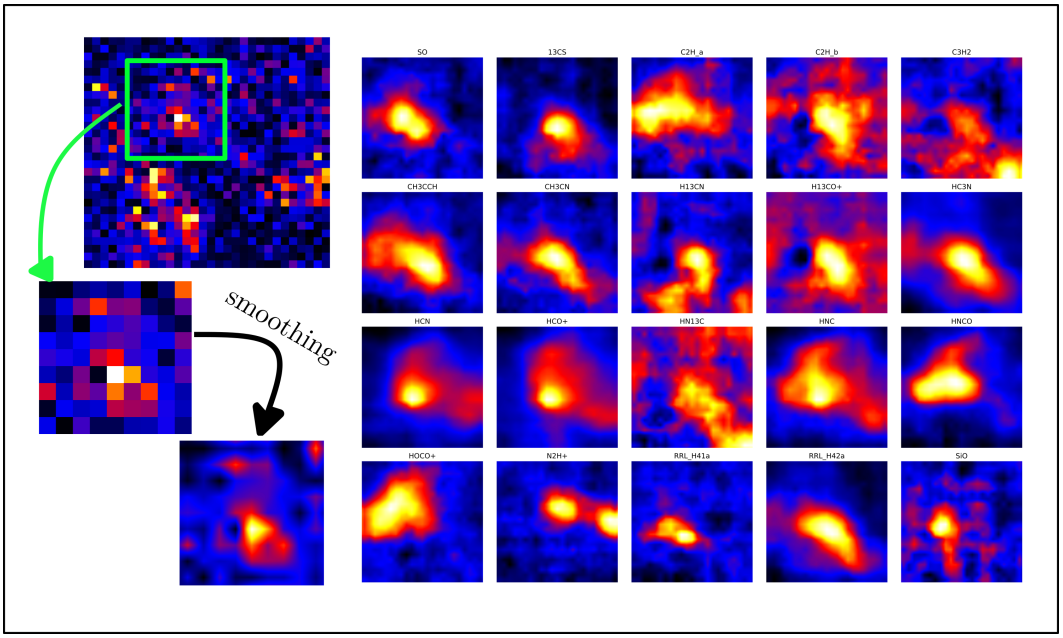

Figure 5.11: Snapshots of 8-bit images (256 × 256 pixels) of steady emission Sgr B2 (*left*). The unsmoothed images are also presented. The best-matched snapshots of MOPRA CMZ 3mm Band survey products (*right*) include 18 molecular lines and 2 atomic lines.

5.2.2 Analysis of Intensity Maps using Pearson Correlation

The tuning frequency of the MOPRA receiver (from 85.3 to 93.3 GHz, centered at 89.3 GHz) was chosen primarily to include the strong emission lines of HCN and HNC. These molecules are known to exhibit some of the strongest emission lines in the 3 mm band. Therefore, I specifically chose these two molecules for further analysis. The HCN and HNC molecular lines exhibit structural similarities with the steady emission. Table 5.3 presents the velocity range corresponding to the highest SSIM values.

Table 5.3: Compatible LSR velocity range for HCN and HNC with steady emission. LSR velocities are given in km s^{-1}.

Molecular Line	**Velocities (km s^{-1})**	
	Sgr B2	**G 0.66**
HCN	(89.92, 99.92)	(-20.07, -10.07)
HNC	(80.41, 90.41)	(-9.58, 0.42)

Figures 5.12 and 5.13 present the moment maps for HCN and HNC, respectively, highlighting notable emission features within the Sgr B2 and G0.66 regions. In the Sgr B2 region, HCN demonstrates emission intensities ranging from 89.92 km s^{-1} to 99.92 km s^{-1} (see left panel of Figure 5.12). Conversely, the G0.66 region exhibits emission intensities ranging from -20.07 km s^{-1} to -10.07 km s^{-1} (see right panel of Figure 5.12). For HNC, the Sgr B2 region shows emission intensities between 80.41 km s^{-1} and 90.41 km s^{-1} (see left panel of Figure 5.13), while G0.66 displays intensities from -9.58 km s^{-1} to 0.42 km s^{-1} (see right panel of Figure 5.13).

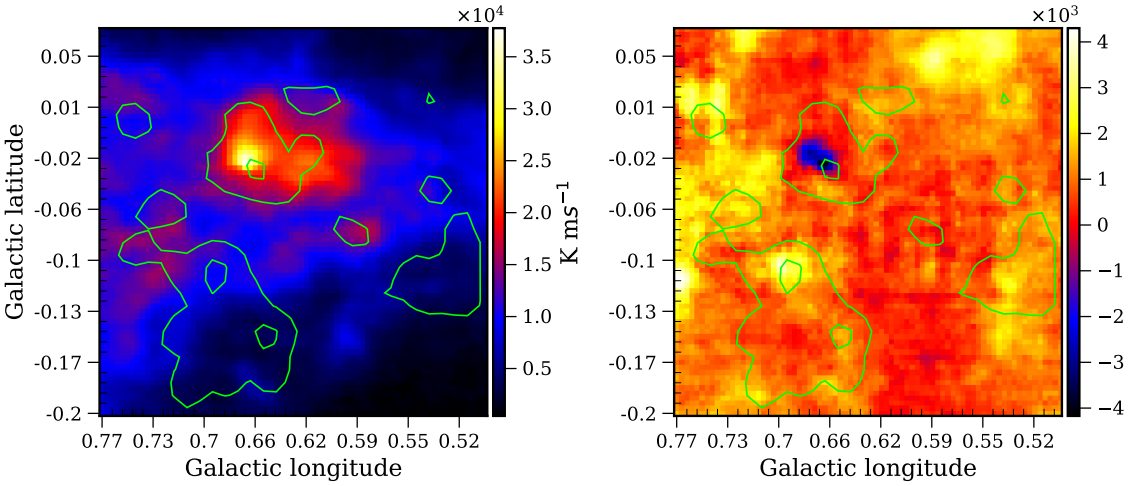

Figure 5.12: Intensity maps for HCN in Sgr B. The left panel shows the integrated LSR map between 89.92 km s^{-1} and 99.92 km s^{-1}, while the right panel shows the integrated LSR map between -20.07 km s^{-1} and -10.07 km s^{-1}. The contour levels indicate the regions with peak steady X-ray intensity.

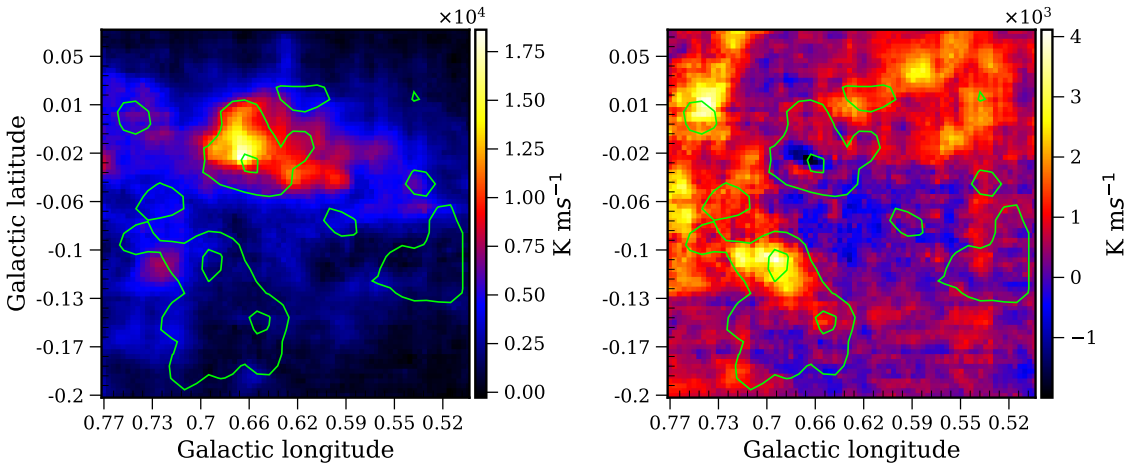

Figure 5.13: Intensity maps for HNC in Sgr B. The left panel shows the integrated LSR map between 80.41 km s^{-1} and 90.41 km s^{-1}, while the right panel shows the integrated LSR map between −9.58 km s^{-1} and 0.42 km s^{-1}. The contour levels indicate the regions with peak steady X-ray intensity.

The SSIM evaluates the structural similarity between two images based on human visual perception, providing a qualitative assessment. However, a statistical measure of linear dependencies between images is required to understand the linear relationship between the steady emission and the gas distribution[6]. For this purpose, metrics such as the Pearson correlation coefficient can be used to assess the linear dependencies between intensity maps and steady emission maps. To conduct the Pearson analysis, the intensity maps (with a resolution of approximately 12″) in Figures 5.12 and 5.13 were downsampled to match the 30″ resolution of the steady emission map. This resampling was achieved using bilinear interpolation. Due to the downsampling process, there is typically a reduction in the total sum of pixel values. To compensate for this reduction and maintain the integrity of the data's original signal strength, the downscaled data were scaled up proportionally. To assess how well the downscaled moment map preserves the characteristics of steady emission, particularly in localized regions, the correlation coefficient was calculated using a moving box of size 5×5 pixels. This moving box method allows for the examination of local properties and variations rather than a global comparison. Figures 5.14 and 5.15 represent the correlation coefficient matrices for HCN and HNC molecules with steady emission using this moving box technique.

[6]It is important to note that the relationship may be more complex than a simple linear relationship, although our focus is on the linear component

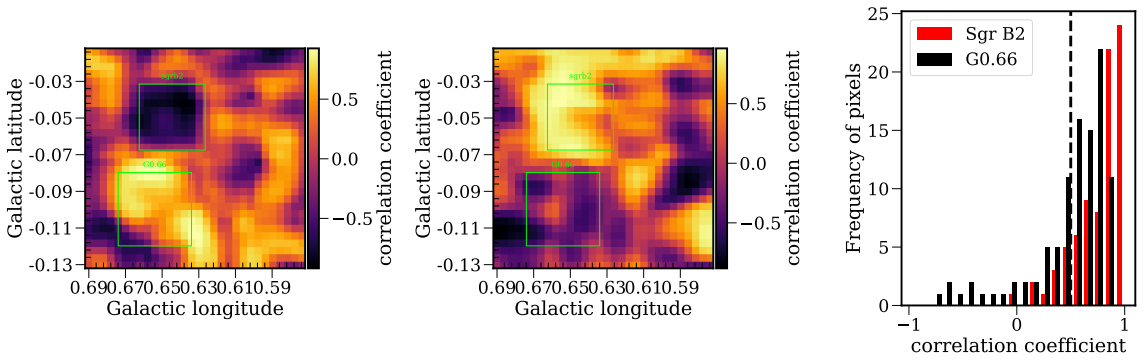

Figure 5.14: Pearson correlation coefficient matrix comparing steady emissions (50% map) with HCN moment maps. Left: Correlation matrix for the G0.66 velocity range. Middle: Correlation matrix for the Sgr B2 velocity range. Right: Histogram of correlation coefficients for G0.66 (in black) and Sgr B2 (in red).

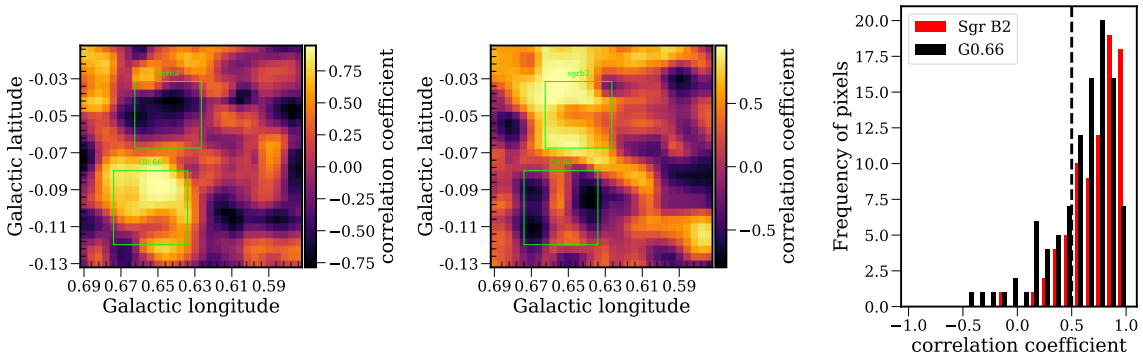

Figure 5.15: Pearson correlation coefficient matrix comparing steady emissions (50% map) with HNC moment maps. Left: Correlation matrix for the G0.66 velocity range. Middle: Correlation matrix for the Sgr B2 velocity range. Right: Histogram of correlation coefficients for G0.66 (in black) and Sgr B2 (in red).

Figures 5.14 and 5.15 show that while there is molecular material where there is steady X-ray emission, the correlation with a given velocity range is not straightforward. The local correlation in the Sgr B2 and G0.66 regions results in some coefficients greater than 0.5. For instance, Figures 5.12 and 5.13 show that the best match velocity range corresponds with the northern part of the X-ray emission. This may hint that other structures may find correspondence with different velocities.

5.2.3 Conclusion

This analysis reveals the complex interactions between molecular line emissions and steady X-ray emission within the Sgr B region. The overall weak correlation coefficients observed for the highly abundant HCN and HNC molecules highlight the challenges of directly linking molecular distributions with steady emission. This discrepancy suggests that the molecular interactions and the steady emission in Sgr B might not be directly interrelated. However, it is also possible that the X-ray signal counterpart is spread across different or multiple velocity ranges or that absorption or shell effects

are preventing a direct comparison. Therefore, a deeper analysis is needed to understand the likely correlation between the two phenomena.

5.3 Spectral Analysis

In this section, a spectral analysis of the observed steady emission in the Sgr B, Sgr B2, and G0.66 regions is conducted. Spectral fitting is performed in two contexts: the full spectra and the steady spectra. For each epoch, spectra of the steady emission were extracted using a pixel-by-pixel comparison against the steady emission maps defined within 50% and 95% confidence levels paired with Poisson maps. Pixels whose flux values from the Poisson map were compatible with those from the steady emission map were selected for spectral extraction. The deep spectra (or merged spectra hereafter) for both cases were created by combining all individual spectra (refer to Section 4.4 for details). The left panel in Figure 5.16 presents the full spectra, including the variable signal for all the XMM-Newton EPIC instruments for Sgr B over a span of 20 years, while the right panel shows their merged full spectrum.

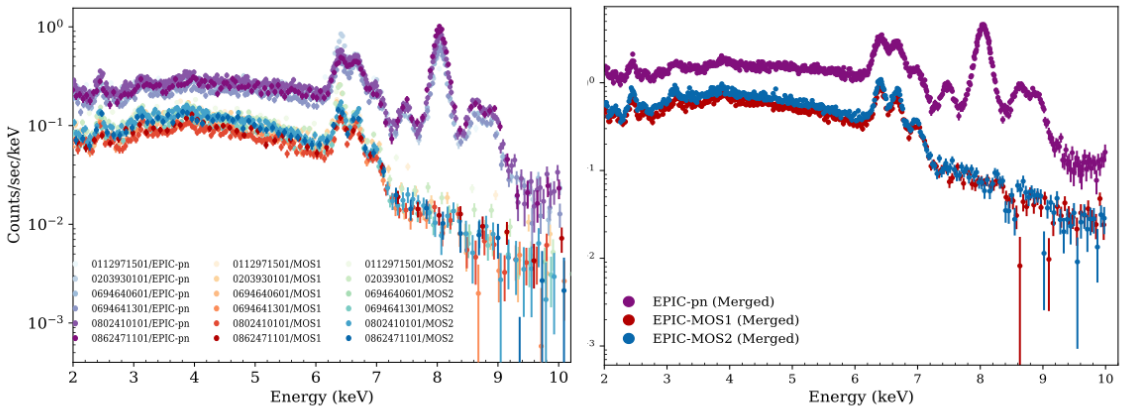

Figure 5.16: The full spectra for all the XMM-Newton EPIC instruments for Sgr B (*left*). Merged full spectrum (*right*). All spectra were grouped with a minimum $SNR = 20$.

For the steady spectrum, it was also observed that certain pixels were only compatible with the steady emission in a single epoch during the comparison. These pixels will be referred to as "single-epoch pixels" henceforth. Single-epoch pixels are more uncertain in determining whether they truly correspond to a steady emission level. The X-ray fluxes of these pixels might have reached the baseline level or may still be decreasing towards it. Figure 5.17 shows the EPIC-pn exposure maps compatible with steady emission (50%) for all the XMM-Newton spectra, excluding single-epoch pixels. In other words, exposed areas in Figure 5.17 in each observation/epoch represent pixels that have shown compatibility with steady emission in at least or greater than two epochs.

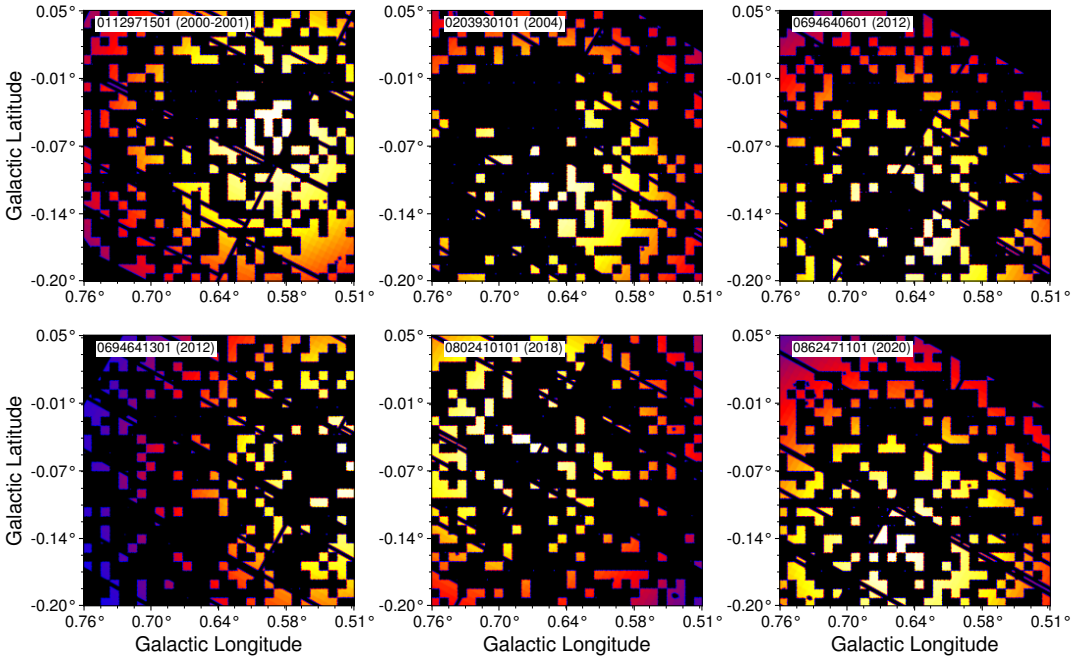

Figure 5.17: XMM-Newton EPIC-pn exposure maps compatible with steady emission (50%) for the observations listed in Table 2.4 (single-epoch pixels excluded).

We also analyzed the steady emission spectra (50% and 95% spectra) in scenarios where single-epoch pixels were both included and excluded for the three regions defined in Chapter 4: Sgr B, the Sgr B2 region, and the G0.66 region. The spectral parameters showed no significant difference based on the inclusion or exclusion of single-epoch pixels. Therefore, this section discusses only the case where single-epoch pixels were excluded.

5.3.1 The Phenomenology of the Sgr B Diffuse Emission

Figure 5.16 illustrates all the diffuse emission components in the Sgr B region, including emission from warm and hot plasma and non-thermal emission (lines and continuum) (see Chapter 1 for the discussion of diffuse emission components). It is crucial to include these components in our analysis in the absence of local background subtraction. To understand the influence of each emission component, we perform X-ray spectroscopy by fitting the obtained spectra with theoretical models. This process involves comparing the data with models that account for emission and absorption lines, continuum emission, and other spectral features from the region of interest. A model based purely on observed phenomena, without necessarily deriving from first principles, is referred to as a phenomenological model. These phenomenological models are constructed to fit observational data effectively and to describe empirical relationships between the observed spectra and the parameters of interest. A major advantage of a phenomenological model is its ability to directly evaluate and quantify specific features within the spectrum (such as the 6.4 keV line) without physical assumptions about the underlying processes. I use a phenomenological `XSPEC` model in `Sherpa` (Freeman et al. 2001) to directly evaluate the 6.4 keV line and other spectral information. This model describes the data from the diffuse Sgr B region and is given by:

$$f(E) = ABS \times (APEC_1 + APEC_2 + NONTHERMAL) + BKG_{\rm INST} \tag{5.1}$$

where,

$$NONTHERMAL = ABS \times PO + GA_{6.4} + GA_{7.06} \tag{5.2}$$

Model 5.1 contains a combination of simpler components to match the characteristics of the non-thermal diffuse emission from Sgr B. These characteristics include the power-law continuum (`pow` or PO) and the neutral Fe Kα (6.4 keV) and Kβ (7.06 keV) lines (`gauss` or PO and GA$_{7.06}$), modeled with an intrinsic absorption column density. Additionally, the model incorporates two thermal plasma (`apec`) emissions using the Astrophysical Plasma Emission Code (APEC). These `apec` components describe soft and hard diffuse X-ray emission. All model components are subject to foreground absorption (ABS). The model 5.1 is influenced by Zhang et al. (2015) and Rogers et al. (2022) with some modifications due to different background subtraction. For instance, both authors used the `wbabs` component in `XSPEC` to model absorption. However, in my study, I opted for the more detailed and updated cross-sections and elemental abundances provided by `tbabs` (ABS). Furthermore, Zhang et al. (2015) and Rogers et al. (2022) employed a single `apec` component after local background subtraction. In contrast, we use two `apec` components (APEC$_1$, APEC$_2$) (Muno et al. 2004a; Walls et al. 2016) to represent thermal emission from hot, ionized gas with instrumental background (BKG$_{INST}$) subtraction similar to Chuard et al. (2018). There are several instrumental background lines due to emission by materials in the vicinity of the detector, which are crucial to be individually resolved and measured. The EPIC-MOS instrument does not have significant instrumental lines in the 2-10 keV band. Unfortunately, the EPIC-pn requires modeling for five lines at $E \sim 7.11$ keV, $E \sim 7.49$ keV, $E \sim 8.05$ keV, $E \sim 8.62$ keV, and $E \sim 8.90$ keV. In my model, five `Sherpa` Gaussian profiles are used to model these line effects. Finally, three constant factors were introduced for the three EPIC instruments (PN,M1,M2) to ensure normalization or cross-calibration between the instruments. The factor PN is fixed to 1, and the EPIC-MOS factors were fitted. The full 2-10 keV model for each instrument is given as follows.

$$\begin{aligned}
\text{EPIC-pn}: \quad & F(E) = PN \times (ABS \times APEC_1 + APEC_2 + ABS \times PO \\
& \quad + GA_{6.4} + GA_{7.06}) + GA_{7.11} + GA_{7.49} + GA_{8.05} + GA_{8.62} + GA_{8.90} \\
\text{EPIC-MOS1}: \quad & F(E) = M1 \times (ABS \times (APEC_1 + APEC_2 + ABS \times PO + GA_{6.4} + GA_{7.06})) \\
\text{EPIC-MOS2}: \quad & F(E) = M2 \times (ABS \times (APEC_1 + APEC_2 + ABS \times PO + GA_{6.4} + GA_{7.06}))
\end{aligned} \tag{5.3}$$

I fitted the phenomenological model 5.1 to the full Sgr B spectra in the 2.0-10.0 keV band. The energies of the Gaussian lines were set to 6.40 and 7.06 keV, while the line widths were maintained at 10 eV. The normalization ratio of Kα/Kβ was constrained to 12% (Ryu et al. 2009). Both the APEC plasma temperatures and the metallicity parameters were fixed. The warm plasma (APEC) temperature was set to 1 keV (Kaneda et al. 1997; Bamba et al. 2002). The hot plasma temperature was set to 6.5 keV (Koyama et al. 2007b). The metallicities for both APEC models were fixed at $Z/Z_\odot = 2$ (Terrier et al. 2010). The APEC normalization parameters were fitted accordingly. The intrinsic and foreground hydrogen column densities, $N_H(i)$ and $N_H(f)$, in the `tbabs` model were also fitted. The spectral index for the `po` component was taken as $\Gamma = 2$ (Zhang et al. 2015; Terrier et al. 2010). The spectral fit and the residuals are shown in the left panel of Figure 5.18. However, this fit yielded a value $(\chi^2/\text{dof}) \geq 2$. Potential reasons for these results are discussed in the following sections.

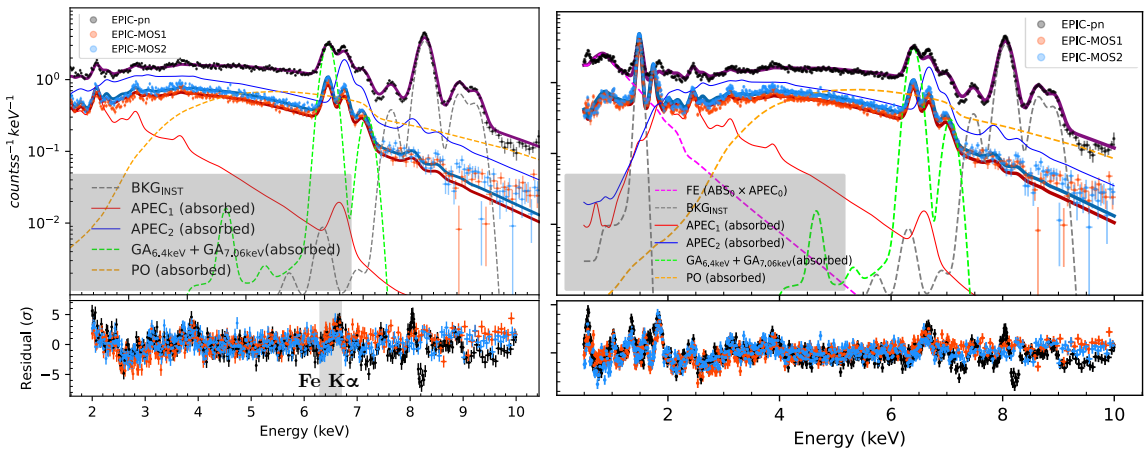

Figure 5.18: Spectral fit and residuals for the XMM-Newton 2.0-10.0 keV merged full spectra in Sgr B (*left*). The spectra were fitted using the $\texttt{ABS} \times (APEC_1 + APEC_2 + \texttt{ABS} \times \texttt{PO} + \texttt{GA}_{6.4} + \texttt{GA}_{7.06}) + BKG_{\texttt{INST}}$ model in `Sherpa`. Spectral fit and residuals for the XMM-Newton 0.5-10.0 keV merged full spectra in Sgr B, including Fe emission below ≤ 2 keV (*right*). The spectra were fitted using the $\texttt{ABS} \times \texttt{APEC}_0 + \texttt{ABS} \times (APEC_1 + APEC_2 + \texttt{ABS} \times \texttt{PO} + \texttt{GA}_{6.4} + \texttt{GA}_{7.06}) + BKG_{\texttt{INST}}$ model in `Sherpa`. The model components are also present. The absorbed hot and warm plasma is shown in red and blue solid lines ($APEC_1$ and $APEC_2$). The instrument line is shown in $BKG_{\rm INST}$ gray, and the absorbed non-thermal lines are in light green. Finally, the absorbed power law is present in orange.

It is also evident from the spectral fit in Fig. 5.18 (left) that the deep XMM-Newton spectra suffer from foreground emission (FE) below ≤ 2 keV (Ryu et al. 2009, 2013) (see residuals).

5.3.2 Foreground Emission

As discussed in Chapter 1, I included the FE component in the broadband XMM-Newton spectra. An absorbed APEC model (ABS × APEC$_O$ in `Sherpa`) was used to fit the data between 0.5-2.0 keV. The full model between $0.5 - 10.0$ keV is given by:

$$f(E) = ABS \times APEC_0 + ABS \times (APEC_1 + APEC_2 + NONTHERMAL) + BKG_{\rm INST} \quad (5.4)$$

When considering the 0.5-10.0 keV spectra, additional background lines appear in both EPIC-pn and EPIC-MOS instruments. For EPIC-pn, the Al line at $E \sim 1.49$ keV is present, and for EPIC-MOS, the Al and Si lines are present at $E \sim 1.49$ keV and $E \sim 1.79$ keV, respectively. The $BKG_{\rm INST}$ component in model 5.4 considers these additional instrument lines (hence for the 0.5-10 keV spectra $BKG_{\rm INST}$ has 5 instrumental lines for EPIC-pn and 2 for EPIC-MOS).

The abundance of foreground plasma was fixed to $Z = 0.011$[7] All other fixed parameters were kept, as discussed in the previous section. The foreground plasma temperature, plasma normalization, and the foreground hydrogen column density were fitted. A fit with $(\chi^2/{\rm dof}) \geq 2$ was obtained. Given the complexity of the spectral model, which includes many physical parameters, it is impractical to fit the data with all parameters simultaneously. Therefore, I froze the best-fit plasma temperature $kT = 0.85 keV$ in further fits. The spectral fit and the residuals are shown in Figure 5.18 (right).

[7] Our best-fit values are consistent with these values (Ryu et al. 2009, 2013).

5.3.3 Comparison of Spectral Parameters

The technique for constraining steady emission based on pixel data influences spectral information. The 95% level spectrum provides deeper data compared to the 50% spectrum. However, transitioning from the 50% spectra to the 95% spectra may introduce variability signatures into our spectrum. Therefore, it is important to understand how spectral parameters are affected between the 50% and 95% levels. I fitted the phenomenological model to the 2.0-10.0 keV full Sgr B and subsequently to the 95% and 50% spectra. All individual spectra and the merged steady spectrum were fitted (see the previous section for fixed parameters). The normalization parameters of the `apec` and `pow` components for both individual and merged spectra were obtained. All normalization components of the individual fit were renormalized by their respective exposure coverage (i.e., the sum of the steady compatible regions in arcmin^{-2}). For the merged spectrum, these parameters were renormalized by the weighted average exposure area ($A_{\rm Merged}$), which is given by:

$$A_{\rm Merged} = \frac{\sum(\mathrm{EXP} \times \mathrm{Area})}{\sum \mathrm{EXP}} \tag{5.5}$$

Figure 5.19 illustrates the distribution of normalized spectral parameters for individual observations and the weighted average normalized spectral parameters for the merged spectrum. Uncertainties are given by the 1σ (68%) confidence level. Table 5.4 shows the weighted mean normalized spectral parameters from individual observations compared to those of the merged spectrum. The means are computed as follows:

$$\mathrm{Mean} = \frac{\sum_{i=1}^{n} w_i n_i}{\sum_{i=1}^{n} w_i} \tag{5.6}$$

$$\mathrm{Error} = \sqrt{\frac{1}{\sum_{i=1}^{n} w_i}} \tag{5.7}$$

Here, the weight $w_i = \frac{1}{\sigma_i^2}$, where n_i and σ_i represent the normalization and the 1σ uncertainty for the ith observation, respectively. The mean values of the individual parameters are also shown as box plots in Figure 5.19. When comparing the 50% and the 95% spectrum, the removal of pixels from the individual observations correlated with the 6.4 keV emission directly affects the Gaussian parameters for the 6.4 keV line, while the plasma components are minimally influenced.

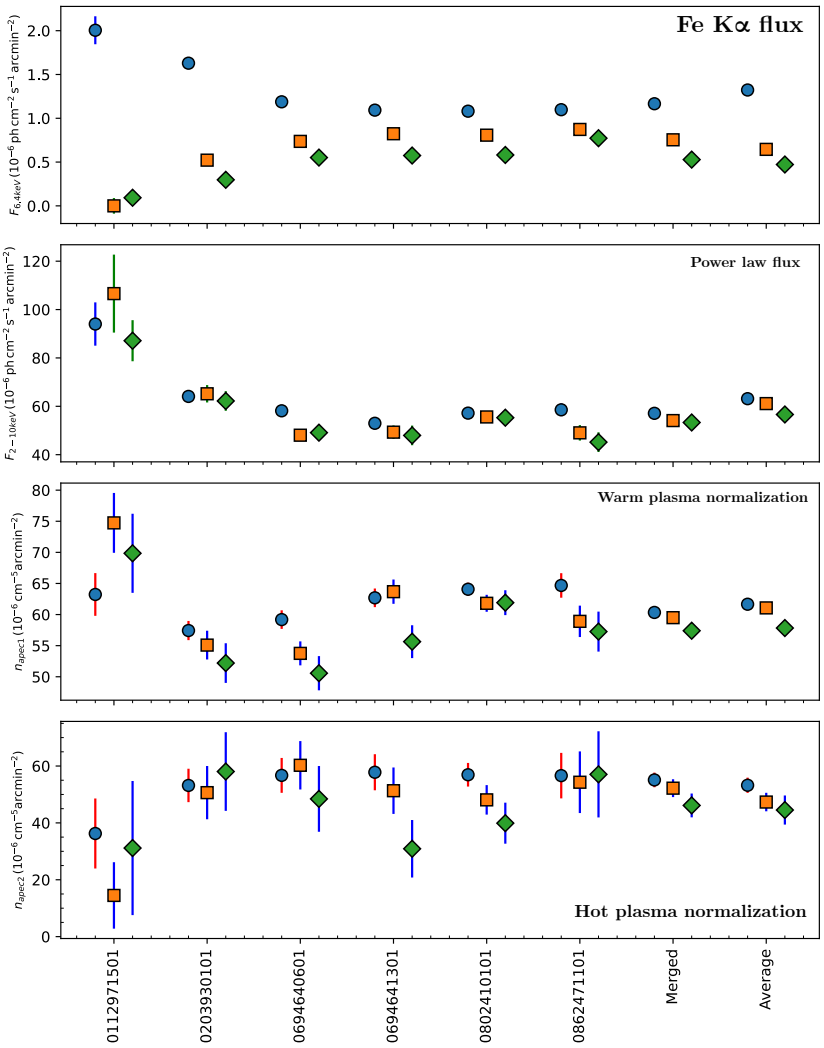

Figure 5.19: Comparison of spectral parameters for the 2-10 keV XMM-Newton/EPIC spectra of individual observations (Table 2.4) and the merged deep spectrum for (i) Sgr B region-Full, (ii) Sgr B-95% steady spectrum, and (iii) Sgr B-50% steady spectrum. Spectra were fitted using the phenomenological model and instrumental background lines (see text). All spectral parameters of individual observations are normalized to the exposure area, and the combined deep spectra are adjusted to a weighted exposure area (see text).

Table 5.4: Comparison of the best-fit normalization parameters for the merged spectrum and the weighted average of individual observations, using the phenomenological model $\texttt{ABS} \times (APEC_1 + APEC_2 + \texttt{ABS} \times \texttt{PO} + \texttt{GA}_{6.4} + \texttt{GA}_{7.06}) + BKG_{\texttt{INST}}$

Parameter	Unit	Sgr B		Sgr B (95%)		Sgr B (50%)	
		Mean	Merged	Mean	Merged	Mean	Merged
$n_{\rm apec1}$	$10^{-5}{\rm cm}^{-5}\,{\rm arcmin}^{-2}$	4.55 ± 0.19	4.52 ± 0.20	4.71 ± 0.26	4.92 ± 0.28	3.96 ± 0.29	4.16 ± 0.30
$n_{\rm apec2}$	$10^{-5}{\rm cm}^{-5}\,{\rm arcmin}^{-2}$	3.98 ± 0.04	3.83 ± 0.05	4.16 ± 0.06	4.08 ± 0.06	3.64 ± 0.06	3.67 ± 0.06
$n_{\rm pl}$	$10^{-5}{\rm cm}^{-5}\,{\rm arcmin}^{-2}$	5.73 ± 0.06	5.57 ± 0.42	5.84 ± 0.08	5.87 ± 0.09	5.27 ± 0.10	5.28 ± 0.01

As reported in Figure 5.19, the averaged plasma and power law normalization parameters of the individual spectra and the merged spectrum are well-matched in all three cases. This deviation from the uniform trend noticeable at epoch 2000 (OBSID: 0112971501) was primarily due to its low statistics.

5.3.4 Comparative Spectral Analysis

5.3.4.1 The Phenomenological Model

The steady emission is first compared with the phenomenological model. All the model components are explained in Section 5.3.1. The phenomenological model is given by:

$$f(E) = \mathrm{ABS} \times \mathrm{APEC}_0 + ABS \times (APEC_1 + APEC_2 + ABS \times PO + GA_{6.4} + GA_{7.06}) + BKG_{\mathrm{INST}} \quad (5.8)$$

The steady spectra were grouped to achieve a minimum signal-to-noise ratio (SNR) of 20 for Sgr B and 10 for Sgr B2 and G0.66 (this grouping will hold for the next models as well). The background-subtracted grouped spectra were then fitted with the model 5.8. All the frozen parameters for the model 5.8 are explained in the previous section. The 6.4 keV line, the `apec` ($APEC_0$, $APEC_1$, $APEC_2$) normalization parameters and power law normalization (`PO`) were fitted. The intrinsic and foreground hydrogen column densities, $N_H(i)$ and $N_H(f)$, in the `tbabs` model were also fitted. The best-fit model parameters are listed in Table 5.5. For the fitting, I used the `Sherpa` Monte Carlo optimization method (`moncar`) and obtained a fit for the 0.5-10.0 keV spectrum, including the foreground.

Table 5.5: Best-fit spectral parameters for the steady emission using the phenomenological model 5.8. The results are presented for three regions: Sgr B, Sgr B2, and G0.66, with the 50% steady spectra excluding *single-epoch pixels*.

Parameter	Unit	Sgr B	Sgr B2	G0.66
$N_H(o)$	10^{22} atoms cm^{-2}	0.16 ± 0.03	0.17 ± 0.03	0.25 ± 0.03
$N_H(f)$	10^{22} atoms cm^{-2}	$8.16^{+0.58}_{-0.56}$	6.75 ± 0.61	7.61 ± 0.61
$N_H(i)$	10^{22} atoms cm^{-2}	$54.95^{+5.50}_{-4.90}$	$31.51^{+2.51}_{-2.28}$	31.80 ± 2.45
n_{apec0}	10^{-5}cm^{-5} arcmin^{-2} [a]	0.95 ± 0.01	1.22 ± 0.10	$1.78^{+0.14}_{-0.13}$
n_{apec1}	10^{-5}cm^{-5} arcmin^{-2} [a]	$4.36^{+0.34}_{-0.33}$	$2.14^{+1.06}_{-0.93}$	$3.09^{+1.02}_{-0.87}$
n_{apec2}	10^{-5}cm^{-5} arcmin^{-2} [a]	5.24 ± 0.11	$6.94^{+0.43}_{-0.42}$	3.89 ± 0.37
$F_{\text{0.5-10 keV}}$	10^{-5} ph cm^{-2} s^{-1} arcmin^{-2} [b]	$5.51^{+0.14}_{-0.13}$	$9.79^{+0.88}_{-0.79}$	$7.82^{+0.41}_{-0.42}$
$F_{\text{6.4 keV}}$	10^{-7} ph cm^{-2} s^{-1} arcmin^{-2} [c]	5.13 ± 0.19	$10.33^{+1.11}_{-1.04}$	1.10 ± 0.07
$EW_{\mathrm{6.4keV}}$	keV	0.36 ± 0.02	0.35 ± 0.05	0.56 ± 0.05
Γ_{pl}	...	1^c	1^c	1^c
f_{pn}	...	1^c	1^c	1^c
f_{MOS1}	...	0.95 ± 0.01	1.10 ± 0.02	1.06 ± 0.02
f_{MOS2}	...	1.13 ± 0.01	1.10 ± 0.02	1.16 ± 0.02
χ^2 (d.o.f)	...	2.56(610)	1.71(235)	1.26(264)

[a] n $= \frac{10^{-14}}{4\pi[D_A(1+z)]^2} \int n_e n_H \, dV$ and D_A is the angular diameter distance to the source in cm, and $(1+z)$ accounts for the redshift of the source.

[b] Photon power law is given by $A(E) = KE^{-\alpha}$, where $n = K$.

[c] A simple Gaussian line profile is given by

$$A(E) = K \frac{1}{\sigma\sqrt{2\pi}} \exp\left(\frac{-(E-E_l)^2}{2\sigma^2}\right)$$

where K is the normalization, which is the total photons/cm^2/s in the line.

5.3.4.2 Sgr B

The phenomenological model failed to fit the 0.5-10.0 keV steady 50% spectra, yielding a poor χ^2/d.o.f ≥ 2. The poor quality is mainly driven by the low-energy residuals. I improved the fit by focusing on the 2.0-10.0 keV spectrum, which resulted in an improved χ^2/d.o.f $= 1.63/451$. One possible reason affecting the overall fit results is the complexity of both the model and the data coverage over a large area, making it challenging to obtain a good fit. Additionally, the higher quality (higher statistics) of the spectrum may contribute to the difficulty in achieving an accurate fit. However, the values for the foreground and intrinsic column densities showed consistency across all three subregions. Figure 5.20 illustrates the spectrum and the residual for the phenomenological model fit to the Sgr B region with and without the foreground emission component.

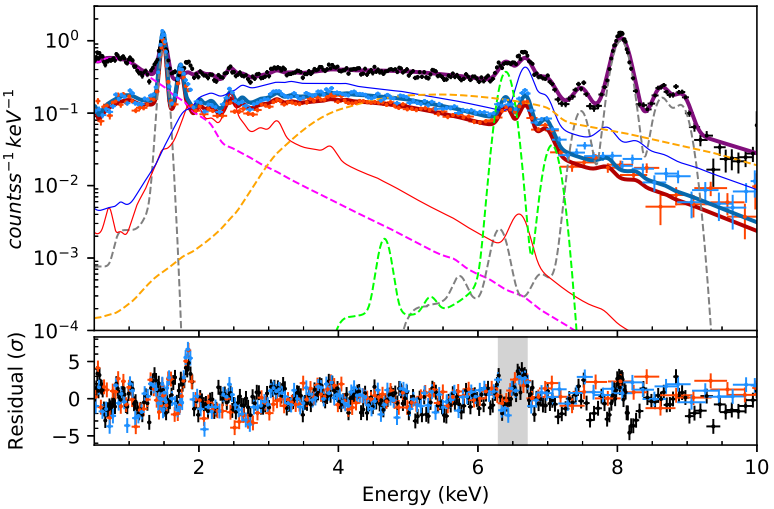

Figure 5.20: Spectral fit and residuals for the XMM-Newton 0.5-10.0 keV merged steady spectra (50%) in Sgr B with $\texttt{ABS} \times \texttt{APEC}_0 + \texttt{ABS} \times (APEC_1 + APEC_2 + \texttt{ABS} \times \texttt{PO} + \texttt{GA}_{6.4} + \texttt{GA}_{7.06}) + BKG_{\texttt{INST}}$ model in `Sherpa`.

5.3.4.3 Sgr B2

I obtained a fit with χ^2/d.o.f $= 1.71/236$ using the phenomenological model for the Sgr B2 region. The best-fit foreground column density (between observer and the GC), $N_{\rm H}(f) = (0.67 \pm 0.06) \times 10^{23}\,{\rm cm}^{-2}$, is fully compatible with the expected value of $0.7 \times 10^{23}\,{\rm cm}^{-2}$ towards the GC. The fitted intrinsic column density (can be seen as the cloud self-absorption), $N_{\rm H}(i) = 3.15^{+0.25}_{-0.28} \times 10^{23}\,{\rm cm}^{-2}$, was consistent with the best-fit value of $4.6^{+0.7}_{-0.6} \times 10^{23}\,{\rm cm}^{-2}$ found with XMM-Newton/NuSTAR (Rogers et al. 2022) within 90″ of the Sgr B2 core (using local background, i.e., a single APEC plasma model). Figure 5.21 illustrates the spectrum and the residuals for the phenomenological model fit to the Sgr B2 region. The 6.4 keV steady flux was obtained as $F_{6.4\ {\rm keV}} = 1.03^{+0.11}_{-0.10} \times 10^{-6}\,{\rm ph\,cm^{-2}\,s^{-1}\,arcmin^{-2}}$ over a weighted average area of 4.6 arcmin^2. The 6.4 keV flux from a recent XMM-Newton study for this region Rogers et al. (2022) was $(6.7 \pm 0.80) \times 10^{-6}\,{\rm ph\,cm^{-2}\,s^{-1}\,arcmin^{-2}}$ over a 90 arcsec^2 region (i.e., 7.06 arcmin^2).

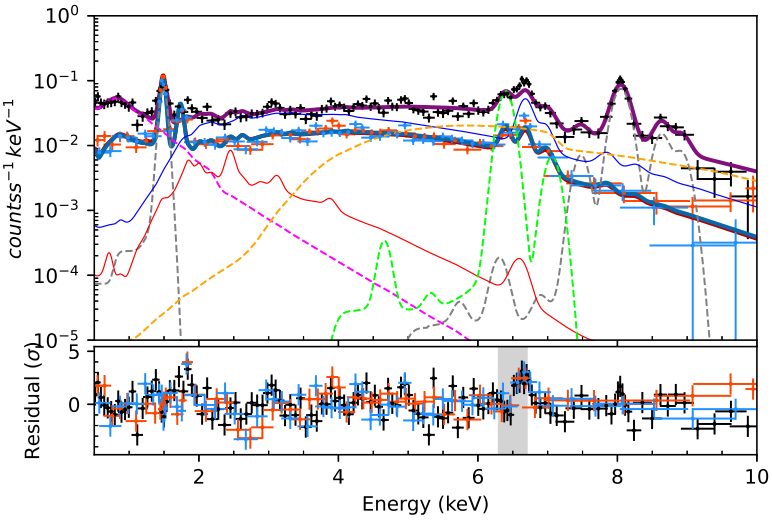

Figure 5.21: Spectral fit and residuals for the XMM-Newton 0.5-10.0 keV merged steady spectra (50%) in Sgr B2 with $\texttt{ABS} \times \texttt{APEC}_0 + \texttt{ABS} \times (APEC_1 + APEC_2 + \texttt{ABS} \times \texttt{PO} + \texttt{GA}_{6.4} + \texttt{GA}_{7.06}) + BKG_{\texttt{INST}}$ model in `Sherpa`.

5.3.4.4 G0.66

The region G0.66 was fitted with a satisfactory fit, yielding χ^2/d.o.f. = 1.26/264. The foreground emission $N_{\rm H}(f) = (0.76 \pm 0.06) \times 10^{23}\,{\rm cm}^{-2}$ is consistent with the GC value. The intrinsic column density of the cloud, $N_{\rm H}(i) = (3.18 \pm 0.24) \times 10^{23}\,{\rm cm}^{-2}$, is on the lower side compared to the values obtained for Sgr B2. The 6.4 keV steady flux was obtained as $(1.10 \pm 0.07) \times 10^{-7}\,{\rm ph\,cm^{-2}\,s^{-1}\,arcmin^{-2}}$ with an equivalent width (EW) of 0.56 ± 0.05 keV. The EW is lower than typical values reported for the variable emission in Sgr B2 (Nobukawa et al. 2011) or other molecular clouds (Ponti et al. 2010). Figure 5.22 illustrates the spectrum and the residuals for the phenomenological model fit to the G0.66 region.

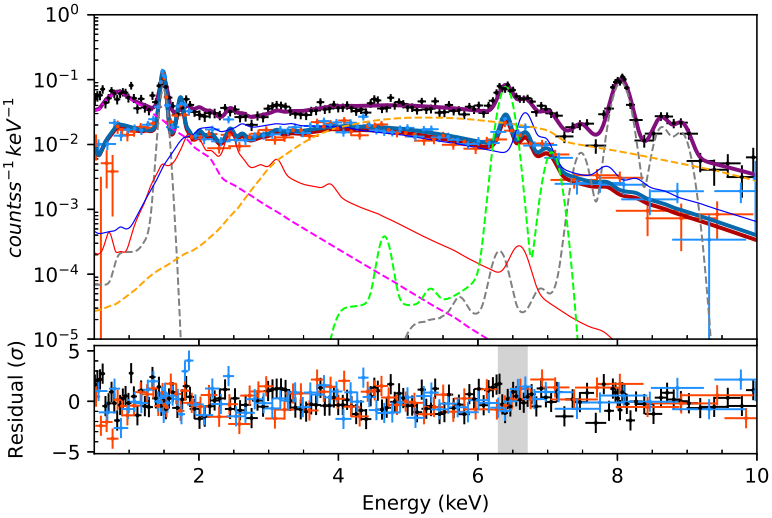

Figure 5.22: Spectral fit and residuals for the XMM-Newton 0.5-10.0 keV merged steady spectra (50%) in G0.66 with $\texttt{ABS} \times \texttt{APEC}_0 + \texttt{ABS} \times (APEC_1 + APEC_2 + \texttt{ABS} \times \texttt{PO} + \texttt{GA}_{6.4} + \texttt{GA}_{7.06}) + BKG_{\texttt{INST}}$ model in `Sherpa`.

5.3.5 Physically Motivated Models

Although the phenomenological model describes the spectrum of the steady emission, it does not provide information on the true nature of the emission and the underlying physical processes. Physically motivated models attempt to describe the fundamental mechanisms underlying a phenomenon, whereas phenomenological models do not necessarily explain the 'why' behind the observations. Instead, they focus on what happens and how it can be described mathematically. In this section, we analyze two important physically motivated models to interpret the observed diffuse steady non-thermal emission.

5.3.5.1 The X-ray Reflection Nebula (XRN) Model

Several physical models of the XRN scenario have been used in the literature, such as `MyTorus` (Zhang et al. 2015) and `pexrav` (Ponti et al. 2010). However, these models do not adequately account for the reflection geometry, which significantly influences the reflection spectrum. The `Monte Carlo` model developed by Walls et al. (2016) (hereafter referred to as the `XRN` model) addresses this issue by incorporating the XRN geometry defined by the line of sight (l.o.s) angle θ.

For this study, I used the `XRN` spectral model developed by Chuard et al. (2018) (following the same method as presented in Walls et al. (2016)) to account for the geometry of the XRN and to determine whether a single cloud could explain the signal we are detecting. The face-on schematic of this single cloud model is shown in Figure 5.23. This model has been designed to take the geometry (defined by the line of sight positions) of the reflection, which has a major influence on the flux and spectral shape of the cloud emission, into account (Walls et al. 2016; Chuard et al. 2018). The geometry is parameterized in the model by the angle θ between the cloud, the illuminating source, and the observer (see Figure 5.23).

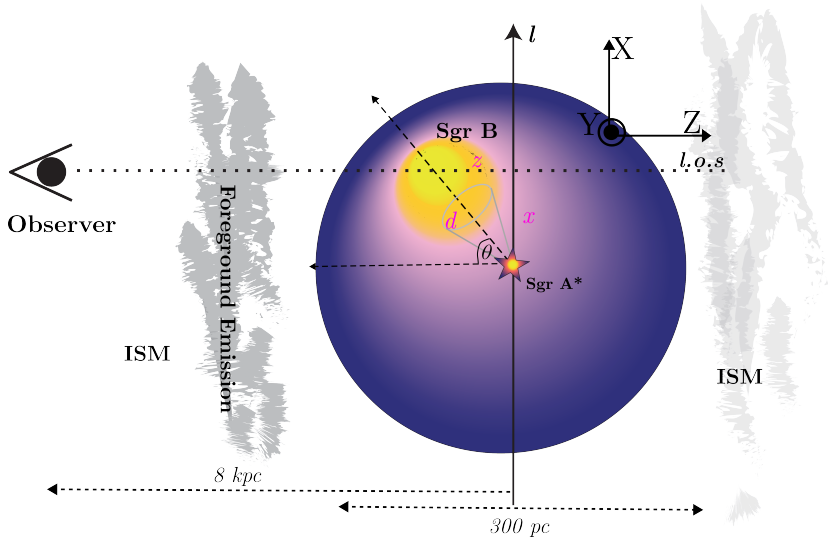

Figure 5.23: Schematic representation of the line of sight (l.o.s) from the observer to the GC, illustrating the positions of Sgr A*, Sgr B (or the cloud of interest), and the ISM. The FE affects observations of the GC cloud region. The diagram includes distance scales of approximately 8 kpc from the observer to the GC. The coordinate system (X, Y, Z) corresponds to the l, b coordinates and the l.o.s. The l.o.s. Angle θ indicates the spatial orientation and observational geometry. This is a face-on view, showing how these elements are aligned along the line of sight. This schematic is based on Ryu et al. (2009).

The external source is assumed to have a power-law spectrum (characterized by photon index

Γ_{XRN}). The photons' movement within the cloud and all of their interactions are simulated using Monte Carlo methods. The output spectrum is constructed from photons escaping the cloud in the direction of the observer. Within the cloud, the photons may be absorbed, Rayleigh scattered, or Compton scattered. They also undergo fluorescence interactions with the K-shell electrons of iron, resulting in the Fe Kα 6.4 keV emission. The full model is given by:

$$f(E) = \mathrm{ABS} \times \mathrm{APEC}_0 + ABS \times (APEC_1 + APEC_2 + ABS \times XRN) + BKG_{\mathrm{INST}} \tag{5.9}$$

The model 5.9 relies on intrinsic cloud absorption and the angle θ. The total continuum flux at low energies notably increases with θ because photons only superficially penetrate the cloud before being scattered toward the observer. Consequently, the scattered photons are more likely to be absorbed in the low-angle case than in the high-angle case. Figure 5.24 (right panel) shows the reflected spectra for different line-of-sight angles. The θ and the cloud column density also affect the strength of the Fe Kα line and the depth of the iron edge (Walls et al. 2016).

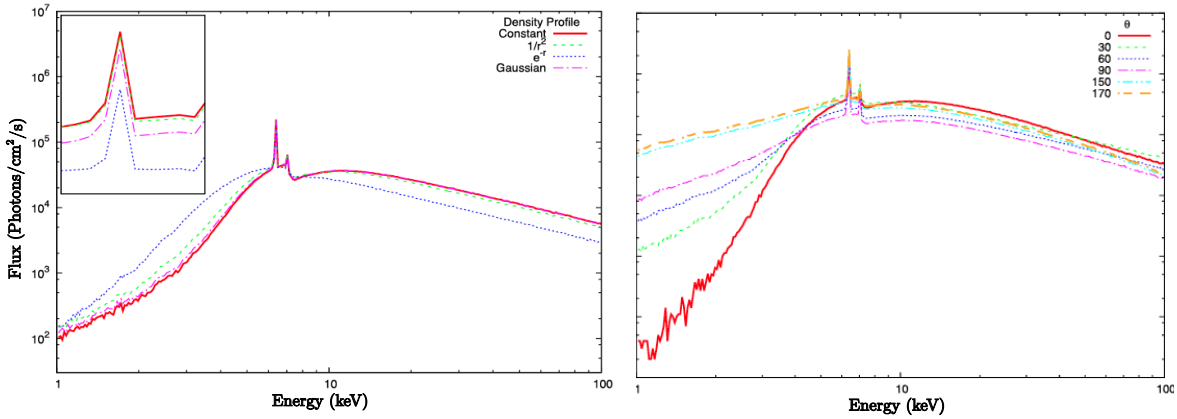

Figure 5.24: MC simulations for the four density profiles for a sphere of constant mass with $\theta = 30°$ (*left*). Spectra produced by the MC code for a 2 pc diameter, uniform density sphere with an N_H of $6 \times 10^{23}\,\mathrm{cm}^{-2}$ and a photon index of 2.0, showing the changes in flux and continuum shape resulting from a changing θ (right). Figure from Walls et al. (2016).

There are several versions of the `MC` model with varying cloud metallicities and density profiles. Figure 5.24 (left panel) shows the simulated spectra for different density profiles (Walls et al. 2016). According to Figure 5.24, the differences between density profiles are negligible, except for the exponential density profile. For our study, I chose the uniform cloud density profile with $Z = Z_{\odot}$.

I have fitted the 50% steady spectra for Sgr B, Sgr B2, and G0.66 with model 5.9. The fit parameters, spectrum, and residuals are discussed in the next sections. Table 5.6 shows the fit results of model 5.9 for Sgr B2 and G0.66.

Table 5.6: Best-fit spectral parameters for deep XMM-Newton observations of diffuse steady emission using the XRN model `ABS` × `APEC`$_0$ + `ABS` × ($APEC_1$ + $APEC_2$ + `ABS` × `XRN`) + $BKG_{\texttt{INST}}$ model in `Sherpa`. The fit result shows two sub-regions: Sgr B2 and G0.66. Analyses were performed excluding *single-epoch pixels*.

Parameter	Unit	Sgr B2	G0.66
$N_H(f)$	10^{22} atoms cm^{-2}	$8.26^{+0.56}_{-0.55}$	$7.68^{+6.46}_{-4.77}$
$N_H(i)$	10^{22} atoms cm^{-2}	$47.65^{+22.80}_{-14.91}$	$5.79^{+1.03}_{-0.70}$
$N_H(o)$	10^{22} atoms cm^{-2}	0.16 ± 0.02	$0.17^{+0.19}_{-0.00}$
$F_{\rm apec0}$	10^{-5} cm^{-5} arcmin^{-2}	$1.23^{+0.10}_{-0.09}$	1.41 ± 0.04
$F_{\rm apec1}$	10^{-5} cm^{-5} arcmin^{-2}	$2.14^{+2.13}_{-0.95}$	$2.26^{+2.23}_{-1.58}$
$F_{\rm apec2}$	10^{-5} cm^{-5} arcmin^{-2}	7.07 ± 0.40	$3.51^{+0.84}_{-7.26}$
Z/Z_o(apec2)	...	2^c	2^c
N_H(cloud)	10^{22} atoms cm^{-2}	< 47.10	$36.60^{+16.30}_{-16.60}$
$\theta_{\rm XRN}$	...	$28^{\circ c}$	$32.19^{+86.66}_{-92.80}$
$N_{\rm XRN}$	...	$0.79^{+16.88}_{-0.41}$	$0.36^{+0.04}_{-0.05}$
$f_{\rm pn}$	...	1^c	1^c
$f_{\rm MOS1}$	...	0.91 ± 0.02	1.06 ± 0.02
$f_{\rm MOS2}$	...	1.10 ± 0.02	1.16 ± 0.02
χ^2 (d.o.f)	...	1.67(235)	1.29(261)

[a] c = frozen values

5.3.5.2 Sgr B

The 50% steady spectra for the larger Sgr B was not successful (χ^2/d.o.f ≥ 2). The primary cause of its failure could be attributed to Sgr B's larger size, which makes it challenging to assume a coherent structure along the line of sight.

5.3.5.3 Sgr B2

The XRN model for Sgr B2 was tested in three cases: (a) all the XRN parameters were set to free, (b) the XRN column density was frozen, and (c) the model angle was frozen. The frozen values were obtained from the 2018 XMM-Newton/NuSTAR fits of Sgr B2 (Rogers et al. 2022). The spectral fits and residuals for all the cases are presented in Figure 5.25.

- **Case (a):** When all the XRN parameters were free, the 50% steady spectra for the Sgr B2 region yielded an unsatisfactory fit with χ^2/d.o.f. = 1.79/236. The best fit was at $\theta > 69.02^{\circ}$, with only the lower bound being constrained by the fit. This marginal value suggests a back-illuminated cloud. For comparison, Rogers et al. (2022) reported $\theta = 28^{+10}_{-16}$. The foreground column density was obtained as $N_H(f) = 8.55^{+0.20}_{-0.20} \times 10^{22}$ cm^{-2}, whereas Rogers et al. (2022) reported $N_H(f) = 0.9^{+0.10}_{-0.20} \times 10^{23}$ cm^{-2}. The intrinsic column density was $N_H(i) = 1.86^{+0.34}_{-0.34} \times 10^{23}$ cm^{-2} (intrinsic absorption for the XRN), which was lower than the corresponding value from the 2018 fit, possibly because Rogers et al. (2022) had only one absorption component. The XRN spectral index and the cloud absorption (N_H(cloud)) could not be constrained by the fit. The higher face value ($\sim 10^{25}$ cm^{-2}) suggested a high intrinsic column density. See Figure 5.25 panel (a) for the residuals of the Case (a) fit.

- **Case (b):** Fixing N_H(cloud) = 7.9×10^{24} cm^{-2} as per Rogers et al. (2022) resulted in χ^2/d.o.f. = 1.71/235, and the cloud angle was obtained as $\theta_{\rm XRN} > 20.64^{\circ}$, with only the lower bound of the angle being constrained. The angle $\theta_{\rm XRN}$ is consistent with Rogers et al. (2022). The XRN model is heavily angle-dependent. The model distribution for different angle profiles is shown in Figure 5.24. The normalization of the model was $N_{XRN} = 0.18^{+0.02}_{-0.01}$. The foreground column density

$N_H(f) = 0.85^{-0.05}_{+0.05} \times 10^{23}\,\mathrm{cm}^{-2}$ was consistent with Rogers et al. (2022); Zhang et al. (2015). However, the fitted intrinsic column density $N_H(i) = 0.61^{-0.27}_{+0.27} \times 10^{23}\,\mathrm{cm}^{-2}$ is significantly lower than previous values. See Figure 5.25 panel (b) for the residuals of the Case (b) fit.

- **Case (c):** Fixing $\theta_{\mathrm{XRN}} = 28^{\circ}$ as per Rogers et al. (2022) gave the most satisfactory fit out of all three cases with $\chi^2/\mathrm{d.o.f.} = 1.67/235$, and the cloud column density was obtained as $N_H(\mathrm{cloud}) < 4.71 \times 10^{23}\,\mathrm{cm}^{-2}$, with only the upper bound being constrained. The normalization was $n = 0.79^{+16.88}_{-0.41}$. Figure 5.25 top panel shows the data and the model component for this fit, and panel (c) shows the residuals of the XRN model for this case. Table 5.6 shows fit results for case (c). The fitted column densities of $N_H(i) = 4.76^{-1.49}_{+2.28} \times 10^{23}\,\mathrm{cm}^{-2}$ and $N_H(f) = 0.82^{-0.05}_{+0.05} \times 10^{22}\,\mathrm{cm}^{-2}$ are consistent with Rogers et al. (2022); Zhang et al. (2015) ($N_H(f) = 0.9^{+0.1}_{-0.2} \times 10^{23}\,\mathrm{cm}^{-2}$ and $N_H(i) = 7.9^{+3.7}_{-2.1} \times 10^{23}\,\mathrm{cm}^{-2}$ for Rogers et al. (2022), respectively).

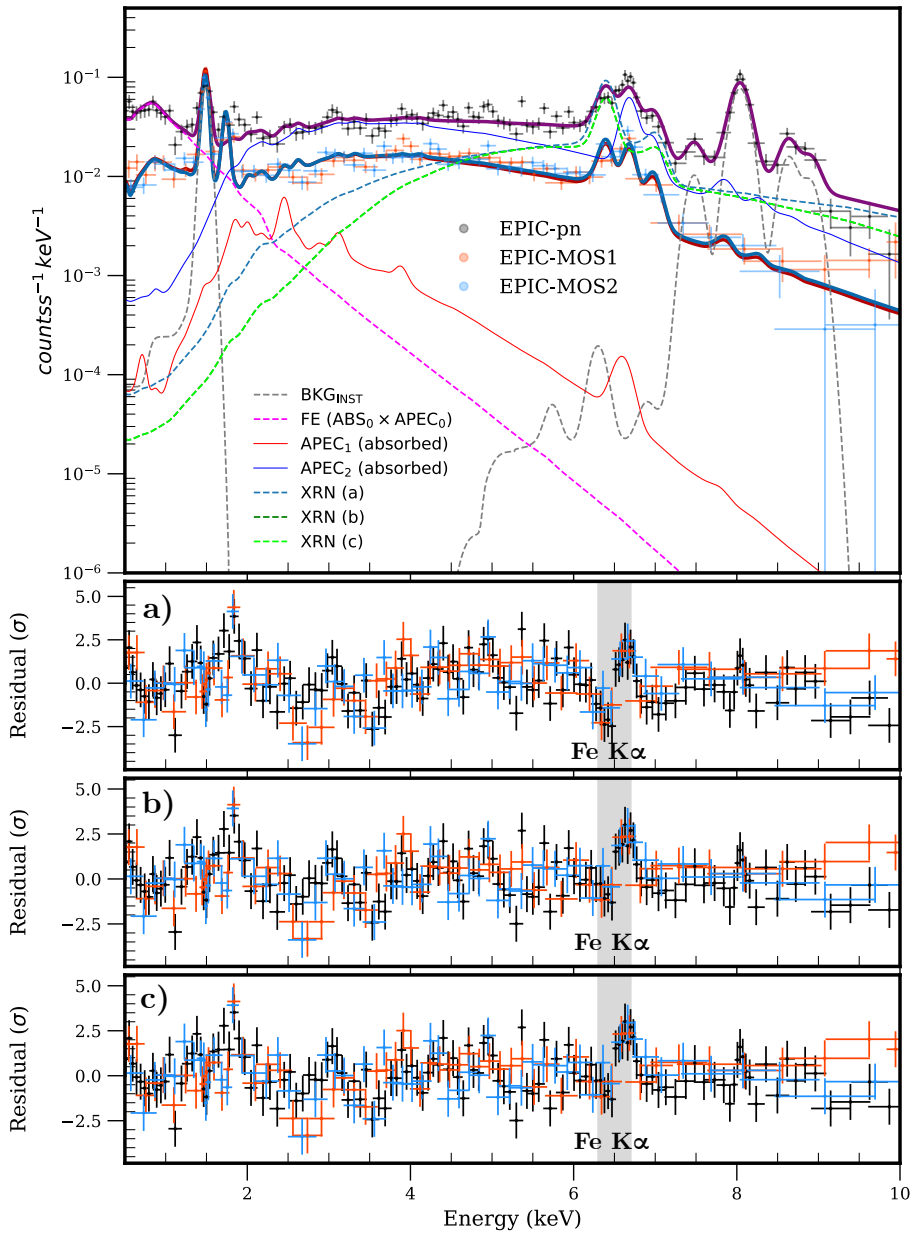

Figure 5.25: Spectral fit and residuals for the XMM-Newton 0.5-10.0 keV merged steady spectra (50%) in Sgr B2. The spectra were fitted using the XRN model `ABS` × `APEC`$_0$ + `ABS` × ($APEC_1$ + $APEC_2$ + `ABS` × `XRN`) + $BKG_{\texttt{INST}}$ in `Sherpa`. Top panel: Best-fit spectrum for the XRN model. Panel (a) shows spectral residuals when all XRN parameters are free. Panel (b) shows fit residuals when the cloud N_H(cloud) is frozen to $N_H(\text{cloud}) = 7.9 \times 10^{24}\,\text{cm}^{-2}$ (Rogers et al. 2022). Panel (c) shows fit residuals when the cloud angle θ_{XRN} is frozen to 28° (Rogers et al. 2022).

5.3.5.4 G0.66

The steady emission revealed the G0.66 cloud feature located in the southeast part of Sgr B2. Interestingly, G0.66 was as bright as Sgr B2 in the steady emission. The XRN model provided a satisfactory fit with χ^2/d.o.f. = 1.29/261 for the G0.66 region. The fitted cloud density was $N_H(\text{cloud}) = 3.66^{+0.54}_{-0.48} \times 10^{23}\,\text{cm}^{-2}$, consistent with the FPMA and FPMB NuSTAR data for G0.660.13 from Zhang et al. (2015). They obtained the intrinsic column density using the `MYTorus` model as $N_H(i) = 3.0^{-1.9}_{+3.8} \times 10^{23}\,\text{cm}^{-2}$. The fitted foreground column density of $N_H(f) = 7.68^{-4.77}_{+6.46} \times 10^{22}\,\text{cm}^{-2}$ is also consistent with $N_H(f) = 8.2^{-4.5}_{+4.3} \times 10^{22}\,\text{cm}^{-2}$ reported by Zhang et al. (2015). The relative position is obtained as $\theta = 32.19^{+4.62}_{-5.32}$ degrees, consistent with the Sgr B2 cloud position (Rogers et al. 2022). This suggests that Sgr B2 and G0.66-0.13 have relatively close cloud positions. Zhang et al. (2015) stated that Sgr B2 and G0.660.13 are about 100 pc away from Sgr A*. The XRN angle θ_{XRN} confirms their findings.

If G0.66 was illuminated by the same outburst from Sgr A* that illuminated Sgr B2, then G0.66 must be located further away along the line of sight. Hence, the distance from Sgr A* to G0.66 is given by:

$$z = \frac{-100\,\text{pc}}{\tan\theta} \tag{5.10}$$

$$= \frac{-100\,\text{pc}}{\tan(32.19^{\circ}{}^{+4.62^{\circ}}_{-5.32^{\circ}})} \tag{5.11}$$

$$= 158.86^{+38.51}_{-25.23}\,\text{pc} \tag{5.12}$$

Where z is the perpendicular distance from the Sgr A* plane to the cloud plane. The negative sign indicates the cloud is in front of Sgr A* with the reference coordinate system. The x is the projected distance from Sgr A* to the line of sight (l.o.s). G0.66 is $100pc$ away from Sgr A*. Hence, the true distance between the cloud and the Sgr A* is,

$$d = \sqrt{z^2 + x^2} = \sqrt{(158.86^{+38.51}_{-25.23})^2 + 100^2}\,\text{pc} \tag{5.13}$$

$$d = 187.71^{+33.55}_{-20.81}\,\text{pc} \tag{5.14}$$

Table 5.6 shows fit results for G0.66 with the XRN model, and Figure 5.26 shows the spectrum, model component, and residual for the fit.

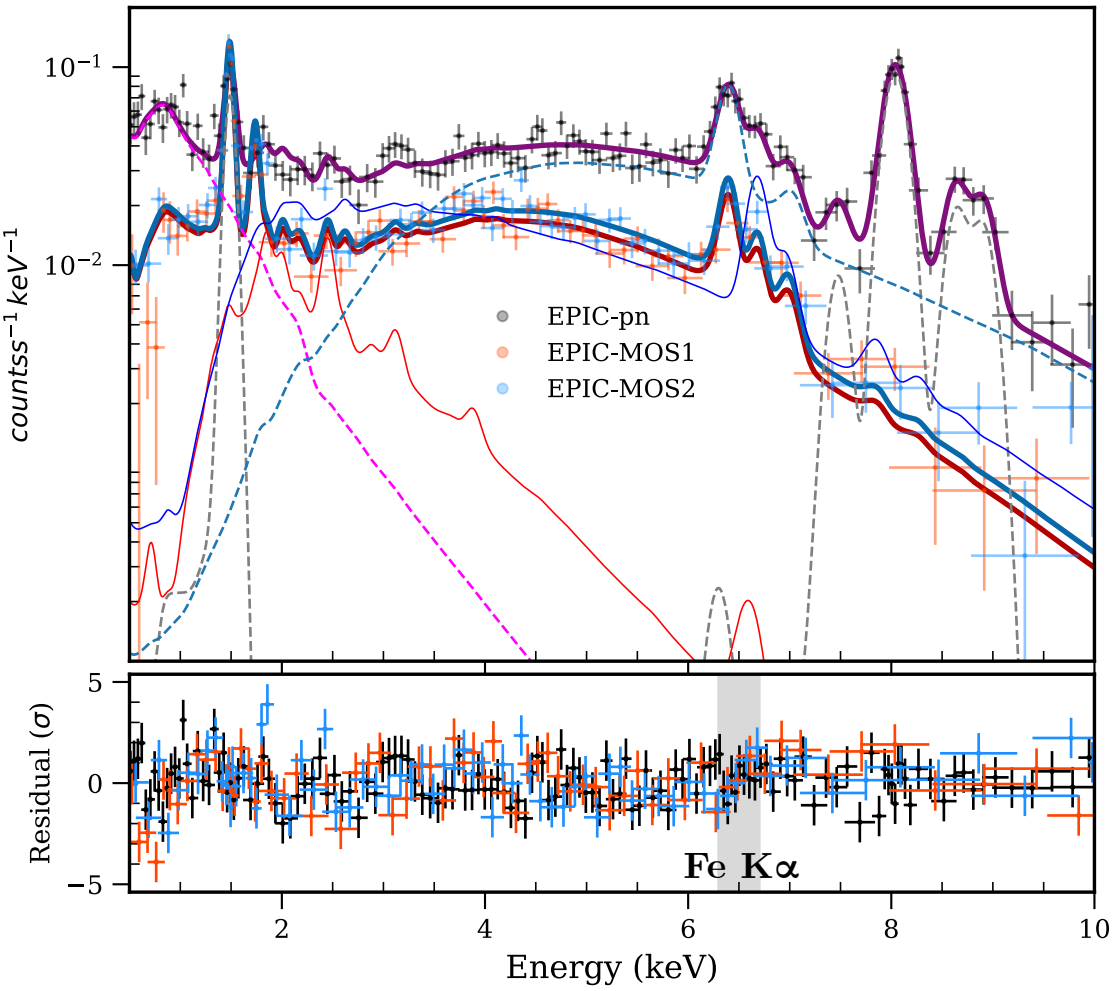

Figure 5.26: Spectral fit and residuals for the XMM-Newton 0.5-10.0 keV merged steady spectra (50%) in G0.66. The spectra were fitted using the XRN model `ABS` × $\texttt{APEC}_0$ + `ABS` × ($APEC_1$ + $APEC_2$ + `ABS` × `XRN`) + $BKG_{\texttt{INST}}$ in `Sherpa`.

5.3.6 Low-energy Cosmic Ray Model

Another possible origin for the observed steady non-thermal emission is the interaction between low-energy cosmic ray ions and a neutral ambient medium in the GC. These X-rays can result from atomic collisions until the ions either stop or escape from the cloud. Tatischeff et al. (2012) investigated the production of non-thermal X-rays through interactions between low-energy cosmic ray electrons and ions with a neutral ambient medium. They used a steady-state slab model, in which accelerated particles penetrate a cloud of neutral gas at a constant rate (see Chapter 1). This model is referred to as `LECRp/e` hereafter (`e` for electrons, `p` for protons).

Zhang et al. (2015) suggested that the Fe Kα emission of the 90″ Sgr B2 region, having reached its constant level in 2013, indicates that LECRp may be a major contributor. This suggestion arises from the unphysically large metallicity $Z/Z_{\odot} = 4.0^{+2.0}_{-0.6}$ and very low electron energy when fitted with electron models. Based on this previous work, we have also rejected the LECRe hypothesis (see also Kuznetsova et al. (2022)) and examined the contribution from CR protons to the steady Fe Kα emission. Hence, the full model that describes the diffuse steady X-ray emission is given by:

$$f(E) = \text{ABS} \times \text{APEC}_0 + \text{ABS} \times (APEC_1 + APEC_2 + \text{ABS} \times \text{LECRp}) + BKG_{\text{INST}} \quad (5.15)$$

The foreground emission, intrinsic absorptions, and plasma components are the same as in the previous two models. According to the `LECRp` model, Sgr B is bombarded by cosmic rays (CRs) from an external source whose spectrum follows a power law with index Γ_{LECRp}. The remaining model parameters, including the path length Λ of CRs in the X-ray production (nonthermal) region of the cloud, the minimum energy E_{min} for a CR to enter the X-ray production region of the cloud, and the metallicity Z, are properties of the molecular cloud (MC). The normalization N_{LECR} describes the injected power of the cosmic rays from E_{min} to 1 GeV, with the power $P_{\text{LECR}} = 4\pi D^2 N_{\text{LECR}}$ from a surface, given distance D to the cloud (see Chapter 1 for more information). For all cases, allowing all the LECRp parameters (Γ_{LECRp}, Λ, E_{min}, and N_{LECRp}) to vary in the fit resulted in an unphysical scenario, with the best-fit Fe abundance being $Z/Z_\odot < 1$, inconsistent with the expected value of $1-2Z_\odot$. Furthermore, we could not constrain the path length Λ. To improve the fit, we fixed $\Lambda = 5 \times 10^{24}$ H-atoms cm^{-2}, a value appropriate for non-relativistic particles propagating in massive molecular clouds in the GC (Tatischeff et al. 2012). The metallicity was fixed at $Z/Z_\odot = 1$. For a hard CR spectrum, the X-ray emission produced by CR protons depends weakly on the minimum ion energy E_{min}. We fixed $E_{\text{min}} = 10^4$ KeV nucleon^{-1}, the value used by Zhang et al. (2015).

The best-fit parameters for the model 5.15 for the Sgr B2 and G0.66 are presented in Table 5.7.

Table 5.7: Best-fit spectral parameters for deep XMM-Newton observations of steady emission in Sgr B2 and G0.66, using the LECRp model $\texttt{ABS}\times\texttt{APEC}_0+\texttt{ABS}\times(APEC_1+APEC_2+\texttt{ABS}\times\texttt{LECRp})+BKG_{\texttt{INST}}$ model in `Sherpa`. The fit results show two subregions: Sgr B2 and G0.66. Analyses were performed excluding *single-epoch pixels*.

Parameter	Unit	Sgr B2	G0.66
$N_H(f)$	10^{22} cm^{-2}	$8.62^{+0.60}_{-0.81}$	$6.50^{+0.70}_{-0.66}$
$N_H(i)$	10^{22} cm^{-2}	$43.06^{+6.72}_{-7.04}$	$21.88^{+3.46}_{-2.40}$
$N_H(o)$	10^{22} cm^{-2}	0.17 ± 0.03	0.25 ± 0.03
F_{apec0}	10^{-5} cm^{-5} arcmin^{-2}	1.26 ± 0.10	1.76 ± 0.14
F_{apec1}	10^{-5} cm^{-5} arcmin^{-2}	$2.18^{+1.14}_{-0.98}$	$2.77^{+0.95}_{-0.81}$
F_{apec2}	10^{-5} cm^{-5} arcmin^{-2}	$7.44^{+0.49}_{-0.73}$	$3.65^{+0.47}_{-0.44}$
Λ	10^{24} H atoms cm^{-2}	5^c	5^c
Γ_{LECRp}	...	$1.84^{+0.54}$	$1.68^{+0.50}_{-0.52}$
E_{min}	keV	10^4	$10^{4\,c}$
N_{LECRp}	10^{-8} erg cm^{-2} s^{-1}	$2.13^{+2.19}_{-1.53}$	$1.84^{+1.75}_{-1.16}$
$Z/Z_\odot$(cloud)	...	1^c	1^c
f_{pn}	...	1^c	1^c
f_{MOS1}	...	$1.10^{+0.02}_{-0.02}$	$1.09^{+0.01}_{-0.01}$
f_{MOS2}	...	$1.10^{+0.02}_{-0.02}$	$1.12^{+0.01}_{-0.01}$
χ^2 (d.o.f)	...	1.78(235)	1.26(264)

[a] [c] Frozen values

5.3.6.1 Sgr B2

For a fixed $E_{\text{min}} = 10^4$ keV nucleon^{-1}, we obtained a fit with χ^2/d.o.f. = 1.77/236. The fit parameters are given in Table 5.7, and the best-fit spectrum is shown in the top panel of Figure 5.27, while the residuals are shown in panel (a) of the same figure. The fitted foreground column density is $N_H(f) = 0.86^{-0.06}_{+0.07} \times 10^{23}$ cm^{-2} and the intrinsic column density is $N_H(i) = 4.30^{-0.70}_{+0.67} \times 10^{23}$ cm^{-2}. These values are in agreement with Rogers et al. (2022) ($N_H(i) = 3.7 \pm 0.7 \times 10^{23}$ cm^{-2} and $N_H(f) = (1.0 \pm 0.1) \times 10^{23}$ cm^{-2}) and Zhang et al. (2015). The best-fit CR proton spectral index is $s \leq 2.32$

(with the lower limit unconstrained), which agrees with the CR proton spectral index derived using the LECRp model for the Sgr B2 region $s = 1.9^{+0.8}_{-0.7}$ by Zhang et al. (2015). Assuming that Sgr B2 is in the plane of Sgr A* at $D = 8.178\,\mathrm{kpc}$ (GRAVITY Collaboration et al. 2019), we estimated the power injected by the LECRp (10 MeV – 1 GeV) in the Sgr B2 region using:

$$\frac{dW}{dt} = 4\pi D^2 N_{\mathrm{LECRp}} \tag{5.16}$$

For Sgr B2, $\frac{dW}{dt} = 0.17^{+0.17}_{-0.13} \times 10^{39}\,\mathrm{erg/s}$. The 10 MeV – 1 GeV $\frac{dW}{dt}$ is consistent with the NuSTAR estimation by Zhang et al. (2015) ($\frac{dW}{dt} = (1.0 \pm 0.3) \times 10^{39}\,\mathrm{erg/s}$), but is approximately 10 times lower than the fit parameters of Kuznetsova et al. (2022) ($\sim 10^{40}\,\mathrm{erg/s}$). The power injected into the cloud by the CR protons depends on the minimum energy E_{min}. We have re-evaluated the fit for $E_{\mathrm{min}} = 1\,\mathrm{MeV}$ and $E_{\mathrm{min}} = 100\,\mathrm{MeV}$, and the residuals for these fits are shown in Figure 5.27 panels (b) and (c), respectively. The best-fit model normalizations are $N_{\mathrm{LECR}} = 1.53^{+2.83}_{-0.92} \times 10^{-7}\,\mathrm{erg\,cm^{-2}\,s^{-1}}$ and $N_{\mathrm{LECR}} = 0.3^{+0.7}_{-0.1} \times 10^{-7}\,\mathrm{erg\,cm^{-2}\,s^{-1}}$, respectively. The corresponding power injected by CR protons is $\frac{dW}{dt}_{E_{\mathrm{min}}=1\,\mathrm{MeV}} = 0.12^{+0.23}_{-0.07} \times 10^{39}\,\mathrm{erg/s}$ and $\frac{dW}{dt}_{E_{\mathrm{min}}=100\,\mathrm{MeV}} = 0.12^{+0.23}_{-0.07} \times 10^{39}\,\mathrm{erg/s}$.

5.3.6.2 G0.66

For a fixed $E_{\mathrm{min}} = 10^4\,\mathrm{keV\,nucleon^{-1}}$, I obtained a satisfactory fit with $\chi^2/\mathrm{d.o.f.} = 1.26/264$. The fit parameters are given in Table 5.7, and the best-fit spectrum is shown in the top panel of Figure 5.28, while the residuals are shown in panel (a) of the same figure. The fitted foreground column density is $N_H(f) = 0.65^{-0.06}_{+0.07} \times 10^{23}\,\mathrm{cm^{-2}}$ and the intrinsic column density is $N_H(i) = 2.18^{-0.24}_{+0.34} \times 10^{23}\,\mathrm{cm^{-2}}$. The best-fit CR proton spectral index is $s = 1.68^{+0.50}_{-0.52}$. Table 5.8 shows N_{LECR} and the power injected into the cloud at different E_{min}. Residuals of each fit are shown in Figure 5.28 panels (a), (b), and (c).

Table 5.8: Power injected into G0.66-0.13 by the CR protons with different energy thresholds (E_{min}). The injected power is given by $\frac{dW}{dt} = 4\pi D^2 N_{\mathrm{LECRp}}$.

E_{min} ($\mathrm{keV\,nucleon^{-1}}$)	N_{LECRp} ($10^{-8}\,\mathrm{erg\,cm^{-2}\,s^{-1}}$)	$\frac{dW}{dt}$ ($\times 10^{39}\,\mathrm{erg/s}$)
10^3	$1.23^{+1.57}_{-0.46}$	$0.10^{+0.13}_{-0.04}$
10^4	$1.84^{+1.75}_{-1.16}$	$0.14^{+0.28}_{-0.05}$
10^5	$0.92^{+0.67}_{-0.35}$	$0.074^{+0.054}_{-0.020}$

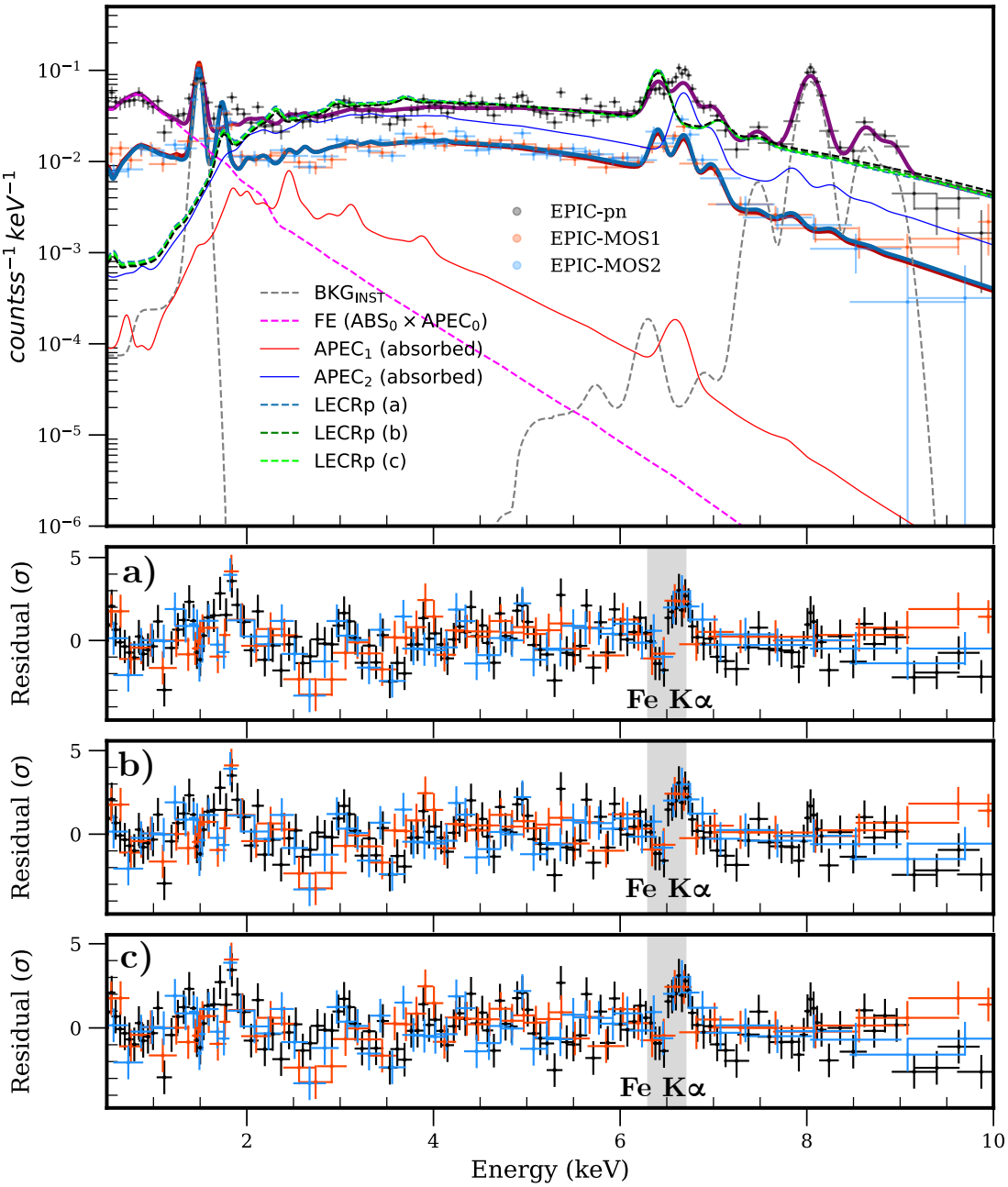

Figure 5.27: Spectral fit and residuals for the XMM-Newton 0.5-10.0 keV merged steady spectra (50%) in Sgr B2. The spectra were fitted using the LECRp model `ABS` × ($APEC_1 + APEC_2 +$ `ABS` × `PO` + $\texttt{GA}_{6.4} + \texttt{GA}_{7.06}$) + $BKG_{\texttt{INST}}$ in `Sherpa`. Top panel: Best-fit spectrum for the LECRp model with $E_{\rm min} = 10^4$ keV nucleon^{-1}. Panel (a) shows residuals for this fit. Panel (b) shows spectral residuals when $E_{\rm min} = 10^3$ keV nucleon^{-1}. Panel (c) shows fit residuals when $E_{\rm min} = 10^5$ keV nucleon^{-1}.

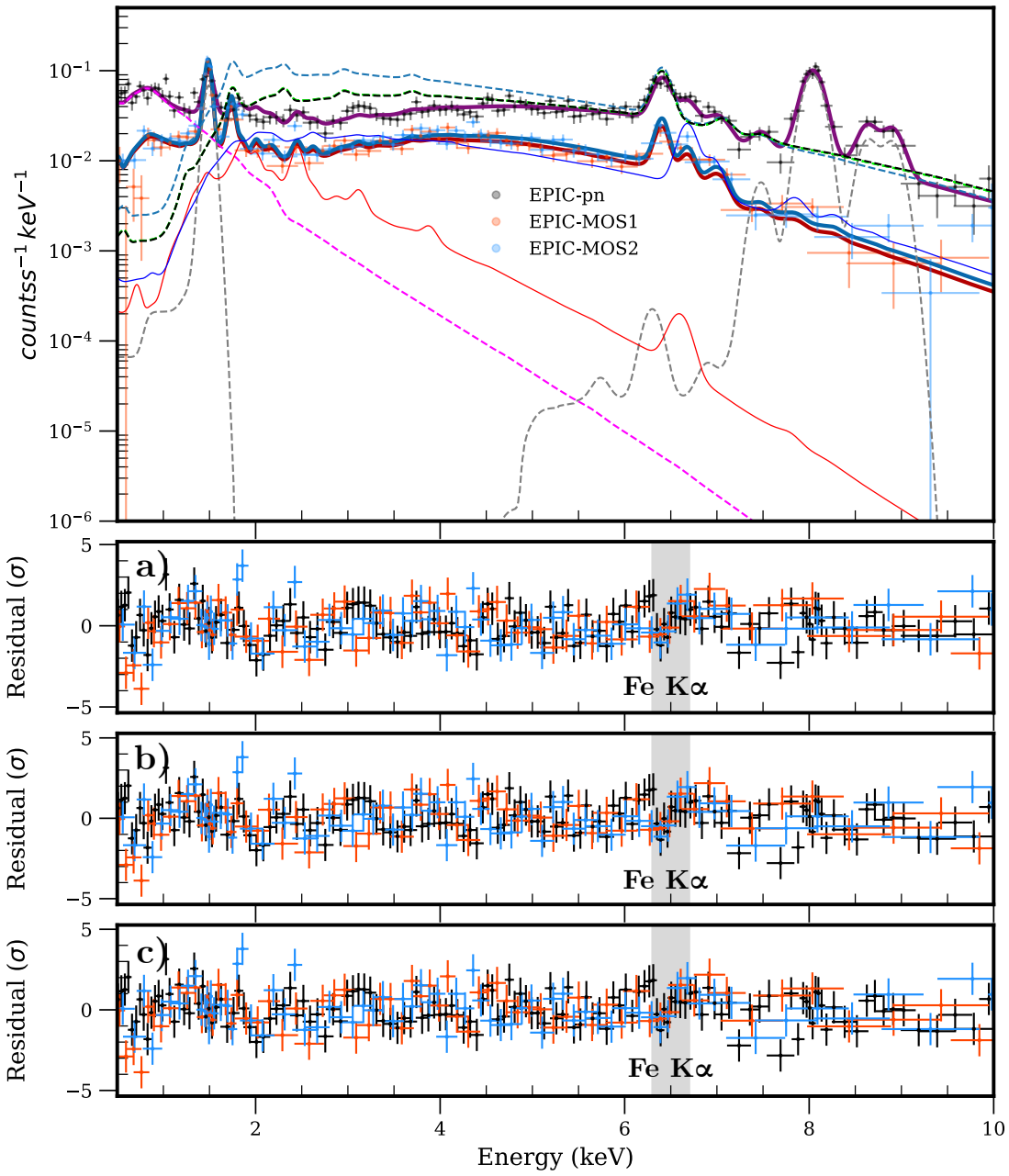

Figure 5.28: Spectral fit and residuals for the XMM-Newton 0.5-10.0 keV merged steady spectra (50%) in G0.66. The spectra were fitted using the LECRp model `ABS` × ($APEC_1 + APEC_2 +$ `ABS` × `PO` + $\texttt{GA}_{6.4} + \texttt{GA}_{7.06}$) + $BKG_{\texttt{INST}}$ in `Sherpa`. Top panel: Best-fit spectrum for the LECRp model with $E_{\rm min} = 10^4$ keV nucleon^{-1}. Panel (a) shows residuals for this fit. Panel (b) shows spectral residuals when $E_{\rm min} = 10^3$ keV nucleon^{-1}. Panel (c) shows fit residuals when $E_{\rm min} = 10^5$ keV nucleon^{-1}.

Chapter 6

Discussion

In this thesis, we examined the non-thermal diffuse steady Fe Kα emission and its application within the Sgr B molecular complex in the GC. This chapter will provide a comprehensive discussion of the findings presented in the previous chapters, linking them to the broader context of the research field. We will analyze the implications of our results, considering both the extraction of steady Fe Kα emission and its possible origin. The results obtained will be discussed and compared with relevant results from the literature.

Contents

6.1 Specificities and Benchmarks

6.1.1 The Poisson Method: A Robust Approach for Faint Signals

We have proposed a novel approach to quantify the level of non-thermal steady Fe Kα emission at 6.4 keV and to select the periods that are compatible with this level of emission. The goal of this study was to reach the faintest levels of Fe Kα observed so far, a depth of analysis not previously identified in the literature. Addressing this complex problem involved exploring various ideas and experimenting with different techniques in order to constrain the very faint signal. Finally, the estimation of the Fe Kα line and the extraction of diffuse emission at the highest resolution were guided by a probabilistic approach. This state-of-the-art developed here is made without prior assumptions about the morphology of the baseline emission or the need for background subtraction. It involved three main parts: (i) the Poisson method for estimating the 6.4 keV Fe Kα line, (ii) the estimation of upper limits of the non-thermal diffuse steady emission, and (iii) deep steady spectra by combining all observations compatible with the upper limit of the steady emission obtained via pixel level comparison. This technique enables the detection of the faintest levels of emission with high statistical accuracy by aggregating data across different epochs, a novel approach that has not been previously implemented.

In general, the continuum subtraction method is widely used for analyzing spectral lines, such as the 6.4 keV Fe Kα line in X-ray astronomy based on discrete photon statistics. However, when applied to small spatial regions, such as individual pixels representing faint fluxes, statistical fluctuations in the continuum estimation will inherently lead to negative estimations of the required line. This necessitates a more sophisticated approach than direct Gaussian assumptions in faint-level analysis, which led to the proposal of the Poisson methodology. The Poisson methodology is well-suited for scenarios with low photon counts but also accommodates higher photon count scenarios driven by Gaussian statistics. The CCDF is justified as a pragmatic method for estimating the steady emission. The upper limits of steady emission are defined as a 50% drop from the maximum density value per epoch. This approach provides a straightforward and easily interpretable threshold based on the value of the CCDF itself. It is sensitive to the overall scale of the data and can be a good indicator of significant changes in the CCDF. A primary challenge of the Poisson method for steady emission derivation is its computational complexity. Unlike Gaussian methods, which often have straightforward computations, the Poisson method involves more complex statistical modeling and numerical integration. Calculating the probability density functions and posterior distributions for Poisson processes, especially when dealing with a large number of pixels and epochs, requires significant computational resources and time. To address this, we employed parallel programming techniques in HPC environments. Since the computations for individual pixels are independent of each other, parallelization effectively reduces computation time, making the Poisson method more feasible for larger-scale analyses such as the entirety of the CMZ. For instance, in extensive regions like Sgr A, where photon counts per pixel are high, the optimization becomes even more useful.

6.1.2 Benchmarking with Previous Works

In this section, our results are benchmarked and compared to those from similar studies in the literature. The benchmark focuses on highlighting two key regions within Sgr B. The main literature in the X-ray domain includes works by Rogers et al. (2022), Kuznetsova et al. (2022), and Zhang et al. (2015). However, direct comparison with these studies has some limitations. First and foremost, our study does not subtract the local background, in contrast to all past studies. During local background subtraction, more extended 6.4 keV emission could be removed, which is not the case in our analysis. Second, the models described in past studies have somewhat different spectral modeling. Lastly, the region descriptions also differ in our case, affecting the comparability of the results. Most importantly, we utilize a steady emission map and deep spectrum accumulated over 20 years, whereas all previous studies have focused solely on the most recent year's data set.

6.1.3 Bright Fe Kα Emission vs Steady Fe Kα Emission

Figure 6.1 shows the non-thermal diffuse steady emission map (50%) derived in this thesis for the first time. This map represents the faintest baseline emission of the Fe Kα line over $\sim$ 20 years, obtained by state of the art developed in our work. Within the 900″ region of Sgr B, it reveals three main subregions that are bright in steady baseline emission: Sgr B2 ($\sim$ 13 square pc corresponds to the size of the upper white box in Figure 6.1), G0.66 ($\sim$ 15 square pc corresponds to the size of the lower white box in Figure 6.1), and part of another region on the eastern side (not investigated further in this work, is likely compatible with G0.56-0.11). Comparison of this steady component with the already studied bright Fe Kα line (Zhang et al. 2015; Terrier et al. 2018; Rogers et al. 2022; Kuznetsova et al. 2022) provides more insights into the associations of two components in these locales. For the comparison, we use the Fe Kα line of Sgr B (with a 450″ radius) by Terrier et al. (2018) (see also Chapter 1).

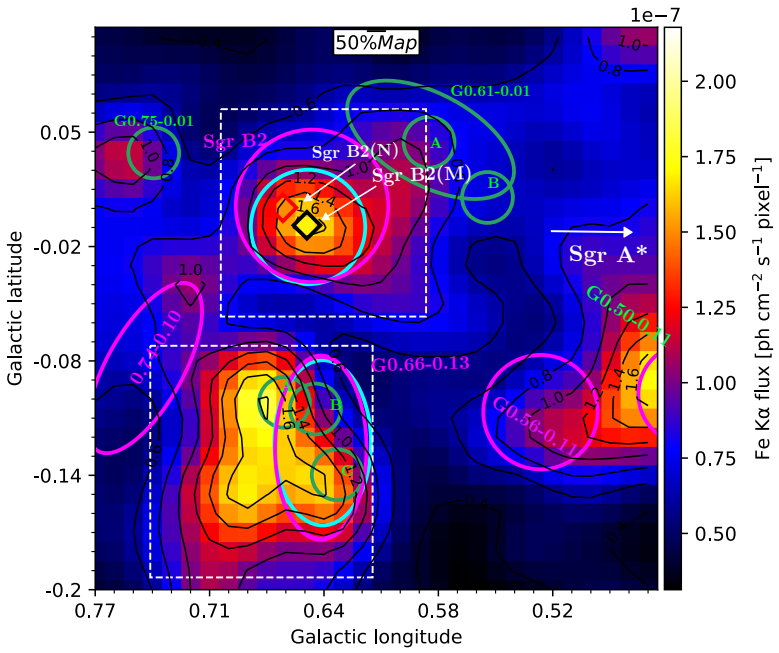

Figure 6.1: Non-thermal diffuse steady emission in Sgr B, highlighting G0.66 and Sgr B2 in the white box regions (this work). The green circles represent A, B, and C substructure of G0.66−0.13, G0.75−0.01, and G0.61−0.01 and its substructure (A, B) from Rogers et al. (2022). The regions in magenta color show G0.66−0.13, G0.74−0.10, Sgr B2, G0.56−0.11, and part of G0.50−0.11 from Terrier et al. (2018), and the cyan ellipse marks the Sgr B2 and G0.66−0.13 from Zhang et al. (2015).

The Sgr B2 subregion in Figure 6.1 showed a similar correlation in the Sgr B2 region in 2000. However, the steady Sgr B2 envelope partially extends towards the northeastern direction (see the left panel and the total gas column density panel in Figure 8 of Terrier et al. (2018)). The steady G0.66

region also has a bright counterpart with different morphological associations. Between 2000 and 2012, two substructures (G0.66–0.13 and G0.74–0.10) with clumpy Fe Kα distribution were identified. However, Figure 6.1 suggests that the steady G0.66 region is mostly between these two subregions, with a partial overlap with G0.66–0.13 with three substructures. The relationship between the steady emission and the time-variable bright component is, therefore, inconclusive for this locale.

The overall steady emission in the Sgr B region shows non-uniform morphology. The association with the bright and steady Fe Kα is not clear as a whole (except for the Sgr B2 core and envelope). Rogers et al. (2022) reported two additional faint substructures, called G0.61–0.00 and G0.75-0.01, which were not reported by previous work and whose variability has not been constrained. The steady component also confirms these structures with association to the G0.75-0.01 and part of the substructure G0.61–0.00. If there is another steady substructure between the Sgr B2 and the molecular clump on the eastern side, all of the steady emission in this region could appear as connected.

In the following sections, we focus on in-depth studies conducted in G0.66 and Sgr B2 subregions.

6.1.3.1 The G0.66 Locale

The G0.66 subregion (G0.66–0.13) has been investigated in the bright Fe Kα line by Zhang et al. (2015); Terrier et al. (2018); Rogers et al. (2022). As discussed earlier, the steady emission and the bright Fe Kα emission in this region show dissociation with different distributions. G0.66–0.13 was identified as an elliptical feature with a major radius of $\sim$ 5 pc and a minor radius of $\sim$ 3 pc (see cyan in Figure 6.1). An increased bright Fe Kα flux of $\sim 1.6 \times 10^{-6}\,\mathrm{cm^{-2}\,s^{-1}\,arcmin^{-2}}$ for the region was observed in 2012 by Terrier et al. (2018). However, Zhang et al. (2015) observed a rapid flux decrease within a year (2012-2013) and suggested that G0.66–0.13 might be an X-ray reflection nebula experiencing a short-duration flaring event propagating through its inner region. The Fe Kα line flux from G0.66–0.13 showed this decreasing trend until 2018. However, the light curves for the substructures within a 40″ radius (regions A, B, and C in Figure 6.1) associated with G0.66–0.13 exhibited different behaviors over time (Rogers et al. 2022). Circle A, which is farthest from Sgr A* in the projected plane, showed an increase in X-ray flux of $\sim 3.6 \times 10^{-6}\,\mathrm{cm^{-2}\,s^{-1}\,arcmin^{-2}}$ in 2018, while regions B and C followed the decreasing pattern of G0.66–0.13.

The steady flux obtained in study for G0.66–0.13 region of Terrier et al. (2018) is $\sim 5{\times}10^{-7}\,\mathrm{cm^{-2}\,s^{-1}\,arcmin^{-2}}$ (see Figure 6.1 lower magenta ellips in G0.66). The steady levels are 68.75% and 86.11% lower than the bright component in 2012 and 2018. Hence, the constrained steady emission is significantly lower than the recent flux measured for this region. This emission has been tested with `XRN` and `LECRp` models to determine whether the steady emission follows similar XRN criteria as its brighter companion or if it has truly stabilized.

6.1.3.2 The Sgr B2 Locale

The Sgr B2 locale has been investigated in the bright Fe Kα line by (Zhang et al. 2015; Terrier et al. 2018; Rogers et al. 2022; Kuznetsova et al. 2022). In contrast to G0.66, the steady emission and the bright Fe Kα emission in Sgr B2 exhibit similar morphology and are located in similar regions. The 120″ radius region showed a bright Fe Kα flux of $\sim 5 \times 10^{-6}\,cm^{-2}\,\mathrm{s^{-1}\,arcmin^{-2}}$ in 2000. After a decade of decreasing, the 2012-2013 bright Fe Kα emission reached 20% of that in 2000 but remained at the same level during 2012-2013 (Zhang et al. 2015). In 2018, Rogers et al. (2022) observed that the bright Fe Kα flux from the inner 90″ of Sgr B2 is (16 $\pm$ 3) % of the value measured in 2000 ($\sim 9.5 \times 10^{-7}\,\mathrm{cm^{-2}\,s^{-1}\,arcmin^{-2}}$ upper limit). Moreover, the decrease since 2012 is not significant considering the statistical uncertainty (Rogers et al. 2022). The upper limit steady flux for the same region was obtained from this study as $5.73 \times 10^{-7}\,\mathrm{cm^{-2}\,s^{-1}\,arcmin^{-2}}$ (cyan circle in Sgr B2 of Figure 6.1). The steady flux is 39.68% lower than the already faint flux levels in 2018.

This bright emission has been tested with `XRN` and `LECRp` models ((Zhang et al. 2015; Kuznetsova et al. 2022)). Based on the decreasing interpretation, Sgr B2 is more likely dominated by multiple scattering. The LECRp-dominated Sgr B2 suggests that if the Fe Kα emission has reached a steady

level, it could be explained by CR proton/ion bombardment in the cloud region (Zhang et al. 2015). The required total CR ion power to sustain this scenario is about 10% of the mechanical power supplied by supernovae in the inner $\sim$ 200 pc of the Galaxy. The CR ionization rate was $\zeta \sim (6-10) \times 10^{-15}\,\mathrm{H}^{-1}\,\mathrm{s}^{-1}$, consistent with the CR ionization rate in the GC environment, supporting the LECRp scenario (Zhang et al. 2015). However, in 2019, Kuznetsova et al. (2022) obtained a CR ionization rate of $\zeta \sim 5 \times 10^{-14}\,\mathrm{H}^{-1}\,\mathrm{s}^{-1}$, an order of magnitude larger than previous and GC values. Due to the high predicted CR ionization rate, they consider the LECRp scenario to be unfavorable.

In Section 5.3.5, we discuss our interpretation of the steady emission in the Sgr B2 locale with both `XRN` and `LECRp` models. Questions on whether the steady level could be explained by a multiple scattering dominated XRN scenario or the cosmic ray proton/ion bombardment scenario will be discussed in the next section. Table 6.1 shows the projected distance (z) and column density obtained along the line of sight for different scattering angles in each case of the `XRN` model scenario (and two previous studies).

Table 6.1: Scattering Angles (θ°_{XRN}), Projected Distances z, and Column Densities for Various `XRN` Models.

Model	Angle (θ°_{XRN})	Z (pc)	N_H(cloud) 10^{24} cm^{-2}
`XRN` a	> 69.02	> -38.35	$\sim 10^{a}$
`XRN` b	> 20.64	> -265.48	7.9^{b}
`XRN` c	28^{c}	-187.07	< 0.4
`CREFL16`^{d}	64	-48.77	$1.23^{+0.79}_{-0.45}$
`Walls`^{e}	28^{+10}_{-16}	-187.07^{-60}_{+283}	$0.79^{+0.31}_{-0.21}$

[a] a = unconstrained face value
[b] b = frozen to Rogers et al. (2022)
[c] c = frozen to Rogers et al. (2022)
[d] d = The CREFL16 model is given by Rogers et al. (2022)
[e] e = The Walls model is given by Rogers et al. (2022)

6.2 Possible Origin of the Steady Emission Towards Sgr B

In Chapter 5, we investigated the morphology and spectroscopy of the non-thermal steady diffuse emission in Sgr B under various settings. We explored different hypotheses related to its origin. The main origin hypotheses considered were contributions from point sources, interactions with molecular material in Sgr B, reflections from past flares, and cosmic ray particle incidents driven by other mechanisms. We confidently ruled out a significant contribution from point sources, as the known point sources cannot explain the morphology of the observed steady emission. The cumulative flux from the faint point source distribution was also negligible compared with the cumulative steady emission flux from spectral fits. Other possible origins are discussed below.

6.2.1 Tentative Correlation with Molecular Clouds

We analyzed 18 molecular lines and 2 atomic lines from the MOPRA 3 mm molecular survey to investigate the presence of molecular material as a possible main contributor to the detected steady non-thermal emission. Using the Structural Similarity Index Measure (SSIM), we examined the structural similarities between the steady emission and the molecular lines in the G0.66 and Sgr B2 subregions. The highest similarity LSR velocity range was obtained through an iterative procedure across the full LSR velocity range with slices of $10\,\mathrm{km\,s^{-1}}$. Although the best fit LSR velocity reveals molecular material along the line of sight towards G0.66 and Sgr B2, a direct one-to-one correlation was not established. This could be due to various factors, such as the emission not corresponding to a specific velocity slice or only part of the cloud is responsible for the emission. For instance, the first and

second panels in Figure 6.2 and Figure 6.3 show the HCN and HNC clouds in the highest similarity LSR velocity range obtained through the SSIM analysis, while the rightmost panel shows the Integrated Intensity maps across the full LSR velocity range (from $-200\,\mathrm{km\,s^{-1}}$ to $200\,\mathrm{km\,s^{-1}}$). In the full integrated molecular map, the northeastern part of the Sgr B2 steady emission shows prominent features highlighting the correlation dependence on the selected velocity range. Establishing a direct link between X-ray emission and molecular clouds, therefore, needs further attention.

Sgr B2 and G0.66 have very different densities, as indicated by their relative antenna temperatures. This difference in density suggests that a uniform process cannot interact equivalently with the entire region. The X-ray map does not trace the densest regions of Sgr B2, which are more effectively probed by other wavelengths, such as submillimeter observations.

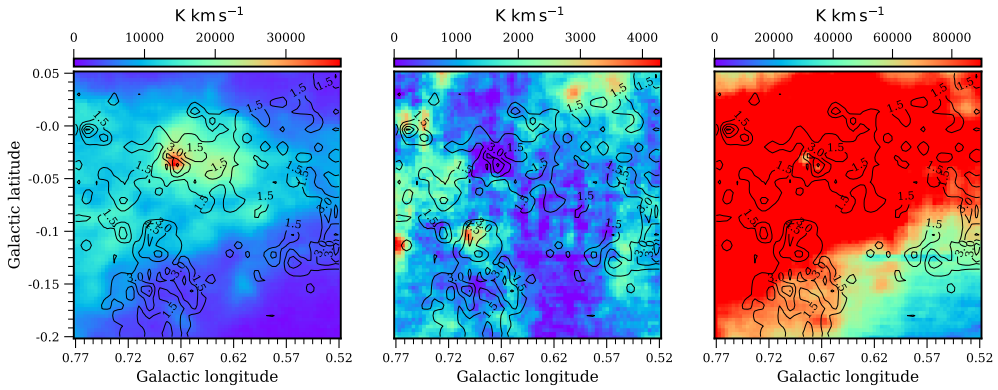

Figure 6.2: Intensity maps for HCN in Sgr B. The left panel shows the integrated LSR map between 89.92 km s^{-1} and 99.92 km s^{-1}, the middle panel shows the integrated LSR map between -20.07 km s^{-1} and -10.07 km s^{-1} (from Chapter 5.2). The rightmost pannel shows the integrated LSR map between -200 km s^{-1} and $+200.0$ km s^{-1}. The contour levels indicate the regions with peak steady X-ray intensity.

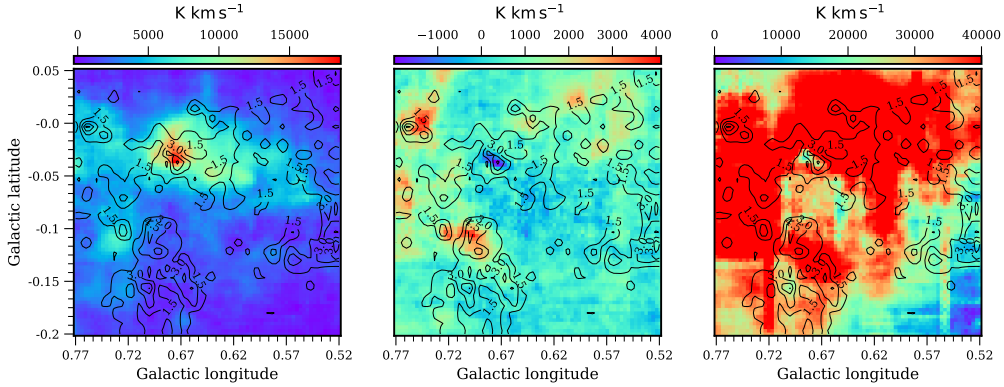

Figure 6.3: Intensity maps for HNC in Sgr B. The left panel shows the integrated LSR map between 80.41 km s^{-1} and 90.41 km s^{-1}, and the middle panel shows the integrated LSR map between -9.58 km s^{-1} and 0.42 km s^{-1} (from Chapter 5.2). The rightmost pannel shows the integrated LSR map between -200 km s^{-1} and $+200.0$ km s^{-1}.The contour levels indicate the regions with peak steady X-ray intensity.

6.2.2 Spectral Constraints for Subregions Sgr B2 and G0.66

The spectral analysis of the very first deep non-thermal steady spectra combining multiple observations was conducted in two ways. The first approach represented the reflection scenario by considering the cloud geometry using the `XRN` model (Chuard et al. 2018), and the second approach involved cosmic ray proton bombardment using the `LECRp` model (Tatischeff et al. 2012) onto the cloud considering the steady levels. The `LECRp` model provided a satisfactory fit for both subregions, while the `XRN` had some degeneracies when fit to Sgr B2, but we obtained a reasonable fit after fixing the scattering angle parameter. In this discussion, we summarize our results and discuss the implications and possible limitations of each model.

6.2.2.1 G0.66

Both the `XRN` and `LECRp` models provided satisfactory fits with χ^2/d.o.f. = 1.29/261 and χ^2/d.o.f. = 1.26/264, respectively. Both models use two absorption components. All the fitted absorption column densities show consistency with previous results within uncertainties, and the possible differences with previous studies could be explained by different absorption modeling.

The `XRN` model provided the *line-of-sight* (l.o.s) geometry of the steady emitting molecular cloud, given by $\theta = 32.19^{+4.62}_{-5.32}$ degrees. The G0.66 is $z \sim 120.35 - 184.09$ pc in front of the projection plane. However, compared to the face value of the G0.66 projected distance (-158 pc), it can be ~ 100 pc in front of Sgr B2[1]. The range $120.35 - 184.09$ pc likely represents the possible independent structure encompassing steady emitting G0.66 along the line of sight. The fitted model column density (both intrinsic absorption of the illuminated part of the cloud and the absorption to the cloud) is one order smaller than the fitted cloud density with a uniform density profile, $N_H(\text{cloud}) = 3.66^{+0.54}_{-0.48} \times 10^{23}$ cm^{-2}

The `LECRp` model provided a CR spectrum with proton spectral index $s = 1.68^{+0.50}_{-0.52}$ for a fixed $E_{\rm min} = 10$ MeV nucleon^{-1}. Such a hard CR spectrum depends weakly on the minimum energy $E_{\rm min}$. However, the total kinetic power required by CR protons in the cloud depends on the minimum energy $E_{\rm min}$. The required total power of the CR protons with energies between $E_{\rm min} = 10$ MeV and $E_{\rm max} = 1$ GeV in the cloud region is $dW/dt = 0.95^{+1.02}_{-0.04} \times 10^{38}$ erg/s. Taking the uncertainty of $E_{\rm min}$ into account (1 MeV $< E_{\rm min} <$ 100 MeV), the required CR proton energy is in the range $dW/dt = (0.5 - 2.2) \times 10^{38}$ erg/s. According to Tatischeff et al. (2012), there is an additional 40% of power that comes from the α-particles with $C_\alpha/C_p = 0.1$. The required kinetic CR ion power is $dW/dt = (0.7 - 3.0) \times 10^{38}$ erg/s, which is roughly 1% of the steady-state mechanical power supplied by supernovae in the inner ~ 200 pc of the Galaxy ($\sim 1.3 \times 10^{40}$ erg/s). To investigate the ionization rate, we first determined the CR power deposited into the G0.66. The power deposited into the cloud is lower than the incident CR ion power because CRs of energy less than $E_{\rm min}$ will not penetrate into the cloud, and CRs of energy greater than 180 MeV can escape from the cloud without depositing energy (Tatischeff et al. 2012). The power deposited by CR ions into G0.66 is obtained using the following formula:

$$\frac{dW_i}{dt} = \int_{E_{\rm min}}^{E_{\rm max}} E \cdot N_{\rm LECRP} \cdot E^{-s}\, dE \tag{6.1}$$

$$\frac{dW_i}{dt} = N_{\rm LECRP} \cdot \frac{E_{\rm max}^{2-s} - E_{\rm min}^{2-s}}{2-s} \tag{6.2}$$

For a CR spectrum with $s = 1.68$, $E_{\rm min} = 10$ MeV, and $E_{\rm max} = 10$ MeV, the power deposited by CR ions into G0.66 is $\dot{W}_d \sim 4.3 \times 10^{37}$ erg/s (45.26% of the dW/dt). If the mass of G0.66 is $M_{G0.66}\, M_\odot$, the CR ionization rate can be calculated using equation 11 in Tatischeff et al. (2012).

[1] Sgr B2 is located 50 pc in front of the projection plane (Chuard et al. 2018)

$$\zeta_H = \frac{1.4 m_p \dot{W}_d}{\epsilon_i M_{G066} M_\odot} \tag{6.3}$$

Where $\epsilon_i \approx 40\,\mathrm{eV}$ is the mean energy required for a fast ion to produce a free electron in a neutral gas mixture of H_2 and He in cosmic proportion. The GC CR ionization rate is $\zeta_H \sim (1-3) \times 10^{-15}\,\mathrm{H^{-1}\,s^{-1}}$. When the ζ_H from G0.66 exceeds the value of the cloud GC CR ionization rate, the CR proton scenario becomes unfavorable as the possible mechanism for steady emission. Hence, the upper limit of the steady emitting G0.66 mass that could hold favorable for the CR scenario is $M_{G0.66}^{upper} = 2.61 \times 10^5\,M_\odot$ (for $\zeta_H = 3 \times 10^{-15}\,\mathrm{H^{-1}\,s^{-1}}$).

The cloud mass could also be constrained by the column density mass equation. For the region of G0.66 ($\sim 14\,\mathrm{pc}^2$) in this study, the mass is given by

$$M_{\mathrm{G0.66}} = A \times N_H \times \mu \times m_p \times M_\odot \tag{6.4}$$

Where A is the cross-sectional area of the cloud, μ is the mean molecular weight with $\mu = 2.33$ towards Sgr B2 (Etxaluze et al. 2013), and m_p and N_H are the mass of the proton and the hydrogen column density, respectively. For $N_H(\mathrm{cloud}) = 3.66 \times 10^{23}\,\mathrm{cm^{-2}}$ the cloud mass $M_{G0.66} = 1.3 \times 10^6\,M_\odot$. The cloud mass obtained by the column density mass equation is the order of magnitude greater than the cloud mass that could hold favorable for the CR scenario ($M_{G0.66}/M_{G0.66}^{upper} \sim 10$). The column density mass does not support the CR scenario.

We proposed that the deep spectra of the faint, steady emission may support the XRN scenario, and the CR scenario was ruled out due to the large cloud column density mass [2]. The XRN-dominated G0.66 is located $\sim 120.35 - 184.09\,\mathrm{pc}$ in front of the projection plane of Sgr $A^\star$, potentially exhibiting a different kinematic structure compared to the bright feature analyzed by Zhang et al. (2015).

6.2.2.2 Sgr B2

The `XRN` and `LECRp` models provided fits with $\chi^2/\mathrm{d.o.f.} = 1.67/235$ and $\chi^2/\mathrm{d.o.f.} = 1.78/235$, respectively. Both models use two absorption components. All the fitted absorption column densities show consistency with previous results within uncertainties, and the possible differences with previous studies could be explained by different absorption modeling. We will also discuss several limitations of the `XRN` model observed for this region.

The `LECRp` model provided a CR spectrum with a proton spectral index $s < 2.38$, with only an upper limit constrained for a fixed $E_{\mathrm{min}} = 10\,\mathrm{MeV\,nucleon^{-1}}$. The required total power of the CR protons with energies between $E_{\mathrm{min}} = 10\,\mathrm{MeV}$ and $E_{\mathrm{max}} = 1\,\mathrm{GeV}$ in the cloud region is $dW/dt = 1.69^{+1.71}_{-1.24} \times 10^{38}\,\mathrm{erg/s}$. The dW/dt obtained by Zhang et al. (2015) (XMM-Newton/NuSTAR) and by Kuznetsova et al. (2022) (INTEGRAL) is significantly greater than the injected power in this study, most probably due to the faint, steady signal representing the lowest value across ~ 20 years in this case ($5.73 \times 10^{-7}\,\mathrm{cm^{-2}\,s^{-1}\,arcmin^{-2}}$ with ~ 30 % lower to the all-time lowest bright Fe K α emission). Moreover, the different spectrum extraction regions could also be a possible reason. Taking the uncertainty of E_{min} into account ($1\,\mathrm{MeV} < E_{\mathrm{min}} < 100\,\mathrm{MeV}$), the required CR proton energy is in the range $dW/dt = (0.49 - 1.21) \times 10^{38}\,\mathrm{erg/s}$. The proton spectral index $s < 2.38$ could not be constrained to determine whether the CR spectrum follows the slope predicted by the diffusive shock acceleration (DSA) theory ($1.5 < s < 2$). Therefore, we do not take into account the contribution from CR ions, and the estimation $dW/dt = (0.49 - 1.21) \times 10^{38}\,\mathrm{erg/s}$ indicates the lower side of the total CR power. To investigate the ionization rate, we first determined the CR power deposited into the Sgr B2 cloud. For the LECRp power is $dW/dt = 1.69^{+1.71}_{-1.24} \times 10^{38}\,\mathrm{erg/s}$ and $s < 2.38$, the power deposited by CR ions into Sgr B2 is $\dot{W}_d < 1.36 \times 10^{38}\,\mathrm{erg/s}$ (80.47% of the dW/dt). Using the total

[2] The ionization rate has to be lower than the previous estimate, and Vice versa

mass of the Sgr B2 molecular cloud $M_{SgrB2} = 6 \times 10^6\, M_\odot$ (Lis & Goldsmith 1990), we obtained the upper limit of the CR ionization rate as $\zeta_H < 4 \times 10^{-16}\,\mathrm{H^{-1}\,s^{-1}}$. This CR ionization rate is 86.67% lower than the GC CR ionization rate $\zeta_H = 3 \times 10^{-15}\,\mathrm{H^{-1}\,s^{-1}}$. Hence, the CR proton bombardment as a possible mechanism for steady emission cannot be excluded based on the ionization rate in the GC.

The `XRN` model failed to fit when all parameters were set to free and provided a marginally satisfactory fit when the scattering angle was frozen to $\theta = 28°$ (Rogers et al. 2022). Moreover, only the upper limit of the cloud density with a uniform density profile was constrained ($N_H(\mathrm{cloud}) < 4.71 \times 10^{23}\,\mathrm{cm^{-2}}$). The high $N_H(\mathrm{cloud})$ indicates a higher density core. These shortcomings of the `XRN` model in Sgr B2 hint towards other factors accounting for this region than primary reflections from the cloud. The fit indicates excess residuals around the 6-7 keV range (see Chapter 5), which could suggest limitations in the spectral model we use. These types of spectral feature alterations hinting at a high-density environment are indicators of multiple scattering. Hence, as previous studies suggested, we propose that the detected steady emission from Sgr B2 could be dominated by multiple scattering. Alternatively, these lower level signals could also be explained by the LECRp model with the estimated upper limit ionization rate $\zeta_H < 4 \times 10^{-16}\,\mathrm{H^{-1}\,s^{-1}}$.

The multiple scatterings alter the spectral features mainly in two ways. First, in the higher energy regime, leading to a characteristic "hump" or broad peak in the spectrum due to the combination of reflected and multiply scattered X-rays (Nandra & George 1994). This feature is known as the "Compton reflection hump" and manifests as a bump[3] in the spectrum approximately between 20-100 keV. The extent of multiple scattering also strongly depends on the scattering angle. The second alteration happens in the lower energy regime, where multiple scatterings alter the features of the Fe Kα line, resulting in a "tail" in the lower energy called the "Compton shoulder" at around 6.4 keV (Yaqoob & Murphy 2011; Odaka et al. 2011). The centroid of the 6.4 keV line can shift toward lower energies as the Compton shoulder becomes a more significant contributor to the overall line flux. This shift occurs because the scattered photons, which have lower energies than the original 6.4 keV photons, add to the detected signal. Additionally, the line profile can become broader and asymmetric due to the combined effects of the unscattered line photons and the scattered photons forming the shoulder. Moreover, this Compton shoulder could only be partially resolvable with the energy resolution of XMM-Newton. When the Compton shoulder is present, a single Gaussian profile cannot best explain the observed features. Figure 6.4 shows the spectral parameters of a simulated cloud (at the position of Sgr B2) as a function of time elapsed since the end of the Sgr A* flare. The multiple scattering regime starts approximately after $t = 125$ years. The hard-X-ray and iron line fluxes gradually decrease while the equivalent width and shoulder-to-peak ratio increase with time. However, the increase is more prominent in dense clouds like Sgr B2 (see green).

[3] Multiple scattering may not be the only cause that produces the hump.

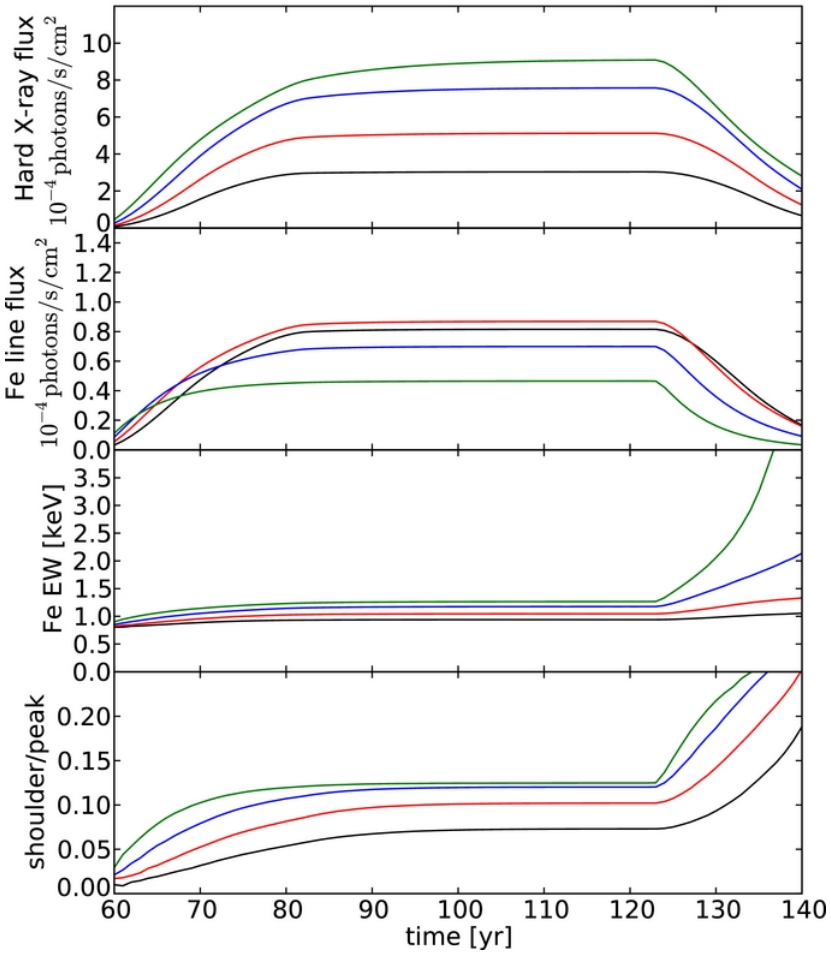

Figure 6.4: Hard-X-ray flux in a range of 20–60 keV (top), iron line flux (second), equivalent width in unit of keV (third), and shoulder-to-peak ratio (bottom) of the Fe K α line as a function of time for cloud masses of $2.5 \times 10^5\,M_\odot$ (Model 1; black), $5.0 \times 10^5\,M_\odot$ (Model 2; red), $1.0 \times 10^6\,M_\odot$ (Model 3; blue), and $2.0 \times 10^6\,M_\odot$ (Model 4; green). The flux unit is 10^{-4} photons s^{-1} cm^{-2}. The cloud position is at $y = -100$ pc. *Figure from Odaka et al. (2011).*

6.2.2.3 Sgr B

This is the first time that the faint, steady emission level can be studied on such a large scale. Both the `XRN` and `LECRp` models failed to provide reasonable fits for the Sgr B region. This is likely due to the large ($36 \times 36\,\mathrm{pc}^2$) area and the non-uniformity of the spatial morphology of the steady emission. Constraining parameters such as cloud scattering angles or the CR spectral index can be challenging in such a large and clumpy region. The morphology of the entire region is concentrated in three main parts: Sgr B2, G0.66, and the area close to the position of Sgr B1 (see Figure 6.1). The phenomenological model provided a weak fit with $\chi^2/\mathrm{d.o.f.} > 2$. However, the 6.4 keV flux from the fit was $F_{6.4\,\mathrm{keV,steady}} = (5.13 \pm 0.19) \times 10^{-7}\,\mathrm{ph\,cm^{-2}\,s^{-1}\,arcmin^{-2}}$. This value is approximately 27.13% smaller than the 6.4 keV flux obtained from imagery analysis by Terrier et al. (2018). The flux in 2012 for the circular region of Sgr B with a ~ 16 pc radius was $F_{6.4\,\mathrm{keV,2012}} = (9.0 \pm 0.2) \times 10^{-7}\,\mathrm{ph\,cm^{-2}\,s^{-1}\,arcmin^{-2}}$.

6.2.3 Conclusion

The first deep XMM-Newton spectral analysis of the non-thermal diffuse steady emission from subregions of Sgr B2 and G0.66 used both the `XRN` and `LECRp` models, with varying success. The `XRN` model supports the observed steady emission in G0.66, but based on the large CR ionization rates, `LECRp` became an unfavorable interpretation. In the case of Sgr B, the `LECRp` model indicated that cosmic ray proton bombardment is a plausible scenario for steady emission. However, the `XRN` model struggled

with the Sgr B2 region, suggesting possible degeneracies when parameters are not well-constrained or multiple scattering is involved. On a global scale, such as in Sgr B, physically motivated models fail due to the larger region size. The steady 6.4 keV flux in the broader Sgr B region was 27.13% smaller than the bright 6.4 keV value obtained in 2012, indicating that our upper limit steady levels remain the lowest on larger scales. We obtained a satisfactory correlation with Sgr B2 and several molecular materials. However, for G0.66, a straightforward correlation was less likely. Submillimeter studies also seem inconclusive in explaining the X-ray emission within the G0.66 region. We discuss possible future works in Chapter 7.

6.3 Methodological and Analytical Limitations

This last section discusses our analysis and interpretation's potential limitations and uncertainties. Understanding these caveats is crucial for interpreting the results and identifying areas for further studies, which will be addressed in the last chapter.

- The technique of deriving the non-thermal diffuse steady emission is based on a probabilistic approach. Without prior information about the morphology of the emission and the absence of faint level analysis, the upper limit we obtained for the steady Fe Kα line is the highest confidence we could reach. Hence, the question may be raised: Is the observed steady Fe K α line truly steady? We don't know yet. Future observations in this region could provide an answer to this question.

- In the Poisson methodology, the estimation that maximizes the probability of the $FeK\alpha$ line (or μ_{line}) depends on both $\mu_{\rm cont}$ and $N_{\rm tot}$. During our analysis, for each epoch and in each pixel, we fixed $\mu_{\rm cont}$ to the estimate provided by Terrier et al. (2018). We then obtained the value of $\mu_{\rm line}$ that maximized the sum of the probabilities for all combinations where $N_{\rm tot} = N_{\rm line} + N_{\rm cont}$. Fixing $\mu_{\rm cont}$ simplifies the maximization approach with the best assumption. However, the uncertainties on $\mu_{\rm cont}$ should be investigated further to assess whether they could impact the 6.4keV characterization.

- In scenarios involving multiple scatterings, the `XRN` model we used may not be effective. More sophisticated models that incorporate partial illumination are needed. Current model limitations, a better understanding of the astrophysical background, and consideration of a combination of different origins for non-thermal emission must be addressed.

Chapter 7

Conclusion and Future Prospects

In this final chapter, I summarize the development of a novel method for observing baseline Fe $K\alpha$ emission, successfully applied to the Sgr B region. Moving forward, this methodology can be expanded to encompass the entire CMZ, providing a more comprehensive understanding of the GC's non-thermal Fe $K\alpha$ emission. This chapter concludes the study and discusses several potential avenues for future research.

Contents

7.1 General Conclusion

The Fe Kα emission in several GC molecular clouds has reached its faintest levels since its discovery in 1993. Several studies have suggested the existence of a baseline level of emission in this region (Kuznetsova et al. 2022; Rogers et al. 2022). In this study, I investigated this baseline called non-thermal diffuse steady emission/steady emission. I achieved the faintest measurement of Fe Kα emission at 6.4 keV in the GC molecular complex Sgr B, with the highest spatial resolution to date. Additionally, the deepest XMM-Newton spectra for this faint emission were obtained. This technique reaches individual pixel levels, providing a generalized method for analyzing faint signals when discrete photon statistics are involved. The interpretation of the Sgr B steady emission has opened new avenues for understanding the current state of this phenomenon. The two subregions (G0.66 and Sgr B2) have been observed currently exhibiting steady emission.

The G0.66 region revealed new features in steady emission not observed in previous studies by bright Fe Kα emission. Three bright cores within the region have been identified. The physics of the observed steady emission is primarily influenced by XRN rather than LECRp/ion. The XRN-dominated G0.66 exists as an independent structure in front of the projection plane of Sgr $A^{\star}$, potentially exhibiting a different structure compared to the bright feature G0.66-0.13 analyzed by Zhang et al. (2015). The cloud density measurements indicate that G0.66 is optically thin. The cloud mass derived from the column density is roughly ~ 10 times higher than the cloud mass limit required to sustain the CR ionization rate in the GC environment. Hence, based on the higher column density mass, the CR scenario was ruled out. The correlation with the molecular materials was inconclusive. Several molecular tracers have some correlation with the northwestern peak of G0.66. However, we have also shown that a single velocity range could not effectively draw all the possible correlations.

The spectral analysis of the steady emission of Sgr B2 suggests both multiple scattering inside the cloud and the LECRp are plausible. The deep steady spectra do not support the current XRN model. Hence, we propose that the observed steady Fe Kα emission from Sgr B2 is mainly driven by multiple scattering in the high-density Sgr B2 core. The complex geometry likely complicates the fitting process with current XRN models. Once the baseline emission is truly reached, the LECRp could play an important role. For example, 30% lower steady emission compared to the already faint 6.4 keV emission has a CR ionization rate lower than the typical values for the GC environment. Monitoring the variability of the 6.4 keV emission in future years should reveal the true contribution of multiple scattering in this level of emission, which is currently assessed as steady with the current dataset. Correlation studies indicate that the steady emission in Sgr B2 could be attributed to the molecular materials, but further analysis is needed.

Neither XRN nor LECRp adequately explain the non-thermal steady emission of the bulk region of Sgr B ($900''^2$). This is likely due to the large area of the region. The morphology of the non-thermal emission is not uniform across the Sgr B, and the large scale complicates the fitting process. For example, XRN assumes a uniform density sphere with a diameter of a few parsecs. Therefore, a focused analysis of the subregions is likely the best approach.

7.2 Future Prospects

The findings of our study open several avenues for future research in understanding the Fe Kα emission in the GC molecular clouds. One of the immediate goals should be to expand the study to the entire CMZ, covering all major molecular clouds within Sgr A, Sgr B, Sgr C, and Sgr D. The estimated steady emission level is by far the faintest level observed. However, our approach is applied to a single molecular complex across five epochs over a 20-year observation period. More observations will place more constraints on upper limit steady Fe Kα levels and confirm whether the derived Fe Kα limit is the true baseline limit or if it is still decreasing (for example, Sgr B2). Integrating data from the latest and next-generation X-ray missions, such as the XRISM (2023) and Athena (2030) observatories, will be crucial. These missions will offer enhanced sensitivity and spectral resolution. Consequently, they could resolve baseline Fe Kα emission with unprecedented clarity and detail, revealing previously unresolvable spectral features. Further investigation into the role of multiple scattering in high-density cores like Sgr B2 is needed at the analysis level. Detailed modeling of the complex geometries could provide deeper insights and help resolve the current ambiguities regarding the emission mechanisms. The tentative correlation with the molecular materials also warrants further investigation. The baseline Fe Kα level in the entire CMZ may also open new insights into its correlation with molecular materials. We hope to significantly advance our knowledge of the processes driving the diffuse Fe Kα emission in the GC environment by addressing these prospects. What exactly occurred with the Fe Kα emission and its future trajectory remains an intriguing and unresolved question.

Bibliography

Aharonian, F., Akhperjanian, A. G., Aye, K. M., et al. 2004, , 425, L13

Anastasopoulou, K., Ponti, G., Sormani, M. C., et al. 2023, , 671, A55

Baganoff, F. K., Bautz, M. W., Brandt, W. N., et al. 2001, , 413, 45

Baganoff, F. K., Maeda, Y., Morris, M., et al. 2003, , 591, 891

Balick, B. & Brown, R. L. 1974a, , 194, 265

Balick, B. & Brown, R. L. 1974b, , 194, 265

Bamba, A., Murakami, H., Senda, A., et al. 2002, arXiv e-prints, astro

Basko, M. M., Sunyaev, R. A., & Titarchuk, L. G. 1974, , 31, 249

Bayes, M. & Price, M. 1763, Philosophical Transactions of the Royal Society of London Series I, 53, 370

Bulbul, E., Kraft, R., Nulsen, P., et al. 2020, APJ, 891, 13

Chuard, D., Terrier, R., Goldwurm, A., et al. 2018, Astronomy Astrophysics, 610, A34

Churazov, E., Sunyaev, R., & Sazonov, S. 2002, Monthly Notices of the Royal Astronomical Society, 330, 817

Clavel, M., Soldi, S., Terrier, R., et al. 2014, , 443, L129

Clavel, M., Terrier, R., Goldwurm, A., et al. 2013, , 558, A32

Dogiel, V., Chernyshov, D., Koyama, K., Nobukawa, M., & Cheng, K.-S. 2011, Publications of the Astronomical Society of Japan, 63, 535

Eisberg, R. & Resnick, R. 1985, Quantum Physics of Atoms, Molecules, Solids, Nuclei, and Particles, 2nd Edition

XMM-Newton SOC: ESA. 2023, *Users Guide to the XMM-Newton Science Analysis System*, XMM-Newton Users Guide

Esposito, P., Rea, N., Borghese, A., et al. 2020, APJL, 896, L30

Etxaluze, M., Goicoechea, J. R., Cernicharo, J., et al. 2013, , 556, A137

Evans, I. N., Primini, F. A., Glotfelty, K. J., et al. 2010, , 189, 37

Freeman, P., Doe, S., & Siemiginowska, A. 2001, in Society of Photo-Optical Instrumentation Engineers (SPIE) Conference Series, Vol. 4477, Astronomical Data Analysis, ed. J.-L. Starck & F. D. Murtagh, 76–87

Fruscione, A., McDowell, J. C., Allen, G. E., et al. 2006, 6270, 62701V

Gehrels, N. 1986, APJ, 303, 336

Genzel, R., Schödel, R., Ott, T., et al. 2003, , 594, 812

Giacconi, R., Gursky, H., Paolini, F. R., & Rossi, B. B. 1962, APS-PRL, 9, 439

Gillessen, S., Genzel, R., Fritz, T. K., et al. 2012, , 481, 51

Gillessen, S., Plewa, P. M., Eisenhauer, F., et al. 2017, , 837, 30

Goldsmith, P. F., Lis, D. C., Lester, D. F., & Harvey, P. M. 1992, , 389, 338

Goodenough, L. & Hooper, D. 2009, arXiv e-prints, arXiv:0910.2998

GRAVITY Collaboration, Abuter, R., Amorim, A., et al. 2019, , 625, L10

Hatchfield, H. P., Battersby, C., Keto, E., et al. 2020, , 251, 14

Heywood, I., Rammala, I., Camilo, F., et al. 2022, , 925, 165

Inui, T., Koyama, K., Matsumoto, H., & Tsuru, T. G. 2009, PASJ, 61, S241

Jansen, F., Lumb, D., Altieri, B., et al. 2001, A&A, 365, L1

Jansky, K. 1933, Proceedings of the Institute of Radio Engineers, 21, 1387

Jones, P. A., Burton, M. G., Cunningham, M. R., et al. 2012, , 419, 2961

Kaneda, H., Makishima, K., Yamauchi, S., et al. 1997, , 491, 638

Koyama, K., Hyodo, Y., Inui, T., et al. 2007a, , 59, 245

Koyama, K., Maeda, Y., Sonobe, T., et al. 1996, , 48, 249

Koyama, K., Tsunemi, H., Dotani, T., et al. 2007b, , 59, 23

Kuznetsova, E., Krivonos, R., Lutovinov, A., & Clavel, M. 2022, , 509, 1605

Lis, D. C. & Goldsmith, P. F. 1990, , 356, 195

Marin, F., Churazov, E., Khabibullin, I., et al. 2023, , 619, 41

McDowell, J. & Rots, A. 1998, Chandra Science Center

McEnery, J. E., Michelson, P. F., Paciesas, W. S., & Ritz, S. 2012, Optical Engineering, 51, 011012

Miniutti, G., Saxton, R. D., Giustini, M., et al. 2019, Nature, 573, 381

Molinari, S., Bally, J., Noriega-Crespo, A., et al. 2011, , 735, L33

Morris, M. & Serabyn, E. 1996, , 34, 645

Mukai, K. 2017, , 129, 062001

Muno, M. P., Baganoff, F. K., Bautz, M. W., et al. 2003, , 589, 225

Muno, M. P., Baganoff, F. K., Bautz, M. W., et al. 2004a, , 613, 326

Muno, M. P., Baganoff, F. K., Bautz, M. W., et al. 2004b, , 613, 326

Muno, M. P., Bauer, F. E., Baganoff, F. K., et al. 2009, , 181, 110

Murakami, H., Koyama, K., Tsujimoto, M., Maeda, Y., & Sakano, M. 2001, , 550, 297

Nandra, K. & George, I. M. 1994, Monthly Notices of the Royal Astronomical Society, 267, 974

Neilsen, J., Nowak, M. A., Gammie, C., et al. 2013, , 774, 42

Nicastro, F., Kaastra, J., Krongold, Y., et al. 2018, Nature, 558, 406

Nobukawa, M., Ryu, S. G., Tsuru, T. G., & Koyama, K. 2011, APJL, 739, L52

Nobukawa, M., Uchiyama, H., Nobukawa, K. K., Yamauchi, S., & Koyama, K. 2016, , 833, 268

Odaka, H., Aharonian, F., Watanabe, S., et al. 2011, , 740, 103

Pagano, M., . G. K. 2018, Principles of Biostatistics (2nd ed.)

Page, K. 2003, XMM-Newton Observations of Type-1 Active Galactic Nuclei, PhD thesis

Pasham, D. R., Remillard, R. A., Fragile, P. C., et al. 2019, Science, 363, 531

Perez, K., Krivonos, R., & Wik, D. R. 2019, , 884, 153

Pierce-Price, D., Richer, J. S., Greaves, J. S., et al. 2000, , 545, L121

Ponti, G., Morris, M. R., Terrier, R., & Goldwurm, A. 2013, Astrophys. Space Sci. Proc., 34, 331

Ponti, G., Morris, M. R., Terrier, R., et al. 2015, , 453, 172

Ponti, G., Terrier, R., Goldwurm, A., Belanger, G., & Trap, G. 2010, , 714, 732

Predehl, P., Costantini, E., Hasinger, G., & Tanaka, Y. 2003, Astronomische Nachrichten, 324, 73

Revnivtsev, M., Sazonov, S., Churazov, E., et al. 2009, , 458, 1142

Revnivtsev, M., Sazonov, S., Gilfanov, M., Churazov, E., & Sunyaev, R. 2006, , 452, 169

Revnivtsev, M., Vikhlinin, A., & Sazonov, S. 2007, , 473, 857

Rogers, F., Zhang, S., Perez, K., Clavel, M., & Taylor, A. 2022, , 934, 19

Ryu, S. G., Koyama, K., Nobukawa, M., Fukuoka, R., & Tsuru, T. G. 2009, , 61, 751

Ryu, S. G., Nobukawa, M., Nakashima, S., et al. 2013, , 65, 33

S. L. Snowden, K. D. K. 2019, Cookbook for Analysis Procedures for XMM-Newton EPIC Observations of Extended Objects and the Diffuse Background

Sanders, J. S., Dennerl, K., Russell, H. R., et al. 2020, A&A, 633, A42

Santa-Maria, M. G., Goicoechea, J. R., Etxaluze, M., Cernicharo, J., & Cuadrado, S. 2021, , 649, A32

Schmiedeke, A., Schilke, P., Möller, T., et al. 2016, A&A, 588, A143

Strüder, L., Briel, U., Dennerl, K., et al. 2001, A&A, 365, L18

Sunyaev, R. & Churazov, E. 1998, , 297, 1279

Sunyaev, R. A., Markevitch, M., & Pavlinsky, M. 1993, , 407, 606

Tatischeff, V., Decourchelle, A., & Maurin, G. 2012, , 546, A88

Terrier, R., Clavel, M., Soldi, S., et al. 2018, A&A, 612, A102

Terrier, R., Ponti, G., Bélanger, G., et al. 2010, APJ, 719, 143

Tiengo, A., Pintore, F., Vaia, B., et al. 2023, APJL, 946, L30

Tsuboi, M., Miyazaki, A., & Uehara, K. 2015, Publications of the Astronomical Society of Japan, 67, 109

Turner, M. J. L., Abbey, A., Arnaud, M., et al. 2001, A&A, 365, L27

Uchiyama, H., Nobukawa, M., Tsuru, T. G., & Koyama, K. 2013, , 65, 19

Valinia, A., Tatischeff, V., Arnaud, K., Ebisawa, K., & Ramaty, R. 2000, , 543, 733

Walls, M., Chernyakova, M., Terrier, R., & Goldwurm, A. 2016, , 463, 2893

Wang, D. and Stolovy, S. 2009, Galactic Center: NASA's Great Observatories Examine the Galactic Center Region, accessed: 15/07/2024

Wang, Z., Bovik, A., Sheikh, H., & Simoncelli, E. 2004, IEEE Transactions on Image Processing, 13, 600

Watson, M. G., Willingale, R., Grindlay, J. E., & Hertz, P. 1981, , 250, 142

Webb, N. A., Coriat, M., Traulsen, I., et al. 2020, , 641, A136

Withers, Christopher, N. S. 2011, Kybernetika, 47, 15

Wolter, H. 1952, Annalen der Physik, 445, 94

XMM-Newton-SOC. 1998, *The European Photon Imaging Camera (EPIC)*, XMM-Newton SOC [Accessed: 2023 Nov]

XMM-Newton-SOC. 2023, The Telescopes of XMM-NEWTON, XMM-Newton Mirror [Accessed: 2023 Nov]

Xu, X.-j., Li, Z., Zhu, Z., et al. 2019, , 882, 164

Yaqoob, T. & Murphy, K. D. 2011, Monthly Notices of the Royal Astronomical Society, 412, 277

Zhang, S., Hailey, C. J., Mori, K., et al. 2015, APJ, 815, 132

Zhu, Z., Li, Z., & Morris, M. R. 2018, , 235, 26